

**Model-based control of transitional and turbulent
wall-bounded shear flows**

**A DISSERTATION
SUBMITTED TO THE FACULTY OF THE GRADUATE SCHOOL
OF THE UNIVERSITY OF MINNESOTA
BY**

Rashad Moarref

**IN PARTIAL FULFILLMENT OF THE REQUIREMENTS
FOR THE DEGREE OF
Doctor of Philosophy**

Professor Mihailo R. Jovanović

January, 2012

© Rashad Moarref 2012
ALL RIGHTS RESERVED

Acknowledgements

It is my great pleasure to thank my advisor, professors, colleagues, friends, and family who made this dissertation possible.

I would like to extend my utmost gratitude to my Ph.D. advisor, Professor Mihailo Jovanović, for building a lively atmosphere for doing research, for his patience and generosity in teaching me all I needed to know, for lots and lots of great ideas and advices that I will never forget, and for his constant support, care, friendship, and encouragement that helped me overcome the hurdles of research. I am truly indebted to Mihailo for directing me into the fascinating world of flow control with its abundance of exciting challenges and opportunities. His passion, research style, and personality have been a source of inspiration throughout my years in graduate school.

I owe sincere thankfulness to the members of my defense committee, Professors Georgiou, Salapaka, and Sverak for their guidance and encouragement. I am grateful to my excellent teachers in University of Minnesota, Professors Balas, Joseph, Longmire, Luo, Mahesh, Saad, and Spirn. I wish to thank the U of M staff and assistants especially Linda Jagerson. I gratefully acknowledge financial support from the National Science Foundation under CAREER Award CMMI-06-44793, from the University of Minnesota Initiative for Renewable Energy and the Environment under Early Career Award RC-0014-11, and from the 3M Science and Technology Fellowship Award. The Minnesota Supercomputing Institute is acknowledged for providing computing resources. My earnest thanks also goes to my great teachers in Iran, in Amirhamidi, Alameh Tabatabaie, and Alavi Elementary Schools, in Tohid High School, and in Sharif University of Technology.

I am obliged to many of my colleagues who supported me at U of M. My officemates, Dr. Shahrouz Takyar, Fu Lin, Binh Lieu, Dr. Xianhua Jiang, Armin Zare, Neil Dhingra, Eric Dahlberg, and Lipeng Ning, made the long and cold Minnesota weekdays warm and pleasant. The numerous activities that we organized together shape the most memorable moments of my time in graduate school. I am specially grateful to Binh Lieu who performed the crucial numerical simulations of Chapters 2 and 3 of this dissertation, and to Fu Lin for many exciting discussions that lead to Chapter 3 of this dissertation; it would not be possible to write this thesis without their contribution. I am also grateful to Professor Makan Fardad and Dr. Donatello Materassi for their friendship and many fruitful discussions.

I owe a great deal of gratitude to all of my friends who made Minneapolis feel like home. My first roommate, Shahrokh, and my best friends, Shahrouz, Baktash, Hamid, Mahmoud Reza, Alireza, Sarah, Sara, Sharareh, Saba, Hossein, Iman, Setareh, Siavash, Mercedeh, Shervin, Amirhossein, Saeed, Maziar, Omid, Elnaz, Ali, Maryam, Morteza, Meysam, Sepehr, Faraz, Mohsen, Mahdi, Kiarash, Haleh, Amir, Samira, Iraj, and many others... It is a great pleasure and honor to be friends with all of you. The countless memories I have with you will remain with me forever. Also, I wish to thank Pat and Art Davis and their family for their friendship over the years and for their kind hospitality on Thanksgiving and Christmas holidays.

I cannot express my gratitude to my family enough. I am indebted to my parents, Zeinab and Masih, and to my brother, Miad, for their infinite love, for teaching me the values that have carried me to this point, for their unwavering encouragements, supports, and sacrifices so I can follow my dreams, and simply for everything. I am grateful to my wonderful wife, Farnoosh, for supporting me throughout this journey with her unconditional love, for standing by me, believing in me, and giving me a reason to continue through the hard times. Finally, I wish to thank my grandparents, aunts, uncles, cousins, and family-in-laws for their love, care, and encouragements over the years.

Dedication

To Zeinab, Masih, Miad, and Farnoosh...

... and to Bertrand Russell for his “Message to our descendants”:

“ I would like to say two things: one intellectual and one moral. The intellectual thing I should want to say to them is this; when you are studying any matter or considering any philosophy, ask yourself only what are the facts and what is the truth that the facts bear out. Never let yourself be diverted either by what you wish to believe or by what you think would have beneficent social effects if it were believed, but look only and solely at what are the facts. [...] The moral thing I should wish to say to them is very simple; I should say love is wise, hatred is foolish. In this world, which is getting more and more closely interconnected, we have to learn to tolerate each other. We have to learn to put up with the fact that some people say things that we don't like. We can only live together in that way, and if we are to live together and not die together, we must learn a kind of charity and a kind of tolerance which is absolutely vital to the continuation of human life on this planet. ”

Abstract

Turbulent flows are ubiquitous in nature and engineering. Dissipation of kinetic energy by turbulent flow around airplanes, ships, and submarines increases resistance to their motion (drag). In this dissertation, we have designed flow control strategies for enhancing performance of vehicles and other systems involving turbulent flows. While traditional flow control techniques combine physical intuition with costly numerical simulations and experiments, we have developed control-oriented models of wall-bounded shear flows that enable simulation-free and computationally-efficient design of flow controllers.

Model-based approach to flow control design has been motivated by the realization that progressive loss of robustness and consequential noise amplification initiate the departure from the laminar flow. In view of this, we have used the Navier-Stokes equations with uncertainty linearized around the laminar flow as a control-oriented model for transitional flows and we have shown that reducing the sensitivity of fluctuations to external disturbances represents a powerful paradigm for preventing transition. In addition, we have established that turbulence modeling in conjunction with judiciously selected linearization of the flow with control can be used as a powerful control-oriented model for turbulent flows.

We have illustrated the predictive power of our model-based control design in three concrete problems: preventing transition by (i) a sensorless strategy based on traveling waves and (ii) an optimal state-feedback controller based on local flow information; and (iii) skin-friction drag reduction in turbulent flows by transverse wall oscillations. We have developed analytical and computational tools based on perturbation analysis (in the control amplitude) for control design by means of spatially- and temporally- periodic flow manipulation in problems (i) and (iii), respectively. In problem (ii), we have utilized tools for designing structured optimal state-feedback gains. Our theoretical results supported by full-scale numerical simulations have revealed that the theory developed in this dissertation for the linearized flow equations with uncertainty has considerable ability to capture full-scale phenomena.

Contents

Acknowledgements	i
Dedication	iii
Abstract	iv
List of Tables	viii
List of Figures	ix
1 Introduction	1
1.1 Transitional and turbulent flows	3
1.1.1 Engineering applications involving turbulent flows	4
1.1.2 Key challenges	5
1.1.3 Thesis objectives	9
1.2 Flow control strategies	9
1.2.1 Feedback control strategies	10
1.2.2 Sensorless control strategies	10
1.3 Model-based flow control	12
1.3.1 Control-oriented modeling	13
1.3.2 Transitional flows	17
1.3.3 Turbulent flows	18
1.4 Preview of main results and contributions	19
2 Controlling the onset of turbulence by streamwise traveling waves	21
2.1 Steady-state analysis	24
2.1.1 Governing equations	24
2.1.2 Base flow	25
2.1.3 Nominal net efficiency	28
2.1.4 Nominal efficiency of laminar controlled flows	29
2.2 Dynamics of fluctuations around traveling waves	32
2.2.1 Evolution model with forcing	32

2.2.2	Frequency representation of the linearized model	33
2.2.3	Energy density of the linearized model	36
2.2.4	Perturbation analysis of energy density	38
2.3	Energy amplification in Poiseuille flow with $R_c = 2000$	40
2.3.1	Energy density of flow with no control	41
2.3.2	Energy amplification of flow with control	41
2.3.3	Effect of control amplitude on energy amplification	46
2.3.4	Energy amplification mechanisms	50
2.4	Direct numerical simulations	53
2.4.1	Base flow and nominal net efficiency	54
2.4.2	Avoidance/promotion of turbulence by streamwise traveling waves	56
2.4.3	Energy amplification mechanisms	67
2.4.4	Flow visualization	69
2.4.5	Relaminarization by downstream waves	72
2.5	Summary	79
3	Localized optimal feedback control of transitional channel flow	81
3.1	Preliminaries	82
3.1.1	Governing equations	82
3.1.2	Actuation along the discrete lattice	84
3.2	Design of localized optimal feedback gains	85
3.2.1	Computation of the structured optimal feedback gains	88
3.3	Localized control of transition	89
3.3.1	Receptivity of the controlled flows	90
3.3.2	Direct numerical simulations	93
3.4	Summary	95
4	Model-based design of transverse wall oscillations for turbulent drag reduction	96
4.1	Problem formulation	99
4.1.1	Turbulent mean velocity	100
4.1.2	Skin-friction drag coefficient and net efficiency	103
4.1.3	The k - ϵ model for ν_T	105
4.2	Stochastically forced flow with control	105
4.2.1	Computation of the velocity correlations	107
4.2.2	Influence of fluctuations on turbulent viscosity	112
4.2.3	Skin-friction drag coefficient and net efficiency	113
4.3	Turbulent drag reduction	114
4.3.1	Saved power	115
4.3.2	Required control power	116
4.3.3	Net efficiency	119
4.3.4	Drag reduction in flows with larger Reynolds numbers	119

4.3.5	Effect of control on turbulent viscosity and turbulent mean velocity	120
4.3.6	Effect of control on turbulent kinetic energy	122
4.4	Turbulent flow structures	123
4.5	Summary	129
5	Conclusions and future directions	133
	References	136
	Appendix A. Determining numerical adjoints	148
	Appendix B. Shanks transformation	149
	Appendix C. Matching the homogeneous isotropic turbulence spectrum by a stochastically-forced linearized model	151
	Appendix D. Perturbation analysis of eigenvalues of a class of self- adjoint operators	154
D.1	Introduction	154
D.2	Preliminaries	155
D.2.1	Perturbation theory	156
D.2.2	Elementary reduction	158
D.2.3	Reduction process	158
D.2.4	Iterating the process	159
D.3	Spectrum perturbation of periodic systems	160
D.4	Example: transient response analysis of a spatially-periodic system . . .	164
D.5	Summary	168
	Appendix E. Remarks on computing the \mathcal{H}_2 norm of incompressible fluids using descriptor state-space formulation	170
E.1	Introduction	170
E.2	Preliminaries	171
E.2.1	Finite dimensional descriptor form	172
E.3	Computing the \mathcal{H}_2 norm	173
E.3.1	Obtaining the Weierstrass-like form	173
E.3.2	Solving the generalized Lyapunov equation	174
E.4	Incompressible plane channel flow	175
E.5	Numerical approximation of spatial operators	178
E.5.1	Operators and their adjoints	179
E.5.2	Change of variables	181
E.6	Summary	182

List of Tables

2.1	The computational domain and spatial discretization considered in simulations of the uncontrolled flow, DTWs with ($c = 5, \omega_x = 2, \alpha = 0.035, 0.050,$ and 0.125), and UTWs with ($c = -2, \omega_x = 0.5, \alpha = 0.015, 0.050,$ and 0.125). Symbols identify the corresponding flow in figures that follow. The box sizes in the streamwise and spanwise directions are denoted by L_x and L_z , respectively. The number of grid points in the streamwise, wall-normal, and spanwise directions are represented by $N_i, i = \{x, y, z\}$, respectively.	54
2.2	Nominal results in Poiseuille flow with $R_\tau = 63.25$. The nominal flux, $U_{B,N}$, and skin-friction drag coefficient, $C_{f,N}$, are computed using the base flow described in § 2.4.1. The produced power, $\% \Pi_{prod}$, required power, $\% \Pi_{req}$, and net power, $\% \Pi_{net}$, are normalized by the power required to drive the uncontrolled flow. The produced and net powers are computed with respect to the laminar uncontrolled flow.	56
2.3	Results of 3D simulations in Poiseuille flow with $R_\tau = 63.25$ for initial conditions of small, moderate, and large energy (respectively, $E(0) = 2.25 \times 10^{-6}, E(0) = 5.0625 \times 10^{-4},$ and $E(0) = 2.5 \times 10^{-3}$). The values of $C_f, \% \Pi_{prod}, \% \Pi_{req},$ and $\% \Pi_{net}$ correspond to $t = 1000$. For small initial energy, the produced and net powers are computed with respect to laminar uncontrolled flow; for moderate and large initial energies, they are computed with respect to turbulent uncontrolled flow.	58
4.1	The parameters used in our study. At each R_τ, c_1 and c_2 are selected to minimize the least squares deviation between the mean streamwise velocity obtained from (4.6)-(4.9) and the mean velocity obtained in DNS [1,2]. The bulk flux U_B is kept constant by adjusting the pressure gradient.	115

List of Figures

1.1	(a) <i>The starry night</i> by Vincent van Gogh in 1889 is suggestive of the swirling motion of galaxies and flow around submerged bodies; (b) Sketch of the vortical motion of water pouring into a pond, by Leonardo da Vinci (1452-1519).	2
1.2	Fluid mechanics pioneers.	2
1.3	(Left) transition from laminar to turbulence over an aircraft wing (efluids photo by Miguel Visbal). (Right) the energy exchange between the solid surface and fluid is larger in a turbulent flow relative to a laminar flow. Therefore, turbulent flows exhibit larger resistance to motion (drag) than laminar flows.	3
1.4	Skin-friction drag is responsible for approximately 50% and 90% fuel consumption in air- and water- vehicles, respectively.	4
1.5	(Left) wind turbines are becoming progressively larger to increase efficiency and reduce electricity cost. (Right) The wake from upstream turbines affects those downstream of wind.	5
1.6	The paths from receptivity to transition (figure taken from [3]).	6
1.7	Experiment and flow visualization of transitional boundary layer over a flat plate [4] The bottom row shows the top view of the flow where x is the flow direction and z is the spanwise direction.	8
1.8	Direct numerical simulations of transitional boundary layer over a flat plate. The panels from top to bottom show the streamwise velocity, respectively, outside, on the edge, and inside the boundary layer (photo courtesy of T. Zaki taken from [5]).	8
1.9	(a) An array of distributed hot-film shear-stress sensors and wall-deformation actuators for feedback flow control [6]; (b) Sketch of a localized control strategy where the actuator placed at (r, s) uses information from only the nearest neighbors on the two-dimensional lattice.	10
1.10	(a) Photograph of a shark dermal denticle; (b) Sketch of a riblet-mounted surface with x denoting the flow direction; (c) Transverse wall oscillations; and (d) Wall transpiration in the form of streamwise traveling wave. . .	11

1.11	(a) Three-dimensional pressure-driven channel flow; (b) Input-output analysis of the Navier-Stokes equations linearized around laminar velocity.	15
1.12	The energy density (\mathcal{H}_2 norm) as a function of streamwise and spanwise wavenumbers, $E(\boldsymbol{\kappa})$, for the flow with no control at $R_c = 2000$ [7]. The axes and the coloring are in logarithmic scale. The wavenumbers corresponding to the streamwise streaks and the TS waves are highlighted.	15
2.1	A pressure driven channel flow with blowing and suction along the walls.	24
2.2	Second order correction to the nominal flux, $U_{B,2}(c, \omega_x)$, for (a) upstream waves; and (b) downstream waves in Poiseuille flow with $R_c = 2000$. Note: the level sets are obtained using a sign-preserving logarithmic scale; e.g., 5 and -3 should be interpreted as $U_{B,2} = 10^5$ and $U_{B,2} = -10^3$, respectively.	26
2.3	(a) The nominal flux, $U_B(\alpha)$; and (b) the nominal skin-friction drag coefficient, $C_f(\alpha)$, for a pair of UTWs and a pair of DTWs in Poiseuille flow with $R_c = 2000$. The results are obtained by solving (2.3) subject to (2.2), in the steady-state, using Newton's method; U_B and C_f of the uncontrolled laminar and turbulent flows are also shown for comparison.	27
2.4	Second order correction to the nominal net efficiency, $\pi_2(c, \omega_x)$, for (a) upstream waves; and (b) downstream waves in Poiseuille flow with $R_c = 2000$. Note: the level sets are obtained using a sign-preserving logarithmic scale; e.g., -4 should be interpreted as $\pi_2 = -10^4$	30
2.5	The steady-state net efficiency, $\% \Pi_{net}$, of <i>laminar</i> controlled flows as a function of control amplitude α for a UTW with ($c = -2$, $\omega_x = 0.5$) and a DTW with ($c = 5$, $\omega_x = 2$) at $R_c = 2000$. The results are obtained by <i>assuming</i> that the uncontrolled flow (a) remains laminar; and (b) becomes turbulent.	30
2.6	The wave amplitude, α_{max} , for which the nominal net efficiency, $\% \Pi_{net}$, is positive at $R_c = 2000$ for (a) a pair of UTWs; and (b) a pair of DTWs. The solid curves are computed using Newton's method, and the dotted curves are computed using (2.10). The results are obtained by <i>assuming</i> that the controlled flow stays laminar while the uncontrolled flow becomes turbulent.	32
2.7	A Bloch wave $\mathbf{d}(x, y, z, t)$ defined in (2.12) is obtained by the superposition of weighted Fourier exponentials with frequencies $(\theta_n, \kappa_z) _{n \in \mathbb{Z}}$, with weights determined by $\bar{\mathbf{d}}_n(y, \kappa_z, t)$	33
2.8	Energy density $\tilde{E}_0(\kappa_x, \kappa_z)$ of the uncontrolled Poiseuille flow with $R_c = 2000$. The plot is given in the log-log-log scale.	40

2.9	For fixed ω_x and θ , $\bar{E}_0(\theta, \kappa_z; \omega_x)$ represents energy density of fluctuations composed of all wavenumbers $\theta_n = \{\theta + n\omega_x\}_{n \in \mathbb{Z}}$; $\bar{E}_0(\theta, \kappa_z; \omega_x) = \sum_{n=-\infty}^{\infty} \tilde{E}_0(\theta + n\omega_x, \kappa_z)$	42
2.10	(a) and (c): Second order correction to the energy amplification, $\hat{g}_2(c, \omega_x)$, of the modes with $(\theta, \kappa_z) = (0, 1.78)$, in the presence of (a) UTWs; and (c) DTWs in Poiseuille flow with $R_c = 2000$. (b) and (d): Second order correction to the nominal required power, $\Pi_{req,2}(\omega_x; c)$, for (b) UTWs; and (d) DTWs. The dot and the square, respectively, denote $(c = -2, \omega_x = 0.5)$ (as selected in [8]) and $(c = 5, \omega_x = 2)$. Note: the plots on the left are obtained using a sign-preserving logarithmic scale; e.g., $\hat{g}_2 = 5$ and $\hat{g}_2 = -3$ should be interpreted as $\bar{E}_2 = 10^5 \bar{E}_0$ and $\bar{E}_2 = -10^3 \bar{E}_0$, respectively.	44
2.11	Second order correction to the energy amplification, $\hat{g}_2(\theta, \kappa_z)$, for traveling waves with (a) $(c = -2, \omega_x = 0.5)$; (b) $(c = 3, \omega_x = 1.5)$; (c) $(c = 5, \omega_x = 0.5)$; and (d) $(c = 5, \omega_x = 2)$ in Poiseuille flow with $R_c = 2000$. . .	45
2.12	Second order correction to the energy amplification, $\hat{g}_2(c, \omega_x)$, of the modes with $(\theta(\omega_x), \kappa_z) = (1.2 - \omega_x \lfloor \frac{1.2}{\omega_x} \rfloor, 0)$, in the presence of (a) UTWs; and (b) DTWs in Poiseuille flow with $R_c = 2000$. The dot and the square, respectively, denote $(c = -2, \omega_x = 0.5)$ and $(c = 5, \omega_x = 2)$	46
2.13	The dark regions identify values of wave speed and frequency that, up to a second order in α , suppress the energy amplification of both most energetic and least stable modes in Poiseuille flow with $R_c = 2000$ subject to: (a) UTWs; and (b) DTWs.	47
2.14	Energy density, $\bar{E}(\kappa_z)$, of the fundamental mode $\theta = 0$ in Poiseuille flow with $R_c = 2000$ and $(c = 5, \omega_x = 2, \alpha = 0.025)$. The controlled flow results are obtained using perturbation analysis up to a second order in α , and Shanks transformation up to a fourth order in α	48
2.15	Energy density, $\bar{E}(\kappa_z)$, of the fundamental mode $\theta = 0$ in Poiseuille flow with $R_c = 2000$ subject to: (a) a UTW with $c = -2$ and $\omega_x = 0.5$; and (b) a DTW with $c = 5$ and $\omega_x = 2$. Shanks transformation up to a fourth order in α is used in computations. The truncation results (hollow circles) are obtained for (a) $\alpha = 0.016$; and (b) $\alpha = 0.1$	48
2.16	Energy density, $\bar{E}(\kappa_z)$, of the fundamental mode $\theta = 0$ in Poiseuille flow with $R_c = 2000$ subject to a UTW with $c = -5$ and $\omega_x = 0.03$. Shanks transformation up to a fourth order in α is used in computations. . . .	49

2.17	Contribution of production and dissipation terms to energy density of $\theta = 0$ mode in Poiseuille flow with $R_c = 2000$ subject to (a)-(c) a DTW with ($c = 5, \omega_x = 2$); and (d)-(f) a UTW with ($c = -2, \omega_x = 0.5$). (a,d) uncontrolled flow; (b,e) second order corrections; and (c,f) controlled flows. In (c,f), the controlled flow results are obtained using approximation up to a second order in α , and the uncontrolled flow results are shown for comparison.	51
2.18	Mean streamwise base velocity, $\bar{U}(y)$, obtained in 2D simulations of the uncontrolled Poiseuille flow with $R_\tau = 63.25$, \times , and controlled flows subject to: (a) DTWs with \square , ($c = 5, \omega_x = 2, \alpha = 0.035$); \circ , ($c = 5, \omega_x = 2, \alpha = 0.05$); \diamond , ($c = 5, \omega_x = 2, \alpha = 0.125$); and (b) UTWs with \triangleleft , ($c = -2, \omega_x = 0.5, \alpha = 0.015$); ∇ , ($c = -2, \omega_x = 0.5, \alpha = 0.05$); Δ , ($c = -2, \omega_x = 0.5, \alpha = 0.125$).	55
2.19	Energy of the velocity fluctuations, $E(t)$, for the initial condition with small energy: (a) \times , uncontrolled; \circ , a DTW with ($c = 5, \omega_x = 2, \alpha = 0.05$); and (b) UTWs with \triangleleft , ($c = -2, \omega_x = 0.5, \alpha = 0.015$); ∇ , ($c = -2, \omega_x = 0.5, \alpha = 0.05$); Δ , ($c = -2, \omega_x = 0.5, \alpha = 0.125$).	59
2.20	(a) Skin-friction drag coefficient, C_f ; (b) normalized required power, $\% \Pi_{req}$; (c) normalized produced power, $\% \Pi_{prod}$; and (d) normalized net power, $\% \Pi_{net}$, for the initial condition with small energy: \times , uncontrolled flow; \circ , DTW with ($c = 5, \omega_x = 2, \alpha = 0.05$); and UTWs with \triangleleft , ($c = -2, \omega_x = 0.5, \alpha = 0.015$); ∇ , ($c = -2, \omega_x = 0.5, \alpha = 0.05$); Δ , ($c = -2, \omega_x = 0.5, \alpha = 0.125$).	61
2.21	(a) Energy of the velocity fluctuations, $E(t)$; (b) skin-friction drag coefficient, $C_f(t)$; (c) normalized required power, $\% \Pi_{req}$; and (d) normalized net power, $\% \Pi_{net}$, for the initial condition with moderate energy: \times , uncontrolled; and UTWs with \triangleleft , ($c = -2, \omega_x = 0.5, \alpha = 0.015$); ∇ , ($c = -2, \omega_x = 0.5, \alpha = 0.05$); Δ , ($c = -2, \omega_x = 0.5, \alpha = 0.125$).	63
2.22	(a) Energy of the velocity fluctuations, $E(t)$; (b) skin-friction drag coefficient, $C_f(t)$; (c) normalized required power, $\% \Pi_{req}$ (solid), normalized produced power, $\% \Pi_{prod}$ (dashed); and (d) normalized net power, $\% \Pi_{net}$, for the initial condition with moderate energy: DTWs with \square , ($c = 5, \omega_x = 2, \alpha = 0.035$); \circ , ($c = 5, \omega_x = 2, \alpha = 0.05$).	64
2.23	(a) Energy of the velocity fluctuations, $E(t)$; (b) skin-friction drag coefficient, $C_f(t)$; (c) normalized required power, $\% \Pi_{req}$ (solid), normalized produced power, $\% \Pi_{prod}$ (dashed); and (d) normalized net power, $\% \Pi_{net}$, for the initial condition with large energy: \times , uncontrolled; DTWs with \circ , ($c = 5, \omega_x = 2, \alpha = 0.05$); and \diamond , ($c = 5, \omega_x = 2, \alpha = 0.125$).	66

2.24	(a) and (b) Production, $P_E(t)$ (solid), and dissipation, $D_E(t)$ (dashed), of kinetic energy in Poiseuille flow with $R_\tau = 63.25$ for the initial condition with small energy: (a) \times , uncontrolled; \circ , DTW with ($c = 5, \omega_x = 2, \alpha = 0.05$); and (b) ∇ , UTW with ($c = -2, \omega_x = 0.5, \alpha = 0.05$); Δ , UTW with $\alpha = 0.125$. (c) $P_E(t) + D_E(t)$ for the UTW with ($c = -2, \omega_x = 0.5, \alpha = 0.05$).	68
2.25	Streamwise velocity fluctuations, $u(x, z)$, at $y = -0.5557$ ($y^+ = 28.11$), (a), (c), (e) $t = 50$; and (b), (d), (f) $t = 120$ for initial condition with moderate energy: uncontrolled flow; UTW with ($c = -2, \omega_x = 0.5, \alpha = 0.05$); and DTW with ($c = 5, \omega_x = 2, \alpha = 0.05$).	70
2.26	Simulation of the uncontrolled flow for the initial condition with moderate energy. (a), (c), (e) 3D visualizations of the isosurfaces of the discriminant, $D > 10^{-6}$ (blue), $D > 10^{-5}$ (green), and $D > 10^{-4}$ (red). (b), (d), (f) 2D visualizations of the crossflow velocity vectors (arrows) and the x -averaged streamwise vorticity (color plots).	73
2.27	Simulation of the DTW with ($c = 5, \omega_x = 2, \alpha = 0.05$) for the initial conditions with moderate energy. (a), (c), (e) 3D visualizations of the isosurfaces of the discriminant, $D > 10^{-6}$ (blue), $D > 10^{-5}$ (green), and $D > 10^{-4}$ (red). (b), (d), (f) 2D visualizations of the crossflow velocity vectors (arrows) and the x - averaged streamwise vorticity (color plots).	74
2.28	Simulation of the UTW with ($c = -2, \omega_x = 0.5, \alpha = 0.05$) for the initial condition with moderate energy. (a), (c), (e) 3D visualizations of the isosurfaces of the discriminant, $D > 10^{-6}$ (blue), $D > 10^{-5}$ (green), and $D > 10^{-4}$ (red). (b), (d), (f) 2D visualizations of the crossflow velocity vectors (arrows) and the x -averaged streamwise vorticity (color plots). Only one quarter of the channel ($x \in [0, 2\pi]$) is shown.	75
2.29	3D visualizations of the isosurfaces of the discriminant, $D > 10^{-5}$ (blue), $D > 10^{-4}$ (green), and $D > 10^{-3}$ (red) for the uncontrolled flow (left figures) and the UTW with ($c = -2, \omega_x = 0.5, \alpha = 0.05$) (right figures) for the initial condition with moderate energy. Only one quarter of the channel ($x \in [0, 2\pi]$) is shown for the UTW.	76
2.30	Energy of velocity fluctuations around base flows. Simulations are initiated by a fully developed turbulent flow with $R_c = 2000$: \times , uncontrolled; DTWs with \square , ($c = 5, \omega_x = 2, \alpha = 0.035$); \circ , ($c = 5, \omega_x = 2, \alpha = 0.05$); and \diamond , ($c = 5, \omega_x = 2, \alpha = 0.125$).	77
2.31	(a) Energy of velocity fluctuations around base flows, $E(t)$; and (b) skin-friction drag coefficient, $C_f(t)$. Simulations are initiated by a fully developed turbulent flow with $R_c = 4300$: \times , uncontrolled; DTWs with \square , ($c = 5, \omega_x = 2, \alpha = 0.035$); \circ , ($c = 5, \omega_x = 2, \alpha = 0.05$); and \diamond , ($c = 5, \omega_x = 2, \alpha = 0.125$).	77

2.32	Mean velocity, $\overline{U}(y)$, and streamwise velocity (colored plots) at $y = -0.7518$. Simulations are initiated by a fully developed turbulent flow with $R_c = 4300$: \times , $t = 0$; \bullet , $t = 100$; $*$, $t = 900$. The dashed line identifies the laminar mean velocity induced by the DTW with ($c = 5$, $\omega_x = 2$, $\alpha = 0.125$).	78
3.1	A periodic channel with size $L_x \times 2 \times L_z$	83
3.2	Sketch of a localized control strategy where the actuator placed at (r, s) uses information from only the nearest neighbors on the two-dimensional lattice.	87
3.3	Energy density of the velocity fluctuations $E(\kappa_n)$ for the uncontrolled flow with $R_c = 2000$ (\circ), optimal centralized (\square), truncated centralized (∇), and localized optimal (\diamond) controllers for (a) $\kappa_m = 0$; (b) $\kappa_m = 0.5$; (c) $\kappa_m = 1$; and (d) $\kappa_m = 1.5$. The truncated controller is unstable for $\kappa_m = \{0.5, 1\}$ and $\kappa_n = \{0, 1\}$ and the energy density is not defined for any combination of these wavenumbers. Note: The energy density is computed at the discrete set of wavenumbers κ_n and κ_m (symbols) and the lines are plotted for visual aid.	91
3.4	(a) Energy of the velocity fluctuations $E(t)$; (b) skin-friction drag coefficient $C_f(t)$; and (c) control energy $(v_u^2(t) + v_l^2(t))/2$ for the flow with no control, and optimal centralized, truncated centralized, and localized optimal controllers. The results are obtained using DNS with $R_c = 2000$	92
3.5	The optimal centralized and localized optimal feedback gains used by the actuator at the lower wall placed at $(r, s) = (0, 0)$, from the wall-normal velocity information at locations (a) $(r, s) = (0, -1)$; (b) $(r, s) = (0, 0)$; and (d) $(r, s) = (-1, 0)$. The results are obtained for the flow with $R_c = 2000$	94
4.1	(a) Pressure driven channel flow; and (b) Channel flow subject to transverse wall oscillations.	99
4.2	(a) The real part; and (b) the imaginary part of the solution $W_{p,0}(y^+; T^+)$ to system (4.8)-(4.9) with $R_\tau = 186$ and $30 \leq T^+ \leq 300$. T^+ increases in the direction of the arrows.	102
4.3	(a) The required power, $\% \Pi_{\text{req},0}(T^+)$, as a function of the period of oscillations T^+ for the flow with $R_\tau = 186$; (b) Comparison between $\% \Pi_{\text{req},0}(T^+)$ (solid curve) and $\% \Pi_{\text{req}}(T^+)$ (symbols). Symbols show DNS data at $R_\tau = 200$ [9] for control amplitudes $\alpha = 2.25$, \circ ; $\alpha = 6$, \square ; and $\alpha = 9$, ∇ . The results in (b) are normalized by their largest values.	103
4.4	Block diagram representing Steps (i)-(iv) of our simulation-free approach for determining the effect of control on skin-friction drag in turbulent flows. The hollow arrows indicate that some of the coefficients in the model of the output subsystems are determined by the outputs of the corresponding input subsystems.	107

4.5	(a) Second-order correction to the saved power, $\% \Pi_{\text{save},2}(T^+)$, as a function of the period of oscillations T^+ for the flow with $R_\tau = 186$; (b) Comparison between $\% \Pi_{\text{save},2}(T^+)$ (solid curve) and $\% \Pi_{\text{save}}(T^+)$ (symbols). Symbols show DNS data at $R_\tau = 200$ [9] for control amplitudes $\alpha = 2.25$, \circ ; $\alpha = 6$, \square ; and $\alpha = 9$, ∇ . The results in (b) are normalized by their largest values.	116
4.6	(a) Fourth-order correction to the required power, $\% \Pi_{\text{req},2}(T^+)$, as a function of the period of oscillations T^+ for the flow with $R_\tau = 186$; (b) Comparison between $\% \Pi_{\text{req},2}(T^+)$ (solid curve) and $\% \Pi_{\text{req}} - \alpha^2 \% \Pi_{\text{req},0}(T^+)$ (symbols). $\% \Pi_{\text{req}}$ is obtained using DNS at $R_\tau = 200$ [9] for $\alpha = 2.25$, \circ ; $\alpha = 6$, \square ; and $\alpha = 9$, ∇ . The results in (b) are normalized by largest values of $ \% \Pi_{\text{req},2}(T^+) $ and $ \% \Pi_{\text{req}} - \alpha^2 \% \Pi_{\text{req},0}(T^+) $	117
4.7	Comparison between second-order correction to the net efficiency $\% \Pi_{\text{net},2}(T^+)$ (solid curve) for the flow with $R_\tau = 186$ (solid curve), and $\% \Pi_{\text{net}}/\alpha^2$ (symbols). Symbols show DNS data at $R_\tau = 200$ [9] for $\alpha = 2.25$, \circ	117
4.8	The second-order correction to (a) the saved power, $\% \Pi_{\text{save},2}(T^+)$; (b) the required power, $\% \Pi_{\text{req},0}(T^+)$; and (d) the net efficiency, $\% \Pi_{\text{net},2}(T^+)$; and (c) the fourth-order correction to the required power, $\% \Pi_{\text{req},2}(T^+)$, as a function of the period of oscillations T^+ for the flows with $R_\tau = 186$, 547, and 934.	118
4.9	(a) The turbulent viscosity, $\nu_{T0}(y^+)$; and (b) the turbulent mean streamwise velocity, $U_0(y^+)$, in the uncontrolled flow with $R_\tau = 186$, 547, and 934.	120
4.10	Second-order correction to (a) the turbulent viscosity, $\nu_{T2}(y^+; T^+)$; and (b) the mean streamwise velocity, $U_2(y^+; T^+)$, for $R_\tau = 186$ and different values of $30 \leq T^+ \leq 300$, where T^+ increases in the direction of the arrows. The thick curves correspond to the T^+ that yields the largest drag reduction (cf. Figure 4.11).	121
4.11	The second-order correction to (a) the turbulent viscosity, $\nu_{T2}(y^+)$; and (b) the mean streamwise velocity, $U_2(y^+)$, for the values of T^+ that yield the largest drag reduction for the flows with $R_\tau = 186$, $T^+ = 102.5$; $R_\tau = 547$, $T^+ = 96$; and $R_\tau = 934$, $T^+ = 94$	122
4.12	(a) Premultiplied DNS-based energy spectrum of the uncontrolled flow, $\kappa_x \kappa_z \bar{E}(\boldsymbol{\kappa})$, at $R_\tau = 186$ [1]; and (b) second-order correction to the energy spectrum, $\kappa_x \kappa_z E_2(\boldsymbol{\kappa})$, for the flow subject to wall oscillations with optimal drag-reducing period $T^+ = 102.5$	123

- 4.13 (Left column) Second-order correction to the turbulent kinetic energy $k_2(y^+)$ (a), and its rate of dissipation $\epsilon_2(y^+)$ (c), for the flow subject to wall oscillations with optimal drag-reducing period $T^+ = 102.5$ at $R_\tau = 186$. (Right column) Comparison between (b) the turbulent kinetic energy in the uncontrolled flow k_0 (black) and in the flow with control $k_0 + \alpha^2 k_2$ (red), and (d) its rate of dissipation in the uncontrolled flow ϵ_0 (black), and in the flow with control $\epsilon_0 + \alpha^2 \epsilon_2$ (red), for $\alpha = 2.25$ 124
- 4.14 (a) Premultiplied largest eigenvalue, $\kappa_x \kappa_z \lambda(\boldsymbol{\kappa})$, of the auto-correlation operator $X_0(\boldsymbol{\kappa})$ in the uncontrolled flow with $R_\tau = 186$; (b) same as (a) with superimposed contours of the relative difference between the premultiplied two largest eigenvalues of $X_0(\boldsymbol{\kappa})$. The contour levels $\{10^{-1}, 10^{-2}, \dots, 10^{-5}\}$ decrease in the direction of the arrow. 125
- 4.15 The real (black) and imaginary (red) parts of the principal eigenfunctions (v , (a); η , (b)) corresponding to the two largest equal eigenvalues of the auto-correlation operator $X_0(\boldsymbol{\kappa})$ for the most energetic mode $\kappa_x = 2.5$ and $\kappa_z = 6.5$ in the uncontrolled flow with $R_\tau = 186$. The two eigenfunctions are differentiated by solid and dotted curves. 126
- 4.16 Three-dimensional iso-surfaces of the streamwise streaks (red and blue) and the vortex core (green) for the characteristic eddy in the flow with no control (left column) and the flow subject to wall oscillations (right column) with optimal drag-reducing period $T^+ = 102.5$ at $R_\tau = 186$. (a)-(b): bird's-eye view; (c)-(d): side view. The fast- (red) and slow- (blue) moving streaks are respectively shown at 70% and 60% of their largest values in the uncontrolled flow, and the vortex core is obtained based on the 'swirling strength' criterion [10] with $\lambda_{ci} > 12$, $|\lambda_{cr}/\lambda_{ci}| < 0.4$, and $\lambda_{ci}/12 - |\lambda_{cr}/\lambda_{ci}|/0.4 = 1.2$ 127
- 4.17 Three-dimensional iso-surfaces of the streamwise streaks (red and blue) and the vortex core (green) for the characteristic eddy in the flow with no control (left column) and the flow subject to wall oscillations (right column) with optimal drag-reducing period $T^+ = 102.5$ at $R_\tau = 186$. (a)-(b): front view; (c)-(d): top view. The fast- (red) and slow- (blue) moving streaks are respectively shown at 70% and 60% of their largest values in the uncontrolled flow, and the vortex core is obtained based on the 'swirling strength' criterion [10] with $\lambda_{ci} > 12$, $|\lambda_{cr}/\lambda_{ci}| < 0.4$, and $\lambda_{ci}/12 - |\lambda_{cr}/\lambda_{ci}|/0.4 = 1.2$ 128

4.18	Cross sections of the streamwise velocity (colored contours) and the spanwise vorticity (black contours) for the characteristic eddy in the flow with no control (left column) and the flow subject to wall oscillations (right column) with optimal drag-reducing period $T^+ = 102.5$ at $R_\tau = 186$. (a)-(b): $z^+ = 0$; (c)-(d): $x^+ = 0$. The streamwise velocity is normalized by its largest absolute value in the uncontrolled flow, and the level sets for the spanwise vorticity correspond to 40%, 60%, and 80% of its largest value in the uncontrolled flow.	130
4.19	Cross sections of the streamwise velocity (colored contours) and the spanwise vorticity (black contours) for the characteristic eddy in the flow with no control (left column) and the flow subject to wall oscillations (right column) with optimal drag-reducing period $T^+ = 102.5$ at $R_\tau = 186$. (a)-(b): $y^+ = 3.8$; (c)-(d): $y^+ = 10.8$. The streamwise velocity is normalized by its largest absolute value in the uncontrolled flow, and the level sets for the spanwise vorticity correspond to 40%, 60%, and 80% of its largest value in the uncontrolled flow.	131
D.1	The maximum eigenvalues of the unperturbed (uncontrolled) matrix $\mathcal{W}_0(\kappa_x)$ for $R = 15, c = 1$	166
D.2	The maximum eigenvalues of the unperturbed (uncontrolled) matrix $\mathcal{W}_{0\theta}$ for $R = 15, c = 1$. (a) $(\Omega, \theta) = (2, 1)$, (b) $(\Omega, \theta) = (2/3, 1/3)$	167
D.3	Perturbation results for the maximum eigenvalues of the perturbed (controlled) matrix for $R = 15, c = 1, \alpha = 0.01$ (a) $(\Omega, \theta) = (2, 1)$, (b) $(\Omega, \theta) = (2/3, 1/3)$	169
E.1	Pressure driven channel flow.	176
E.2	(a) \mathcal{H}_2 norm computed from descriptor and standard state-space formulations for $R_c = 2000$ and $\kappa_x = 0$, (b) relative error.	183
E.3	(a) \mathcal{H}_2 norm computed from descriptor and standard state-space formulations for $R_c = 2000$ and $\kappa_z = 0$, (b) relative error.	183

Chapter 1

Introduction

The flow of fluids is among the most fascinating natural phenomena known to mankind. It has captivated the curious minds across a variety of disciplines including art, physics, mathematics, and engineering. For example, Vincent van Gogh, who was perhaps not familiar with fluid mechanics, was inspired by the swirling sky to draw one of the most famous paintings of all time, *The starry night* (see Figure 1.1(a)), which is suggestive of the motion of galaxies and the vortical flow around submerged bodies. The scientific visualization of fluid flows was pioneered in the fifteenth century by Leonardo da Vinci who sketched the motion of water pouring into a pond (see Figure 1.1(b)) and wrote [11]: “Observe the motion of the surface of the water, which resembles that of hair, which has two motions, of which one is caused by the weight of the hair, the other by the direction of the curls; thus the water has eddying motions, one part of which is due to the principal current, the other to the random and reverse motion.” His observation is reminiscent of the famous Reynolds decomposition in turbulent flows, and of the importance of what later became known as vortical flow structures [11]. The scientific approach to studying fluid mechanics can be traced back to Archimedes who examined the buoyancy in fluids at rest. Modern advancements in understanding fluid mechanics was pioneered by scientists like Torricelli (barometer), Newton (viscosity), Pascal (hydraulic fluids), Bernoulli (Bernoulli’s principle describing the relationship between velocity, pressure, and potential in inviscid flows), Poiseuille and Hagen (viscous flows), Reynolds, Kolmogorov, and Taylor (turbulence), Prandtl, Blasius, and von Kármán (boundary layers), Euler, d’Alembert, Lagrange, Laplace, and Poisson (inviscid flows), and Navier and Stokes (formulation of the Navier-Stokes equations for conservation of linear momentum in Newtonian viscous flows); see Figure 1.2.

In this section, we provide a brief overview of the main concepts and ideas upon which this dissertation is built. Our introductory presentation is organized as follows: In § 1.1, the importance of controlling transitional and turbulent flows is discussed and the key challenges are outlined. A brief overview of different flow control strategies is provided in § 1.2. In § 1.3, we introduce the key ideas that are pursued in this thesis.



Figure 1.1: (a) *The starry night* by Vincent van Gogh in 1889 is suggestive of the swirling motion of galaxies and flow around submerged bodies; (b) Sketch of the vortical motion of water pouring into a pond, by Leonardo da Vinci (1452-1519).

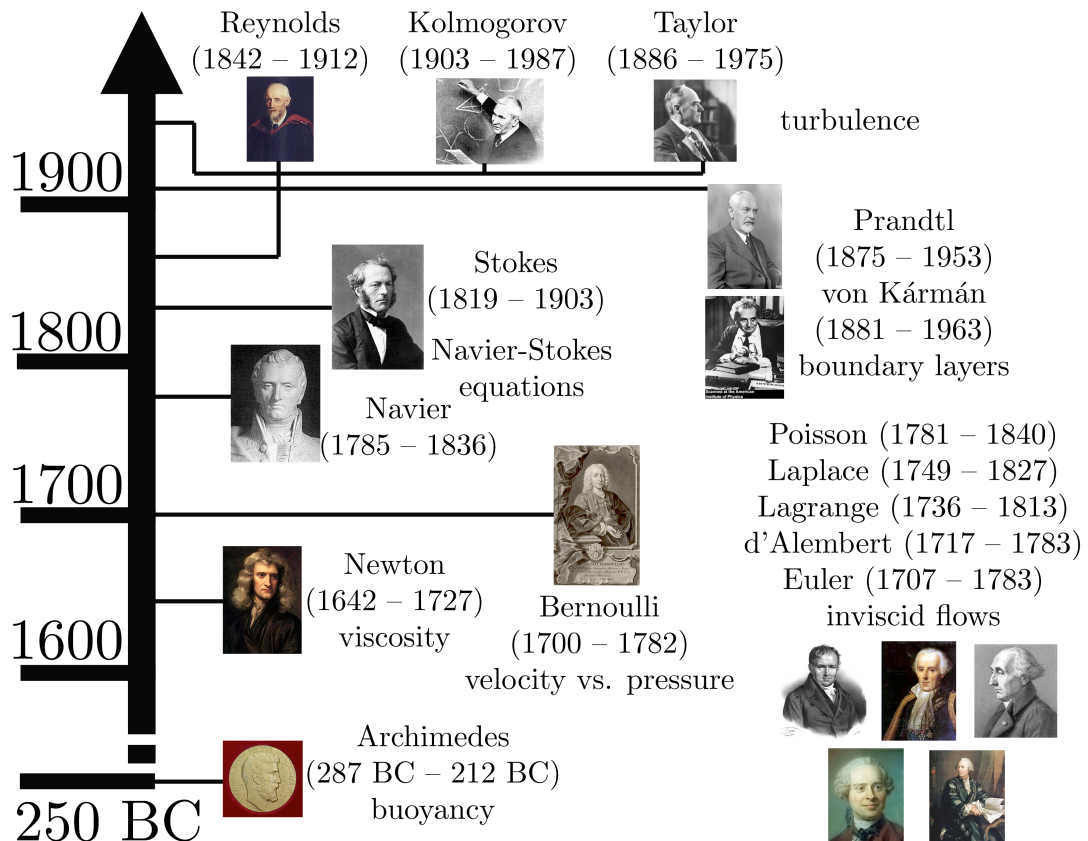


Figure 1.2: Fluid mechanics pioneers.

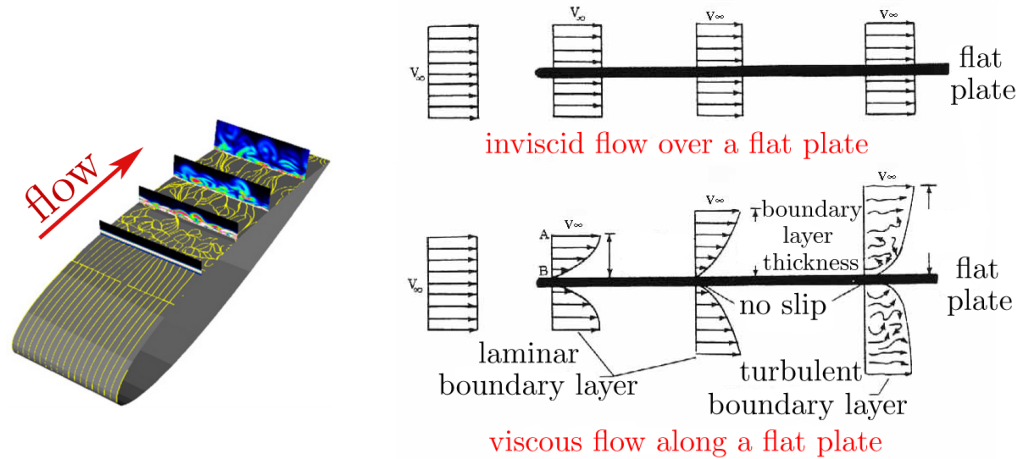


Figure 1.3: (Left) transition from laminar to turbulence over an aircraft wing (effluids photo by Miguel Visbal). (Right) the energy exchange between the solid surface and fluid is larger in a turbulent flow relative to a laminar flow. Therefore, turbulent flows exhibit larger resistance to motion (drag) than laminar flows.

A preview of our main results and contributions is provided in § 1.4.

1.1 Transitional and turbulent flows

Consider the flow of air over a cross-section of an aircraft wing; see Figure 1.3 (left). The ordered and smooth (laminar) flow at the leading edge becomes disordered and complex (turbulent) as it moves over the wing. In laminar flows, fluid particles move in parallel layers where there is no disruption between the layers, whereas in turbulent flows they move in random unsteady fashion [12]. The velocity and pressure in a turbulent flow undergo rapid variations with a broad range of spatial and temporal scales. The change from laminar to turbulent flow is called transition to turbulence. Figure 1.3 (right) shows that if a solid surface is placed in an inviscid fluid (an ideal fluid with zero viscosity), the fluid does not interact with the surface. On the other hand, the flow particles in a viscous fluid attach to the solid surface and result in an energy exchange between the surface and the flow. The region around the surface where the energy exchange takes place is called the boundary layer. A turbulent boundary layer exhibits a much larger resistance to motion (drag) relative to a laminar boundary layer. This is because the large fluctuations in a turbulent boundary layer yield large exchange of energy between the surface and the flow.



Figure 1.4: Skin-friction drag is responsible for approximately 50% and 90% fuel consumption in air- and water- vehicles, respectively.

1.1.1 Engineering applications involving turbulent flows

In engineering applications, turbulence may be beneficial or disadvantageous. For example, while turbulence provides desired mixing conditions for chemical processes and combustion engines, it exhibits a much larger drag than a laminar flow. Therefore, whether we want to promote or suppress turbulence depends on the specific application. Here, we briefly discuss the effect of turbulence on air- and water- transportation, and on energy generation from wind turbines.

Designing fuel-efficient air- and water- vehicles (see Figure 1.4) has become increasingly important due to the global energy crisis. Turbulence around the wings of an aircraft increases resistance to motion and results in larger fuel consumption. In particular, the skin-friction drag is responsible for 50% and 90% of fuel consumption in passenger aircrafts and in submarines [11, 13], respectively. In view of this, there is a critical demand for development and utilization of advanced theoretical and computational turbulence suppression techniques. Most of currently available strategies rely on physical intuition along with extensive numerical and experimental studies. Progress in this area has been hampered by the lack of understanding of complex flow dynamics and the absence of tractable models and theoretical tools for analysis and control thereof. In this thesis, we introduce a model-based approach to control of transitional and turbulent flows which facilitates systematic design of efficient turbulence suppression techniques.

Another important application concerns renewable energy sources, such as wind energy. The renewed interest in environmentally-friendly energy sources stems from the desire to achieve fossil-fuel independence, thereby indirectly addressing both the global warming and global energy crises. In order to produce cheaper electricity, wind turbines are becoming progressively larger (see Figure 1.5) which poses significant technological challenges for their design and control. During its operation, a wind turbine is subject to severe uncertainties arising from atmospheric turbulence, near-ground effects, and spatial variations in wind. These effects play an integral role in efficiency and longevity of turbines. In addition, modeling aerodynamics of the turbine blades and the effects from upstream wind turbines is extremely challenging. For example, the wake of upstream turbines can deteriorate the operation of the downstream turbines; see Figure 1.5 (right).



Figure 1.5: (Left) wind turbines are becoming progressively larger to increase efficiency and reduce electricity cost. (Right) The wake from upstream turbines affects those downstream of wind.

Therefore, enhancing the efficiency of wind farms relies heavily on distributed control design, where the control objective is to improve the efficiency of the wind farm as a whole rather than maximizing the efficiency of individual wind turbines.

1.1.2 Key challenges

Some of the main challenges for designing efficient flow control strategies include

- (i) Understanding the physics of transitional and turbulent flows;
- (ii) Designing flow control strategies;
- (iii) Developing control-oriented models and analytical tools for flow control design.

(i) Understanding the physics of transitional and turbulent flows. Transition to turbulence takes place at large Reynolds numbers. The Reynolds number is a dimensionless parameter that determines the ratio of inertial to viscous forces in the flow; it is proportional to the flow speed and a characteristic length that depends on the flow geometry (e.g. diameter in pipe flow and height in channel flow), and it is inversely proportional to the kinematic viscosity of the fluid. There is an abundance of experimental and numerical studies for better understanding the transitional and turbulent flows; for example, see the survey papers [3, 14, 15] for transitional flows and the survey papers [16–19] for turbulent flows. The critical Reynolds number above which transition takes place depends on the experimental conditions such as the amount of background disturbances, flow uniformity, and wall-roughness. Figure 1.6 shows a diagram of different paths to transition [3]. Deviation from laminar flow is initiated in the presence of environmental disturbances, such as non-uniformity or turbulence in the free-stream, acoustic noise, and wall roughness. The initial stage of transition is related to the so-called flow receptivity [20] to these disturbances. The receptivity determines the flow

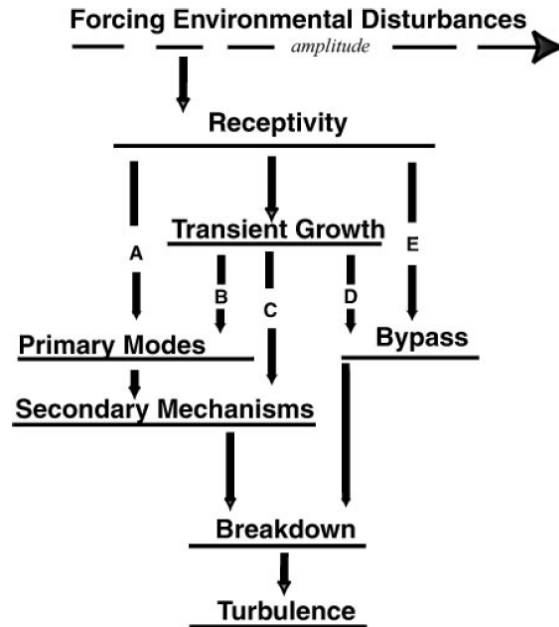


Figure 1.6: The paths from receptivity to transition (figure taken from [3]).

structures that emerge from the external disturbances. Depending on the amplitude and spatial shape of these structures, several paths from receptivity to breakdown to transition have been identified; these paths may occur individually or simultaneously. For infinitesimally small disturbances, the breakdown relies on emergence of primary modes; these are the least linearly stable modes of the flow also known as the Tollmien-Schlichting (TS) waves. The primary modes can become unstable as Reynolds number grows and result in breakdown to turbulence. Another possibility is that the primary modes with large initial amplitudes trigger three-dimensional (secondary) instabilities via nonlinear interactions. The secondary instabilities take place at Reynolds number that are smaller than the Reynolds number for which the flow becomes linearly unstable.

The scenarios that do not require emergence of unstable primary modes are called bypass scenarios. Direct bypass may occur when the primary disturbances are so large that breakdown takes place without secondary instabilities. On the other hand, recent research has emphasized that bypass transition may take place as a consequence of transient growth of linearly stable modes [4, 21–23]. This is because the velocity fluctuations can undergo large transient growth owing to the non-normality of the linearized flow dynamics [24–26]. The dominant flow structures that emerge as a consequence of transient growth of non-normal modes are in the form of streaky structures that are elongated in the streamwise direction and are periodic in the spanwise direction.

The mechanisms for emergence of streamwise streaks are by now well-understood. It was shown that these structures are not a consequence of linear instability, rather they are closely related to lack of robustness which manifests itself in large sensitivity of flow fluctuations to external disturbances and modeling imperfections [7, 25, 27, 28]; see § 1.3.1 for details. Recently, sensitivity analysis has also been used to better understand the possibility for transition to elastic turbulence in viscoelastic fluids. The energy amplification and spatio-temporal frequency responses in channel flows of viscoelastic fluids was studied in [29, 30], and it was shown that elasticity can amplify the disturbances even when inertial effects are small. Analysis of the transient responses in viscoelastic fluids was used to draw parallels between streamwise-constant inertial flows of Newtonian fluids and streamwise-constant creeping flows of viscoelastic fluids [31]. In addition, it was shown that strong nonmodal amplification of disturbances provides a possible route for the early stages of a bypass transition to elastic turbulence [32].

The omnipresence of streamwise streaks in wall-bounded shear flows (such as the flow around aircrafts) has motivated several researchers to closely analyze their properties. An experimental investigation of transition over a boundary layer on a flat plate subject to free-stream turbulence was conducted in [4]; see Figure 1.7. The turbulence in the free-stream was generated by placing a mesh upstream of the leading edge of the plate, and the flow was visualized by smoke. It was shown that the streamwise streaks emerge in the presence of relatively small magnitudes of free-stream turbulence. When the magnitude of free-stream turbulence was increased, some streaks developed streamwise waviness which lead to their breakdown and formation of turbulent spots. Similar structures are also observed in direct numerical simulations (DNS) of transitional boundary layers [5, 33]; see Figure 1.8.

The prevailing point of view is that secondary instability of the streaks leads to their breakdown [34]. It has been postulated that the streaks' waviness is due to non-linear interactions between the three-dimensional fluctuations that evolve around the streaks [34, 35]. However, numerical simulations of boundary layers subject to free-stream turbulence suggest that streak-breakdown may happen even in the absence of these instabilities [22, 36]. Over the last decade, there has been a lot of effort for better understanding the role of streaks receptivity to external disturbances (such as noise and wall-roughness) in breakdown to turbulence [37–41].

In this thesis, we develop and utilize control-oriented models that enable analytical study of transitional and turbulent flows; see § 1.3 for more details.

(ii) Designing flow control strategies. Flow control is based on manipulating the flow for the purpose of achieving desired objectives such as preventing/delaying transition, reducing skin-friction drag in turbulent flows, and preventing separation in laminar or turbulent boundary layers. The difficulty in designing strategies for flow manipulation arises from the inherent limitations on sensing and actuating authority. These limitations are at least twofold: (a) The sensors and actuators are typically mounted on a solid surface. Consequently, the sensors can only measure local flow quantities and

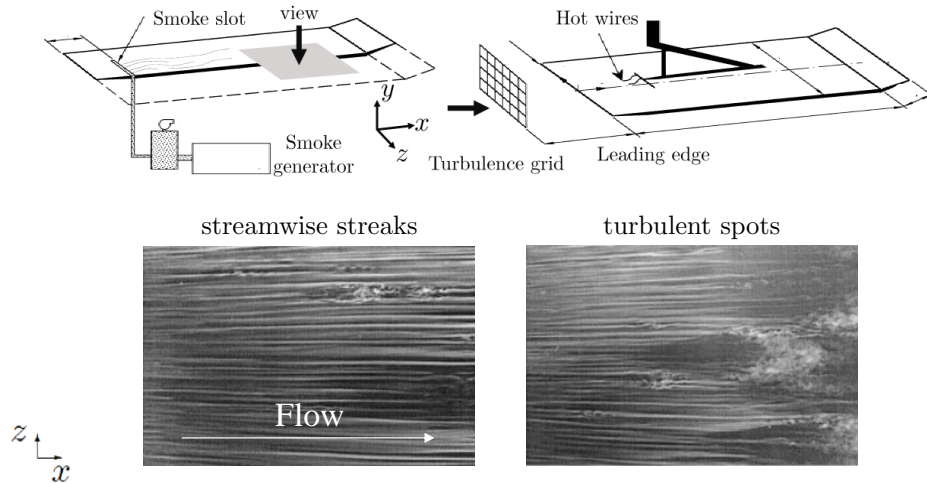
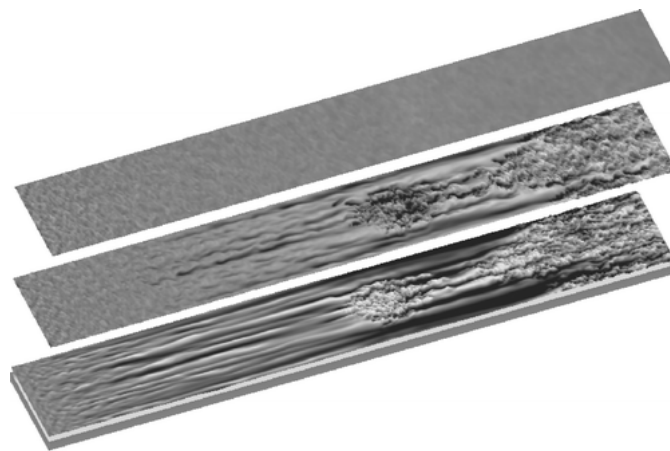


Figure 1.7: Experiment and flow visualization of transitional boundary layer over a flat plate [4] The bottom row shows the top view of the flow where x is the flow direction and z is the spanwise direction.




 Durbin P, Wu X. 2007.
Annu. Rev. Fluid Mech. 39:107–28

Figure 1.8: Direct numerical simulations of transitional boundary layer over a flat plate. The panels from top to bottom show the streamwise velocity, respectively, outside, on the edge, and inside the boundary layer (photo courtesy of T. Zaki taken from [5]).

determination of the flow quantities away from the solid surface requires flow modeling and estimation. In addition, since the actuators can perturb the flow only locally, a related question is design of actuating techniques that can target and modify the relevant flow features. (b) Even though the flow is continuous, the sensors and actuators have limited spatial range. In view of this, the sensors and actuators are often placed on a few isolated spatial locations, or on a discrete lattice for distributed sensing and actuating capabilities. In § 1.2, we present an overview of different flow control strategies.

(iii) Developing control-oriented models and analytical tools for flow control design. A key step in designing efficient control strategies for transitional and turbulent flows is to develop models of complex flow dynamics that are amenable to control design and optimization. The predictions of classical hydrodynamic stability theory are at odds with experimental observations for wall-bounded shear flows. As discussed earlier, recent research has demonstrated the importance of understanding how uncertainty influences the dynamics of fluid flows. This observation suggests that turbulence is not solely a consequence of flow instabilities; rather, it is related to large sensitivity of the flow fields to the disturbances naturally present in the environment. Over the last two decades, there has been a significant amount of effort for model-based flow control design using techniques from linear systems theory; for example, see [42]. In this thesis, we develop and verify control-oriented models that contain essential features of transitional and turbulent flows and, yet, are simple enough for convenient control design.

1.1.3 Thesis objectives

The objectives of this thesis are:

- (a) developing control-oriented models of transitional and turbulent flows;
- (b) designing model-based sensorless and feedback flow control strategies for preventing transition;
- (c) designing model-based sensorless flow control strategies for skin-friction drag reduction in turbulent flows;
- (d) developing analytical tools that enable computationally-efficient flow control design by means of temporally- or spatially- periodic flow manipulation.

1.2 Flow control strategies

Controlling turbulent flows is a viable approach for reducing the unfavorable effects of turbulence such as large skin-friction drag [11, 43–45]. In this section, we briefly overview two general categories of flow control techniques that are based on sensorless and feedback strategies.

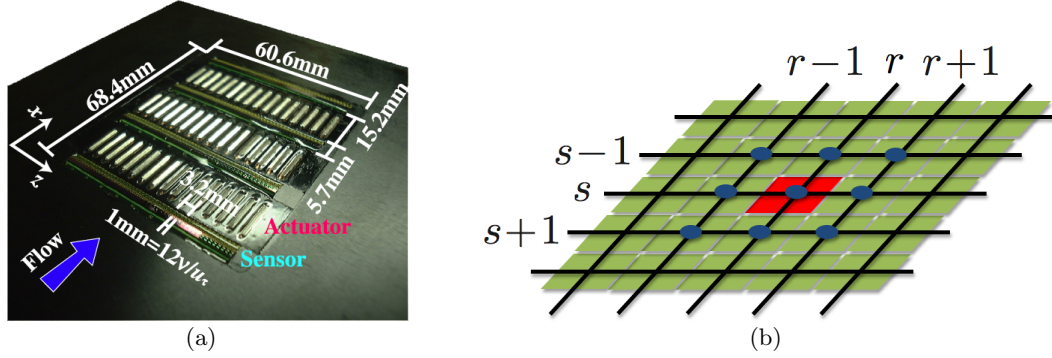


Figure 1.9: (a) An array of distributed hot-film shear-stress sensors and wall-deformation actuators for feedback flow control [6]; (b) Sketch of a localized control strategy where the actuator placed at (r, s) uses information from only the nearest neighbors on the two-dimensional lattice.

1.2.1 Feedback control strategies

Owing to recent developments in micro-electro-mechanical (MEMS) devices, feedback control of turbulence has become possible using wall-mounted arrays of sensors and actuators [6, 46–48]. The relevant flow quantities such as velocity, pressure, and shear stresses are measured by sensors and the flow is actuated by wall-deformation actuators and compliant surfaces via a feedback rule. Feedback strategies for control of fluid flows involve individual system components that are capable of sensing, computation, and actuation (see Figure 1.9(a)). Therefore, an important question in design of flow controllers is related to the interconnection structure between these components. A centralized controller yields best performance at the expense of excessive communication and computation. A fully decentralized controller, while advantageous from a communications perspective, may sacrifice performance. A reasonable middle ground between these competing approaches is offered by localized strategies where each component exchanges information with a limited number of nearby components. For example, Figure 1.9(b) illustrates a situation where information from only the nearest neighbors is used. In Chapter 3 of this thesis, we have designed a localized optimal controller for preventing transition to turbulence.

1.2.2 Sensorless control strategies

Skin-friction drag reduction by sensorless mechanisms is a promising technology for implementation. Despite significant advances in the area of MEMS devices for flow actuation and sensing, the development of distributed arrays of sensors and actuators for active feedback control is still in its early stages. Furthermore, measurement of the

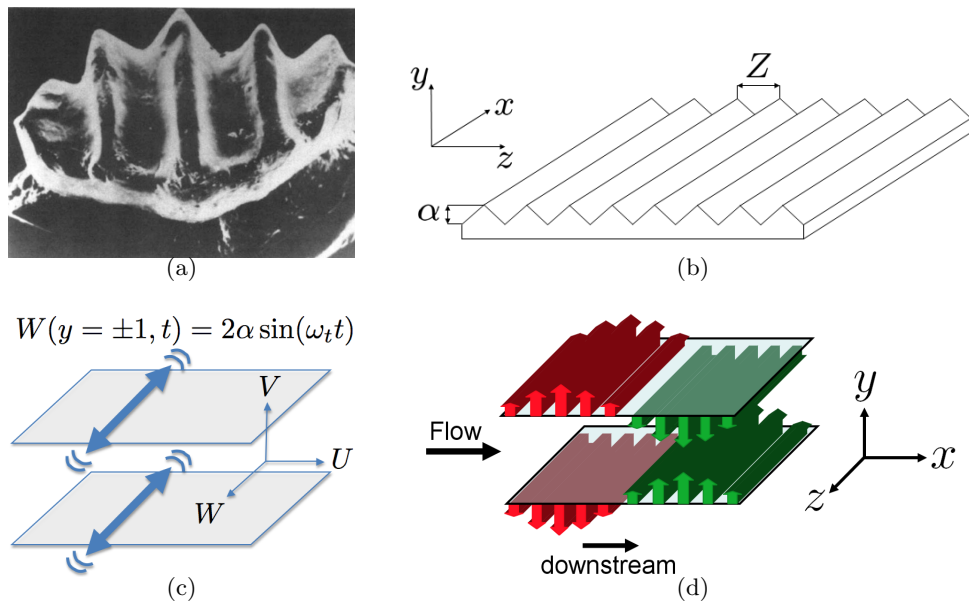


Figure 1.10: (a) Photograph of a shark dermal denticle; (b) Sketch of a riblet-mounted surface with x denoting the flow direction; (c) Transverse wall oscillations; and (d) Wall transpiration in the form of streamwise traveling wave.

relevant flow quantities in the high-Reynolds-number flows may be inefficient or even infeasible owing to the smallness of the length and time scales [11, 49]. Sensorless flow control represents a much simpler alternative to feedback flow control with wall-mounted arrays of sensors and actuators. These mechanisms rely on the understanding of the basic flow physics and control designs without measurement of the relevant flow quantities. Some of these strategies are nature-inspired [50]. For example, the shark skin is covered in denticles (see Figure 1.10(a)) which help sharks swim much faster than their body mass would allow if the flow around them was turbulent. The skin patterns can be modeled as micro-grooves of a regular geometric shape mounted over a flat surface called riblets [51] (see Figure 1.10(b)). Other examples of the sensorless schemes include transverse wall oscillations and wall transpiration in the form of streamwise traveling waves (see Figures 1.10(c) and 1.10(d)). All these strategies are characterized by the absence of sensing capabilities. In other words, control is implemented without measurement of the relevant flow quantities and disturbances. Rather, the dynamical properties of the underlying system are changed by either modifying geometry (riblets) or base velocity (traveling waves). Although several numerical and experimental studies show that properly designed sensorless strategies may yield significant turbulence suppression, an obstacle to fully utilizing these approaches is the absence of a theoretical framework for their design and optimization. In this thesis, we have used control-oriented models to design sensorless strategies based on traveling waves for controlling the onset of turbulence (Chapter 2), and to design wall oscillations for controlling turbulent flows (Chapter 4).

1.3 Model-based flow control

Many control strategies based on either sensorless or feedback designs have been successfully tested and verified in numerical simulations and experiments. For example, a number of simulations on turbulent drag reduction by means of spanwise wall oscillation was conducted by [9]. However, conducting experiments and simulations for control design and optimization is often prohibitively expensive or time-consuming. In particular, simulating the full Navier-Stokes (NS) equations becomes increasingly difficult as Reynolds number increases. In addition, the development of a supporting theory that would provide guidelines for a selection of control parameters, e.g. wall geometry or traveling wave parameters, has been lacking. Even though DNS and experiments offer valuable insight into flow control strategies, their utility can be significantly enhanced by developing a model-based framework for flow control design. This has motivated a significant body of research that utilizes models obtained from the linearized Navier-Stokes equations in conjunction with tools from linear systems theory for flow control design [42, 44, 52–63]. In this thesis, we develop models of transitional and turbulent wall-bounded shear flows that govern the dynamics of fluctuations in the presence of control. The wall geometry or traveling wave parameters enter as coefficients (that

multiply system's state), and the free-stream turbulence or surface roughness enter as stochastic excitations into these equations. We demonstrate the predictive power of these models using DNS.

1.3.1 Control-oriented modeling

Control-oriented models should describe the essential physics of the underlying system, yet be simple enough to allow convenient control design. The models that we develop are not able to emulate the full complexity of turbulence in wall-bounded shear flows. On the other hand, the more realistic models of turbulence, e.g. the full nonlinear Navier-Stokes equations used in the DNS studies, do not lend themselves easily to a thorough theoretical analysis. In view of this, we assess flow control strategies using the least complex models that capture the essential features that are commonly observed in experimental and numerical studies. Our approach is in concert with a standard practice in control theory, where the design is performed on a simple model that represents an adequate approximation of the controlled system. Once the controller has been designed, it is usually tested on either the real system or the high fidelity computational model. These results are used to refine the model and, if necessary, redesign the controller. Ideally, the control-oriented models will contain statistical description of flow disturbances that optimally approximate experimentally and numerically generated turbulent flow statistics.

We build on recent research that has demonstrated the utility of stochastically forced Navier-Stokes equations linearized around the laminar velocity profile to reveal the dominant flow structures at the early stages of transition [7,27,28]. Consider the flow of incompressible Newtonian fluids between two infinite plates; see Figure 1.11(a). Here, x , y , and z are streamwise, spanwise, and wall-normal coordinates, respectively, and the corresponding velocity components and forcing directions are denoted by (u, v, w) and (d_1, d_2, d_3) . The evolution of fluctuations up to first order is governed by the linearized Navier-Stokes equation around the laminar parabolic velocity $U(y) = 1 - y^2$

$$\begin{aligned}\boldsymbol{\psi}_t(x, y, z, t) &= A\boldsymbol{\psi}(x, y, z, t) + B\mathbf{d}(x, y, z, t), \\ \mathbf{v}(x, y, z, t) &= C\boldsymbol{\psi}(x, y, z, t).\end{aligned}\tag{1.1}$$

Here, $\mathbf{v} = [u \ v \ w]^T$ is the output vector, $\mathbf{d} = [d_1 \ d_2 \ d_3]^T$ is the input vector, and $\boldsymbol{\psi} = [v \ \eta]^T$ is the state vector where $\eta = u_z - w_x$ is the wall-normal vorticity, and t is time. The subscripts denote spatial and temporal derivatives, e.g. $\boldsymbol{\psi}_t = \partial\boldsymbol{\psi}/\partial t$, and A ,

B , and C are integro-differential operators

$$\begin{aligned}
A &= \begin{bmatrix} \Delta^{-1}((1/R_c)\Delta^2 + (U'' - U\Delta)\partial_x) & 0 \\ -U'\partial_z & (1/R_c)\Delta - U\partial_x \end{bmatrix}, \\
B &= [B_1 \ B_2 \ B_3] = \begin{bmatrix} -\Delta^{-1}\partial_{xy} & \Delta^{-1}(\partial_{xx} + \partial_{zz}) & -\Delta^{-1}\partial_{yz} \\ \partial_z & 0 & -\partial_x \end{bmatrix}, \\
C &= \begin{bmatrix} C_u \\ C_v \\ C_w \end{bmatrix} = (\partial_{xx} + \partial_{zz})^{-1} \begin{bmatrix} -\partial_{xy} & \partial_z \\ \partial_{xx} + \partial_{zz} & 0 \\ -\partial_{yz} & -\partial_x \end{bmatrix},
\end{aligned} \tag{1.2}$$

where $\Delta = \partial_{xx} + \partial_{yy} + \partial_{zz}$ is the Laplacian, and $\{v(x, y = \pm 1, z, t) = v'(x, y = \pm 1, z, t) = \eta(x, y = \pm 1, z, t) = 0\}$. Here, $R_c = U_c h / \nu$ is the Reynolds number based on the centerline streamwise velocity U_c and the channel half height h , ν is the kinematic viscosity, and $U' = dU/dy$.

Applying spatial Fourier transform in invariant directions, x and z , brings the evolution model to a set of linear equations parameterized by the streamwise and spanwise wavenumbers $\boldsymbol{\kappa} = (\kappa_x, \kappa_z)$

$$\begin{aligned}
\psi_t(y, \boldsymbol{\kappa}, t) &= A(\boldsymbol{\kappa}) \psi(y, \boldsymbol{\kappa}, t) + B(\boldsymbol{\kappa}) \mathbf{d}(y, \boldsymbol{\kappa}, t), \\
\mathbf{v}(y, \boldsymbol{\kappa}, t) &= C(\boldsymbol{\kappa}) \psi(y, \boldsymbol{\kappa}, t).
\end{aligned} \tag{1.3}$$

Note that the same symbols are used for denoting the functions and operators in physical and frequency spaces (the distinction should be clear from the context). The operators A , B , and C in frequency space are given by

$$\begin{aligned}
A &= \begin{bmatrix} \Delta^{-1}((1/R_c)\Delta^2 + i\kappa_x(U'' - U\Delta)) & 0 \\ -i\kappa_z U' & (1/R_c)\Delta - i\kappa_x U \end{bmatrix}, \\
B &= [B_1 \ B_2 \ B_3] = \begin{bmatrix} -i\kappa_x \Delta^{-1} \partial_y & -\kappa^2 \Delta^{-1} & -i\kappa_z \Delta^{-1} \partial_y \\ i\kappa_z I & 0 & -i\kappa_x I \end{bmatrix}, \\
C &= \begin{bmatrix} C_u \\ C_v \\ C_w \end{bmatrix} = \frac{1}{\kappa^2} \begin{bmatrix} i\kappa_x \partial_y & -i\kappa_z I \\ \kappa^2 I & 0 \\ i\kappa_z \partial_y & i\kappa_x I \end{bmatrix},
\end{aligned} \tag{1.4}$$

where $\Delta = \partial_{yy} - \kappa^2$, $\Delta^2 = \partial_{yyyy} - 2\kappa^2 \partial_{yy} + \kappa^4$, $\{v(\pm 1, \boldsymbol{\kappa}, t) = v'(\pm 1, \boldsymbol{\kappa}, t) = \eta(\pm 1, \boldsymbol{\kappa}, t) = 0\}$, I is the identity operator, and $i = \sqrt{-1}$.

One way to quantify the flow receptivity is by studying the spatio-temporal frequency

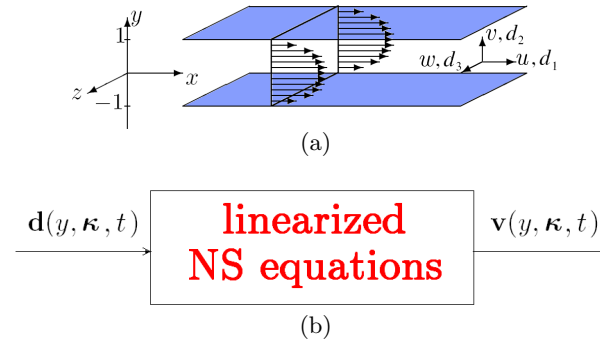


Figure 1.11: (a) Three-dimensional pressure-driven channel flow; (b) Input-output analysis of the Navier-Stokes equations linearized around laminar velocity.

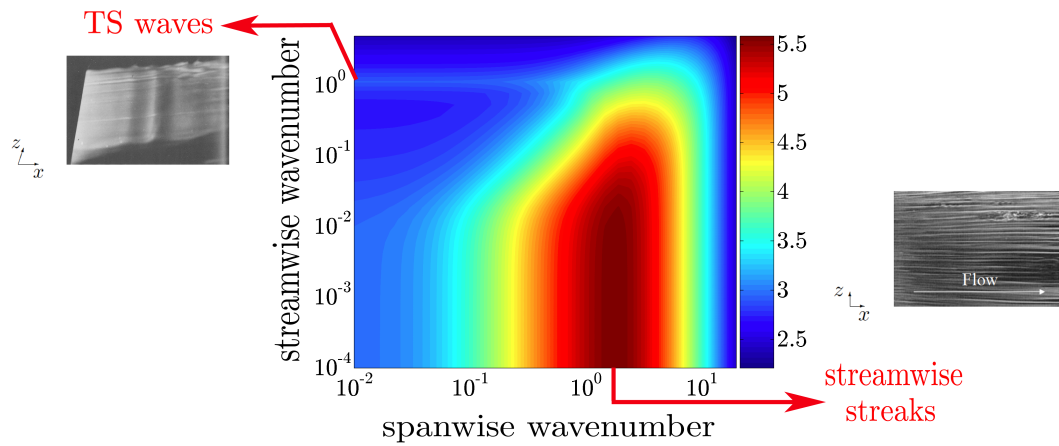


Figure 1.12: The energy density (\mathcal{H}_2 norm) as a function of streamwise and spanwise wavenumbers, $E(\boldsymbol{\kappa})$, for the flow with no control at $R_c = 2000$ [7]. The axes and the coloring are in logarithmic scale. The wavenumbers corresponding to the streamwise streaks and the TS waves are highlighted.

responses of system (1.3) [7] (see Figure 1.11(b))

$$\underbrace{\begin{bmatrix} d_1 \\ d_2 \\ d_3 \end{bmatrix}}_{\mathbf{d}} \xrightarrow{\text{amplification}} \underbrace{\begin{bmatrix} u \\ v \\ w \end{bmatrix}}_{\mathbf{v}}.$$

For example, the so-called \mathcal{H}_2 norm of system (1.3)-(1.4) can be interpreted as the steady-state energy density of fluctuations in the presence of zero-mean white (in t and y) stochastic disturbances, and can be obtained from

$$E(\boldsymbol{\kappa}) = \lim_{t \rightarrow \infty} \langle \mathbf{v}(\cdot, \boldsymbol{\kappa}, t), \mathbf{v}(\cdot, \boldsymbol{\kappa}, t) \rangle.$$

Here, $\langle \cdot, \cdot \rangle$ denotes the $L_2[-1, 1]$ inner product and averaging in time, i.e.,

$$\begin{aligned} \langle \mathbf{v}, \mathbf{v} \rangle &= \mathcal{E} \left\{ \int_{-1}^1 \mathbf{v}^*(y, \boldsymbol{\kappa}, t) \mathbf{v}(y, \boldsymbol{\kappa}, t) dy \right\}, \\ \mathcal{E} \{ \mathbf{v}(\cdot, t) \} &= \lim_{T \rightarrow \infty} \frac{1}{T} \int_0^T \mathbf{v}(\cdot, t + \tau) d\tau, \end{aligned}$$

where $*$ denotes the complex conjugate transpose. For the linear system (1.3)-(1.4), it is a standard fact that the \mathcal{H}_2 norm is determined by

$$E(\boldsymbol{\kappa}) = \text{trace} (X C^+ C).$$

Here, $^+$ denotes the operator adjoint and $X(\boldsymbol{\kappa})$ is obtained efficiently from the solution to a $\boldsymbol{\kappa}$ -parameterized family of algebraic Lyapunov equations

$$A(\boldsymbol{\kappa}) X(\boldsymbol{\kappa}) + X(\boldsymbol{\kappa}) A^+(\boldsymbol{\kappa}) = -B(\boldsymbol{\kappa}) B^+(\boldsymbol{\kappa}). \quad (1.5)$$

For the channel flow with $R_c = 2000$, the energy density $E(\boldsymbol{\kappa})$ is shown in Figure 1.12 [7]. We see that the most energetic modes (dark red) take place at zero streamwise wavenumber, and a spanwise wavenumber of order one. These modes correspond to the streamwise streaks that are observed at early stages of transition in experimental and numerical studies. This illustrates the predictive power of the stochastically forced linearized model for determining the most energetic flow structures in the early stages of transition. In addition, Figure 1.12 shows that the least stable modes of the linearized model (1.3) are located in the narrow light blue region corresponding to zero spanwise wavenumber and streamwise wavenumber of order one. We see that relative to the streamwise streaks, the least stable modes (TS waves) are orders of magnitude less amplified by the linearized model. The TS waves can only be obtained in carefully controlled experiments where background noise is very small and the flow is perturbed by the appropriate frequencies. Therefore, the linear hydrodynamic stability theory cannot predict the dominant

flow structures in transitional flows. This suggests that transition is not a problem of linear instability, rather it is closely related to robustness of the flow dynamics to external disturbances [7, 25, 27, 64]. In view of this, we develop control-oriented models for transitional and turbulent flows.

1.3.2 Transitional flows

As discussed in § 1.3.1, transition is initiated by large flow receptivity to external disturbances. This is supported by large transient growth in response to perturbations and by large variance amplification in the presence of stochastic disturbances. In addition, the dynamics of velocity fluctuations exhibit large sensitivity to modeling imperfections which leads to small stability margins in the linearized model. In this thesis, we have designed flow control strategies for controlling the onset of turbulence based on reducing the large flow receptivity.

In Chapter 2, we have designed a sensorless control based on blowing and suction of fluid at the walls in the form of streamwise traveling waves. Recent research has shown the effectiveness of upstream traveling waves for drag reduction in turbulent flows [8]. It has also been shown that traveling waves induce a nonzero bulk flux even in the absence of a driving pressure gradient [65]. We have used the stochastically forced NS equations linearized around the nominal velocity that is induced by wall-actuation to study the effect of traveling wave parameters (amplitude, frequency, and speed of the wave) on flow receptivity. The inherent periodicity of the resulting flows poses significant challenges on their analysis even in the linearized case. We have overcome these challenges by using perturbation analysis in the control amplitude. This is facilitated by considering small wave amplitudes since large amplitudes require large control effort and, consequently, result in poor net efficiency. Our results based on perturbation analysis are supported by high fidelity numerical simulations, and they have illustrated that reducing the flow receptivity represents a powerful paradigm for controlling the onset of turbulence. Our results have revealed that downstream traveling waves prevent transition while upstream waves promote transition even in the case where the flow with no control stays laminar. In addition, we have shown that the properly selected downstream traveling waves maintain the laminar flow with positive net efficiency.

In Chapter 3, we have designed an optimal state-feedback controller based on local flow information for preventing transition to turbulence. The optimal state-feedback control problem with no structural constraints on the feedback gains yields a centralized solution meaning that the actuation depends on the flow information at all points in the spatial domain. It was shown that the linearized NS equations can be used to design optimal centralized state-feedback controllers for preventing transition by minimizing the energy of velocity fluctuations in the flow subject to stochastic excitations [56, 57]. These authors used spatial truncation of the resulting feedback kernels to obtain kernels with finite spatial spread. Spatial truncation is justified by the fact that for a wide

class of systems governed by partial differential equations, the magnitude of the optimal feedback kernels decays exponentially with spatial distance from the origin [66,67]. However, we have demonstrated the dangers of spatial truncation for obtaining a localized feedback controller in Chapter 3. For a channel flow with an array of sensors and actuators on a two-dimensional discrete lattice along the walls, we have shown that using the optimal centralized feedback gains while paying attention to the flow information from only the nearest neighbors can destabilize the laminar flow. Our numerical simulations have verified that truncation of centralized feedback gains can trigger transition to turbulence even in response to perturbations for which the flow with no control remains laminar. In view of this, we have utilized tools for designing structured optimal feedback gains [68,69] to design localized optimal feedback controllers. We have shown that the localized optimal controller can guarantee stability and achieve similar receptivity reduction to the optimal centralized controller. Our simulations have illustrated the effectiveness of the localized optimal gains for preventing transition.

1.3.3 Turbulent flows

Control-oriented turbulence modeling is challenging because of the complex flow physics that arises from intricate interactions between the turbulent fluctuations and the mean velocity. Turbulent flow models describe the statistical properties of turbulence, such as mean velocity and velocity correlations. The closure problem in turbulence necessitates modeling of unknown higher order statistical moments of turbulence in terms of known lower order moments. For example, the turbulent viscosity hypothesis expresses the second order moments (Reynolds-stress terms) in terms of the mean velocities [70–72]. One of the main challenges in modeling turbulent flows is obtaining the model parameters. In the case of the turbulent viscosity hypothesis, the parameter that needs to be determined is the turbulent viscosity profile (that gives the ratio between the Reynolds-stresses and the elements of the rate-of-strain tensor).

We have built on recent research that demonstrates considerable predictive power of linearized analysis even in turbulent flows [73–75]. These papers have shown that the equations linearized around turbulent mean velocity, with molecular viscosity augmented by turbulent viscosity, qualitatively capture features of turbulent flows with no control. In Chapter 4, we have designed a control strategy based on wall oscillations for skin-friction drag reduction in turbulent flows. For the flow subject to control, we examine the class of linearized models considered by [73–75] and use turbulent viscosity hypothesis to quantify the influence of turbulent fluctuations on the mean velocity.

The model that we have developed approximates the turbulent mean velocity and the fluctuations’ second-order statistics at the steady-state. This model has several advantages over the current turbulent models which makes it especially suitable for the purpose of control. Similar to the model for transitional flows, the evolution of fluctuations around the turbulent mean flow is determined by linear partial-differential equations that are driven by stochastic forcing. This enables efficient computation of

the turbulent kinetic energy and the rate of turbulent dissipation at the steady-state by solving Lyapunov equations. Moreover, by algebraizing the differential equations using spatial Fourier transforms, the Lyapunov equations can be solved independently. As a result, k and ϵ are computed in a fully parallel way. These quantities are next used to compute the modification to the turbulent viscosity, the turbulent mean velocity, and thereby the skin-friction drag in the flow with control.

Since the evolution model for flows subject to wall oscillations is time periodic, a stationary stochastic forcing induces velocity fluctuations with cyclo-stationary statistics. Computing these statistics is challenging even in the linearized case. Motivated by the observation that large control amplitudes yield poor net efficiency, we have used perturbation analysis (in the amplitude of oscillations) to quantify the effect of control on the turbulent statistics in a computationally efficient manner.

1.4 Preview of main results and contributions

A brief overview of the main contributions of the thesis is provided in this section. The numerical simulations of Chapters 2 and 3 are performed by Binh K. Lieu; his contribution in writing the discussion of the results is also gratefully acknowledged.

- **Chapter 2** presents a method for designing sensorless strategies for controlling the onset of turbulence. In particular, we examine the efficacy of streamwise traveling waves generated by a zero-net-mass-flux surface blowing and suction for controlling the onset of turbulence in a channel flow. For small amplitude actuation, we utilize weakly nonlinear analysis to determine base flow modifications and to assess the resulting net power balance. Receptivity analysis of the velocity fluctuations around this base flow is then employed to design the traveling waves. Our simulation-free approach reveals that, relative to the flow with no control, the downstream traveling waves with properly designed speed and frequency can significantly reduce receptivity which makes them well-suited for controlling the onset of turbulence. In contrast, the velocity fluctuations around the upstream traveling waves exhibit larger receptivity to disturbances. Our theoretical predictions, obtained by perturbation analysis (in the wave amplitude) of the linearized Navier-Stokes equations with spatially periodic coefficients, are verified using full-scale simulations of the nonlinear flow dynamics. In flows driven by a fixed pressure gradient, a positive net efficiency as large as 25% relative to the uncontrolled turbulent flow can be achieved with downstream waves. Furthermore, we show that these waves can also relaminarize fully developed turbulent flows at low Reynolds numbers. We conclude that the theory developed for the linearized flow equations with uncertainty has considerable ability to predict full-scale phenomena.
- In **Chapter 3**, we study the design of localized optimal state-feedback controllers for the problem of controlling the onset of turbulence in a channel flow. The

actuation is generated by blowing and suction at the walls, and the actuators are placed along a two-dimensional lattice of equally spaced points with each actuator using information from only a limited number of nearby neighbors. We utilize recently developed tools for designing structured optimal feedback gains to reduce receptivity of velocity fluctuations to flow disturbances in the presence of control. Our preliminary DNS result, conducted at a low Reynolds number, show that this approach can indeed maintain the laminar flow. This is in contrast to the localized strategies obtained by spatial truncation of optimal centralized controllers, which may introduce instability and promote transition even in the situations where the uncontrolled flow stays laminar.

- **Chapter 4** develops a model-based and simulation-free approach to skin-friction drag reduction in turbulent flows using transverse wall oscillations. Over the last two decades, both experiments and simulations have demonstrated that transverse wall oscillations with properly selected amplitude and frequency can reduce turbulent drag by as much as 40%. In this thesis, we develop a model-based approach for designing oscillations that suppress turbulence in a channel flow. We utilize judiciously selected linearization of the flow with control in conjunction with turbulence modeling to determine skin-friction drag in a simulation-free manner. The turbulent viscosity hypothesis and the k - ϵ model are used to quantify the effect of fluctuations on the mean velocity in the flow subject to control. In contrast to the traditional approach that relies on numerical simulations, we determine the turbulent viscosity from the second order statistics of the linearized model driven by white-in-time stochastic forcing. The spatial power spectrum of the forcing is selected to ensure that the linearized model for the flow with no control reproduces the turbulent energy spectrum. The resulting correction to the turbulent mean velocity induced by small amplitude wall movements is then used to identify the optimal frequency of drag reducing oscillations. In addition, the control net efficiency and the turbulent flow structures that we obtain agree well with the results of numerical simulations and experiments. This demonstrates the predictive power of our model-based approach to controlling turbulent flows and paves the way for successful flow control at higher Reynolds numbers than currently possible.
- **Chapter 5** summarizes the thesis contributions and provides an outlook for future research.

Chapter 2

Controlling the onset of turbulence by streamwise traveling waves

The problem of turbulence suppression in a channel flow using feedback control with wall-mounted arrays of sensors and actuators has recently received a significant attention. This problem is viewed as a benchmark for turbulence suppression in a variety of geometries, including boundary layers. Also, there has been mounting evidence that the linearized Navier-Stokes (NS) equations represent a good control-oriented model for the dynamics of transition. Recent research suggests that, in wall-bounded shear flows, one must account for modeling imperfections in the linearized NS equations since they are exceedingly sensitive to external excitations and unmodelled dynamics; for example, see [7, 25, 27, 64]. This has motivated several research groups to use the linearized NS equations for model-based design of estimators and controllers in a channel flow [42, 53–62]. These results suggest that the proper turbulence suppression design paradigm is that of disturbance attenuation or robust stabilization rather than modal stabilization.

An alternative approach to feedback flow control relies on the understanding of the basic flow physics and the open-loop implementation of controls (i.e., without measurement of the relevant flow quantities and disturbances). Examples of sensorless strategies include: wall geometry deformation such as riblets, transverse wall oscillations, and control of conductive fluids using the Lorentz force. Although several numerical and experimental studies show that properly designed sensorless strategies may yield significant drag reduction, an obstacle to fully utilizing these physics-based approaches is the absence of a theoretical framework for their design and optimization.

An enormous potential of sensorless strategies was exemplified by [8], where direct numerical simulations (DNS) were used to show that a surface blowing and suction in the form of an upstream traveling wave (UTW) results in a sustained sub-laminar drag

in a fully developed turbulent channel flow. The underlying mechanism for obtaining drag smaller than in a laminar flow is the generation of the wall region Reynolds shear stresses of the opposite signs compared to what is expected based on the mean shear. By assuming that a wall actuation *only* influences the velocity fluctuations, [8] determined an explicit solution to the two dimensional NS equations linearized around parabolic profile; they further used an expression for skin-friction drag in fully developed channel flows [76, 77], and showed that the drag is increased with the downstream traveling waves (DTWs) and decreased with the upstream traveling waves.

A comparison of laminar and turbulent channel flows with and without control was presented by [78], where a criterion for achieving sub-laminar drag was derived. This study considered effectiveness of streamwise traveling waves at high Reynolds numbers and discussed why such controls can achieve sub-laminar drag. Another recent study [65] emphasized that the UTWs introduce a larger flux compared to the uncontrolled flow which motivated the authors to characterize the observed mechanism as a *pumping* rather than as a drag reduction. It was shown that, even with no driving pressure gradient, blowing and suction along the walls induces pumping action in a direction opposite to that of the wave propagation. By considering flows in the absence of velocity fluctuations [65] showed that it costs more to drive a fixed flux with wall-transpiration type of actuation than with standard pressure gradient type of actuation. A fundamental limitation on the balance of power in a channel flow was recently examined by [79]; this study showed that any transpiration-based control strategy that results in a sub-laminar drag necessarily has negative net efficiency compared to the laminar flow with no control. Furthermore, [80] showed that a lower bound on the net driving power in a duct flow with arbitrary constant streamline curvature is determined by the power required to drive the Stokes flow. It was thus concluded that the flow has to be relaminarized in order to be driven with the smallest net power. However, since the difference between the turbulent and laminar drag coefficients grows quadratically with the Reynolds number, [78] argued that relaminarization may not be possible in strongly inertial flows. An alternative approach is to design a controller that reduces skin-friction drag in turbulent flows; provided that the control power is less than the saved power, a positive net efficiency can still be achieved.

In this chapter, we show that a positive net efficiency can be achieved in a channel flow subject to streamwise traveling waves if the controlled flow stays laminar while the uncontrolled flow becomes turbulent. Starting from this observation, we develop a framework for design of the traveling waves that are capable of (i) improving dynamical properties of the flow; and (ii) achieving positive net efficiency. We quantify receptivity of the NS equations linearized around UTWs and DTWs to stochastic disturbances by computing the *ensemble average energy density* of the statistical steady-state. Motivated by our desire to have low cost of control we confine our study to small amplitude blowing and suction along the walls. This also facilitates derivation of an

explicit formula for energy amplification (in flows with control) using perturbation analysis techniques. Our simulation-free design reveals that the UTWs are poor candidates for preventing transition; conversely, we demonstrate that *properly designed* DTWs are capable of substantially reducing receptivity of three dimensional fluctuations (including streamwise streaks and Tollmien-Schlichting (TS) waves). This indicates that the DTWs can be used as an effective means for controlling the onset of turbulence. Moreover, we show the existence of DTWs that result in a positive net efficiency compared to the uncontrolled flow that becomes turbulent. Our theoretical predictions are verified in using DNS of the NS equations. Thus, our work (i) demonstrates that the theory developed for the linearized equations with uncertainty has considerable ability to capture full-scale phenomena; and (ii) exhibits the predictive power of the proposed perturbation-analysis-based method for designing traveling waves.

This chapter represents an outgrowth of the study performed during the 2006 Center for Turbulence Research Summer Program [81]. While [81] only focused on receptivity of UTWs with large wavelength, our current study does a comprehensive analysis of the influence of both UTWs and DTWs on the fluctuations' kinetic energy and the overall efficiency. We also note that linear stability and transient growth of traveling waves were recently examined by [82]. For selected values of parameters, it was shown that the UTWs destabilize the laminar flow for control amplitudes as small as 1.5% of the centerline velocity; on the other hand, the DTWs with phase speeds larger than the centerline velocity remain stable even for large wave amplitudes. Moreover, the UTWs (DTWs) exhibit larger (smaller) transient growth relative to the uncontrolled flow. Our study confirms all of these observations; it also extends them at several different levels. First, we pay close attention to a net efficiency by computing the net power gained (positive efficiency) or lost (negative efficiency) in the presence of wall-actuation. Second, we conduct much more detailed study of the influence of traveling waves on velocity fluctuations; this is done by a thorough analysis of the influence of the wave speed, frequency, and amplitude on receptivity of full three dimensional fluctuations. Third, we confirm all of our theoretical predictions and highlight remaining research challenges.

Our presentation is organized as follows: in § 4.1, we formulate the governing equations in the presence of traveling wave wall-actuation. The influence of control on the nominal bulk flux and the nominal net efficiency is also discussed in this section. A frequency representation of the NS equations linearized around base velocity induced by traveling waves is presented in § 2.2. We further discuss a notion of the ensemble average energy density of the statistical steady-state and describe an efficient method for determining this quantity in flows subject to small amplitude traveling waves. In § 2.3, we employ perturbation analysis to derive an explicit formula for energy amplification. This formula is used to identify the values of wave frequency and speed that reduce receptivity of the linearized NS equations; we show that the essential trends are captured by perturbation analysis up to a second order in traveling wave amplitude. We

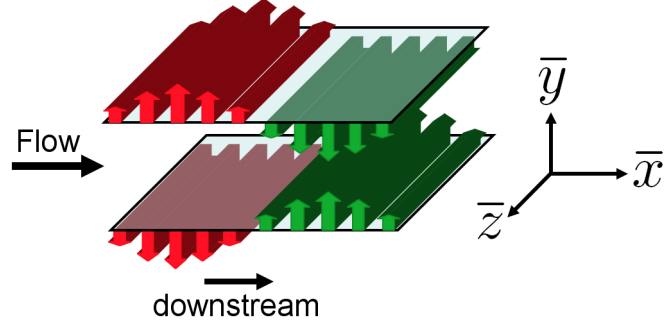


Figure 2.1: A pressure driven channel flow with blowing and suction along the walls.

also discuss influence of amplitude on energy of velocity fluctuations and reveal physical mechanisms for energy amplification. A brief summary of the main results along with an overview of remaining research challenges is provided in § 2.5.

2.1 Steady-state analysis

2.1.1 Governing equations

Consider a channel flow governed by the non-dimensional incompressible NS equations

$$\mathbf{u}_{\bar{t}} = -(\mathbf{u} \cdot \nabla) \mathbf{u} - \nabla P + (1/R_c) \Delta \mathbf{u} + \mathbf{F}, \quad 0 = \nabla \cdot \mathbf{u}, \quad (2.1)$$

with the Reynolds number defined in terms of the centerline velocity of the parabolic laminar profile U_c and channel half-height δ , $R_c = U_c \delta / \nu$. The kinematic viscosity is denoted by ν , the velocity vector is given by \mathbf{u} , P is the pressure, \mathbf{F} is the body force, ∇ is the gradient, and $\Delta = \nabla \cdot \nabla$ is the Laplacian. The spatial coordinates and time are represented by $(\bar{x}, \bar{y}, \bar{z})$ and \bar{t} , respectively.

In addition to a constant pressure gradient, $P_{\bar{x}}$, the flow is exposed to a zero-net-mass-flux surface blowing and suction in the form of a streamwise traveling wave (see Figure 3.1 for illustration). In the absence of the nominal body force, $\bar{\mathbf{F}} \equiv 0$, base velocity $\mathbf{u}_b = (U, V, W)$ represents the steady-state solution to (4.1) subject to

$$\begin{aligned} V(\bar{y} = \pm 1) &= \mp 2\alpha \cos(\omega_x(\bar{x} - c\bar{t})), \quad \bar{\mathbf{F}} \equiv 0, \\ U(\pm 1) &= V_{\bar{y}}(\pm 1) = W(\pm 1) = 0, \quad P_{\bar{x}} = -2/R_c, \end{aligned} \quad (2.2)$$

where ω_x , c , and α , respectively, identify frequency, speed, and amplitude of the traveling wave. Positive values of c define a DTW, whereas negative values of c define a UTW. The time dependence in $V(\pm 1)$ can be eliminated by the Galilean transformation, $(x = \bar{x} - c\bar{t}, y = \bar{y}, z = \bar{z}, t = \bar{t})$. This change of coordinates does not influence the spatial

differential operators, but it transforms the time derivative to $\partial_{\bar{t}} = \partial_t - c \partial_x$, which adds an additional convective term to the NS equations

$$\mathbf{u}_t = c\mathbf{u}_x - (\mathbf{u} \cdot \nabla) \mathbf{u} - \nabla P + (1/R_c)\Delta \mathbf{u} + \mathbf{F}, \quad 0 = \nabla \cdot \mathbf{u}. \quad (2.3)$$

In new coordinates, i.e. in the frame of reference that travels with the wave, the wall-actuation (2.2) induces a two dimensional base velocity, $\mathbf{u}_b = (U(x, y), V(x, y), 0)$, which represents the steady-state solution to (2.3). Note that the spatially periodic wall actuation, $V(y = \pm 1) = \mp 2\alpha \cos(\omega_x x)$, induces base velocity which is periodic in x .

The equations describing dynamics (up to a first order) of velocity fluctuations $\mathbf{v} = (u, v, w)$ around base velocity, \mathbf{u}_b , are obtained by decomposing each field in (2.3) into the sum of base and fluctuating parts, i.e., $\{\mathbf{u} = \mathbf{u}_b + \mathbf{v}, P = P + p, \mathbf{F} = 0 + \mathbf{d}\}$, and by neglecting the quadratic term in \mathbf{v}

$$\mathbf{v}_t = c\mathbf{v}_x - (\mathbf{u}_b \cdot \nabla) \mathbf{v} - (\mathbf{v} \cdot \nabla) \mathbf{u}_b - \nabla p + (1/R_c)\Delta \mathbf{v} + \mathbf{d}, \quad 0 = \nabla \cdot \mathbf{v}. \quad (2.4)$$

Note that the boundary conditions (2.2) are satisfied by base velocity and, thus, velocity fluctuations acquire homogeneous Dirichlet boundary conditions.

2.1.2 Base flow

Let us first consider a surface blowing and suction of a small amplitude α . In this case, a weakly nonlinear analysis can be employed to solve (2.3) subject to (2.2) and determine the corrections to base parabolic profile; similar approach was previously used by [65, 81]. We only present the equations for corrections up to a second order in α ; similar equations can be obtained for higher order corrections. Stream functions, $\Psi_{1,\pm 1}(y)$, can be used to determine the first harmonic in Fourier series representation of the base velocity (cf. (2.5))

$$U_{1,\pm 1}(y) = \Psi'_{1,\pm 1}(y), \quad V_{1,\pm 1}(y) = \mp i\omega_x \Psi_{1,\pm 1}(y),$$

where $\Psi_{1,\pm 1}(y)$ are solutions to

$$(1/R_c)\Delta_{\omega_x}^2 \Psi_{1,\pm 1} \pm i\omega_x ((c - U_0) \Delta_{\omega_x} \Psi_{1,\pm 1} + U_0'' \Psi_{1,\pm 1}) = 0, \\ \Psi_{1,-1}(\pm 1) = \pm i/\omega_x, \quad \Psi_{1,1}(\pm 1) = \mp i/\omega_x, \quad \Psi'_{1,\pm 1}(\pm 1) = 0.$$

Here, $\Delta_{\omega_x} = \partial_{yy} - \omega_x^2$ with Dirichlet boundary conditions and $\Delta_{\omega_x}^2 = \partial_{yyyy} - 2\omega_x^2 \partial_{yy} + \omega_x^4$ with Cauchy boundary conditions. Moreover, $U_{2,0}$ is obtained by equating terms of order α^2 in the streamwise averaged x -momentum equation

$$(1/R_c)U_{2,0}'' = V_{1,1}U'_{1,-1} - U_{1,1}V'_{1,-1} + V_{1,-1}U'_{1,1} - U_{1,-1}V'_{1,1}, \quad U_{2,0}(\pm 1) = 0.$$

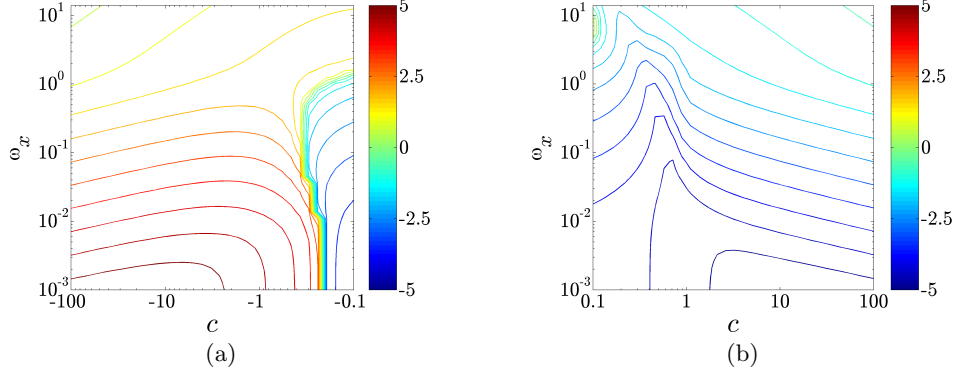


Figure 2.2: Second order correction to the nominal flux, $U_{B,2}(c, \omega_x)$, for (a) upstream waves; and (b) downstream waves in Poiseuille flow with $R_c = 2000$. Note: the level sets are obtained using a sign-preserving logarithmic scale; e.g., 5 and -3 should be interpreted as $U_{B,2} = 10^5$ and $U_{B,2} = -10^3$, respectively.

Therefore, up to a second order in control amplitude α , $U(x, y)$ and $V(x, y)$ can be represented as

$$\begin{aligned} U(x, y) &= U_0(y) + \alpha U_1(x, y) + \alpha^2 U_2(x, y) + \mathcal{O}(\alpha^3), \\ V(x, y) &= \alpha V_1(x, y) + \alpha^2 V_2(x, y) + \mathcal{O}(\alpha^3), \end{aligned}$$

where $U_0(y) = 1 - y^2$ denotes base velocity in Poiseuille flow and

$$\begin{aligned} U_1(x, y) &= U_{1,-1}(y) e^{-i\omega_x x} + U_{1,1}(y) e^{i\omega_x x}, \\ V_1(x, y) &= V_{1,-1}(y) e^{-i\omega_x x} + V_{1,1}(y) e^{i\omega_x x}, \\ U_2(x, y) &= U_{2,0}(y) + U_{2,-2}(y) e^{-2i\omega_x x} + U_{2,2}(y) e^{2i\omega_x x}, \\ V_2(x, y) &= V_{2,-2}(y) e^{-2i\omega_x x} + V_{2,2}(y) e^{2i\omega_x x}. \end{aligned} \tag{2.5}$$

[65] recently showed that, in the absence of driving pressure gradient, the traveling waves induce nominal bulk flux (i.e., *pumping*) in the direction opposite to the direction in which the wave travels. While the first order of correction to the base velocity is purely oscillatory, the quadratic interactions in the NS equations introduce mean flow correction $U_{2,0}(y)$ at the level of α^2 . The nominal bulk flux is determined by $U_B = (1/2) \int_{-1}^1 \overline{U}(y) dy$ where the overline denotes averaging over horizontal directions. In the presence of a pressure gradient, the nominal flux in flow with no control is $U_{B,0} = (1/2) \int_{-1}^1 U_0(y) dy = 2/3$, and the second order correction (in α) to U_B is given by $U_{B,2} = (1/2) \int_{-1}^1 U_{2,0}(y) dy$. Figure 2.2 shows $U_{B,2}$ as a function of wave frequency, ω_x , and wave speed, c , in Poiseuille flow with $R_c = 2000$. Except for a narrow region

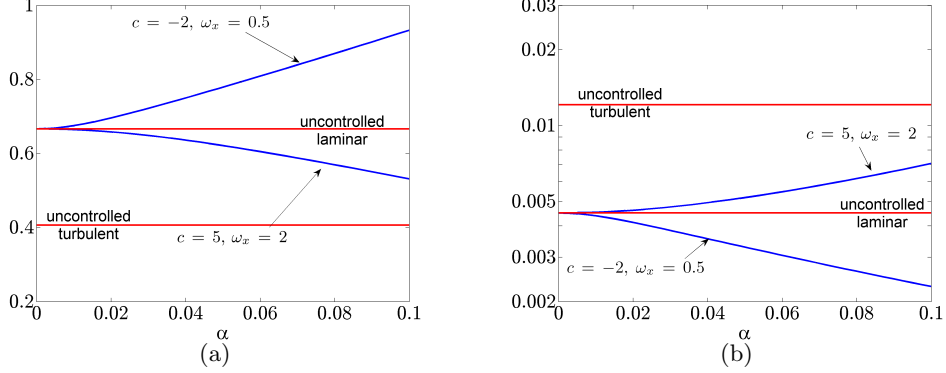


Figure 2.3: (a) The nominal flux, $U_B(\alpha)$; and (b) the nominal skin-friction drag coefficient, $C_f(\alpha)$, for a pair of UTWs and a pair of DTWs in Poiseuille flow with $R_c = 2000$. The results are obtained by solving (2.3) subject to (2.2), in the steady-state, using Newton’s method; U_B and C_f of the uncontrolled laminar and turbulent flows are also shown for comparison.

in the vicinity of $c = 0$, the upstream and downstream waves increase and reduce the nominal flux, respectively. Furthermore, for a given wave speed c , the magnitude of the induced flux increases as the wave frequency is decreased.

Figure 2.3 is obtained by finding the steady-state solution of (2.3) subject to (2.2) using Newton’s method. Originally, we have used base flow resulting from the weakly nonlinear analysis to initialize Newton iterations; robustness of our computations is confirmed using initialization with many different incompressible base flow conditions. The nominal flux and its associated nominal drag coefficient for a UTW with $c = -2$ and $\omega_x = 0.5$, and a DTW with $c = 5$ and $\omega_x = 2$ are shown in this figure. The flux and drag coefficient of both laminar and turbulent flows with no control are also given for comparison. The nominal skin-friction drag coefficient is defined as [70]

$$C_f = 2\bar{\tau}_w/U_B^2 = -2P_x/U_B^2,$$

where $\bar{\tau}_w$ is the nondimensional average wall-shear stress. For the fixed pressure gradient, $P_x = -2/R_c$, the nominal skin-friction drag coefficient is inversely proportional to square of the nominal flux and, in uncontrolled laminar flow with $R_c = 2000$, we have $C_f = 4.5 \times 10^{-3}$. The UTWs produce larger nominal flux (and, consequently, smaller nominal drag coefficient) compared to both laminar and turbulent uncontrolled flows. On the other hand, the DTWs yield smaller nominal flux (and, consequently, larger nominal drag coefficient) compared to uncontrolled laminar flow. In situations where flow with no control becomes turbulent, however, the DTWs with amplitudes

smaller than a certain threshold value may have lower nominal drag coefficient than the uncontrolled turbulent flow; e.g., for a DTW with $c = 5$ and $\omega_x = 2$ this threshold value is given by $\alpha = 0.16$ (cf. Figure 2.3(b)).

2.1.3 Nominal net efficiency

For the fixed pressure gradient, the difference between the flux of the controlled and the uncontrolled flows results in production of a driving power (per unit horizontal area of the channel)

$$\Pi_{prod} = -2P_x (U_{B,c} - U_{B,u}),$$

where $U_{B,c}$ and $U_{B,u}$ are the nominal flux of the controlled and uncontrolled flows, respectively. On the other hand, the required control power exerted at the walls (per unit horizontal area of the channel) is given by [83]

$$\Pi_{req} = \overline{VP}|_{y=-1} - \overline{VP}|_{y=1}. \quad (2.6)$$

The control net efficiency is determined by the difference of the produced and required powers [9]

$$\Pi_{net} = \Pi_{prod} - \Pi_{req},$$

where Π_{net} signifies the net power gained (positive Π_{net}) or lost (negative Π_{net}), in the presence of wall-actuation.

For small control amplitudes, the produced power can be represented as

$$\Pi_{prod} = \Pi_{prod,0} + \alpha^2 \Pi_{prod,2} + \mathcal{O}(\alpha^4),$$

where

$$\Pi_{prod,0} = -2P_x (U_{B,0} - U_{B,u}), \quad \Pi_{prod,2} = -2P_x U_{B,2}.$$

The nominal required control power can be determined from (2.6) by evaluating the horizontal average of the product between base pressure, P , and base wall-normal velocity, V , at the walls. Since, at the walls, the nonzero component of V contains *only* first harmonic in x (cf. (2.5)), we need to determine the first harmonic (in x) of P to compute Π_{req} . Base pressure can be obtained by solving the two dimensional Poisson equation

$$P_{xx} + P_{yy} = -(U_x U_x + 2V_x U_y + V_y V_y), \quad (2.7)$$

where P satisfies the following Neumann boundary conditions

$$P_y|_{y=\pm 1} = ((V_{xx} + V_{yy})/R_c + c V_x)|_{y=\pm 1}.$$

These are determined by evaluating the y -momentum equation at the walls. For small values of α , weakly nonlinear analysis, in conjunction with the expressions for U and V

given in § 2.1.2, can be employed to solve (2.7) for base pressure

$$\begin{aligned} P(x, y) &= \alpha P_1(x, y) + \mathcal{O}(\alpha^2), \\ P_1(x, y) &= P_{1,-1}(y) e^{-i\omega_x x} + P_{1,1}(y) e^{i\omega_x x}, \end{aligned}$$

where $P_{1,-1}$ and $P_{1,1}$ are determined from

$$\begin{aligned} P''_{1,\pm 1}(y) - \omega_x^2 P_{1,\pm 1}(y) &= \mp 2i\omega_x V_{1,\pm 1}(y) U'_0(y), \\ P'_{1,-1}(\pm 1) &= (V''_{1,-1}(\pm 1) - \omega_x^2 V_{1,-1}(\pm 1))/R_c - ci\omega_x V_{1,-1}(\pm 1), \\ P'_{1,1}(\pm 1) &= (V''_{1,1}(\pm 1) - \omega_x^2 V_{1,1}(\pm 1))/R_c + ci\omega_x V_{1,1}(\pm 1). \end{aligned}$$

Here, the prime denotes the partial derivative with respect to y , and the required power can be represented as

$$\begin{aligned} \Pi_{req} &= \alpha^2 \Pi_{req,2} + \mathcal{O}(\alpha^4), \\ \Pi_{req,2} &= (P_{1,-1} V_{1,1} + P_{1,1} V_{1,-1})|_{y=-1} - (P_{1,-1} V_{1,1} + P_{1,1} V_{1,-1})|_{y=1}. \end{aligned}$$

Since the second order correction to the nominal produced power, $\Pi_{prod,2}$, is directly proportional to $U_{B,2}$, $\Pi_{prod,2}$ is positive for UTWs and negative for DTWs. It turns out that smaller choices of ω_x result in larger produced (for UTWs) or lost (for DTWs) power. One of the main points of this chapter, however, is to show that it may be misleading to rely on the produced power as the *only* criterion for selection of control parameters; in what follows, we demonstrate that the required control power as well as the dynamics of velocity fluctuations need to be taken into account when designing the traveling waves.

2.1.4 Nominal efficiency of laminar controlled flows

We next examine the nominal efficiency of *laminar* controlled flows. Since we are interested in expressing the nominal efficiency relative to the power required to drive flow with no control, we provide comparison with both laminar and turbulent uncontrolled flows. The net efficiency in fraction of the power required to drive the uncontrolled laminar flow is determined by

$$\% \Pi_{net} = \Pi_{net}/\Pi_0 = -\alpha^2 |\pi_2(R_c; c, \omega_x)| + \mathcal{O}(\alpha^4), \quad (2.8)$$

where $\Pi_0 = -2P_x U_{B,0}$ and $\pi_2 = (\Pi_{prod,2} - \Pi_{req,2})/\Pi_0$. It can be shown that the second order correction to $\% \Pi_{net}$, π_2 , is negative for all choices of c and ω_x (see Figure 2.4). This is because the required power for maintaining the traveling wave grows faster than the produced power as α is increased. In addition, Figure 2.4 shows that $|\pi_2|$ is minimized for small wave speeds and for $\omega_x \in (1, 4)$. Formula (2.8) demonstrates that the control net efficiency is negative whenever the uncontrolled flow stays laminar (cf. Figure 2.5(a)). This is a special case of more general results by [79] and [80] which have

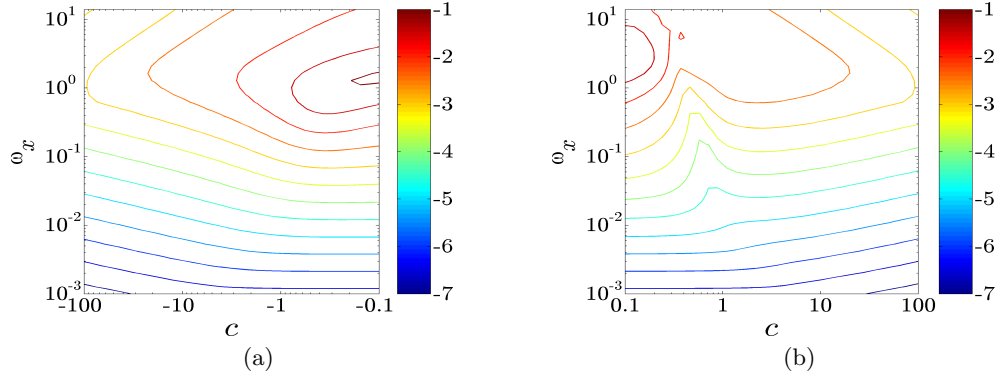


Figure 2.4: Second order correction to the nominal net efficiency, $\pi_2(c, \omega_x)$, for (a) upstream waves; and (b) downstream waves in Poiseuille flow with $R_c = 2000$. Note: the level sets are obtained using a sign-preserving logarithmic scale; e.g., -4 should be interpreted as $\pi_2 = -10^4$.

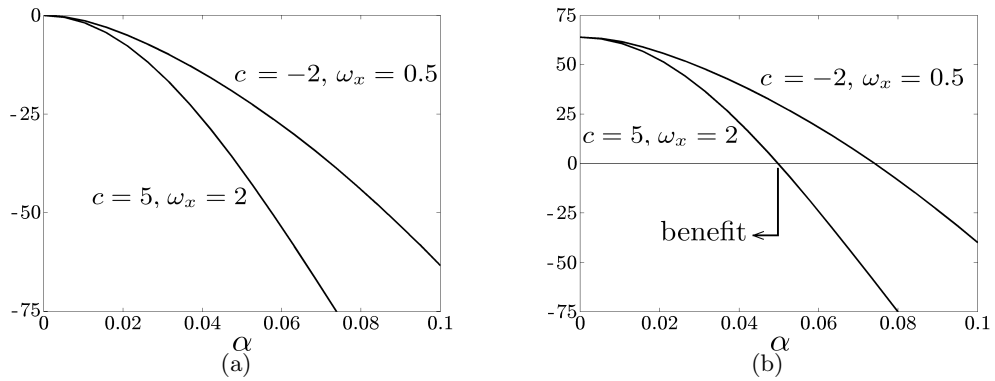


Figure 2.5: The steady-state net efficiency, $\% \Pi_{net}$, of *laminar* controlled flows as a function of control amplitude α for a UTW with $(c = -2, \omega_x = 0.5)$ and a DTW with $(c = 5, \omega_x = 2)$ at $R_c = 2000$. The results are obtained by *assuming* that the uncontrolled flow (a) remains laminar; and (b) becomes turbulent.

established that any transpiration-based control strategy necessarily has negative net efficiency compared to the laminar uncontrolled flow.

On the other hand, the net efficiency of the laminar controlled flow in fraction of the power required to drive the uncontrolled turbulent flow is determined by

$$\% \Pi_{net} = \frac{\Pi_{net}}{\Pi_{turb}} = \frac{U_{B,0}}{U_{B,turb}} \left(\underbrace{1 - \frac{U_{B,turb}}{U_{B,0}}}_{>0} - \alpha^2 |\pi_2(R_c, c, \omega_x)| \right) + \mathcal{O}(\alpha^4), \quad (2.9)$$

where $\Pi_{turb} = -2P_x U_{B,turb}$. Since the bulk flux of the uncontrolled turbulent flow is smaller than that of the uncontrolled laminar flow (i.e., $U_{B,turb} < U_{B,0}$), it is possible to obtain a positive net efficiency for sufficiently small values of α . Note that formula (2.9) is derived under the assumption that the controlled flow stays laminar while the uncontrolled flow becomes turbulent. Clearly, this formula represents an idealization since it assumes that laminar flow can be maintained by both UTWs and DTWs even with infinitesimal control amplitudes. It also indicates that increasing the control amplitude always decreases the nominal net efficiency. In a nutshell, the control amplitude needs to be large enough to maintain a laminar flow but increasing the control amplitude beyond certain value brings the efficiency down and eventually leads to negative efficiency. If the efficiency is negative, maintaining a laminar flow does not lead to any net benefit in the presence of control. This is further illustrated in Figure 2.5(b) where Newton's method is used to show that a positive net efficiency can be achieved for control amplitudes smaller than a certain threshold value (e.g., $\alpha < 0.05$ for the DTW with $c = 5$ and $\omega_x = 2$). In addition, the net efficiency monotonically decreases as α is increased, as predicted by the weakly nonlinear analysis up to a second order in α (cf. (2.9)).

An estimate for the maximum value of α for which a positive net efficiency is attainable can be obtained by solving the following equation (obtained using weakly nonlinear analysis)

$$(1 - U_{B,turb}/U_{B,0}) - \alpha_{max}^2 |\pi_2(R_c, c, \omega_x)| = 0. \quad (2.10)$$

Figure 2.6 shows α_{max} as a function of ω_x for different values of c . The dotted curves denote the approximation for α_{max} obtained using (2.10). The values of α_{max} (solid curves) obtained using Newton's method are also shown for comparison; we see that the predictions based on the second order correction capture the essential trends and provide good estimates for α_{max} (especially for large wave speeds and for wave frequencies between 0.1 and 10). Figures 2.5 and 2.6 are obtained by assuming that the flow with control stays laminar while the flow with no control becomes turbulent. Whether or not the traveling waves can control the onset of turbulence depends on the velocity fluctuations; addressing this question requires analysis of the dynamics, which is a topic of § 2.2 and § 2.3, where we examine receptivity of velocity fluctuations around UTWs and DTWs to stochastic disturbances.

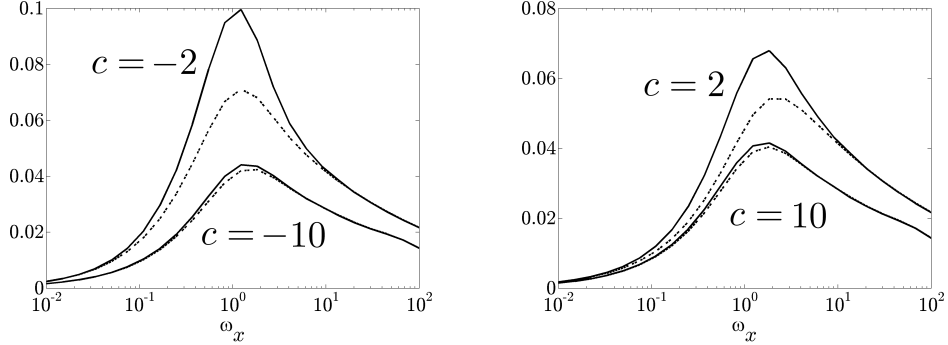


Figure 2.6: The wave amplitude, α_{\max} , for which the nominal net efficiency, $\% \Pi_{net}$, is positive at $R_c = 2000$ for (a) a pair of UTWs; and (b) a pair of DTWs. The solid curves are computed using Newton's method, and the dotted curves are computed using (2.10). The results are obtained by *assuming* that the controlled flow stays laminar while the uncontrolled flow becomes turbulent.

2.2 Dynamics of fluctuations around traveling waves

2.2.1 Evolution model with forcing

A standard conversion of (2.4) to the wall-normal velocity (v)/vorticity (η) formulation removes the pressure from the equations and yields the following evolution model with *forcing*

$$\begin{aligned} E \boldsymbol{\psi}_t(x, y, z, t) &= F \boldsymbol{\psi}(x, y, z, t) + G \mathbf{d}(x, y, z, t), \\ \mathbf{v}(x, y, z, t) &= C \boldsymbol{\psi}(x, y, z, t). \end{aligned} \quad (2.11)$$

This model is driven by the body force fluctuation vector $\mathbf{d} = (d_1, d_2, d_3)$, which can account for flow disturbances. We refer the reader to a recent review article [64] and a monograph [84] for a comprehensive discussion explaining why it is relevant to study influence of these excitations on velocity fluctuations. The internal state of (2.11) is determined by $\boldsymbol{\psi} = (v, \eta)$, with Cauchy (both Dirichlet and Neumann) boundary conditions on v and Dirichlet boundary conditions on η . All operators in (2.11) are matrices of differential operators in three coordinate directions x , y , and z . Operator C in (2.11) captures a kinematic relation between $\boldsymbol{\psi}$ and \mathbf{v} , operator G describes how forcing enters into the evolution model, whereas operators E and F determine internal properties of the linearized NS equations (e.g., modal stability). While operators E , G , and C do not depend on base velocity, operator F is base-velocity-dependent and, hence, it determines changes in the dynamics owing to changes in \mathbf{u}_b (see § 2.2.2). Moreover, for base velocity of § 2.1.2, F inherits spatial periodicity in x from \mathbf{u}_b and it can be represented

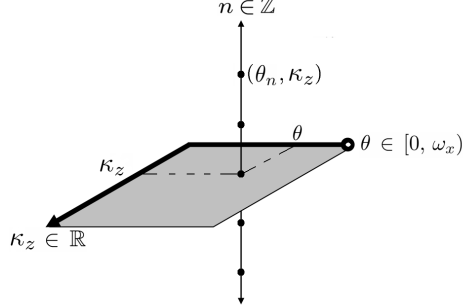


Figure 2.7: A Bloch wave $\mathbf{d}(x, y, z, t)$ defined in (2.12) is obtained by the superposition of weighted Fourier exponentials with frequencies $(\theta_n, \kappa_z) |_{n \in \mathbb{Z}}$, with weights determined by $\bar{\mathbf{d}}_n(y, \kappa_z, t)$.

as

$$F = F_0 + \sum_{l=1}^{\infty} \alpha^l \sum_{r \underline{\leq} -l}^l e^{ir\omega_x x} F_{l,r},$$

where F_0 and $F_{l,r}$ are spatially invariant operators in the streamwise and spanwise directions and $\sum_{r \underline{\leq} -l}^l$ signifies that r takes the values $\{-l, -l+2, \dots, l-2, l\}$. This expansion isolates spatially invariant and spatially periodic parts of operator F , which is well-suited for representation of (2.11) in the frequency domain.

2.2.2 Frequency representation of the linearized model

Owing to the structure of the linearized NS equations, the differential operators E , G , and C are invariant with respect to translations in horizontal directions. On the other hand, operator F is invariant in z and periodic in x . Thus, the Fourier transform in z can be applied to algebraize the spanwise differential operators. In other words, the normal modes in z are the spanwise waves, $e^{i\kappa_z z}$, where κ_z denotes the spanwise wavenumber. On the other hand, the appropriate normal modes in x are given by the so-called *Bloch waves* [85,86], which are determined by a product of $e^{i\theta x}$ and the $2\pi/\omega_x$ periodic function in x , with $\theta \in [0, \omega_x)$. Based on the above, each signal in (2.11) (for example, \mathbf{d}) can be expressed as

$$\left. \begin{aligned} \mathbf{d}(x, y, z, t) &= e^{i\kappa_z z} e^{i\theta x} \bar{\mathbf{d}}(x, y, \kappa_z, t) \\ \bar{\mathbf{d}}(x, y, \kappa_z, t) &= \bar{\mathbf{d}}(x + 2\pi/\omega_x, y, \kappa_z, t) \end{aligned} \right\} \kappa_z \in \mathbb{R}, \quad \theta \in [0, \omega_x),$$

where only real parts are to be used for representation of physical quantities. Expressing $\bar{\mathbf{d}}(x, y, \kappa_z, t)$ in Fourier series yields (see Figure 2.7 for an illustration)

$$\mathbf{d}(x, y, z, t) = \sum_{n=-\infty}^{\infty} \bar{\mathbf{d}}_n(y, \kappa_z, t) e^{i(\theta_n x + \kappa_z z)}, \quad \begin{array}{l} \theta_n = \theta + n\omega_x, \\ \kappa_z \in \mathbb{R}, \theta \in [0, \omega_x), \end{array} \quad (2.12)$$

where $\{\bar{\mathbf{d}}_n(y, \kappa_z, t)\}_{n \in \mathbb{Z}}$ are the coefficients in the Fourier series expansions of $\bar{\mathbf{d}}(x, y, \kappa_z, t)$.

The frequency representation of the linearized NS equations is obtained by substituting (2.12) into (2.11)

$$\begin{aligned} \partial_t \boldsymbol{\psi}_\theta(y, \kappa_z, t) &= \mathcal{A}_\theta(\kappa_z) \boldsymbol{\psi}_\theta(y, \kappa_z, t) + \mathcal{B}_\theta(\kappa_z) \mathbf{d}_\theta(y, \kappa_z, t), \\ \mathbf{v}_\theta(y, \kappa_z, t) &= \mathcal{C}_\theta(\kappa_z) \boldsymbol{\psi}_\theta(y, \kappa_z, t). \end{aligned} \quad (2.13)$$

This representation is parameterized by κ_z and θ and $\boldsymbol{\psi}_\theta(y, \kappa_z, t)$ denotes a bi-infinite column vector, $\boldsymbol{\psi}_\theta(y, \kappa_z, t) = \text{col}\{\boldsymbol{\psi}(\theta_n, y, \kappa_z, t)\}_{n \in \mathbb{Z}}$. The same definition applies to $\mathbf{d}_\theta(y, \kappa_z, t)$ and $\mathbf{v}_\theta(y, \kappa_z, t)$. On the other hand, for each κ_z and θ , $\mathcal{A}_\theta(\kappa_z)$, $\mathcal{B}_\theta(\kappa_z)$, and $\mathcal{C}_\theta(\kappa_z)$ are bi-infinite matrices whose elements are one dimensional integro-differential operators in y . The structure of these operators depends on frequency representation of E , F , G , and C in (2.11). In short, $\mathcal{B}_\theta(\kappa_z)$ and $\mathcal{C}_\theta(\kappa_z)$ are block-diagonal operators and

$$\mathcal{A}_\theta = \mathcal{A}_{0\theta} + \sum_{l=1}^{\infty} \alpha^l \mathcal{A}_{l\theta},$$

where $\mathcal{A}_{0\theta}$ and $\mathcal{A}_{l\theta}$ are structured operators. The particular structure of $\mathcal{A}_{0\theta}$ and $\mathcal{A}_{l\theta}$ is exploited in perturbation analysis of the energy amplification for small control amplitudes α in § 2.2.4. The details of the frequency representation are explained next.

We first describe how base velocity modified by the traveling waves enters in evolution model (2.11). Frequency representation of the evolution model is discussed next. It turns out that the components of base velocity determine coefficients of operator F in (2.11). For base velocity, $\mathbf{u}_b = (U(x, y), V(x, y), 0)$, F is a 2×2 block-operator with components

$$\begin{aligned} F^{11} &= (1/R_c)\Delta^2 + ((\Delta U) - (U - cI)\Delta)\partial_x - (\Delta V)\partial_y - V\Delta\partial_y - \\ &\quad 2V_x\partial_{xy} + U_x(\Delta - 2\partial_{xx}) - (\Delta V_y) + (2(\Delta V)\partial_x + \Delta V_x + \\ &\quad V_x(\Delta - 2\partial_{yy}) - 2U_x\partial_{xy})(\partial_{xx} + \partial_{zz})^{-1}\partial_{xy}, \\ F^{12} &= -(2(\Delta V)\partial_x + \Delta V_x + V_x(\Delta - 2\partial_{yy}) - 2U_x\partial_{xy})(\partial_{xx} + \partial_{zz})^{-1}\partial_z, \\ F^{21} &= -(U_y\partial_z + V_x(\partial_{xx} + \partial_{zz})^{-1}\partial_{yyz}), \\ F^{22} &= (1/R_c)\Delta - (U_x + (U - cI)\partial_x + V\partial_y) - V_x(\partial_{xx} + \partial_{zz})^{-1}\partial_{xy}, \end{aligned}$$

where $(\partial_{xx} + \partial_{zz})^{-1}$ is defined by

$$(\partial_{xx} + \partial_{zz})^{-1} : f \mapsto g \Leftrightarrow \begin{cases} f = (\partial_{xx} + \partial_{zz})g \\ = g_{xx} + g_{zz}. \end{cases}$$

Frequency representation (2.13) of the linearized evolution model (2.11) can be determined using the following simple rules [87]:

- (a) A *spatially invariant* operator L with Fourier symbol $L(\kappa_x)$ has a block-diagonal representation $\mathcal{L}_\theta = \text{diag}\{L(\theta_n)\}_{n \in \mathbb{Z}}$. For example, if $L = \partial_x$, then $\mathcal{L}_\theta = \text{diag}\{i(\theta + n\omega_x)I\}_{n \in \mathbb{Z}}$. Operators E , G , C , F_0 , and $F_{l,r}$ in (2.11) are spatially invariant and, thus, their representations are block-diagonal.
- (b) A *spatially periodic function* $T(x)$ with Fourier series coefficients $\{T_n\}_{n \in \mathbb{Z}}$ has a θ -independent block-Toeplitz representation

$$\mathcal{T} = \text{toep} \left\{ \cdots, T_2, T_1, \boxed{T_0}, T_{-1}, T_{-2}, \cdots \right\} = \begin{bmatrix} \ddots & & & & & & \\ & T_0 & T_{-1} & T_{-2} & & & \\ & T_1 & T_0 & T_{-1} & & & \\ & T_2 & T_1 & T_0 & & & \\ & & & & \ddots & & \\ & & & & & & \ddots \end{bmatrix},$$

where the box denotes the element on the main diagonal of \mathcal{T} . For example, $T(x) = e^{-irx}$ has a block-Toeplitz representation $\mathcal{T} = \mathcal{S}_r$ with the only non-zero element $T_{-r} = I$.

- (c) A representation of the sums and cascades of spatially periodic functions and spatially invariant operators is readily determined from these special cases. For example, a matrix representation of operator $e^{-irx}\partial_x$ is given by $\mathcal{S}_r \text{diag}\{i(\theta + n\omega_x)I\}_{n \in \mathbb{Z}}$.

Based on these, we get the following representations for \mathcal{A}_θ , \mathcal{B}_θ , and \mathcal{C}_θ in (2.13)

$$\begin{aligned} \mathcal{A}_\theta &= \mathcal{E}_\theta^{-1} \mathcal{F}_\theta = \mathcal{E}_\theta^{-1} \mathcal{F}_{0\theta} + \sum_{l=1}^{\infty} \alpha^l \sum_{r \stackrel{\geq}{\leq} -l} \mathcal{E}_\theta^{-1} \mathcal{S}_{-r} \mathcal{F}_{l,r\theta} = \mathcal{A}_{0\theta} + \sum_{l=1}^{\infty} \alpha^l \mathcal{A}_{l\theta}, \\ \mathcal{B}_\theta &= \mathcal{E}_\theta^{-1} \mathcal{G}_\theta, \quad \mathcal{G}_\theta = \text{diag}\{G(\theta_n)\}_{n \in \mathbb{Z}}, \quad \mathcal{C}_\theta = \text{diag}\{C(\theta_n)\}_{n \in \mathbb{Z}}, \end{aligned}$$

where we have used the fact that $\mathcal{E}_\theta = \text{diag}\{E(\theta_n)\}_{n \in \mathbb{Z}}$ is an invertible operator. For convenience of later algebraic manipulations, we rewrite $\mathcal{A}_{l\theta}$ as $\mathcal{A}_{l\theta} = \sum_{r \stackrel{\geq}{\leq} -l} \mathcal{S}_{-r} \mathcal{A}_{l,r\theta}$ where $\mathcal{A}_{l,r\theta} = \text{diag}\{A_{l,r}(\theta_n)\}_{n \in \mathbb{Z}} = \text{diag}\{E^{-1}(\theta_{n+r})F_{l,r}(\theta_n)\}_{n \in \mathbb{Z}}$. In other words, for a given $l \geq 1$ operator $\mathcal{A}_{l\theta}$ has non-zero blocks only on r th sub-diagonals with $r \in \{-l, -l+2, \dots, l-2, l\}$. The frequency symbols of the operators $E(\theta_n)$, $G(\theta_n)$, $C(\theta_n)$,

and $F_{l,r}(\theta_n)$ are given by

$$\begin{aligned} F_0^{11}(\theta_n, \kappa_z) &= (1/R_c)\Delta^2 + i\theta_n(U_0'' - (U_0 - c)\Delta), \quad F_0^{12}(\theta_n, \kappa_z) = 0, \\ F_0^{21}(\theta_n, \kappa_z) &= -i\kappa_z U_0', \quad F_0^{22}(\theta_n, \kappa_z) = (1/R_c)\Delta - i\theta_n(U_0 - c), \end{aligned}$$

and

$$\begin{aligned} F_{l,r}^{11}(\theta_n, \kappa_z) &= i\theta_n ((\Delta_{r\omega_x} U_{l,r}) - U_{l,r} \Delta - 2i(r\omega_x)V_{l,r}\partial_y) - \\ &\quad ((\Delta_{r\omega_x} V_{l,r}) + V \Delta) \partial_y + ir\omega_x U_{l,r}(\Delta + 2\theta_n^2) + ir\omega_x(\Delta_{r\omega_x} U_{l,r}) - \\ &\quad (\theta_n/\kappa^2)(2\theta_n((-\Delta_{r\omega_x} V_{l,r})\partial_y + ir\omega_x U_{l,r}\partial_{yy}) - \\ &\quad r\omega_x((\Delta_{r\omega_x} V_{l,r}) + V_{l,r}(\Delta - 2\partial_{yy}))\partial_y), \\ F_{l,r}^{12}(\theta_n, \kappa_z) &= (\kappa_z/\kappa^2)(2\theta_n((-\Delta_{r\omega_x} V_{l,r}) + ir\omega_x U_{l,r}\partial_y) - \\ &\quad r\omega_x((\Delta_{r\omega_x} V_{l,r}) + V_{l,r}(\Delta - 2\partial_{yy}))), \\ F_{l,r}^{21}(\theta_n, \kappa_z) &= -i\kappa_z (U_{l,r}' - (ir\omega_x/\kappa^2)V_{l,r}\partial_{yy}), \\ F_{l,r}^{22}(\theta_n, \kappa_z) &= -V_{l,r}\partial_y - ir\omega_x U_{l,r} + i\theta_n((ir\omega_x/\kappa^2)V_{l,r}\partial_y - U_{l,r}), \end{aligned}$$

where $\kappa^2 = \theta_n^2 + \kappa_z^2$, $\Delta = \partial_{yy} - \kappa^2$ and $\Delta_{r\omega_x} = \partial_{yy} - (r\omega_x)^2$ with Dirichlet boundary conditions, and $\Delta^2 = \partial_{yyyy} - 2\kappa^2\partial_{yy} + \kappa^4$ with Cauchy boundary conditions. Operators E , G , and C are given by

$$\begin{aligned} E(\theta_n, \kappa_z) &= \begin{bmatrix} \Delta & 0 \\ 0 & I \end{bmatrix}, \quad G(\theta_n, \kappa_z) = \begin{bmatrix} -i\theta_n\partial_y & -\kappa^2 I & -i\kappa_z\partial_y \\ i\kappa_z I & 0 & -i\theta_n I \end{bmatrix}, \\ C(\theta_n, \kappa_z) &= \begin{bmatrix} i(\theta_n/\kappa^2)\partial_y & -i(\kappa_z/\kappa^2)I \\ I & 0 \\ i(\kappa_z/\kappa^2)\partial_y & i(\theta_n/\kappa^2)I \end{bmatrix}. \end{aligned}$$

2.2.3 Energy density of the linearized model

Frequency representation (2.13) contains a large amount of information about linearized dynamics. For example, it can be used to assess stability properties of the base flow. However, since the *early stages of transition* in wall-bounded shear flows are not appropriately described by the stability properties of the linearized equations (for example, see [64, 84]), we perform receptivity analysis of stochastically forced model (2.13) to assess the effectiveness of the proposed control strategy. Namely, we set the initial conditions in (2.13) to zero and study the responses of the linearized dynamics to uncertain body forces. When the body forces are absent, the response of stable flows decays asymptotically to zero. However, in the presence of stochastic body forces, the linearized NS equations are capable of maintaining high levels of the steady-state variance [7, 27, 28]. Our analysis quantifies the effect of imposed streamwise traveling waves on the asymptotic levels of variance and describes how receptivity changes in the presence of control.

We note that there are substantial differences between the problem considered here and in [7]; these differences arise from lack of homogeneity in the streamwise direction which introduces significant computational challenges which we discuss below. Furthermore, even though our study is similar in spirit to [88], current work studies dynamics of fluctuations around spatially periodic base velocity, whereas [88] considered dynamics of fluctuations around time periodic base velocity. Theoretical framework for quantifying receptivity in these two conceptually different cases was developed by [87] and [89], respectively.

Let us assume that a stable system (2.13) is subject to a zero-mean white stochastic process (in y and t), $\mathbf{d}_\theta(y, \kappa_z, t)$. Then, for each κ_z and θ , the ensemble average energy density of the statistical steady-state is determined by

$$\begin{aligned}\bar{\mathbf{E}}(\theta, \kappa_z) &= \lim_{t \rightarrow \infty} \langle \mathbf{v}_\theta(\cdot, \kappa_z, t), \mathbf{v}_\theta(\cdot, \kappa_z, t) \rangle \\ &= \text{trace} \left(\lim_{t \rightarrow \infty} \mathcal{E} \{ \mathbf{v}_\theta(\cdot, \kappa_z, t) \otimes \mathbf{v}_\theta(\cdot, \kappa_z, t) \} \right),\end{aligned}$$

where $\langle \cdot, \cdot \rangle$ denotes the $L_2[-1, 1]$ inner product and averaging in time, i.e.,

$$\begin{aligned}\langle \mathbf{v}_\theta, \mathbf{v}_\theta \rangle &= \mathcal{E} \left\{ \int_{-1}^1 \mathbf{v}_\theta^*(y, \kappa_z, t) \mathbf{v}_\theta(y, \kappa_z, t) dy \right\}, \\ \mathcal{E} \{ v(\cdot, t) \} &= \lim_{T \rightarrow \infty} \frac{1}{T} \int_0^T v(\cdot, t + \tau) d\tau,\end{aligned}\tag{2.14}$$

and $\mathbf{v}_\theta \otimes \mathbf{v}_\theta$ is the tensor product of \mathbf{v}_θ with itself. We note that $\bar{\mathbf{E}}(\theta, \kappa_z)$ determines the asymptotic level of energy (i.e., variance) maintained by a stochastic forcing in (2.13). Typically, this quantity is computed by running DNS of the NS equations until the statistical steady-state is reached. However, for linearized system (2.13), the energy density $\bar{\mathbf{E}}(\theta, \kappa_z)$ can be determined using the solution to the following operator Lyapunov equation [87]

$$\mathcal{A}_\theta(\kappa_z) \mathcal{X}_\theta(\kappa_z) + \mathcal{X}_\theta(\kappa_z) \mathcal{A}_\theta^+(\kappa_z) = -\mathcal{B}_\theta(\kappa_z) \mathcal{B}_\theta^+(\kappa_z),\tag{2.15}$$

as

$$\bar{\mathbf{E}}(\theta, \kappa_z) = \text{trace} \left(\mathcal{X}_\theta(\kappa_z) \mathcal{C}_\theta^+(\kappa_z) \mathcal{C}_\theta(\kappa_z) \right).$$

Here, $^+$ denotes the adjoint of an operator, and $\mathcal{X}_\theta(\kappa_z)$ represents the autocorrelation operator of ψ_θ , that is

$$\mathcal{X}_\theta(\kappa_z) = \lim_{t \rightarrow \infty} \mathcal{E} \{ \psi_\theta(\cdot, \kappa_z, t) \otimes \psi_\theta(\cdot, \kappa_z, t) \}.$$

Since $\mathcal{C}_\theta^+(\kappa_z)\mathcal{C}_\theta(\kappa_z)$ is an identity operator, we have

$$\bar{\mathbb{E}}(\theta, \kappa_z) = \text{trace}(\mathcal{X}_\theta(\kappa_z)) = \sum_{n=-\infty}^{\infty} \text{trace}(X_d(\theta_n, \kappa_z)), \quad (2.16)$$

where $X_d(\theta_n, \kappa_z)$ denotes the elements on the main diagonal of operator \mathcal{X}_θ . We note that $\bar{\mathbb{E}}$ also has an interesting deterministic interpretation; namely, if $\mathbf{v}_\theta(\cdot, \kappa_z, t)$ denotes the impulse response of (2.13), then

$$\bar{\mathbb{E}}(\theta, \kappa_z) = \int_0^\infty \text{trace}(\mathbf{v}_\theta(\cdot, \kappa_z, t) \otimes \mathbf{v}_\theta(\cdot, \kappa_z, t)) dt.$$

Thus, the same quantity can be used to assess receptivity of the linearized NS equations to exogenous disturbances of either stochastic or deterministic origin.

2.2.4 Perturbation analysis of energy density

Solving (2.15) is computationally expensive; a discretization of the operators (in y) and truncation of the bi-infinite matrices convert (2.15) into a large-scale matrix Lyapunov equation. Our computations suggest that in order to obtain convergence of

$$\bar{\mathbb{E}}(\theta, \kappa_z) \approx \sum_{n=-N}^N \text{trace}(X_d(\theta_n, \kappa_z)),$$

a choice of N between ten (for $\omega_x \sim \mathcal{O}(1)$) and a few thousands (for $\omega_x \sim \mathcal{O}(0.01)$) is required. Since we aim to conduct a detailed study of the influence of streamwise traveling waves on dynamics of velocity fluctuations, determining energy density for a broad range of traveling wave parameters, κ_z and θ still poses significant computational challenges.

Instead, we employ an efficient perturbation analysis based approach introduced by [90] for solving equation (2.15). For our problem, this approach turns out to be at least 20 times faster than the truncation approach. This method is well-suited for systems with small amplitude spatially periodic terms and it converts (2.15) into a set of conveniently coupled system of operator-valued Lyapunov and Sylvester equations. A finite dimensional approximation of these equations yields a set of algebraic matrix equations whose order is determined by the product between the number of fields in the evolution model (here 2, the wall-normal velocity and vorticity) and the size of discretization in y . While consideration of small wave amplitudes simplifies analysis by providing an explicit expression for energy density, it is also motivated by our earlier observation that large values of α introduce high cost of control which is not desirable from a physical point of view.

For sufficiently small values of α , the solution of (2.15) can be expressed as a perturbation series $\mathcal{X}_\theta = \sum_{m=0}^{\infty} \alpha^m \mathcal{X}_{m\theta}$. After substituting into (2.15) and collecting equal power in α , we have

$$\begin{aligned} \alpha^0: \quad \mathcal{A}_{0\theta} \mathcal{X}_{0\theta} + \mathcal{X}_{0\theta} \mathcal{A}_{0\theta}^+ &= -\mathcal{B}_\theta \mathcal{B}_\theta^+, \\ \alpha^m: \quad \mathcal{A}_{0\theta} \mathcal{X}_{m\theta} + \mathcal{X}_{m\theta} \mathcal{A}_{0\theta}^+ &= -\sum_{l=1}^m (\mathcal{A}_{l\theta} \mathcal{X}_{m-l\theta} + \mathcal{X}_{m-l\theta} \mathcal{A}_{l\theta}^+), \quad m \geq 1 \end{aligned} \quad (2.17)$$

Since operator $\mathcal{A}_{0\theta}$ is block-diagonal, $\mathcal{X}_{m\theta}$ inherits the same structure as the right-hand-side of (2.17). One can show that $\mathcal{X}_{m\theta}$ has non-zero blocks only on the first $s \leq m$ odd (for odd m) or even (for even m) upper and lower sub-diagonals. Up to a second order in α , we have

$$\begin{aligned} \mathcal{X}_{0\theta} &= \mathcal{X}_{0,0\theta}, \\ \mathcal{X}_{1\theta} &= \mathcal{S}_1 \mathcal{X}_{1,1\theta} + \mathcal{X}_{1,1\theta}^+ \mathcal{S}_{-1}, \\ \mathcal{X}_{2\theta} &= \mathcal{S}_2 \mathcal{X}_{2,2\theta} + \mathcal{X}_{2,0\theta} + \mathcal{X}_{2,2\theta}^+ \mathcal{S}_{-2}, \end{aligned} \quad (2.18)$$

where $\mathcal{X}_{m,s\theta} = \text{diag} \{X_{m,s}(\theta_n)\}_{n \in \mathbb{Z}}$ and \mathcal{S}_r is defined in § 2.2.2. Substituting into (2.17) yields

$$\begin{aligned} \mathcal{A}_{0\theta} \mathcal{X}_{0,0\theta} + \mathcal{X}_{0,0\theta} \mathcal{A}_{0\theta}^+ &= -\mathcal{B}_\theta \mathcal{B}_\theta^+, \\ \mathcal{A}_{0\theta} \mathcal{S}_1 \mathcal{X}_{1,1\theta} + \mathcal{S}_1 \mathcal{X}_{1,1\theta} \mathcal{A}_{0\theta}^+ &= -\left(\mathcal{S}_1 \mathcal{A}_{1,-1\theta} \mathcal{X}_{0,0\theta} + \mathcal{X}_{0,0\theta} \mathcal{A}_{1,1\theta}^+ \mathcal{S}_1 \right), \\ \mathcal{A}_{0\theta} \mathcal{X}_{2,0\theta} + \mathcal{X}_{2,0\theta} \mathcal{A}_{0\theta}^+ &= -\left(\mathcal{A}_{2,0\theta} \mathcal{X}_{0,0\theta} + \mathcal{X}_{0,0\theta} \mathcal{A}_{2,0\theta}^+ + \mathcal{S}_{-1} \mathcal{A}_{1,1\theta} \mathcal{S}_1 \mathcal{X}_{1,1\theta} + \right. \\ &\quad \left. \mathcal{S}_1 \mathcal{A}_{1,-1\theta} \mathcal{X}_{1,1\theta}^+ \mathcal{S}_{-1} + \mathcal{S}_1 \mathcal{X}_{1,1\theta} \mathcal{A}_{1,-1\theta}^+ \mathcal{S}_{-1} + \mathcal{X}_{1,1\theta}^+ \mathcal{S}_{-1} \mathcal{A}_{1,1\theta}^+ \mathcal{S}_1 \right). \end{aligned} \quad (2.19)$$

Finally, each block on the main diagonal of $\mathcal{X}_{m,s\theta}$ in (2.19) is obtained from

$$\begin{aligned} A_0(\theta_n) X_{0,0}(\theta_n) + X_{0,0}(\theta_n) A_0^+(\theta_n) &= -B(\theta_n) B^+(\theta_n), \\ A_0(\theta_{n-1}) X_{1,1}(\theta_n) + X_{1,1}(\theta_n) A_0^+(\theta_n) &= -\left(A_{1,-1}(\theta_n) X_{0,0}(\theta_n) + X_{0,0}(\theta_{n-1}) A_{1,1}^+(\theta_{n-1}) \right), \\ A_0(\theta_n) X_{2,0}(\theta_n) + X_{2,0}(\theta_n) A_0^+(\theta_n) &= -\left(A_{2,0}(\theta_n) X_{0,0}(\theta_n) + X_{0,0}(\theta_n) A_{2,0}^+(\theta_n) + \right. \\ &\quad \left. A_{1,1}(\theta_{n-1}) X_{1,1}(\theta_n) + A_{1,-1}(\theta_{n+1}) X_{1,1}^+(\theta_{n+1}) + \right. \\ &\quad \left. X_{1,1}(\theta_{n+1}) A_{1,-1}^+(\theta_{n+1}) + X_{1,1}^+(\theta_n) A_{1,1}^+(\theta_{n-1}) \right). \end{aligned}$$

Therefore, the energy density of system (2.11) can be represented as

$$\bar{\mathbb{E}}(\theta, \kappa_z; R_c, \alpha, c, \omega_x) = \bar{\mathbb{E}}_0(\theta, \kappa_z; R_c, \omega_x) + \sum_{l=1}^{\infty} \alpha^{2l} \bar{\mathbb{E}}_{2l}(\theta, \kappa_z; R_c, c, \omega_x), \quad 0 < \alpha \ll 1. \quad (2.20)$$

Thus, only terms with even powers in α contribute to $\bar{\mathbb{E}}$, which in controlled flow

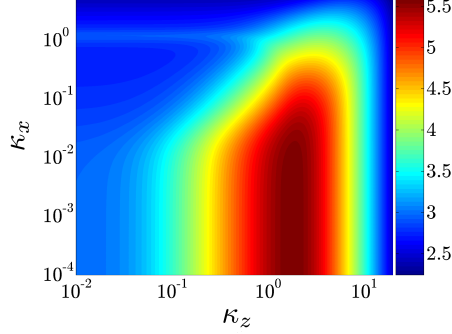


Figure 2.8: Energy density $\tilde{E}_0(\kappa_x, \kappa_z)$ of the uncontrolled Poiseuille flow with $R_c = 2000$. The plot is given in the log-log-log scale.

depends on six parameters. Since our objective is to identify trends in energy density, we confine our attention to a perturbation analysis up to a second order in α . We briefly comment on the influence of higher order corrections in § 2.3.3 where it is shown that the essential trends are correctly predicted by the second order of correction. A method for numerically determining the adjoint of the underlying operators is provided in Appendix A.

2.3 Energy amplification in Poiseuille flow with $R_c = 2000$

In this section, we study energy amplification of stochastically forced linearized NS equations in Poiseuille flow controlled with streamwise traveling waves. Equation (2.20) reveals the dependence of the energy density on traveling wave amplitude α , for $0 < \alpha \ll 1$. However, since the operators in (2.13) depend on the spatial wavenumbers (θ and κ_z), R_c , ω_x , and c , the energy density is also a function of these parameters. Finding the optimal triple (α, c, ω_x) that maximally reduces the energy of the velocity fluctuations is outside the scope of the current study; instead, we identify the values of c and ω_x that are capable of reducing receptivity in the presence of small amplitude streamwise traveling waves. Since we are interested in energy amplification of the transitional Poiseuille flow, we choose $R_c = 2000$ in all of our subsequent computations. This value is selected because it is between the critical Reynolds number at which linear instability takes place, $R_c = 5772$, and the value at which transition is observed in experiments and DNS, $R_c \approx 1000$. The same Reynolds number was used by [8] in their DNS study.

2.3.1 Energy density of flow with no control

We briefly comment on the energy density in uncontrolled Poiseuille flow with $R_c = 2000$; for an in-depth treatment see [7]. The appropriate normal modes in the uncontrolled flow are purely harmonic streamwise and spanwise waves, $e^{i\kappa_x x} e^{i\kappa_z z}$, where κ_x denotes the streamwise wavenumber. Figure 2.8 illustrates the energy density of the uncontrolled flow as a function of κ_x and κ_z , which we denote by $\tilde{E}_0(\kappa_x, \kappa_z)$. The streamwise constant fluctuations with $\mathcal{O}(1)$ spanwise wavenumbers carry most energy in flow with no control. Namely, the largest value of $\tilde{E}_0(\kappa_x, \kappa_z)$ occurs at $(\kappa_x = 0, \kappa_z \approx 1.78)$, which means that the most amplified flow structures (the streamwise streaks) are infinitely elongated in the streamwise direction and have the spanwise length scale of approximately 3.5δ , where δ is the channel half-height. We note that these input-output resonances do not correspond to the least-stable modes of the linearized NS equations. Rather, they arise because of the coupling from the wall-normal velocity v to the wall-normal vorticity η . Physically, this coupling is a product of the vortex tilting (lift-up) mechanism [91]; the base shear is tilted in the wall-normal direction by the spanwise changes in v , which lead to a nonmodal amplification of η . This mechanism does not take place either when the base shear is zero (i.e., $U' = 0$), or when there are no spanwise variations in v (i.e., $\kappa_z = 0$). On the other hand, the least-stable modes (TS waves) of uncontrolled flow create a local peak in $\tilde{E}_0(\kappa_x, \kappa_z)$ around $(\kappa_z = 0, \kappa_x \approx 1.2)$, with a magnitude significantly lower compared to the magnitude achieved by the streamwise constant flow structures. Finally, we note that the uncontrolled energy density $\bar{E}_0(\theta, \kappa_z; \omega_x)$ as appeared in (2.20) can be obtained from $\tilde{E}_0(\kappa_x, \kappa_z)$ using the following expression

$$\bar{E}_0(\theta, \kappa_z; \omega_x) = \sum_{n=-\infty}^{\infty} \tilde{E}_0(\theta_n, \kappa_z) = \sum_{n=-\infty}^{\infty} \tilde{E}_0(\theta + n\omega_x, \kappa_z).$$

In other words, for fixed ω_x and θ , $\bar{E}_0(\theta, \kappa_z; \omega_x)$ represents the energy density of velocity fluctuations that are composed of all wavenumbers $\kappa_x = \{\theta + n\omega_x\}_{n \in \mathbb{Z}}$. In comparison, $\tilde{E}_0(\kappa_x, \kappa_z)$ is the energy density of velocity fluctuations composed of a single wavenumber κ_x (see Figure 2.9 for an illustration).

2.3.2 Energy amplification of flow with control

We next consider energy amplification of velocity fluctuations in Poiseuille flow with $R_c = 2000$ in the presence of both UTWs and DTWs. As shown in § 2.2.4, for small amplitude blowing and suction along the walls, the perturbation analysis yields an *explicit formula* for energy amplification (cf. (2.20)),

$$\frac{\bar{E}(\theta, \kappa_z; \alpha, c, \omega_x)}{\bar{E}_0(\theta, \kappa_z; \omega_x)} = 1 + \alpha^2 g_2(\theta, \kappa_z; c, \omega_x) + \mathcal{O}(\alpha^4), \quad 0 < \alpha \ll 1.$$

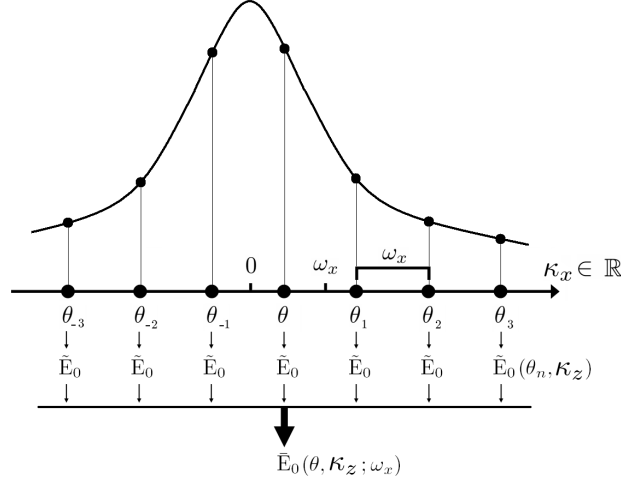


Figure 2.9: For fixed ω_x and θ , $\bar{E}_0(\theta, \kappa_z; \omega_x)$ represents energy density of fluctuations composed of all wavenumbers $\theta_n = \{\theta + n\omega_x\}_{n \in \mathbb{Z}}$; $\bar{E}_0(\theta, \kappa_z; \omega_x) = \sum_{n=-\infty}^{\infty} \tilde{E}_0(\theta + n\omega_x, \kappa_z)$.

Thus, for small wave amplitudes the influence of control can be assessed by evaluating function $g_2 = \bar{E}_2/\bar{E}_0$ that quantifies energy amplification up to a second order in α . Sign of g_2 determines whether energy density is increased or decreased in the presence of control; positive (negative) values of g_2 identify wave speed and frequency that increase (decrease) receptivity. Since function g_2 is sign-indefinite with vastly different magnitudes, it is advantageous to visualize g_2 using a sign-preserving logarithmic scale

$$\hat{g}_2 = \text{sign}(g_2) \log_{10}(1 + |g_2|).$$

For example, $\hat{g}_2 = 5$ or $\hat{g}_2 = -3$, respectively, signify $\bar{E}_2 = 10^5 \bar{E}_0$ or $\bar{E}_2 = -10^3 \bar{E}_0$. Since $\hat{g}_2(\theta, \kappa_z; c, \omega_x)$ depends on four parameters, for visualization purposes, we confine our attention to cross-sections of \hat{g}_2 by fixing two of the four parameters. We first study energy amplification of the modes with $\kappa_x = 1.78$ and $\kappa_x = 0$ as a function of c and ω_x ; these spanwise wavenumbers are selected in order to capture influence of control on streamwise streaks and TS waves, respectively. Since, in uncontrolled flow, streamwise streaks (respectively, TS waves) occur at $\kappa_x = 0$ (respectively, $\kappa_x = 1.2$), fluctuations with $\theta = 0$ (respectively, $\theta(\omega_x) = 1.2 - \omega_x \lfloor 1.2/\omega_x \rfloor$) are considered; these values of θ are chosen to make sure that streamwise streaks (respectively, TS waves) represent modes of the controlled flow as well. (Here, $\lfloor a \rfloor$ denotes the largest integer not greater than a .) We then analyze the energy amplification of disturbances with different values of θ and κ_z for a fixed set of control parameters c and ω_x . Our analysis illustrates the ability of properly designed traveling waves to weaken the intensity of both most energetic and

least stable modes of the uncontrolled flow. Direct numerical simulations of § 2.4 show that this can be done with positive net efficiency.

Since most amplification in flow with no control occurs for fluctuations with $(\kappa_x = 0, \kappa_z = 1.78)$, it is relevant to first study the influence of controls on these most energetic modes. In flow with control, the streamwise-constant flow structures are imbedded in the fundamental mode, i.e. fluctuations with $\theta = 0$ (cf. § 2.2.2). As the plots of $\hat{g}_2(c, \omega_x)$ in Figures 2.10(a) and 2.10(c) reveal, the values of c and ω_x determine whether these structures are amplified or attenuated by the traveling waves. Up to a second order in α , the control parameters associated with the dark regions in these two figures reduce the energy amplification of the uncontrolled flow. As evident from Figure 2.10(a), only a narrow range of UTWs with $\omega_x \lesssim 0.1$ is capable of reducing the energy amplification. However, since the required power for maintaining the nominal flow for such low frequency controls is prohibitively large (cf. Figure 2.10(b)), the choice of UTWs for transition control is not favorable from efficiency point of view (receptivity reduction by these UTWs is further discussed in § 2.3.3). On the other hand, a large range of DTW parameters with $c \gtrsim 1$ and $\omega_x \gtrsim 0.1$ is capable of making the controlled flow less sensitive to stochastic excitations (cf. Figure 2.10(c)). Moreover, Figure 2.10(d) shows that the $\omega_x \gtrsim 0.1$ region contains the smallest required power for sustaining the DTWs. These two features identify properly designed DTWs as suitable candidates for controlling the onset of turbulence with positive net efficiency (as confirmed by DNS in § 2.4).

It is noteworthy that traveling waves with parameters considered in [8] (i.e., $\omega_x = \{0.5, 1, 1.5, 2\}$ and $-4 < c < 0$) increase amplification of the most energetic modes of the uncontrolled flow (cf. Figure 2.10(a)). This is in agreement with a recent study of [82] where a transient growth larger than that of the laminar uncontrolled flow was observed for UTWs with $c = \{-1, -2\}$ and $\omega_x = 1.5$. Furthermore, it is shown in § 2.4 that such UTWs promote turbulence even for initial conditions for which the uncontrolled flow stays laminar.

The above analysis illustrates the ability of the DTWs to weaken the intensity of the most energetic modes of the uncontrolled flow; this is achieved by reducing receptivity to stochastic disturbances. However, an important aspect in the evaluation of any control strategy is to consider the influence of controls on all of the system's modes. In view of this, we next discuss how control affects the full three dimensional fluctuations. Since for a given ω_x the energy amplification is symmetric around $\theta = \omega_x/2$, it suffices to only consider the modes with $\theta \in [0, \omega_x/2]$. Figure 2.11 shows $\hat{g}_2(\theta, \kappa_z)$ for a UTW with $(c = -2, \omega_x = 0.5)$, and three DTWs with $(c = 3, \omega_x = 1.5)$, $(c = 5, \omega_x = 0.5)$, and $(c = 5, \omega_x = 2)$. As evident from Figure 2.10, the selected UTW increases amplification of the fundamental mode with $\kappa_z = 1.78$; on the other hand, all three DTWs reduce energy amplification of modes with $(\theta = 0, \kappa_z = 1.78)$. Figure 2.11 further reveals that the largest change in amplification for all of these traveling waves takes place at $(\theta = 0, \kappa_z \approx 1.78)$, which is precisely where the uncontrolled flow contains most energy.

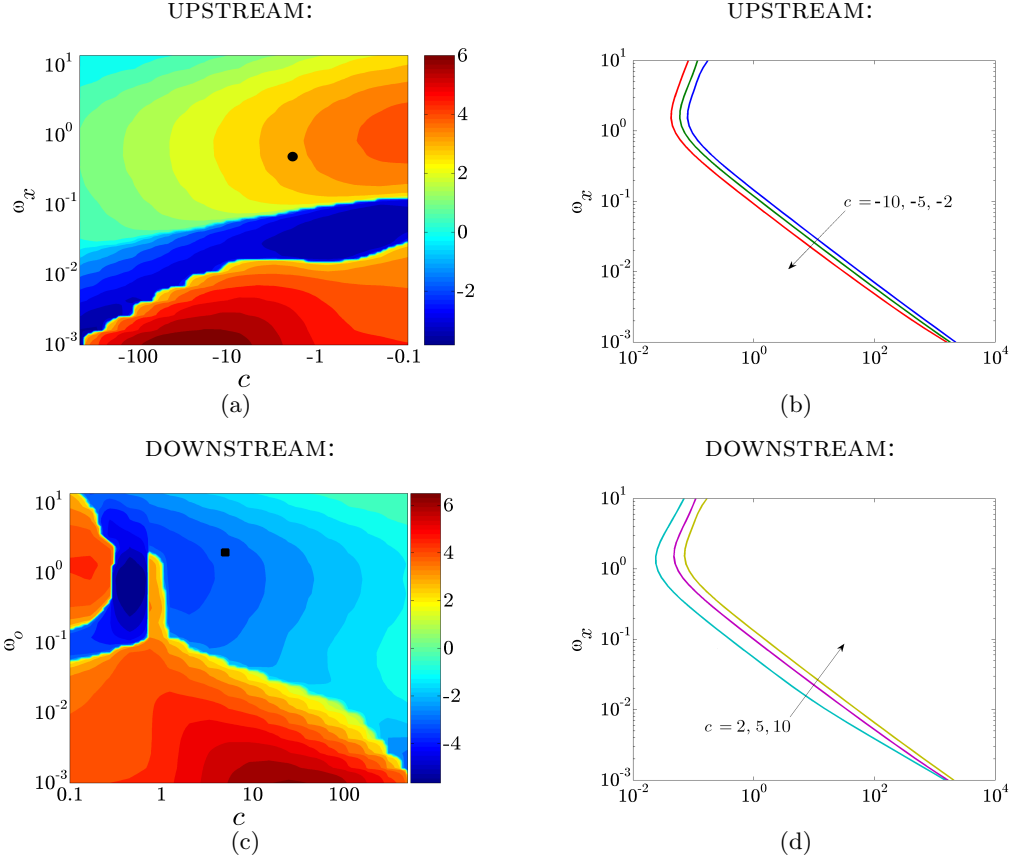


Figure 2.10: (a) and (c): Second order correction to the energy amplification, $\hat{g}_2(c, \omega_x)$, of the modes with $(\theta, \kappa_z) = (0, 1.78)$, in the presence of (a) UTWs; and (c) DTWs in Poiseuille flow with $R_c = 2000$. (b) and (d): Second order correction to the nominal required power, $\Pi_{req,2}(\omega_x; c)$, for (b) UTWs; and (d) DTWs. The dot and the square, respectively, denote $(c = -2, \omega_x = 0.5)$ (as selected in [8]) and $(c = 5, \omega_x = 2)$. Note: the plots on the left are obtained using a sign-preserving logarithmic scale; e.g., $\hat{g}_2 = 5$ and $\hat{g}_2 = -3$ should be interpreted as $\bar{E}_2 = 10^5 \bar{E}_0$ and $\bar{E}_2 = -10^3 \bar{E}_0$, respectively.

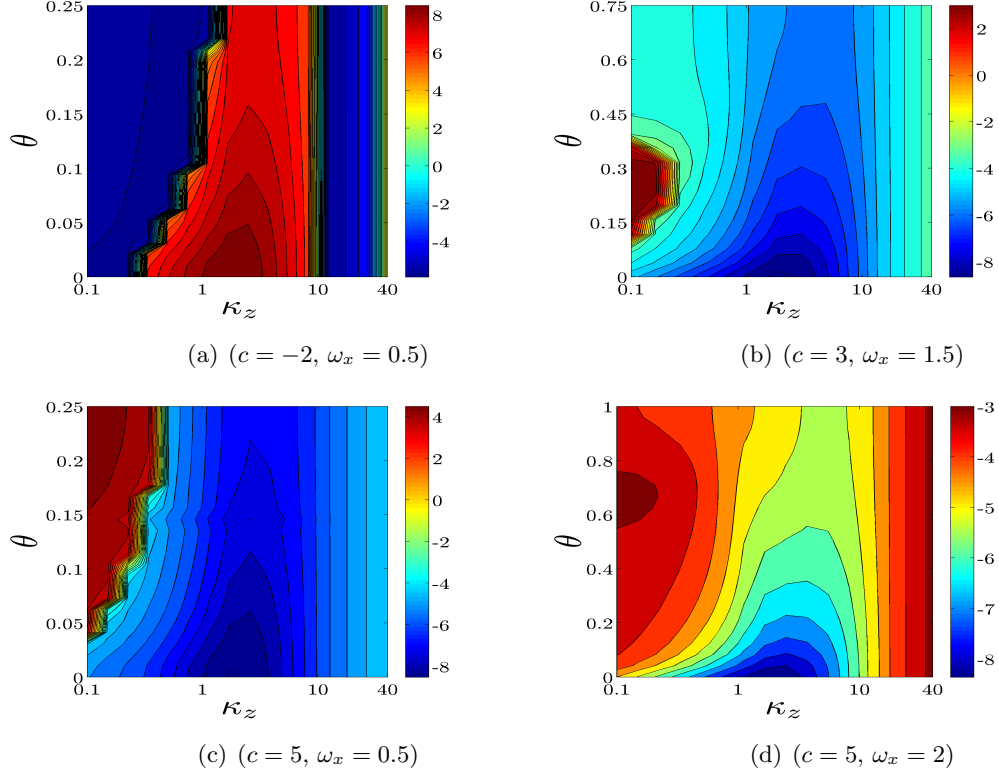


Figure 2.11: Second order correction to the energy amplification, $\hat{g}_2(\theta, \kappa_z)$, for traveling waves with (a) ($c = -2, \omega_x = 0.5$); (b) ($c = 3, \omega_x = 1.5$); (c) ($c = 5, \omega_x = 0.5$); and (d) ($c = 5, \omega_x = 2$) in Poiseuille flow with $R_c = 2000$.

This observation suggests presence of resonant interactions between the traveling waves and the most energetic modes of the uncontrolled flow. Additionally, as can be seen from Figures 2.11(a) and 2.11(d), the energy of modes with $\kappa_z \approx 0$ is reduced by a UTW with ($c = -2, \omega_x = 0.5$) and a DTW with ($c = 5, \omega_x = 2$) for all θ . On the other hand, Figure 2.11(b) shows that a DTW with ($c = 3, \omega_x = 1.5$) increases amplification of fluctuations with ($0.1 \lesssim \theta \lesssim 0.4, \kappa_z \approx 0$); similarly, receptivity of fluctuations with ($0.05 \lesssim \theta \lesssim 0.45, \kappa_z \approx 0$) is increased by a DTW with ($c = 2, \omega_x = 0.5$) (cf. Figure 2.11(c)). Thus, from the four considered cases, only a DTW with ($c = 5, \omega_x = 0.5$) can be used to inhibit intensity of full three dimensional velocity fluctuations (i.e., for all values of θ and κ_z).

While the fundamental mode is most influential in determining the effect of control on the energy amplification, Figures 2.11(b) and 2.11(c) indicate that the modes with $\theta \neq 0$ and large spanwise wavelengths (i.e., $\kappa_z \approx 0$) can be significantly amplified by

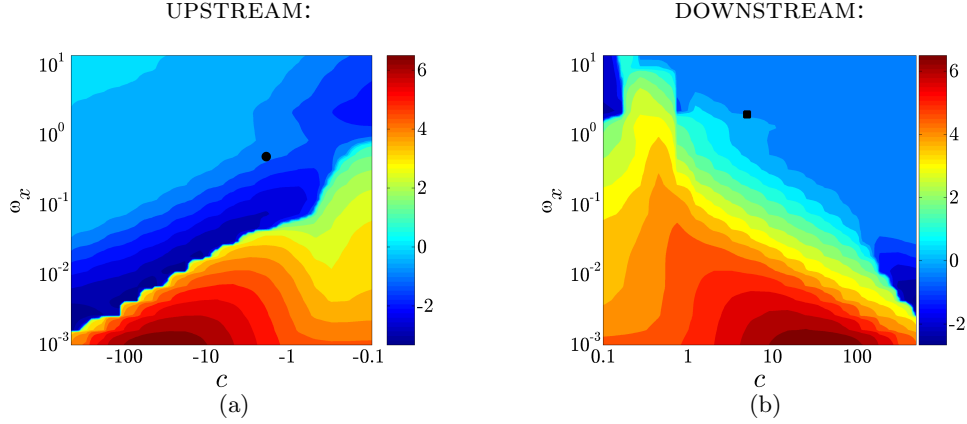


Figure 2.12: Second order correction to the energy amplification, $\hat{g}_2(c, \omega_x)$, of the modes with $(\theta(\omega_x), \kappa_z) = (1.2 - \omega_x \lfloor \frac{1.2}{\omega_x} \rfloor, 0)$, in the presence of (a) UTWs; and (b) DTWs in Poiseuille flow with $R_c = 2000$. The dot and the square, respectively, denote $(c = -2, \omega_x = 0.5)$ and $(c = 5, \omega_x = 2)$.

the traveling waves. We thus take a closer look at how control affects the spanwise constant fluctuations. The TS waves are characterized by $(\kappa_x = 1.2, \kappa_z = 0)$ and, for a given ω_x , they are imbedded in the modes of the controlled flow for fluctuations with $\theta(\omega_x) = 1.2 - \omega_x \lfloor 1.2/\omega_x \rfloor$. Figure 2.12 shows the second order correction $\hat{g}_2(c, \omega_x)$ to the energy amplification of the modes with $\kappa_z = 0$ subject to both UTWs and DTWs. Note that Figure 2.12 correctly captures the increased intensity of the TS waves by DTWs with $(c = 3, \omega_x = 1.5)$ and $(c = 5, \omega_x = 0.5)$, as already observed in Figures 2.11(b) and 2.11(c). We also see that the traveling waves considered in [8] reduce energy of the TS waves (we recall that these promote amplification of the streamwise streaks; cf. Figures 2.10(a) and 2.12(a)). On the other hand, the DTW with $c = 5$ and $\omega_x = 2$ decreases energy amplification of both streamwise streaks and TS waves (cf. Figures 2.10(c) and 2.12(b)). The values of c and ω_x capable of reducing the energy amplification (up to a second order in α) of both most energetic and least stable modes of the uncontrolled flow are marked by the dark region in Figure 2.13.

2.3.3 Effect of control amplitude on energy amplification

We next discuss influence of control amplitude on the energy amplification. We show that perturbation analysis (up to a second order in α) correctly predicts the essential trends. This is done by comparing perturbation analysis results with computations obtained using large-scale truncation of the operators in Lyapunov equation (2.15).

The limit of the perturbation series (2.20) can be obtained by applying Shanks transformation [92, 93] on the perturbation-analysis-based correction coefficients in (2.20).

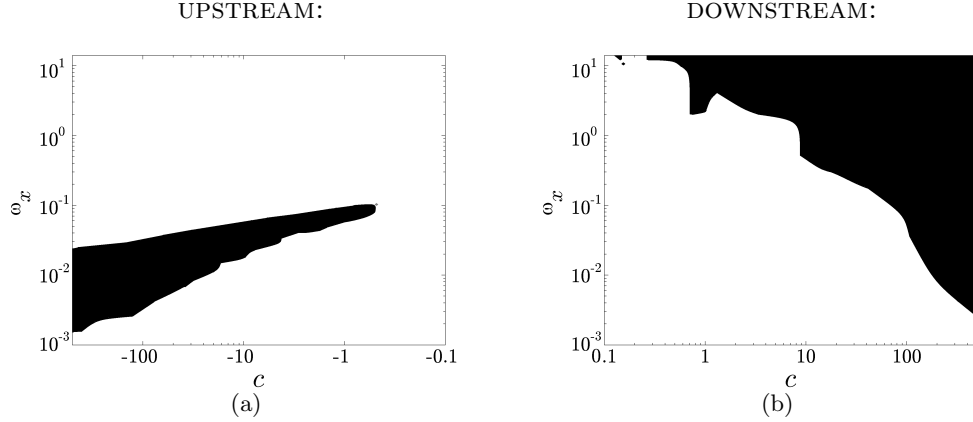


Figure 2.13: The dark regions identify values of wave speed and frequency that, up to a second order in α , suppress the energy amplification of both most energetic and least stable modes in Poiseuille flow with $R_c = 2000$ subject to: (a) UTWs; and (b) DTWs.

This transformation represents an effective means for providing convergence (respectively, faster convergence) to a divergent (respectively, slowly convergent) series [94], see Appendix B for more details. It turns out that Shanks transformation significantly increases the maximum value of α for which series (2.20) converges. Figure 2.14 shows the energy density of the fundamental mode, as a function of κ_z , in the uncontrolled Poiseuille flow with $R_c = 2000$ and a flow subject to a DTW with ($c = 5$, $\omega_x = 2$, $\alpha = 0.025$). The controlled flow results are obtained using truncation of series (2.20) up to a second order in α , and Shanks transformation up to a fourth order in α . Note that even though the second order correction overestimates the amount of receptivity reduction, it correctly captures the essential trends.

Figure 2.15 compares energy density of the fundamental mode in uncontrolled Poiseuille flow with $R_c = 2000$, and in the controlled flows subject to: (a) a UTW with $c = -2$ and $\omega_x = 0.5$, Figure 2.15(a); and (b) a DTW with $c = 5$ and $\omega_x = 2$, Figure 2.15(b). The controlled flow results are obtained using Shanks transformation up to a fourth order in α , and they closely match the large-scale truncation results (hollow circles). Figure 2.15(b) shows that the properly designed DTWs with amplitudes equal to 5%, 10%, and 20% of the base centerline velocity reduce the largest energy density of the uncontrolled flow by approximately 28%, 60%, and 80%, respectively. It is noteworthy that substantial reduction is obtained at the expense of relatively small increase (compared to the laminar flow) in the nominal drag coefficient, which approximately increases by 1%, 4%, and 13%. Further increase in the amplitude of a DTW with $c = 5$ and $\omega_x = 2$ results even in larger receptivity reduction. We demonstrate in § 2.4 that this approach can be successfully used for controlling the onset of turbulence in

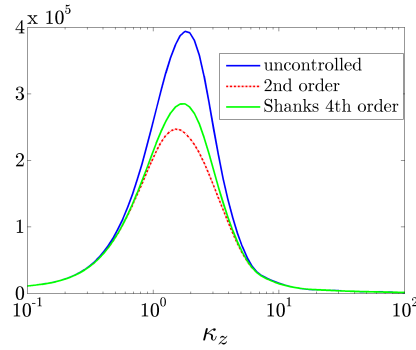


Figure 2.14: Energy density, $\bar{E}(\kappa_z)$, of the fundamental mode $\theta = 0$ in Poiseuille flow with $R_c = 2000$ and $(c = 5, \omega_x = 2, \alpha = 0.025)$. The controlled flow results are obtained using perturbation analysis up to a second order in α , and Shanks transformation up to a fourth order in α .

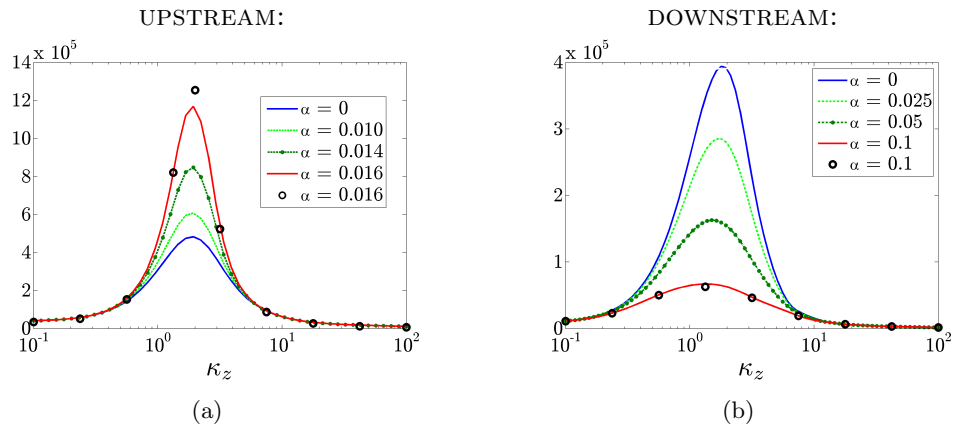


Figure 2.15: Energy density, $\bar{E}(\kappa_z)$, of the fundamental mode $\theta = 0$ in Poiseuille flow with $R_c = 2000$ subject to: (a) a UTW with $c = -2$ and $\omega_x = 0.5$; and (b) a DTW with $c = 5$ and $\omega_x = 2$. Shanks transformation up to a fourth order in α is used in computations. The truncation results (hollow circles) are obtained for (a) $\alpha = 0.016$; and (b) $\alpha = 0.1$.

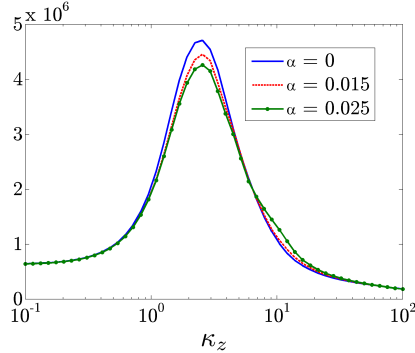


Figure 2.16: Energy density, $\bar{E}(\kappa_z)$, of the fundamental mode $\theta = 0$ in Poiseuille flow with $R_c = 2000$ subject to a UTW with $c = -5$ and $\omega_x = 0.03$. Shanks transformation up to a fourth order in α is used in computations.

flows subject to large initial disturbances. However, the power required for maintaining laminar flow under these conditions is prohibitively large, which limits the advantage of using DTWs for transition control from efficiency point of view.

In contrast to DTWs, Figure 2.15(a) demonstrates that the UTW with $c = -2$ and $\omega_x = 0.5$ increases receptivity. We note that all of these trends are correctly captured by the second order correction (in α) to the energy amplification and that our results agree with the transient growth study of [82]. Furthermore, large energy amplification of the UTWs may be thought of as a precursor to flow instability; namely, it turns out that the UTWs destabilize the flow for $\alpha > 0.03$ which is a smaller value compared to the amplitudes chosen in [8] ($\alpha = 0.05$ and $\alpha = 0.125$, respectively).

As described in § 2.3.2, Figure 2.10(a) suggests that the UTWs with $\omega_x \lesssim 0.1$ can reduce the intensity of the most energetic modes of the uncontrolled flow. Here, we demonstrate that such UTWs lead to a very modest receptivity reduction. Figure 2.16 illustrates that a UTW with ($c = -5$, $\omega_x = 0.03$, $\alpha = 0.025$) reduces energy amplification by about 8%. On the other hand, modal stability analysis can be used to show that amplitudes as small as $\alpha \approx 0.03$ make the flow linearly unstable. Therefore, relative to flow with no control, the UTWs at best exhibit similar receptivity to disturbances.

For control amplitudes shown in Figures 2.15 and 2.16, we have verified stability of fluctuations around base velocities in both UTWs and DTWs by computing the eigenvalues of the large-scale truncation of operator $\mathcal{A}_\theta(\kappa_z)$ in (2.13). Compared to solving the truncated version of Lyapunov equation (2.15), perturbation analysis in conjunction with Shanks transformation provides much more efficient way for determining energy amplification. For example, while it takes four days on a PC to obtain the truncated results (hollow circles) in Figure 2.15(b), the Shanks approximation is computed in four hours on the same PC. Moreover, once the correction coefficients in (2.20) have been

determined, the energy amplification for a reasonably wide range of control amplitudes can be obtained at no further cost.

2.3.4 Energy amplification mechanisms

The energy of velocity fluctuations around a given base flow can also be obtained from the Reynolds-Orr equation [84]. This equation can be used to elucidate the energy amplification mechanisms and facilitate better understanding of the influence of UTWs and DTWs on transitional channel flows. In this section, we consider the Reynolds-Orr equation for the fundamental modes (i.e., modes with $\theta = 0$; cf. equation (2.12)). Our results reveal that, relative to the uncontrolled flow, the DTWs reduce the production of kinetic energy, thereby enabling the smaller receptivity to disturbances. As opposed to the DTWs, the UTWs increase the production of kinetic energy. For the streamwise-periodic base flow, $\mathbf{u}_b = (U(x, y), V(x, y), 0)$, the time evolution of the kinetic energy of the fundamental modes, $\bar{E}(\theta = 0, \kappa_z; t) = \langle \mathbf{v}_\theta(\cdot, \kappa_z, t), \mathbf{v}_\theta(\cdot, \kappa_z, t) \rangle |_{\theta=0}$, is governed by

$$\begin{aligned} \frac{1}{2} \frac{d\bar{E}}{dt} = & -\langle u_\theta, \mathcal{U}_y v_\theta \rangle - \langle v_\theta, \mathcal{V}_y v_\theta \rangle - \langle u_\theta, \mathcal{U}_x u_\theta \rangle - \langle v_\theta, \mathcal{V}_x u_\theta \rangle + \\ & (1/R_c) (\langle \mathbf{v}_\theta, \mathcal{D}_{xx} \mathbf{v}_\theta \rangle + \langle \mathbf{v}_\theta, \partial_{yy} \mathbf{v}_\theta \rangle - \kappa_z^2 \langle \mathbf{v}_\theta, \mathbf{v}_\theta \rangle) + \langle \mathbf{v}_\theta, \mathbf{d}_\theta \rangle, \quad \theta = 0, \end{aligned} \quad (2.21)$$

where, for example, $\mathbf{v}_\theta = \text{col} \{ \mathbf{v}(n\omega_x, y, \kappa_z, t) \}_{n \in \mathbb{Z}}$ for the fundamental modes. In (2.21), \mathcal{D}_{xx} is a diagonal operator with $\{(-n\omega_x)^2 I\}_{n \in \mathbb{Z}}$ on its main diagonal, I is the identity operator, $\langle \cdot, \cdot \rangle$ denotes the $L_2[-1, 1]$ inner product and averaging in time (cf. equation (2.14)), and \mathcal{U}_y , \mathcal{V}_y , \mathcal{U}_x , and \mathcal{V}_x are block-Toeplitz operators whose r th sub-diagonals are determined by the r th harmonic in the Fourier series representation of $U_y(x, y)$, $V_y(x, y)$, $U_x(x, y)$, and $V_x(x, y)$ (see § 2.2.2 for details). The first four terms on the right-hand-side of (2.21) denote the work of Reynolds stresses on the base shear and they contribute to production of the kinetic energy. The next group of terms represents viscous dissipation and the last term accounts for the direct work of the forcing on the velocity fluctuations. It can be shown that the direct work of \mathbf{d} on \mathbf{v} is balanced by a fixed portion of the viscous dissipation, and that the difference between the production terms and the remaining dissipation terms determines the energy density (cf. Figure 2.17).

In the steady-state limit, (2.21) can be used to obtain the following expression for the energy density of the fundamental mode, $\bar{E}(0, \kappa_z) = \lim_{t \rightarrow \infty} \bar{E}(0, \kappa_z; t)$,

$$\bar{E}(0, \kappa_z) = \bar{E}_p(0, \kappa_z) + \bar{E}_d(0, \kappa_z).$$

Here, $\bar{E}_p(0, \kappa_z)$ denotes the contribution of production terms to the energy density and $\bar{E}_d(0, \kappa_z)$ represents the joint contribution of viscous dissipation and the work of

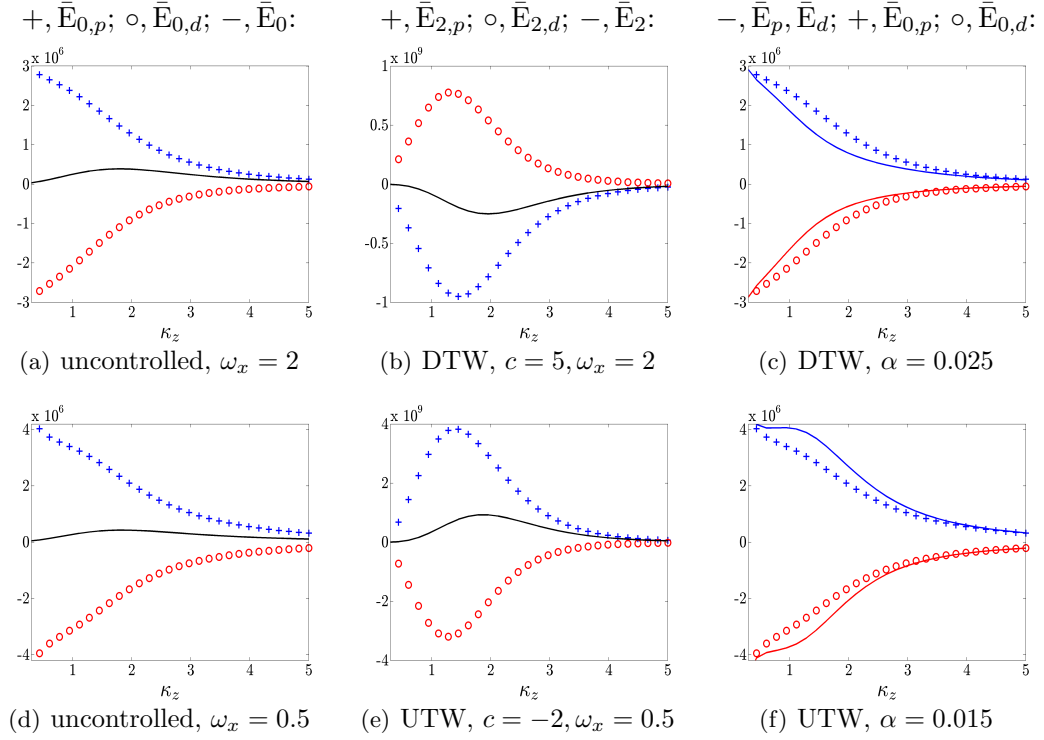


Figure 2.17: Contribution of production and dissipation terms to energy density of $\theta = 0$ mode in Poiseuille flow with $R_c = 2000$ subject to (a)-(c) a DTW with ($c = 5$, $\omega_x = 2$); and (d)-(f) a UTW with ($c = -2$, $\omega_x = 0.5$). (a,d) uncontrolled flow; (b,e) second order corrections; and (c,f) controlled flows. In (c,f), the controlled flow results are obtained using approximation up to a second order in α , and the uncontrolled flow results are shown for comparison.

disturbances

$$\begin{aligned}\bar{E}_p(0, \kappa_z) &= -(R_c/\kappa_z^2) (\langle u_\theta, \mathcal{U}_y v_\theta \rangle + \langle v_\theta, \mathcal{V}_y v_\theta \rangle + \langle u_\theta, \mathcal{U}_x u_\theta \rangle + \langle v_\theta, \mathcal{V}_x u_\theta \rangle), \\ \bar{E}_d(0, \kappa_z) &= (1/\kappa_z^2) (\langle \mathbf{v}_\theta, \mathcal{D}_{xx} \mathbf{v}_\theta \rangle + \langle \mathbf{v}_\theta, \partial_{yy} \mathbf{v}_\theta \rangle) + (R_c/\kappa_z^2) \langle \mathbf{v}_\theta, \mathbf{d}_\theta \rangle, \quad \theta = 0.\end{aligned}\quad (2.22)$$

In flows subject to small amplitude traveling waves, a perturbation analysis can be employed to study the effect of each term on the right-hand-side of (2.22) on the energy density

$$\begin{aligned}\bar{E}(0, \kappa_z) &= \bar{E}_0(0, \kappa_z) + \alpha^2 \bar{E}_2(0, \kappa_z) + \mathcal{O}(\alpha^4), \\ \bar{E}_0(0, \kappa_z) &= \bar{E}_{0,p}(0, \kappa_z) + \bar{E}_{0,d}(0, \kappa_z), \\ \bar{E}_2(0, \kappa_z) &= \bar{E}_{2,p}(0, \kappa_z) + \bar{E}_{2,d}(0, \kappa_z),\end{aligned}\quad (2.23)$$

where all the above terms can be readily determined from the solution to the Lyapunov equation (2.15).

Figure 2.17 illustrates $\bar{E}_p(0, \kappa_z)$ and $\bar{E}_d(0, \kappa_z)$ in the uncontrolled flow and in flows subject to a DTW with ($c = 5$, $\omega_x = 2$) and a UTW with ($c = -2$, $\omega_x = 0.5$). As expected, in the uncontrolled flow the joint contribution of dissipation and forcing is negative while the contribution of production is positive (see Figures 2.17(a) and 2.17(d)). The energy density (solid curve) is determined by the sum of $\bar{E}_{0,p}$ and $\bar{E}_{0,d}$, and it peaks at $\kappa_z \approx 1.78$. The second order corrections (in α) to \bar{E}_p and \bar{E}_d are shown in Figures 2.17(b) (for the DTW) and 2.17(e) (for the UTW). In flows subject to a DTW, the correction to \bar{E}_p is negative while the correction to \bar{E}_d is positive. Furthermore, the effect of $\bar{E}_{2,p}$ dominates that of $\bar{E}_{2,d}$ which implies that the DTW reduces the energy density of the uncontrolled flow (solid curve in Figure 2.17(b) shows that a DTW introduces a negative correction to \bar{E}_0). On the other hand, flows subject to a UTW exhibit opposite trends; the correction to \bar{E}_p is positive, the correction to \bar{E}_d is negative, and since $\bar{E}_{2,p}$ has the dominant effect, the UTW increases the energy density of the uncontrolled flow (solid curve in Figure 2.17(e) shows that a UTW introduces a positive correction to \bar{E}_0). In Figures 2.17(c) and 2.17(f) perturbation analysis up to a second order in α is used to show \bar{E}_p and \bar{E}_d (solid curves) for a DTW with $\alpha = 0.025$ and for a UTW with $\alpha = 0.015$. Relative to the uncontrolled flow (symbols), the DTW decreases both production and dissipation terms. On the contrary, the UTW increases both of these terms. For both UTWs and DTWs, production dominates dissipation and determines whether the energy is increased or decreased. In addition, our computations show that $\langle u_\theta, \mathcal{U}_y v_\theta \rangle$ is orders of magnitude larger than the other production terms. Moreover, $\langle u, \partial_{yy} u \rangle$ completely dominates other dissipation terms. Therefore, the work of the Reynolds stress uv against the base shear U_y is responsible for almost all of the energy production and the maximum viscous dissipation is associated with the wall-normal diffusion of the streamwise velocity fluctuation. These results are confirmed by DNS of the NS equations in § 2.4.

2.4 Direct numerical simulations

The effectiveness of DTWs and UTWs in preventing or enhancing transition is examined in this section. In contrast to the current practice, we do not use DNS as a design tool; rather, we utilize them as a means for verification and validation of theoretical predictions offered in this study. Namely, we use DNS to confirm that the DTWs with parameters selected in § 2.3 can control the onset of turbulence and achieve positive net efficiency relative to the uncontrolled flow that becomes turbulent. On the contrary, the UTWs enhance transient growth and induce turbulence even when the uncontrolled flow stays laminar. In spite of promoting turbulence, the UTWs with large amplitudes can provide sub-laminar drag coefficient. However, we show that this comes at the expense of poor net power balance in flows driven by a fixed pressure gradient. This is in agreement with [65], where it was shown that it costs more to achieve the same amount of pumping using wall-transpiration than pressure gradient type of actuation. Our numerical simulations show the predictive power of the theoretical framework developed in this chapter and suggest that the linearized Navier-Stokes (NS) equations with uncertainty represent an effective control-oriented model for maintaining the laminar flow.

The streamwise traveling waves, considered theoretically in § 2.3, are tested in DNS of a 3D transitional Poiseuille flow in this work. All DNS calculations are obtained using the code developed by [95]. A multistep semi-implicit Adams-Bashforth/Backward-Differentiation (AB/BDE) scheme described in [96] is used for time discretization. The AB/BDE treats the linear terms implicitly and the nonlinear terms explicitly. A spectral method [97] is used for the spatial derivatives with Chebyshev polynomial expansion in the wall-normal direction and Fourier series expansion in the streamwise and spanwise directions. Aliasing errors from the evaluation of the nonlinear terms are removed by the 3/2-rule when the horizontal FFTs are computed. We modified the code to account for the streamwise traveling wave boundary conditions (2.2).

The NS equations are integrated in time with the objective of computing fluctuations' kinetic energy, skin-friction drag coefficient, and net power balance, § 2.4.2. The velocity field is first initialized with the laminar parabolic profile in the absence of 3D fluctuations, § 2.4.1; this yields the 2D base flow which is induced by the fixed pressure gradient, $P_x = -2/R_c$, and the boundary conditions (2.2). In simulations of the full 3D flows (cf. § 2.4.2), an initial 3D perturbation is superimposed to the base velocity, \mathbf{u}_b . As the initial perturbation, we consider a random velocity field developed by [95] which has the ability to trigger turbulence by exciting all the relevant Fourier and Chebyshev modes. This divergence-free initial condition is composed of random spectral coefficients that decay exponentially and satisfy homogenous Dirichlet boundary conditions at the walls. The flux and energy of the velocity fluctuations are computed at each time step.

A *fixed pressure gradient* is enforced in all simulations which are initiated at $R_c = 2000$; this value corresponds to the Reynolds number $R_\tau = 63.25$ based on the friction velocity, u_τ . Owing to the fixed pressure gradient, the steady-state value of R_τ is the same for all simulations, $R_\tau = 63.25$. In addition, we consider a streamwise box

Case	Symbol	c	ω_x	α	L_x/δ	L_z/δ	N_y	N_x	N_z
0	×	—	—	—	2π	$4\pi/3$	65	50	50
1	□	5	2	0.035	2π	$4\pi/3$	65	50	50
2	○	5	2	0.050	2π	$4\pi/3$	65	50	50
3	◇	5	2	0.125	2π	$4\pi/3$	65	50	50
4	◁	-2	0.5	0.015	8π	$4\pi/3$	65	200	50
5	▽	-2	0.5	0.050	8π	$4\pi/3$	65	200	50
6	△	-2	0.5	0.125	8π	$4\pi/3$	65	200	50

Table 2.1: The computational domain and spatial discretization considered in simulations of the uncontrolled flow, DTWs with ($c = 5$, $\omega_x = 2$, $\alpha = 0.035, 0.050$, and 0.125), and UTWs with ($c = -2$, $\omega_x = 0.5$, $\alpha = 0.015, 0.050$, and 0.125). Symbols identify the corresponding flow in figures that follow. The box sizes in the streamwise and spanwise directions are denoted by L_x and L_z , respectively. The number of grid points in the streamwise, wall-normal, and spanwise directions are represented by N_i , $i = \{x, y, z\}$, respectively.

length, $L_x = 4\pi/\omega_x$, for all controlled flow simulations. This box length captures the streamwise modes $\kappa_x = \{0, \pm\omega_x/2, \pm\omega_x, \pm 3\omega_x/2, \dots\}$; relative to § 2.3, these modes correspond to the union of the fundamental ($\kappa_x = \{0, \pm\omega_x, \pm 2\omega_x, \dots\}$) and subharmonic ($\kappa_x = \{\pm\omega_x/2, \pm 3\omega_x/2, \dots\}$) modes. In addition to the uncontrolled flow, we consider three DTWs with ($c = 5$, $\omega_x = 2$, $\alpha = \{0.035, 0.050, 0.125\}$), and three UTWs with ($c = -2$, $\omega_x = 0.5$, $\alpha = \{0.015, 0.050, 0.125\}$). The complete list of the parameters along with the computational domain sizes and the number of spatial grid points is shown in table 4.1. The total integration time is $t_{\text{tot}} = 1000 \delta/U_c$. We have verified our simulations by making sure that the changes in results are negligible by increasing the number of wall-normal grid points to $N_y = 97$.

2.4.1 Base flow and nominal net efficiency

Base velocity, $\mathbf{u}_b = (U(x, y, t), V(x, y, t), 0)$, is computed using DNS of 2D Poiseuille flow with $R_\tau = 63.25$ in the presence of streamwise traveling wave boundary control (2.2). Figure 2.18 shows the mean velocity profiles, $\overline{U}(y)$ (with overline denoting the average over horizontal directions), in uncontrolled flow and in flows subject to selected DTWs and UTWs; these results agree with the results obtained using Newton’s method. The nominal bulk flux, which quantifies the area under $\overline{U}(y)$,

$$U_{B,N} = \frac{1}{2} \int_{-1}^1 \overline{U}(y) dy,$$

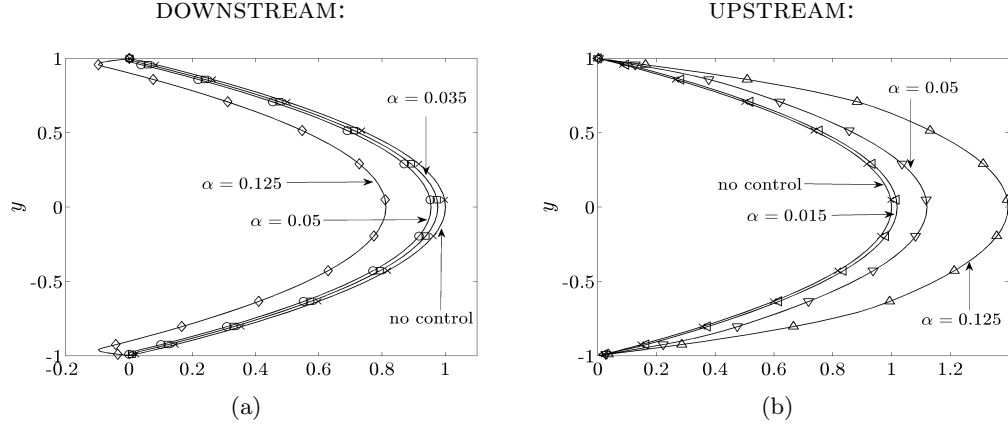


Figure 2.18: Mean streamwise base velocity, $\bar{U}(y)$, obtained in 2D simulations of the uncontrolled Poiseuille flow with $R_\tau = 63.25$, \times , and controlled flows subject to: (a) DTWs with \square , ($c = 5$, $\omega_x = 2$, $\alpha = 0.035$); \circ , ($c = 5$, $\omega_x = 2$, $\alpha = 0.05$); \diamond , ($c = 5$, $\omega_x = 2$, $\alpha = 0.125$); and (b) UTWs with \triangleleft , ($c = -2$, $\omega_x = 0.5$, $\alpha = 0.015$); ∇ , ($c = -2$, $\omega_x = 0.5$, $\alpha = 0.05$); \triangle , ($c = -2$, $\omega_x = 0.5$, $\alpha = 0.125$).

and the nominal skin-friction drag coefficient for three UTWs and three DTWs are reported in table 2.2. For fixed pressure gradient, $P_x = -2/R_c$, the nominal skin-friction drag coefficient is inversely proportional to square of the nominal flux, i.e.,

$$C_{f,N} = -2 P_x / U_{B,N}^2. \quad (2.24)$$

As shown by [65], compared to the uncontrolled laminar flow, the nominal flux is reduced (increased) by DTWs (UTWs); according to (2.24), this results in larger (smaller) nominal drag coefficients, respectively.

The above results suggest that properly chosen traveling waves can exhibit increased flux compared to the uncontrolled flow. For fixed pressure gradient, this results in production of a driving power

$$\Pi_{prod} = -P_x (U_{B,c} - U_{B,u}) (2L_x L_z),$$

where $U_{B,c}$ and $U_{B,u}$ denote the flux of the controlled and uncontrolled flows. The normalized produced power $\% \Pi_{prod}$ is expressed as a percentage of the power spent to drive the uncontrolled flow, $\Pi_u = -P_x U_{B,u} (2L_x L_z)$,

$$\% \Pi_{prod} = 100 (U_{B,c} - U_{B,u}) / U_{B,u}.$$

On the other hand, the input power required for maintaining the traveling waves is

Case	c	ω_x	α	$U_{B,N}$	$10^3 C_{f,N}$	$\% \Pi_{prod}$	$\% \Pi_{req}$	$\% \Pi_{net}$
0	–	–	–	0.6667	4.5000	0	0	0
1	5	2	0.035	0.6428	4.8404	–3.58	16.64	–20.22
2	5	2	0.050	0.6215	5.1778	–6.77	31.74	–38.51
3	5	2	0.125	0.4821	8.6050	–27.69	136.50	–164.19
4	–2	0.5	0.015	0.6703	4.4513	2.70	5.46	–2.76
5	–2	0.5	0.050	0.7791	3.2949	16.86	37.69	–20.83
6	–2	0.5	0.125	1.0133	1.9478	51.99	145.05	–93.06

Table 2.2: Nominal results in Poiseuille flow with $R_\tau = 63.25$. The nominal flux, $U_{B,N}$, and skin-friction drag coefficient, $C_{f,N}$, are computed using the base flow described in § 2.4.1. The produced power, $\% \Pi_{prod}$, required power, $\% \Pi_{req}$, and net power, $\% \Pi_{net}$, are normalized by the power required to drive the uncontrolled flow. The produced and net powers are computed with respect to the laminar uncontrolled flow.

obtained from [83]

$$\Pi_{req} = \left(\overline{VP}|_{y=-1} - \overline{VP}|_{y=1} \right) L_x L_z,$$

and the normalized required power $\% \Pi_{req}$ is expressed as

$$\% \Pi_{req} = 100 \frac{\overline{VP}|_{y=-1} - \overline{VP}|_{y=1}}{-2 P_x U_{B,u}}.$$

In order to assess the efficacy of traveling waves for controlling transitional flows, the control net power is defined as the difference between the produced and required powers [9]

$$\% \Pi_{net} = \% \Pi_{prod} - \% \Pi_{req},$$

where $\% \Pi_{net}$ signifies how much net power is gained (positive $\% \Pi_{net}$) or lost (negative $\% \Pi_{net}$) in the controlled flow as a percentage of the power spent to drive the uncontrolled flow.

The nominal efficiency of the selected streamwise traveling waves in 2D flows, i.e. in the absence of velocity fluctuations, is shown in table 2.2. Note that the nominal net power is negative for all controlled 2D simulations. This is in agreement with a recent study of [65] where it was shown that the net power required to drive a flow with wall transpiration is always larger than in the standard pressure gradient type of actuation.

2.4.2 Avoidance/promotion of turbulence by streamwise traveling waves

It was shown that a positive net efficiency can be achieved in a situation where the controlled flow stays laminar but the uncontrolled flow becomes turbulent. Whether the controlled flow can remain laminar depends on velocity fluctuations around the

modified base flow. In this section, we study the influence of streamwise traveling waves on the dynamics and the control net efficiency. This problem is addressed by simulating a 3D channel flow with initial perturbations which are superimposed on the base velocity induced by the wall actuation. Depending on the kinetic energy of the initial condition, we distinguish three cases: (i) both the uncontrolled and properly designed controlled flows remain laminar (*small* initial energy); (ii) the uncontrolled flow becomes turbulent, while the controlled flow stays laminar for the appropriate choice of traveling wave parameters (*moderate* initial energy); and (iii) both the uncontrolled and controlled flows become turbulent for selected traveling wave parameters (*large* initial energy). Our simulations indicate, however, that *poorly* designed traveling waves can promote turbulence even for initial conditions for which the uncontrolled flow stays laminar. It was demonstrated in § 2.3 that properly designed DTWs are capable of significantly reducing receptivity of velocity fluctuations which makes them well-suited for preventing transition; on the other hand, compared to the uncontrolled flow, the velocity fluctuations around the UTWs at best exhibit similar receptivity to background disturbances. Following § 2.3, we present our main results for DTWs with ($c = 5$, $\omega_x = 2$); these results are compared to UTWs with ($c = -2$, $\omega_x = 0.5$) (as selected in [8]). In both cases, three wave amplitudes are selected (cf. table 4.1).

The 3D simulations, which are summarized in table 2.3, confirm and complement the theoretical predictions of § 2.3 at two levels. At the level of controlling the onset of turbulence, we illustrate that the UTWs increase receptivity of velocity fluctuations and promote turbulence even for initial perturbations for which the uncontrolled flow stays laminar. In contrast, the DTWs can prevent transition even in the presence of initial conditions with moderate and large energy. At the level of net power efficiency, it is first shown that the net power is negative when the uncontrolled flow stays laminar. However, for the uncontrolled flow that becomes turbulent, we demonstrate that the DTWs can result in a positive net efficiency. The positive net efficiency is achieved if the required power for maintaining the laminar DTW is less than the produced power. In addition, we highlight an important trade-off that limits the advantages of DTWs in controlling the onset of turbulence in flows subject to large initial conditions. Namely, we show that in this case preventing transition by DTWs requires a large input power that results in a negative efficiency. Our simulations reveal that although UTWs become turbulent, a positive net efficiency can be achieved for small enough wave amplitudes. For the initial conditions with moderate energy, we further point out that the achievable positive net efficiency for UTWs is much smaller than for the DTWs that sustain the laminar flow.

Small initial energy

We first consider the initial perturbations with small kinetic energy, $E(0) = 2.25 \times 10^{-6}$, which cannot trigger turbulence in flow with no control. Our simulations show that the DTWs selected in § 2.3 of this study improve transient response of the velocity

Initial Energy	Case	c	ω_x	α	$10^3 C_f$	$\% \Pi_{prod}$	$\% \Pi_{req}$	$\% \Pi_{net}$
Small	0	—	—	—	4.5002	0	0	0
	2	5	2	0.050	5.1778	-6.77	31.77	-38.54
	4	-2	0.5	0.015	4.3204	-1.54	5.14	-3.60
	5	-2	0.5	0.050	5.9426	-16.52	23.22	-39.74
	6	-2	0.5	0.125	3.6853	12.20	108.41	-96.21
Moderate	0	—	—	—	10.3000	0	0	0
	1	5	2	0.035	4.9244	52.07	26.44	25.63
	2	5	2	0.050	5.2273	47.35	50.40	-3.05
	4	-2	0.5	0.015	8.7866	11.36	4.53	6.83
	5	-2	0.5	0.050	6.7406	31.15	41.96	-10.81
	6	-2	0.5	0.125	3.9264	77.03	155.80	-78.77
Large	0	—	—	—	11.2000	0	0	0
	2	5	2	0.050	11.9000	-3.37	47.90	-51.27
	3	5	2	0.125	12.1000	-11.31	196.89	-208.20
	5	-2	0.5	0.050	7.4438	13.68	34.19	-20.51
	6	-2	0.5	0.125	3.9872	57.75	142.92	-85.17

Table 2.3: Results of 3D simulations in Poiseuille flow with $R_\tau = 63.25$ for initial conditions of small, moderate, and large energy (respectively, $E(0) = 2.25 \times 10^{-6}$, $E(0) = 5.0625 \times 10^{-4}$, and $E(0) = 2.5 \times 10^{-3}$). The values of C_f , $\% \Pi_{prod}$, $\% \Pi_{req}$, and $\% \Pi_{net}$ correspond to $t = 1000$. For small initial energy, the produced and net powers are computed with respect to laminar uncontrolled flow; for moderate and large initial energies, they are computed with respect to turbulent uncontrolled flow.

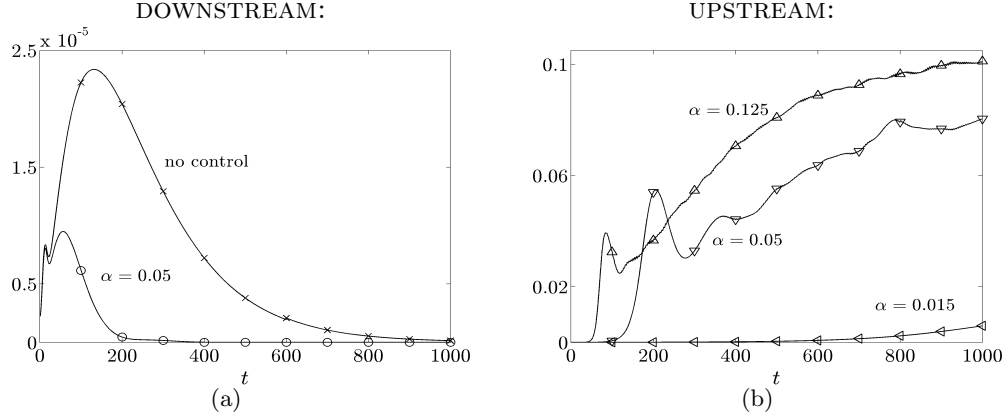


Figure 2.19: Energy of the velocity fluctuations, $E(t)$, for the initial condition with small energy: (a) \times , uncontrolled; \circ , a DTW with $(c = 5, \omega_x = 2, \alpha = 0.05)$; and (b) UTWs with \triangleleft , $(c = -2, \omega_x = 0.5, \alpha = 0.015)$; ∇ , $(c = -2, \omega_x = 0.5, \alpha = 0.05)$; \triangle , $(c = -2, \omega_x = 0.5, \alpha = 0.125)$.

fluctuations; on the contrary, the UTWs considered in [8] lead to deterioration of the transient response and, consequently, promote turbulence. Since the uncontrolled flow stays laminar, both DTWs and UTWs lead to the negative net efficiency.

The energy of velocity fluctuations is given by

$$E(t) = \frac{1}{\Omega} \int_{\Omega} (u^2 + v^2 + w^2) d\Omega,$$

where $\Omega = 2L_x L_z$ is the volume of the computational box. Figure 2.19 shows the fluctuations' kinetic energy as a function of time for the uncontrolled flow and controlled flows subject to a DTW with $(c = 5, \omega_x = 2, \alpha = 0.05)$ and three UTWs with $(c = -2, \omega_x = 0.5, \alpha = \{0.015, 0.05, 0.125\})$. As evident from Figure 2.19(a), the energy of the uncontrolled flow exhibits a transient growth followed by an exponential decay to zero (i.e., to the laminar flow). We see that a DTW moves the transient response peak to a smaller time, which is about half the time at which peak of $E(t)$ in the uncontrolled flow takes place. Furthermore, maximal transient growth of the uncontrolled flow is reduced by approximately 2.5 times, and a much faster disappearance of the velocity fluctuations is achieved. On the other hand, Figure 2.19(b) clearly exhibits the negative influence of the UTWs on a transient response. In particular, the two UTWs with larger amplitudes significantly increase the energy of velocity fluctuations. We note that the fluctuations' kinetic energy in a flow subject to a UTW with an amplitude as small as $\alpha = 0.015$ at $t = 1000$ is already about two orders of magnitude larger than the maximal transient growth of the flow with no control.

Figure 2.20(a) shows the skin-friction drag coefficient,

$$C_f(t) = \frac{2\bar{\tau}_w}{U_B^2} = \frac{1}{R_c U_B^2} \left[\left(\frac{d\bar{U}}{dy} + \frac{d\bar{u}}{dy} \right) \Big|_{y=-1} - \left(\frac{d\bar{U}}{dy} + \frac{d\bar{u}}{dy} \right) \Big|_{y=1} \right],$$

as a function of time for the traveling waves considered in Figure 2.19. Here, $\bar{\tau}_w$ denotes the non-dimensional average wall-shear stress and

$$U_B(t) = \frac{1}{2} \int_{-1}^1 (\bar{U}(y) + \bar{u}(y,t)) dy,$$

is the total bulk flux. Since both the uncontrolled flow and the flow subject to a DTW stay laminar, their steady-state drag coefficients agree with the nominal values computed in the absence of velocity fluctuations (cf. tables 2.2 and 2.3). On the other hand, the drag coefficients of the UTWs that become turbulent are about twice the values predicted using the base flow analysis. The large amplification of velocity fluctuations by UTWs is responsible for this increase. The velocity fluctuations in the UTW with $\alpha = 0.015$ are not amplified enough to have a pronounced effect on the drag coefficient. Furthermore, the drag coefficients for the UTWs with ($c = -2$, $\omega_x = 0.5$, $\alpha = \{0.05, 0.125\}$) at $t = 1000$ agree with the results of [8] computed for the fully developed turbulent channel flow. This indicates that the UTWs with larger amplitudes in our simulations have transitioned to turbulence. The above results confirm the theoretical prediction of § 2.3 where it is shown that the UTWs are poor candidates for controlling the onset of turbulence for they increase receptivity relative to the uncontrolled flow.

The normalized required, produced, and net powers for the initial conditions with small kinetic energy are shown in Figures 2.20(b) - 2.20(d). Note that the normalized net power for all traveling waves is negative (cf. Figure 2.20(d)). This confirms the prediction of § 2.3 that the net power is negative whenever the uncontrolled flow stays laminar. It is noteworthy that the UTW with $\alpha = 0.125$ has a negative net power despite its significantly smaller drag coefficient compared to the laminar uncontrolled flow. As evident from Figures 2.20(b) and 2.20(c), this is because the required power for maintaining this UTW is much larger than the power produced by reducing drag. The above results agree with the studies of [79] and [80] where it was established that the net cost to drive a flow by any transpiration-based strategy is larger than in the uncontrolled laminar flow. Therefore, aiming for sub-laminar drag may not be advantageous from efficiency point of view. Instead, one can design control strategies that yield smaller drag than the uncontrolled turbulent flow and provide positive net power balance.

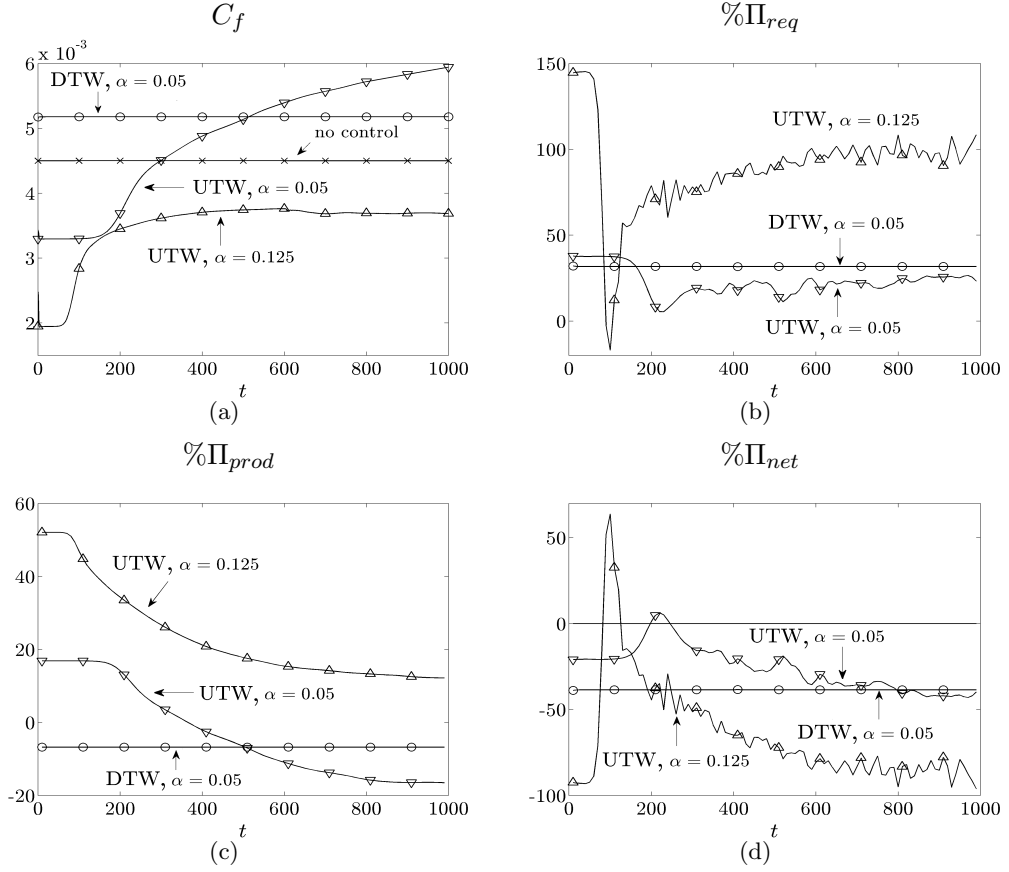


Figure 2.20: (a) Skin-friction drag coefficient, C_f ; (b) normalized required power, $\% \Pi_{req}$; (c) normalized produced power, $\% \Pi_{prod}$; and (d) normalized net power, $\% \Pi_{net}$, for the initial condition with small energy: \times , uncontrolled flow; \circ , DTW with ($c = 5$, $\omega_x = 2$, $\alpha = 0.05$); and UTWs with ∇ , ($c = -2$, $\omega_x = 0.5$, $\alpha = 0.015$); ∇ , ($c = -2$, $\omega_x = 0.5$, $\alpha = 0.05$); Δ , ($c = -2$, $\omega_x = 0.5$, $\alpha = 0.125$).

Moderate initial energy

We next consider the velocity fluctuations with moderate initial energy, $E(0) = 5.0625 \times 10^{-4}$. This selection illustrates a situation where the initial conditions are large enough to trigger turbulence in the uncontrolled flow but small enough to allow the properly chosen DTWs to maintain the laminar flow and achieve positive net power balance. As shown for small initial energy, the UTWs trigger turbulence even for the initial conditions whose kinetic energy is about 200 times smaller than the value considered here.

The energy of the velocity fluctuations and drag coefficients as a function of time for the uncontrolled flow and UTWs are shown in Figures 2.21(a) and 2.21(b). Figure 2.21(a) indicates that the kinetic energy of the uncontrolled flow and the flow subject to UTWs with ($c = -2$, $\omega_x = 0.5$, $\alpha = \{0.015, 0.05, 0.125\}$) is increased by orders of magnitude which eventually results in transition to turbulence. This large energy amplification of UTWs is captured by the linear analysis around the laminar base flows. As evident from Figure 2.21(b), the large fluctuations' energy in both the uncontrolled flow and in UTWs yields much larger drag coefficients compared to the nominal values reported in table 2.2. In addition, Figure 2.21(b) is in agreement with [8] where it was shown that the skin-friction drag coefficients of the UTWs are smaller than in the uncontrolled flow that becomes turbulent, and that the UTW with ($c = -2$, $\omega_x = 0.5$, $\alpha = 0.125$) achieves a sub-laminar drag. The normalized required and net powers for the UTWs are shown in Figures 2.21(c) and 2.21(d). Note that the required power for maintaining the UTW with $\alpha = 0.125$ (which yields sub-laminar drag) is so large that it results in a negative net power balance (cf. Figure 2.21(d)). On the other hand, the UTW with $\alpha = 0.015$ is capable of producing a small positive net power for two main reasons: (i) it has a smaller drag coefficient than the uncontrolled turbulent flow (although it becomes turbulent itself); and (ii) it requires a much smaller power compared to the UTW with $\alpha = 0.125$.

The fluctuations' kinetic energy and skin-friction drag coefficient for the DTWs are shown in Figures 2.22(a) and 2.22(b). Figure 2.22(a) shows that the DTWs with ($c = 5$, $\omega_x = 2$, $\alpha = \{0.035, 0.05\}$) significantly weaken intensity of the velocity fluctuations, thereby facilitating maintenance of the laminar flow. From Figure 2.22(b) we also see that the small transient growth of fluctuations' kinetic energy results in a small transient increase in the drag coefficients which eventually decay to their nominal values reported in table 2.2. Even though these drag coefficients are larger than in the uncontrolled laminar flow, they are still approximately two times smaller than in the uncontrolled flow that becomes turbulent (cf. table 2.3).

The normalized produced, required, and net powers for DTWs are shown in Figures 2.22(c) and 2.22(d). As can be seen from Figure 2.22(c), the normalized produced power for the DTWs is positive by virtue of the fact that the uncontrolled flow becomes turbulent while the controlled flows stay laminar. Figure 2.22(d) shows that the DTW with $\alpha = 0.035$ (respectively, $\alpha = 0.05$) has a positive (respectively, negative)

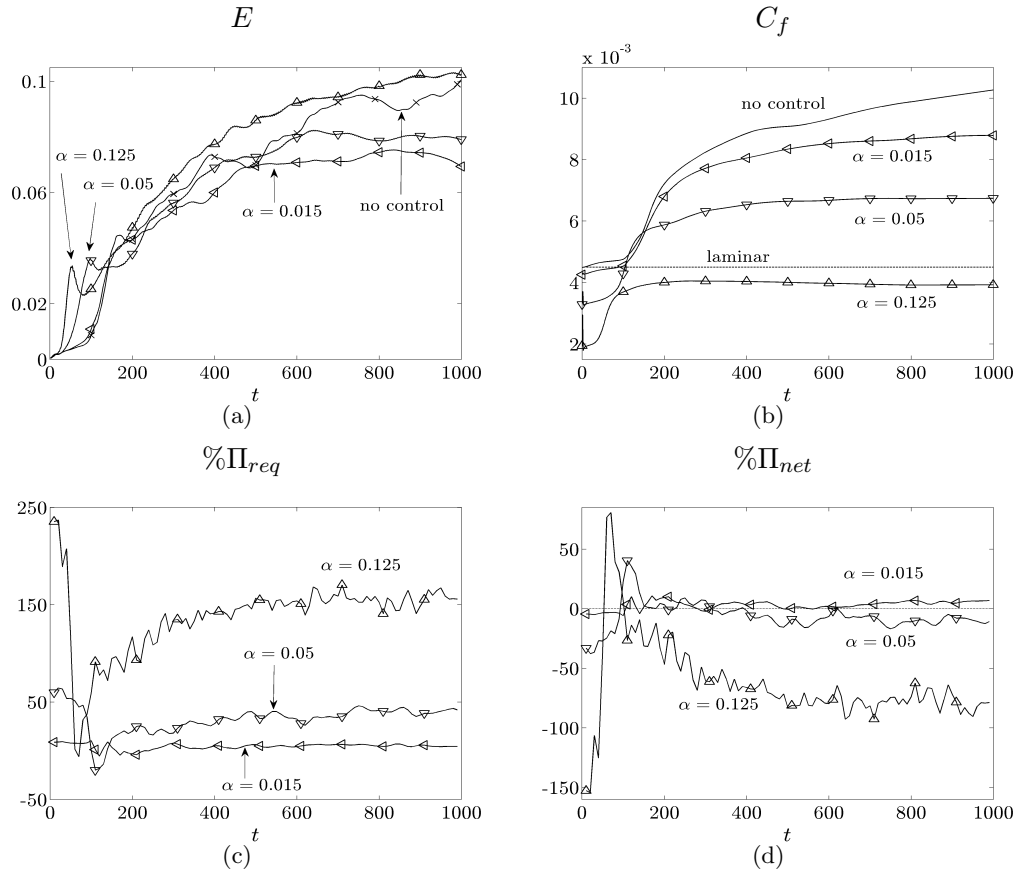


Figure 2.21: (a) Energy of the velocity fluctuations, $E(t)$; (b) skin-friction drag coefficient, $C_f(t)$; (c) normalized required power, $\% \Pi_{req}$; and (d) normalized net power, $\% \Pi_{net}$, for the initial condition with moderate energy: \times , uncontrolled; and UTWs with \triangleleft , ($c = -2, \omega_x = 0.5, \alpha = 0.015$); ∇ , ($c = -2, \omega_x = 0.5, \alpha = 0.05$); \triangle , ($c = -2, \omega_x = 0.5, \alpha = 0.125$).

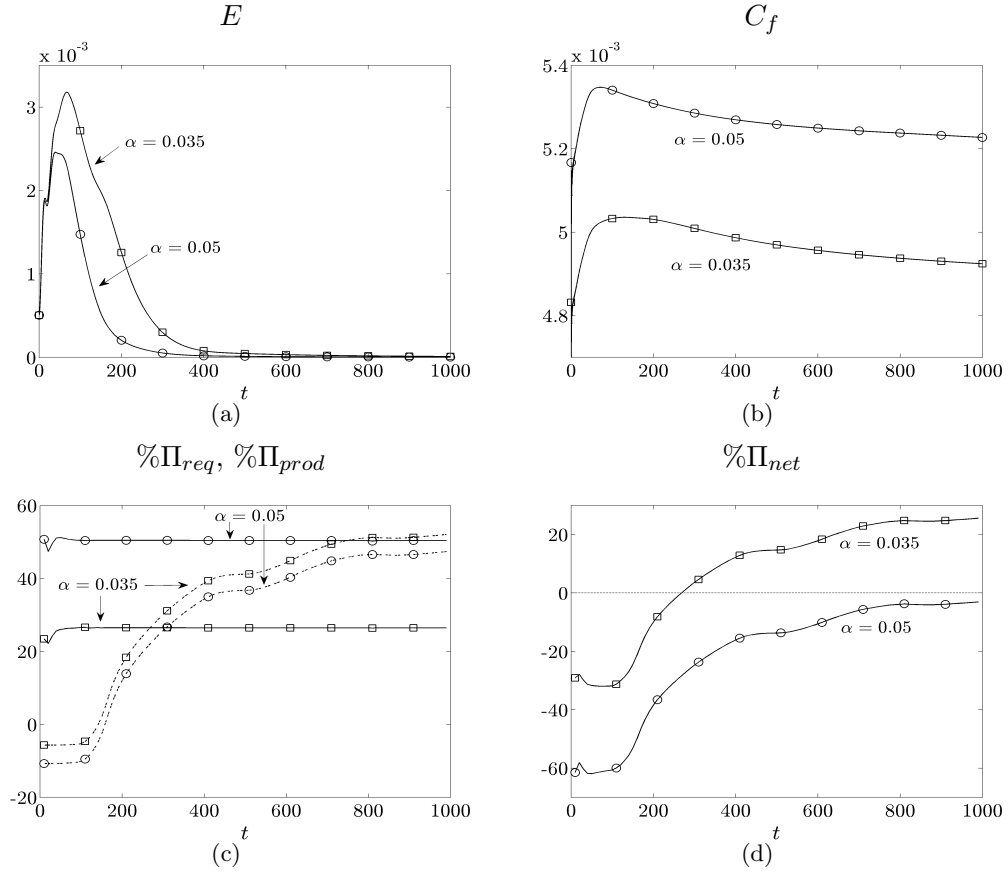


Figure 2.22: (a) Energy of the velocity fluctuations, $E(t)$; (b) skin-friction drag coefficient, $C_f(t)$; (c) normalized required power, $\% \Pi_{req}$ (solid), normalized produced power, $\% \Pi_{prod}$ (dashed); and (d) normalized net power, $\% \Pi_{net}$, for the initial condition with moderate energy: DTWs with \square , ($c = 5, \omega_x = 2, \alpha = 0.035$); \circ , ($c = 5, \omega_x = 2, \alpha = 0.05$).

net power balance. The reason for this is twofold: first, as evident from Figure 2.22(c), the DTW with larger α results in a smaller produced power since it induces a larger negative nominal bulk flux than the DTW with smaller α ; and second, the required power to maintain the DTW with larger α is bigger than in the DTW with smaller α . Furthermore, at $t = 1000$, the DTW with $\alpha = 0.035$ has a larger net power than the UTW with $\alpha = 0.015$ ($\% \Pi_{net} = 25.63$ vs. $\% \Pi_{net} = 6.83$; cf. table 2.3). This is because the DTW with $\alpha = 0.035$, in contrast to the UTW with $\alpha = 0.015$, remains laminar and produces a much larger power than it requires.

In summary, the results of this section highlight an important trade-off that needs to be taken into account when designing the traveling waves. Large amplitudes of properly designed downstream waves yield larger receptivity reduction which is desirable for controlling the onset of turbulence. However, this is accompanied by an increase in drag coefficient and required control power. Thus, to maximize net efficiency, it is advantageous to select the smallest possible amplitude of wall-actuation that can maintain the laminar flow.

Large initial energy

We illustrated the capability of properly designed DTWs to maintain the laminar flow in the presence of initial conditions that induce transition in the uncontrolled flow. In this section, we demonstrate that, as the energy of the initial perturbation increases, a DTW with larger amplitude is needed to prevent transition. Our results confirm the prediction made in § 2.3 that maintaining a laminar flow with a larger DTW amplitude comes at the expense of introducing a negative net power balance.

Simulations in this section are done for the initial condition with large kinetic energy, $E(0) = 2.5 \times 10^{-3}$. The time evolution of the fluctuations' energy for a pair of DTWs with $(c = 5, \omega_x = 2, \alpha = \{0.05, 0.125\})$ is shown in Figure 2.23(a). The uncontrolled flow becomes turbulent and exhibits similar trends in the evolution of $E(t)$ as the corresponding flow initiated with moderate energy perturbations (cf. Figures 2.21(a) and 2.23(a)). On the other hand, Figure 2.23(a) shows that the DTW with $\alpha = 0.05$ is not capable of maintaining the laminar flow; in comparison, the same set of control parameters prevented transition for the perturbations of moderate initial energy (cf. Figures 2.22(a) and 2.23(a)). Conversely, the DTW with $\alpha = 0.125$ remains laminar even though $E(t)$ transiently reaches about half the energy of the turbulent uncontrolled flow. Therefore, the DTWs with frequency and speed selected in § 2.3 and sufficiently large amplitudes are capable of maintaining the laminar flow even in the presence of large initial perturbations.

Figure 2.23(b) shows the skin-friction drag coefficients for the flows considered in Figure 2.23(a). For the DTW with $\alpha = 0.05$ the steady-state value of C_f is given by $C_f = 11.9 \times 10^{-3}$, which is a slightly larger value than in the turbulent uncontrolled flow, $C_f = 11.2 \times 10^{-3}$ (cf. table 2.3). We note that the drag coefficient of the DTW that stays laminar initially reaches values that are about 50 % larger than in the uncontrolled

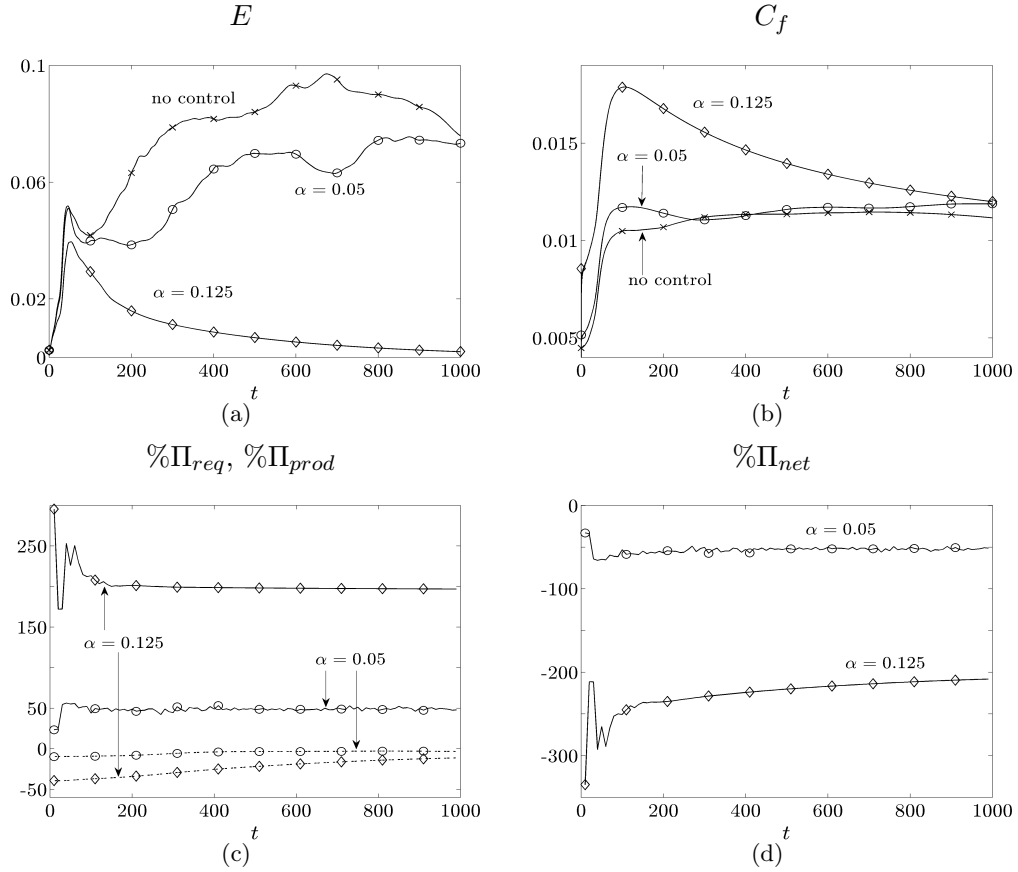


Figure 2.23: (a) Energy of the velocity fluctuations, $E(t)$; (b) skin-friction drag coefficient, $C_f(t)$; (c) normalized required power, $\% \Pi_{req}$ (solid), normalized produced power, $\% \Pi_{prod}$ (dashed); and (d) normalized net power, $\% \Pi_{net}$, for the initial condition with large energy: \times , uncontrolled; DTWs with \circ , ($c = 5, \omega_x = 2, \alpha = 0.05$); and \diamond , ($c = 5, \omega_x = 2, \alpha = 0.125$).

flow; after this initial increase, $C_f(t)$ then gradually decays to the value predicted using the base flow analysis, $C_f = 8.6 \times 10^{-3}$ (cf. table 2.2). Figures 2.23(c) and 2.23(d) show the normalized required, produced, and net powers for the initial condition with large kinetic energy. As evident from Figure 2.23(d), the net power balance is negative for all considered flows. The DTW with $\alpha = 0.05$ becomes turbulent, and it has a larger drag coefficient than the uncontrolled flow which consequently leads to negative produced and net powers. Moreover, even though the DTW with $\alpha = 0.125$ can sustain laminar flow, its net power balance is very poor. There are two main reasons for the lack of efficiency of this control strategy: first, its nominal drag coefficient is significantly larger than in a DTW with smaller amplitudes which consequently yields very small produced power (at larger times not shown in Figure 2.23(c)); and second, a prohibitively large power is required to maintain this large amplitude DTW.

The results of this section show that preventing transition by DTWs in the presence of large initial conditions comes at the expense of large negative net power balance. We also highlight that in the presence of large initial perturbations (or, equivalently, at large Reynolds numbers), transition to turbulence may be inevitable. Furthermore, the results of § 2.4.2 show that the UTWs may reduce the turbulent skin-friction drag and achieve positive net efficiency. The approach used in this chapter considers dynamics of fluctuations around laminar flows and, thus, it cannot be used for explaining the positive efficiency of the UTWs that become turbulent.

2.4.3 Energy amplification mechanisms

The Reynolds-Orr equation can be used to quantify the evolution of fluctuations' kinetic energy around a given base flow [84]. In this section, we use this equation to examine mechanisms that contribute to production and dissipation of kinetic energy in flows subject to traveling waves. For base velocity, $\mathbf{u}_b = (U(x, y, t), V(x, y, t), 0)$, the evolution of the energy of velocity fluctuations, $E(t)$, is determined by

$$\begin{aligned} \frac{1}{2} \frac{dE}{dt} &= P_E(t) + D_E(t), \\ P_E(t) &= -\frac{1}{\Omega} \int_{\Omega} (uvU_y + uvV_x + v^2V_y + u^2U_x) d\Omega, \\ D_E(t) &= \frac{1}{R_c \Omega} \int_{\Omega} \mathbf{v} \cdot \Delta \mathbf{v} d\Omega. \end{aligned} \tag{2.25}$$

Here, P_E represents the production of kinetic energy and is associated with the work of the Reynolds stresses on the base shear, whereas D_E accounts for viscous dissipation.

We confine our attention to the simulations for initial conditions with small energy. This situation is convenient for explaining why the DTWs exhibit improved transient behavior compared to the laminar uncontrolled flow while the UTWs promote transition

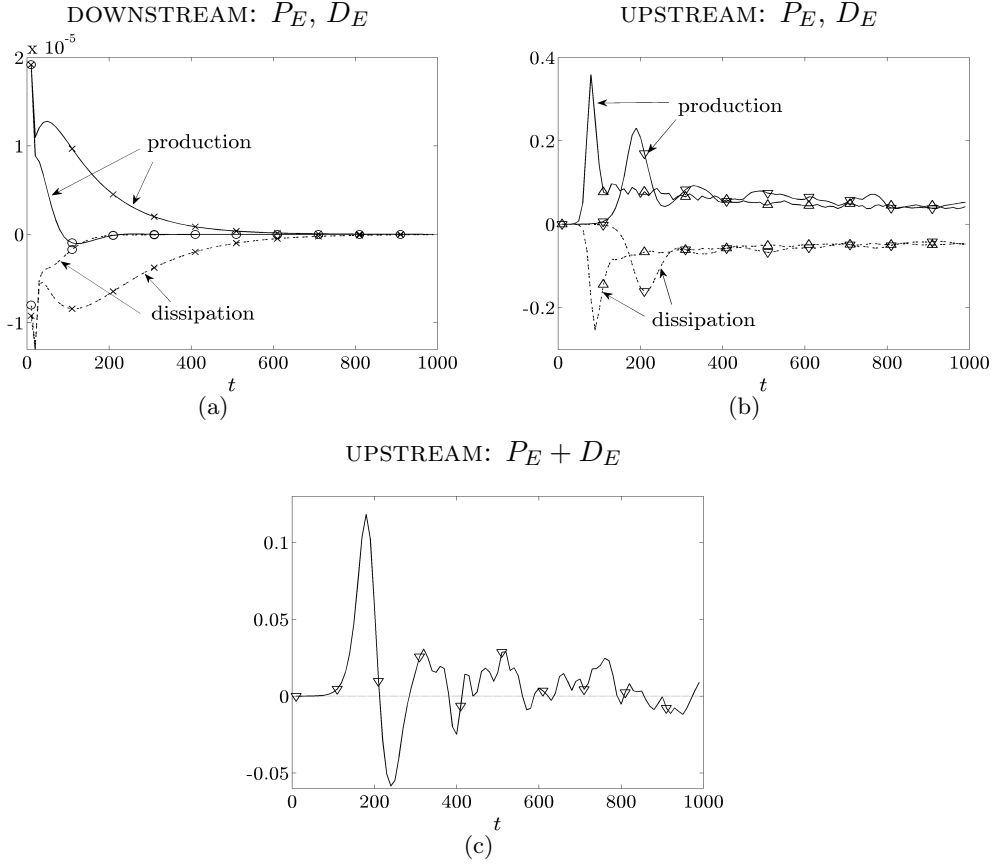


Figure 2.24: (a) and (b) Production, $P_E(t)$ (solid), and dissipation, $D_E(t)$ (dashed), of kinetic energy in Poiseuille flow with $R_\tau = 63.25$ for the initial condition with small energy: (a) \times , uncontrolled; \circ , DTW with $(c = 5, \omega_x = 2, \alpha = 0.05)$; and (b) ∇ , UTW with $(c = -2, \omega_x = 0.5, \alpha = 0.05)$; Δ , UTW with $\alpha = 0.125$. (c) $P_E(t) + D_E(t)$ for the UTW with $(c = -2, \omega_x = 0.5, \alpha = 0.05)$.

to turbulence. Figure 2.24(a) shows production and dissipation terms for the uncontrolled flow and for the flow subject to a DTW with ($c = 5$, $\omega_x = 2$, $\alpha = 0.05$). For the uncontrolled flow, P_E is always positive, D_E is always negative, and they both decay to zero at large times. On the contrary, the production term for the DTW becomes negative for $80 \lesssim t \lesssim 220$. We see that, at early times, P_E and D_E for the DTW follow their uncontrolled flow counterparts. However, after this initial period, they decay more rapidly to zero. These results confirm the prediction of § 2.3 that the DTWs reduce the production of kinetic energy. In contrast, Figure 2.24(b) shows that the UTWs with ($c = -2$, $\omega_x = 0.5$, $\alpha = \{0.05, 0.125\}$) increase both P_E and D_E by about four orders of magnitude compared to the values reported in Figure 2.24(a). This verifies the theoretical prediction of § 2.3 that the UTWs increase the production of kinetic energy. Moreover, production dominates dissipation transiently, thereby inducing large growth of kinetic energy observed in Figure 2.19(b). For the UTW with $\alpha = 0.05$, this is further illustrated in Figure 2.24(c) by showing that P_E accumulates more energy than D_E dissipates (i.e., the area under the curve in Figure 2.24(c) is positive). We also note that, in the above simulations, the work of Reynolds stress uv on the base shear U_y dominates the other energy production terms. Furthermore, our results show that the wall-normal diffusion of u is responsible for the largest viscous energy dissipation.

2.4.4 Flow visualization

In § 2.4.2, transition was identified by examining fluctuations' kinetic energy and skin-friction drag coefficients. Large levels of sustained kinetic energy and substantial increase in drag coefficients (compared to base flows) were used as indicators of transition. Here, we use flow visualization to identify coherent structures in both the uncontrolled and controlled flows.

The onset of turbulence in a bypass transition is usually characterized by formation of streamwise streaks and their subsequent break-down. For the initial condition with moderate energy, Figure 2.25 shows the streamwise velocity fluctuations at $y = -0.5557$ ($y^+ = 28.11$ in wall units) for the uncontrolled flow and flows subject to a UTW with ($c = -2$, $\omega_x = 0.5$, $\alpha = 0.05$) and a DTW with ($c = 5$, $\omega_x = 2$, $\alpha = 0.05$). Clearly, the initial perturbations evolve into streamwise streaks in all three flows (cf. Figures 2.25(a) - 2.25(e) for $t = 50$). At $t = 120$, the growth of velocity fluctuations results in a break-down of the streaks both in the flow with no control and in the flow subject to UTWs (cf. Figures 2.25(b) and 2.25(d)). We see that the streaks evolve into complex flow patterns much faster in the latter case. For the UTWs, the streak distortion occurs as early as $t = 50$ and a broad range of spatial scales is observed at $t = 120$. On the contrary, Figure 2.25(f) shows that, at $t = 120$, the DTWs have reduced the magnitude of velocity fluctuations to about half the value at $t = 50$, thereby weakening intensity of the streaks and maintaining the laminar flow.

In § 2.4.2, transition was identified by examining fluctuations' kinetic energy and

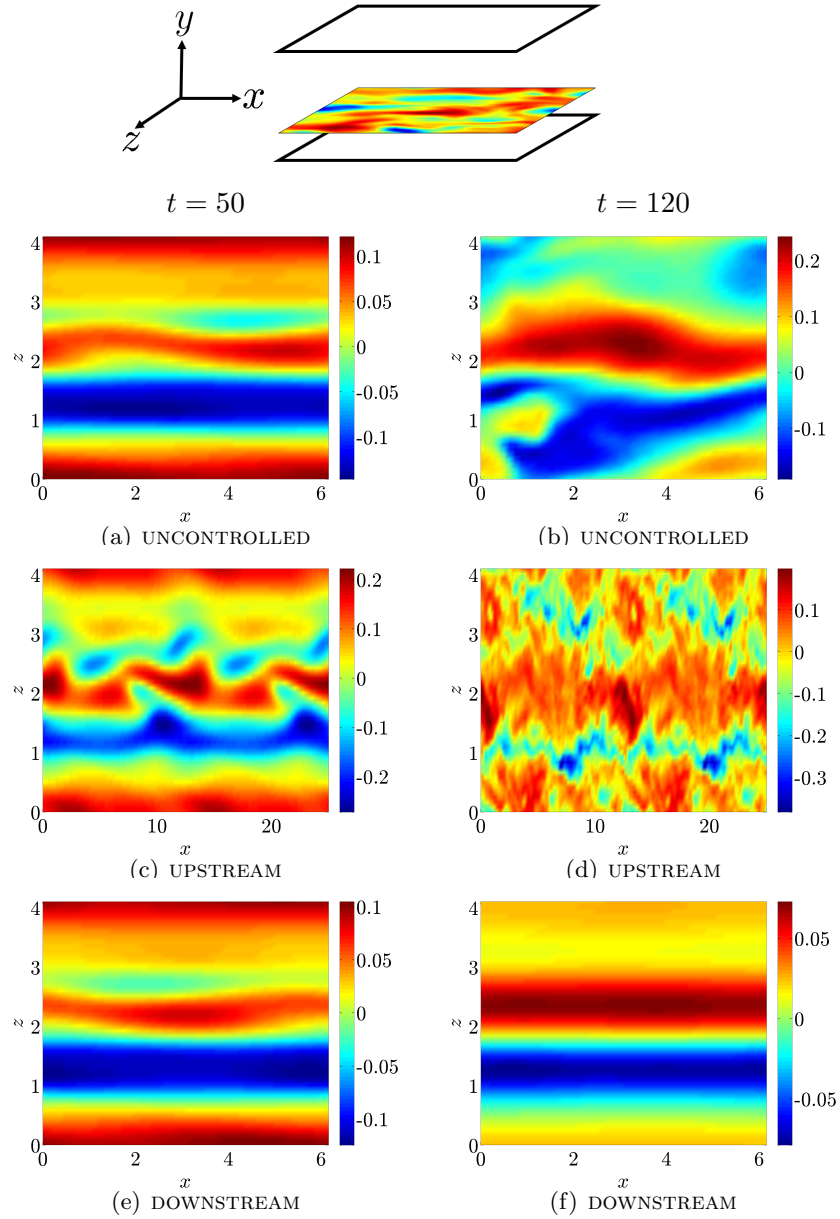


Figure 2.25: Streamwise velocity fluctuations, $u(x, z)$, at $y = -0.5557$ ($y^+ = 28.11$), (a), (c), (e) $t = 50$; and (b), (d), (f) $t = 120$ for initial condition with moderate energy: uncontrolled flow; UTW with ($c = -2$, $\omega_x = 0.5$, $\alpha = 0.05$); and DTW with ($c = 5$, $\omega_x = 2$, $\alpha = 0.05$).

skin-friction drag coefficient. Large levels of sustained kinetic energy and substantial increase of the drag coefficient (compared to base flow) were used as indicators of transition. Here, we use flow visualization to identify coherent structures in both the uncontrolled and controlled flows. In particular, we look at the flow regions that exhibit *vortex-like* motion [98]. We illustrate that, relative to the uncontrolled flow that becomes turbulent, the DTWs eliminate the formation of strong vortical motions. We also compare the transient and steady-state features of the uncontrolled flow with the flow subject to the UTWs.

Flow visualization has been used extensively to understand the nature of transitional and turbulent flows; for example, see [99–101]. The utility of critical point analysis in quantifying vortical motions in complex flows is discussed in [98, 102, 103]. In particular, [98] showed that discriminant, $D(x, y, z, t)$, of the velocity gradient tensor provides information about focal regions in the flow. The vortex cores are characterized by $D > 0$, and they are associated with the regions where the rate of rotation tensor dominates the rate of strain tensor [98]. Therefore, 3D visualization of D is a useful technique for recognizing vortex motions in the flow. The discriminant is obtained from $D = (27/4)R^2 + Q^3$, where $Q = (\text{tr}(\mathbf{A})^2 - \text{tr}(\mathbf{A}^2))/2$ and $R = -\det(\mathbf{A})$ are the second and third invariants of the velocity gradient tensor, \mathbf{A} , defined as $\mathbf{A}_{ij} = \partial u_i / \partial x_j$.

In order to visualize the effect of traveling waves on transition, an initial condition of moderate energy is considered. The isosurfaces of D , greater than a threshold value, for the uncontrolled flow and the flows subject to a DTW with ($c = 5$, $\omega_x = 2$, $\alpha = 0.05$) and a UTW with ($c = -2$, $\omega_x = 0.5$, $\alpha = 0.05$) are shown in Figures 2.26, 2.27, and 2.28, respectively. The cross-flow velocity vectors in the (y, z) -plane and the x -average of the streamwise vorticity are also plotted for comparison. We see that the regions of strong vorticity are correctly captured by the discriminant of the velocity gradient tensor. Figures 2.26(a) and 2.27(a) show that, at $t = 30$, the uncontrolled flow and the DTW have similar vortical structures. However, at $t = 50$ and $t = 70$, the uncontrolled flow exhibits large vortical motions close to the upper channel wall; these motions are considerably suppressed by the DTW. In addition, at $t = 70$, the magnitude of the streamwise vorticity for the DTW is about two times smaller than in the uncontrolled flow. In contrast, Figure 2.28 shows build-up of vorticity by the UTW of approximately two times larger magnitude than in the uncontrolled flow. Note that, in the early stages of transition, the vortical structures with $D > 10^{-6}$ are significantly more abundant in flows subject to the UTW than in the uncontrolled flow (cf. Figures 2.28(e) and 2.26(e)).

For $t \gtrsim 100$, the mixing of the lower and upper channel halves breaks the aforementioned elongated structures into smaller ones which leads to formation of new vortices throughout the channel (see [99] for the uncontrolled flow discussion). Figure 2.29 illustrates this behavior both in the uncontrolled flow and in the flow subject to the UTW. In the uncontrolled flow, the strong vortical motions in the upper half of the channel at $t = 100$ spread to the lower half at $t \approx 200$ (cf. Figures 2.29(a) and 2.29(c)). We see that the isosurfaces of the discriminant are in the form of tubes that extend from the lower

wall to the channel centerplane (cf. Figure 2.29(g)); similar structures were reported in turbulent wall-bounded shear flows by [101, 103]. We note that transition occurs much faster in the UTW with ($c = -2$, $\omega_x = 0.5$, $\alpha = 0.05$) than in the uncontrolled flow. For example, at $t = 100$, the UTW populates the entire channel with strong vortical motions. In the uncontrolled flow, however, these structures appear only in certain portions of the upper half of the channel. This is in agreement with Figure 2.21(a) where deterioration of the transient response of the uncontrolled flow by this UTW was observed. Our results also show that, for $t > 100$, in the DTW with ($c = 5$, $\omega_x = 2$, $\alpha = 0.05$) the discriminant is nowhere larger than 10^{-8} . This indicates that the DTWs are effective in suppressing the vortical motions that may arise naturally as a result of flow disturbances.

2.4.5 Relaminarization by downstream waves

Thus far we have shown that properly designed DTWs represent an effective means for controlling the onset of turbulence. In this section, we demonstrate that the DTWs designed in § 2.3 can also relaminarize fully developed turbulent flows. Since the lifetime of turbulence depends on the Reynolds number [104–107], we examine turbulent flows with $R_c = 2000$ (i.e., $R_\tau \approx 63.25$) and $R_c = 4300$ (i.e., $R_\tau \approx 92.80$).

We simulate the turbulent flow with $R_c = 4300$. The number of grid points in the streamwise, wall-normal, and spanwise directions is increased to $80 \times 97 \times 80$. The velocity field is initialized with a fully developed turbulent flow obtained in the absence of control. The surface blowing and suction that generates DTWs is then introduced (at $t = 0$), and the kinetic energy and drag coefficients are computed at each time step.

The fluctuations' kinetic energy for the uncontrolled flow and for the flows subject to DTWs with ($c = 5$, $\omega_x = 2$, $\alpha = \{0.035, 0.05, 0.125\}$) at $R_c = 2000$ are shown in Figure 2.30. The energy of velocity fluctuations around base flows \mathbf{u}_b (parabola for flow with no control; traveling waves for flow with control) are shown; relaminarization occurs when the energy of velocity fluctuations converges to zero. Clearly, large levels of fluctuations in the flow with no control are maintained up until $t \approx 1100$. After this time instant, however, velocity fluctuations exhibit gradual decay. On the other hand, fluctuations in flows subject to DTWs start decaying much earlier, thereby indicating that the lifetime of turbulence is reduced by surface blowing and suction. Relative to the uncontrolled flow, the fluctuations' kinetic energy for the DTWs considered here converge much faster to zero. We also see that the rate of decay increases as the wave amplitude gets larger.

We next consider a turbulent flow with $R_c = 4300$. The energy of velocity fluctuations around base flows \mathbf{u}_b is shown in Figure 2.31(a). In both the uncontrolled flow and the flows subject to the DTWs with ($c = 5$, $\omega_x = 2$, $\alpha = \{0.035, 0.05\}$) the energy oscillates around large values that identify turbulent flow. This indicates that the DTWs with smaller amplitudes cannot eliminate turbulence. On the contrary, the DTW with $\alpha = 0.125$ reduces the energy of velocity fluctuations, thereby relaminarizing the flow.

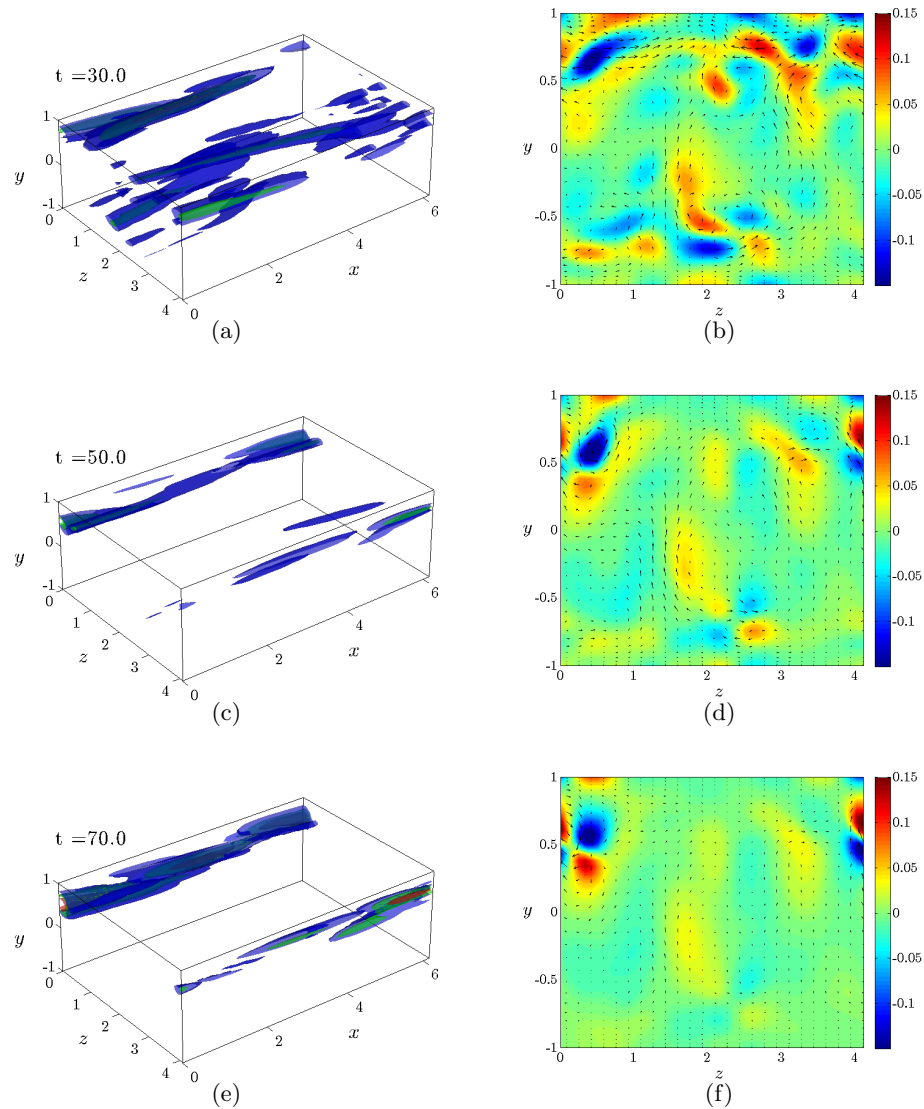


Figure 2.26: Simulation of the uncontrolled flow for the initial condition with moderate energy. (a), (c), (e) 3D visualizations of the isosurfaces of the discriminant, $D > 10^{-6}$ (blue), $D > 10^{-5}$ (green), and $D > 10^{-4}$ (red). (b), (d), (f) 2D visualizations of the crossflow velocity vectors (arrows) and the x -averaged streamwise vorticity (color plots).

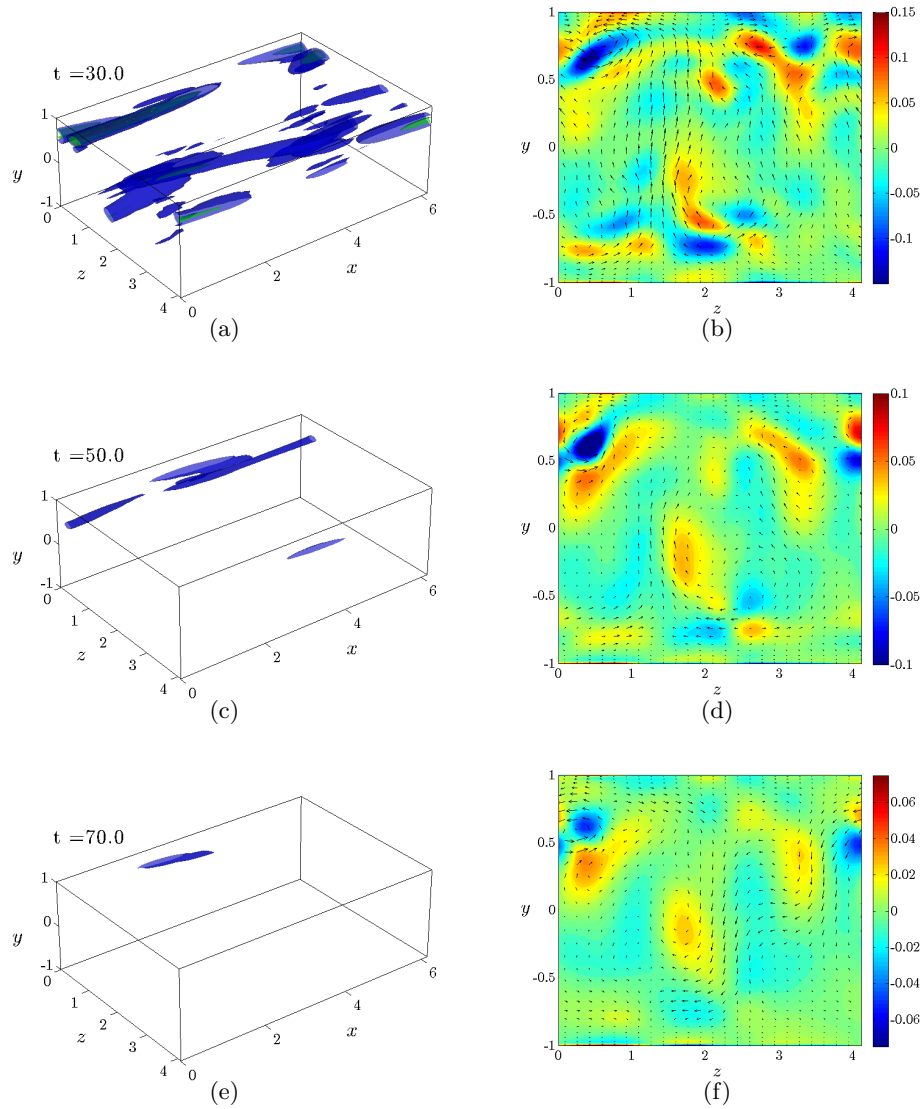


Figure 2.27: Simulation of the DTW with ($c = 5$, $\omega_x = 2$, $\alpha = 0.05$) for the initial conditions with moderate energy. (a), (c), (e) 3D visualizations of the isosurfaces of the discriminant, $D > 10^{-6}$ (blue), $D > 10^{-5}$ (green), and $D > 10^{-4}$ (red). (b), (d), (f) 2D visualizations of the crossflow velocity vectors (arrows) and the x - averaged streamwise vorticity (color plots).

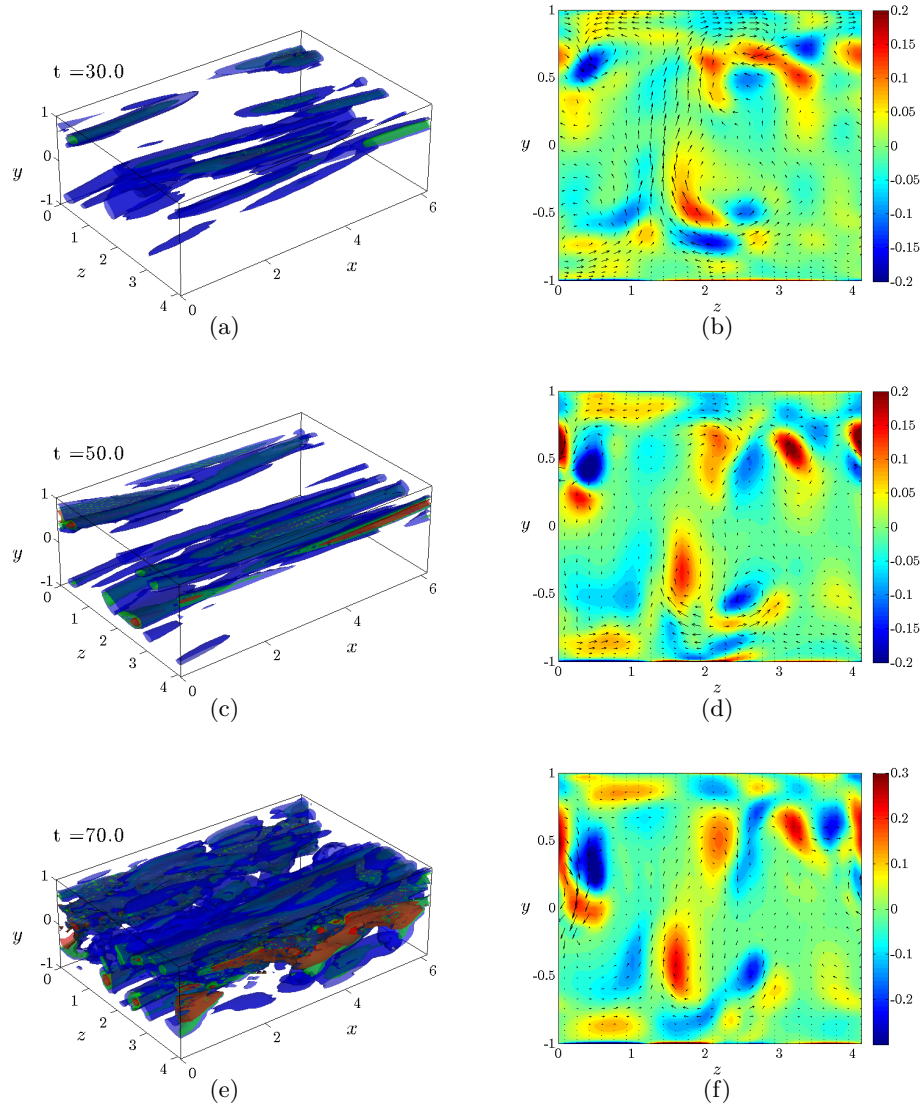


Figure 2.28: Simulation of the UTW with ($c = -2$, $\omega_x = 0.5$, $\alpha = 0.05$) for the initial condition with moderate energy. (a), (c), (e) 3D visualizations of the isosurfaces of the discriminant, $D > 10^{-6}$ (blue), $D > 10^{-5}$ (green), and $D > 10^{-4}$ (red). (b), (d), (f) 2D visualizations of the crossflow velocity vectors (arrows) and the x -averaged streamwise vorticity (color plots). Only one quarter of the channel ($x \in [0, 2\pi]$) is shown.

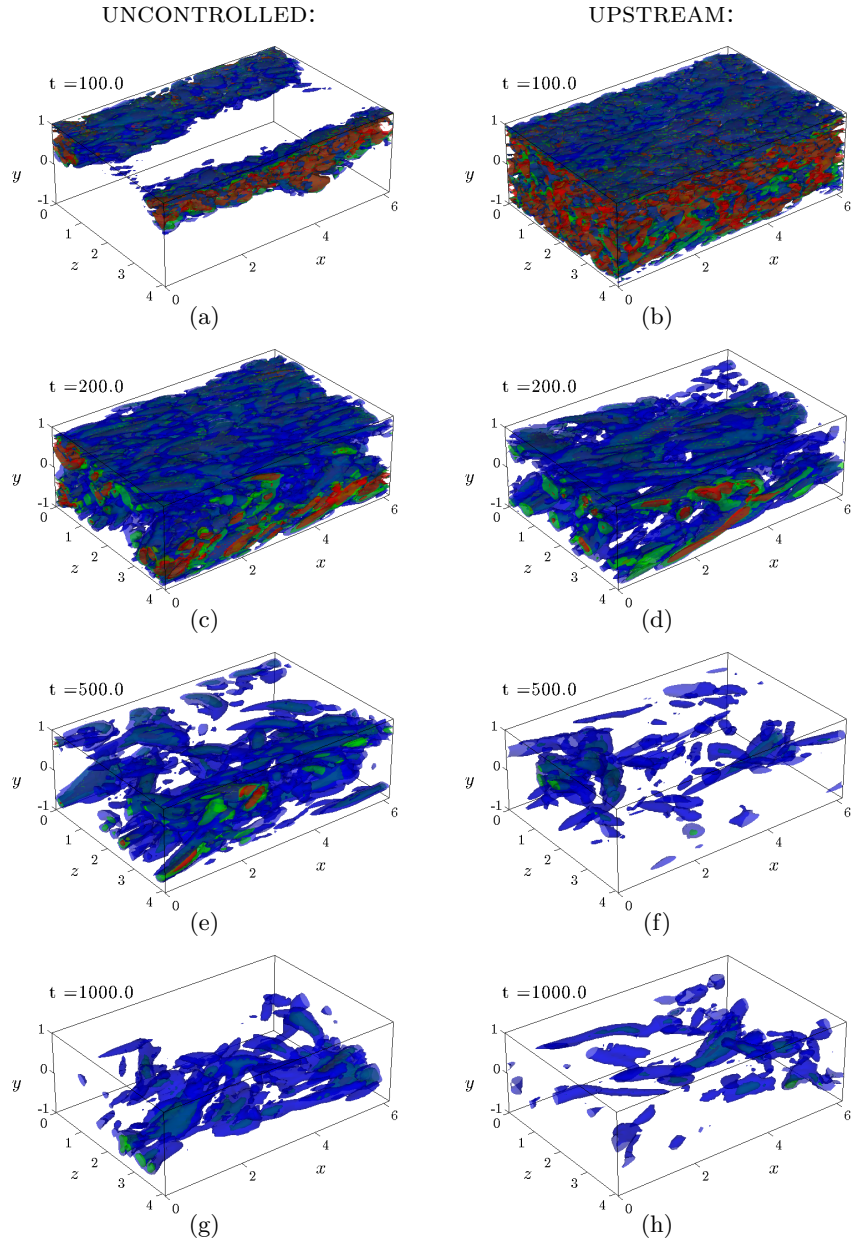


Figure 2.29: 3D visualizations of the isosurfaces of the discriminant, $D > 10^{-5}$ (blue), $D > 10^{-4}$ (green), and $D > 10^{-3}$ (red) for the uncontrolled flow (left figures) and the UTW with ($c = -2$, $\omega_x = 0.5$, $\alpha = 0.05$) (right figures) for the initial condition with moderate energy. Only one quarter of the channel ($x \in [0, 2\pi]$) is shown for the UTW.

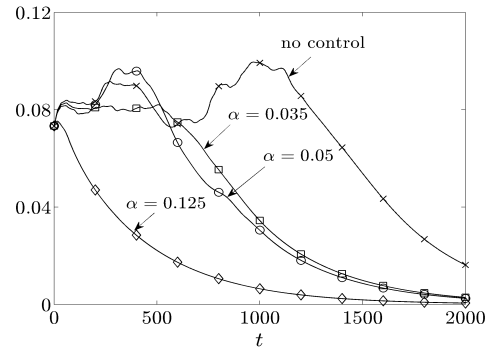


Figure 2.30: Energy of velocity fluctuations around base flows. Simulations are initiated by a fully developed turbulent flow with $R_c = 2000$: \times , uncontrolled; DTWs with \square , ($c = 5, \omega_x = 2, \alpha = 0.035$); \circ , ($c = 5, \omega_x = 2, \alpha = 0.05$); and \diamond , ($c = 5, \omega_x = 2, \alpha = 0.125$).

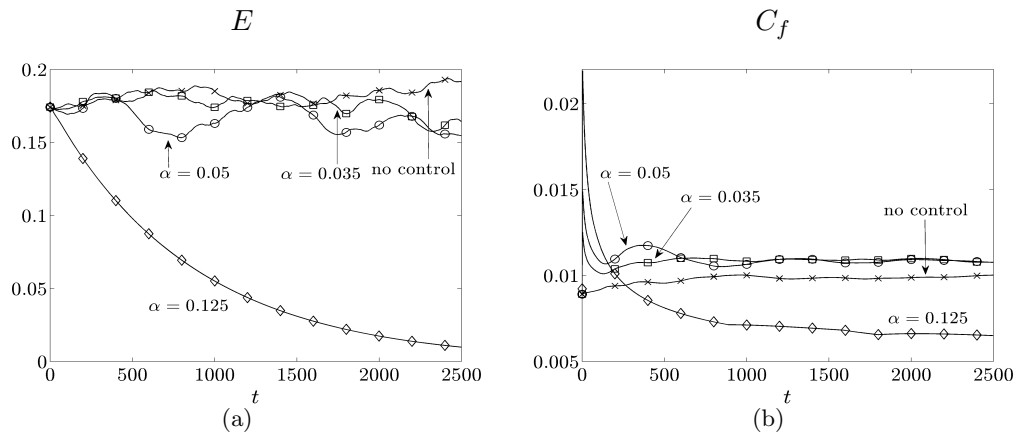


Figure 2.31: (a) Energy of velocity fluctuations around base flows, $E(t)$; and (b) skin-friction drag coefficient, $C_f(t)$. Simulations are initiated by a fully developed turbulent flow with $R_c = 4300$: \times , uncontrolled; DTWs with \square , ($c = 5, \omega_x = 2, \alpha = 0.035$); \circ , ($c = 5, \omega_x = 2, \alpha = 0.05$); and \diamond , ($c = 5, \omega_x = 2, \alpha = 0.125$).

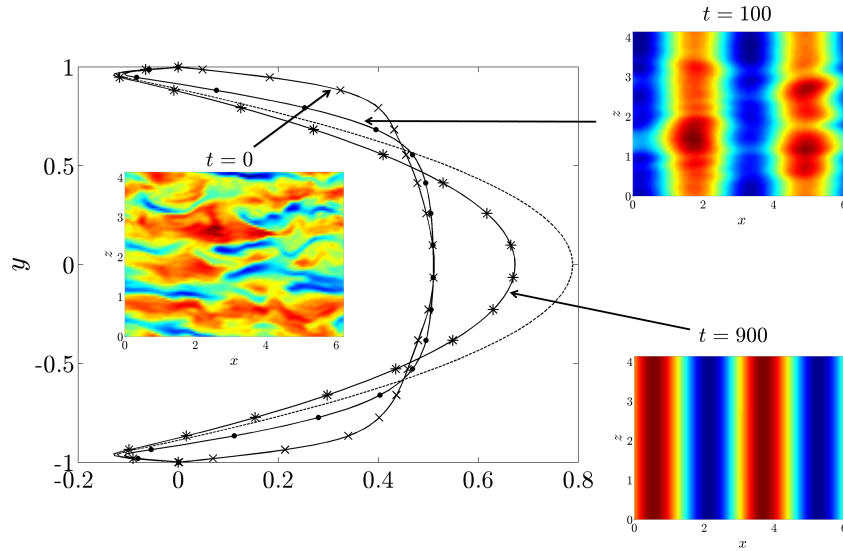


Figure 2.32: Mean velocity, $\bar{U}(y)$, and streamwise velocity (colored plots) at $y = -0.7518$. Simulations are initiated by a fully developed turbulent flow with $R_c = 4300$: \times , $t = 0$; \bullet , $t = 100$; $*$, $t = 900$. The dashed line identifies the laminar mean velocity induced by the DTW with ($c = 5$, $\omega_x = 2$, $\alpha = 0.125$).

Figure 2.31(b) shows that the skin-friction drag coefficient for the uncontrolled flow and for the DTWs with smaller amplitudes is approximately constant throughout the simulation. On the other hand, owing to relaminarization, the drag coefficient for the DTW with $\alpha = 0.125$ is smaller than that of the uncontrolled turbulent flow. However, relaminarization comes at the expense of poor net efficiency. This is because of the large required power (i.e., high cost of control), which reduces the appeal of using DTWs for control of turbulent flows.

Figure 2.32 shows the mean velocity, $\bar{U}(y)$, at three time instants in the flow subject to the DTW with ($c = 5$, $\omega_x = 2$, $\alpha = 0.125$). The instantaneous values of streamwise velocity in the (x, z) -plane at $y = -0.7518$ are also shown. As time advances, the initial turbulent mean velocity at $R_c = 4300$ moves towards the laminar mean velocity induced by the surface blowing and suction (dashed line). The colored plots illustrate how the initial turbulent flow evolves into the DTW laminar base flow. We conjecture that receptivity reduction is important not only for controlling the onset of turbulence but also for relaminarization of fully developed flows. Explaining the effect of traveling waves on turbulent flows requires additional control-oriented modeling and further scrutiny.

2.5 Summary

This chapter disentangles three distinct effects of blowing and suction along the walls on pumping action, required control power, and kinetic energy reduction. We have shown that analysis of dynamics is paramount to designing the streamwise traveling waves. If velocity fluctuations are well-behaved then the pumping action and required control power can be ascertained from the steady-state analysis. The proposed method uses receptivity analysis of the linearized NS equations to study the fluctuations' energy in transitional channel flows. Motivated by our observation that a positive net efficiency can be achieved by preventing transition, we develop a framework for design of the traveling waves that reduce receptivity to three dimensional body force fluctuations. Direct numerical simulations of the NS equations verify that the traveling waves identified here are indeed an effective means for controlling the onset of turbulence. This demonstrates the predictive power of model-based approach to sensorless flow control; our simulation-free approach captures the essential trends in a computationally efficient manner and avoids the need for DNS and experiments in the early design stages.

Our perturbation analysis has revealed that properly designed DTWs can significantly reduce energy amplification of three dimensional fluctuations, including the streamwise streaks and the TS waves, which makes them well-suited for preventing transition. The DNS results confirm that transient response of fluctuations' kinetic energy can be maintained at low levels using the values of wave frequency and speed that reduce receptivity of the linearized NS equations. This facilitates maintenance of laminar flow; positive net efficiency can be achieved if the wave amplitude necessary for controlling the onset of turbulence is not prohibitively large. On the other hand, we show that the UTWs are poor candidates for preventing transition for they, at best, exhibit similar receptivity to background disturbances as the uncontrolled flow. In particular, the UTWs considered by [8] largely amplify the most energetic modes of the uncontrolled flow, thereby promoting turbulence even when the uncontrolled flow stays laminar.

Simulations of nonlinear flow dynamics have demonstrated that the DTWs can maintain laminar flow and achieve positive net efficiency. In contrast, the UTWs promote turbulence even with the initial conditions for which the uncontrolled flow remains laminar. Our analysis of the Reynolds-Orr equation shows that, compared to the uncontrolled flow, the DTWs (UTWs) reduce (increase) the production of kinetic energy.

We have also examined the effects of DTWs on fully developed turbulent flows at low Reynolds numbers. It turns out that the DTWs with speed and frequency selected in § 2.3 and large enough amplitudes can eliminate turbulence (i.e., relaminarize the flow). We also note that, in spite of promoting turbulence, the UTWs may still achieve smaller drag coefficients compared to the uncontrolled flow. By increasing the UTW amplitude, even sub-laminar drag can be attained [8]. It is to be noted, however, that large wave amplitudes introduce poor net efficiency in flows subject to a fixed pressure gradient. Nevertheless, these traveling waves may still be utilized when the primal

interest is to eliminate turbulence (with DTWs) or reduce the skin-friction drag (with UTWs) irrespective of the cost of control.

All simulations in the present study are enforced by a fixed pressure gradient, as opposed to the constant mass flux simulations of [8]. Even though these setups are equivalent in steady flows [108], they can exhibit fundamentally different behavior in unsteady flows. For example, the two simulations may possess different stability characteristics and yield structurally different solutions for near-wall turbulence [109, 110]. Moreover, [110] remarked that the dynamical properties of the two simulations can significantly differ in small computational domains. Also, [111] suggested that specifying the simulation type comes next to defining the boundary conditions.

In order to examine the effect of simulation type on transition, skin-friction drag coefficient, and control net efficiency, we have repeated some of the simulations by adjusting the pressure gradient to maintain a constant mass flux. Our results reveal that regardless of the simulation type, the DTWs designed in § 2.3 are effective in preventing transition while the UTWs promote turbulence. Moreover, the steady-state skin-friction drag coefficients are almost identical in both cases. However, the control net efficiency depends significantly on the simulation type. This is because of the difference in the definition of the produced power: in the fixed pressure gradient setup, the produced power is captured by the difference between the bulk fluxes in the uncontrolled and controlled flows; in the constant mass flux setup, the produced power is determined by the difference between the driving pressure gradients in the uncontrolled and controlled flows. It turns out that the produced power is larger in the constant mass flux simulation than in the fixed pressure gradient simulation, whereas the required power remains almost unchanged. Consequently, both DTWs and UTWs have larger efficiency in constant mass flux simulations. For example, in fixed pressure gradient setup of the present study, the UTWs with ($c = -2$, $\omega_x = 0.05$ $\alpha = \{0.05, 0.125\}$) have negative efficiency. The efficiency of these UTWs is positive, however, in constant mass flux simulations [8]. Our ongoing effort is directed towards understanding the reason behind this disagreement which may be ultimately related to the fundamental difference between these two types of simulations.

Chapter 3

Localized optimal feedback control of transitional channel flow

Feedback strategies for control of fluid flows involve individual system components that are capable of sensing, computation, and actuation. Therefore, an important question in design of flow controllers is related to the interconnection structure between these components. A centralized controller yields best performance at the expense of excessive communication and computation. A fully decentralized controller, while advantageous from a communications perspective, may sacrifice performance. A reasonable compromise between these competing approaches is offered by localized strategies where each component exchanges information with a limited number of nearby components.

Early flow control efforts have focused on drag reduction in turbulent flows. These include the opposition control [112] and gradient-based strategies where the optimal control problem is solved over infinitesimal [113,114] or finite [101] time horizons. During the last decade, the emphasis has shifted to model-based techniques from linear control theory which represent an efficient means for design of optimal flow controllers; see [42] for recent developments. In this chapter, we study the problem of controlling the onset of turbulence. Since the early stages of transition are initiated by large flow receptivity [7,24,25,28], we formulate an optimal control problem aimed at reducing this receptivity. For transition control at low Reynolds numbers, this strategy has proven successful in both vibrational sensor-less [115,116] and centralized feedback [56] setups. These references show that, by substantially reducing large flow receptivity, transition to turbulence can be prevented and even relaminarization of a fully-developed turbulent flow can be achieved.

The main difference between the problem addressed here and by [56] is that we consider control designs that are localized in space. Namely, the actuation at a certain location depends only on local flow information. The localized controller is obtained

using recently developed tools for optimal design of feedback gains subject to structural constraints [68, 69]. We compare the performance of the localized optimal controller with that of the optimal centralized controller and the controller that is obtained by spatial truncation of the centralized feedback gain. When the actuators use information from only the nearest neighbor components, we demonstrate the danger of enforcing the constraint by spatial truncation. On the other hand, we show that the localized optimal controller achieves performance comparable to that of the optimal centralized controller.

The chapter is organized as follows. In § 3.1, the evolution model for channel flow subject to body force disturbances and boundary actuation is derived. The problem of optimal state-feedback design in the presence of structural constraints is formulated in § 3.2. In addition, a gradient descent method for solving necessary conditions for optimality is briefly described. In § 3.3, the effectiveness of the designed feedback gains for controlling the onset of turbulence is examined by comparing the receptivity of the controlled flows and the flow with no control. Our design is further verified using direct numerical simulations of the nonlinear flow dynamics. We conclude the chapter in § 3.4.

3.1 Preliminaries

3.1.1 Governing equations

We consider an incompressible channel flow, driven by a fixed pressure gradient and subject to a control actuation in the form of blowing and suction along the walls. The evolution of infinitesimal fluctuations around the laminar parabolic profile $U(y)$ is governed by the linearized Navier-Stokes (NS) equations

$$\mathbf{v}_t = -U \mathbf{v}_x - U' v \mathbf{i} - \nabla p + (1/R_c) \Delta \mathbf{v} + \mathbf{d}, \quad 0 = \nabla \cdot \mathbf{v}, \quad (3.1)$$

where \mathbf{i} denotes the unit vector in the streamwise direction, and $R_c = U_c \delta / \nu$ is the Reynolds number defined in terms of the centerline velocity of the parabolic laminar profile U_c and channel half-height δ . The spatial coordinates and time are denoted by (x, y, z) and t , respectively. The kinematic viscosity is denoted by ν , p is the pressure, the velocity fluctuations are given by $\mathbf{v} = (u, v, w)$, and $\mathbf{d} = (d_1, d_2, d_3)$ represents the body force disturbance. Here, the indices 1, 2, and 3 correspond to x , y , and z coordinates, respectively, ∇ is the gradient, $\Delta = \nabla \cdot \nabla$ is the Laplacian, and $U'(y) = dU(y)/dy$. Actuation along the walls imposes the following boundary conditions on the wall-normal velocity

$$v(x, y = -1, z, t) = v_l(x, z, t), \quad v(x, y = 1, z, t) = v_u(x, z, t), \quad (3.2)$$

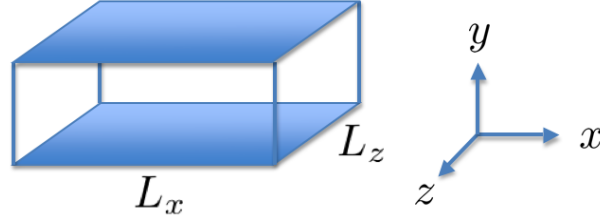


Figure 3.1: A periodic channel with size $L_x \times 2 \times L_z$.

where v_l and v_u denote actuations at the lower and upper walls. The horizontal velocity components satisfy Dirichlet boundary conditions

$$u(x, y = \pm 1, z, t) = w(x, y = \pm 1, z, t) = 0.$$

To obtain the standard control formulation, the actuation must enter as an explicit input into the evolution equation [117]. The following change of variables

$$v(x, y, z, t) = \bar{v}(x, y, z, t) + f_l(y) v_l(x, z, t) + f_u(y) v_u(x, z, t), \quad (3.3)$$

can be used to achieve this objective, where f_l and f_u are specified by the requirement that \bar{v} satisfies Dirichlet and Neumann boundary conditions at the walls:

$$f_l(y) = (y^3 - 3y + 2) / 4, \quad f_u(y) = -(y^3 - 3y - 2) / 4.$$

The evolution model is obtained from Eq. (3.1) by eliminating pressure via a standard choice of wall-normal velocity and vorticity (v, η) as the flow variables. By incorporating the change of variables introduced by Eq. (3.3), and augmenting the flow variables by the boundary actuation, we obtain the state vector $\phi = [\phi_1^T(x, y, z, t) \ \phi_2^T(x, z, t)]^T$. Here, $\phi_1 = [\bar{v} \ \eta]^T$, where $\eta = u_z - w_x$ denotes the wall-normal vorticity, and $\phi_2 = [v_l \ v_u]^T$ is the boundary-actuation-vector. This choice brings the time-derivative of the boundary actuation $\mathbf{u} = [u_1 \ u_2]^T = \phi_{2t}$ as an explicit input to the evolution model. The evolution model for the controlled flow is determined by

$$\phi_t = \mathcal{A} \phi + \mathcal{B}_1 \mathbf{d} + \mathcal{B}_2 \mathbf{u}, \quad \mathbf{v} = \mathcal{C}_1 \phi. \quad (3.4)$$

The operator \mathcal{A} represents the dynamical generator of Eq. (3.4), \mathcal{B}_1 and \mathcal{B}_2 determine how disturbances and control enter into Eq. (3.4), and \mathcal{C}_1 specifies the kinematic relation between velocity fluctuations \mathbf{v} and state ϕ . The operators in the evolution model are determined by

$$\mathcal{A} = \begin{bmatrix} \mathcal{A}_{11} & \mathcal{A}_{12} \\ 0 & 0 \end{bmatrix}, \quad \mathcal{B}_1 = \begin{bmatrix} \mathcal{B}_{11} \\ 0 \end{bmatrix}, \quad \mathcal{B}_2 = \begin{bmatrix} \mathcal{B}_{21} \\ \mathcal{B}_{22} \end{bmatrix}, \quad \mathcal{C}_1 = [\mathcal{C}_{11} \ \mathcal{C}_{12}],$$

where

$$\begin{aligned} \mathcal{A}_{11} &= \begin{bmatrix} \Delta^{-1} ((1/R_c)\Delta^2 - (U_0\Delta - U_0'') \partial_x) & 0 \\ -U_0' \partial_z & (1/R_c)\Delta - U_0 \partial_x \end{bmatrix}, \\ \mathcal{A}_{12} &= \begin{bmatrix} \mathcal{A}_{12,1} & \mathcal{A}_{12,2} \\ -U_0' f_l \partial_z & -U_0' f_u \partial_z \end{bmatrix}, \\ \mathcal{A}_{12,1} &= \Delta^{-1} ((2 f_l'' (\partial_x^2 + \partial_z^2) + f_l (\partial_x^2 + \partial_z^2)^2) / R_c - (U_0 f_l'' + U_0 f_l (\partial_x^2 + \partial_z^2) - U_0'' f_l) \partial_x), \\ \mathcal{A}_{12,2} &= \Delta^{-1} ((2 f_u'' (\partial_x^2 + \partial_z^2) + f_u (\partial_x^2 + \partial_z^2)^2) / R_c - (U_0 f_u'' + U_0 f_u (\partial_x^2 + \partial_z^2) - U_0'' f_u) \partial_x), \\ \mathcal{B}_{11} &= \begin{bmatrix} \Delta^{-1} (-\partial_{xy}) & \Delta^{-1} (\partial_x^2 + \partial_z^2) & \Delta^{-1} (-\partial_{yz}) \\ \partial_z & 0 & -\partial_x \end{bmatrix}, \\ \mathcal{B}_{21} &= \begin{bmatrix} \Delta^{-1} (-f_l'' - f_l (\partial_x^2 + \partial_z^2)) & \Delta^{-1} (-f_u'' - f_u (\partial_x^2 + \partial_z^2)) \\ 0 & 0 \end{bmatrix}, \quad \mathcal{B}_{22} = \begin{bmatrix} 1 & 0 \\ 0 & 1 \end{bmatrix}, \\ \mathcal{C}_{11} &= \begin{bmatrix} -\partial_{xy} (\partial_x^2 + \partial_z^2)^{-1} & \partial_z (\partial_x^2 + \partial_z^2)^{-1} \\ I & 0 \\ -\partial_{yz} (\partial_x^2 + \partial_z^2)^{-1} & -\partial_x (\partial_x^2 + \partial_z^2)^{-1} \end{bmatrix}, \\ \mathcal{C}_{12} &= \begin{bmatrix} -f_l' \partial_x (\partial_x^2 + \partial_z^2)^{-1} & -f_u' \partial_x (\partial_x^2 + \partial_z^2)^{-1} \\ f_l & f_u \\ -f_l' \partial_z (\partial_x^2 + \partial_z^2)^{-1} & -f_u' \partial_z (\partial_x^2 + \partial_z^2)^{-1} \end{bmatrix}, \end{aligned}$$

with $\Delta = \partial_x^2 + \partial_y^2 + \partial_z^2$ denoting the three-dimensional Laplacian.

3.1.2 Actuation along the discrete lattice

In what follows, we impose periodic boundary conditions in the horizontal directions; see Figure 3.1 for geometry. The size of the computational domain is given by $L_x \times 2 \times L_z$, where L_x and L_z denote the channel lengths in x and z . We use N_x and N_z Fourier modes to represent differential operators in the streamwise and spanwise directions, respectively. In physical space, this yields a two-dimensional lattice of equally-spaced points $(x_r = r h_x, z_s = s h_z)$, with $r \in \mathbb{N}_x = \{0, 1, \dots, N_x - 1\}$ and $s \in \mathbb{N}_z = \{0, 1, \dots, N_z - 1\}$. The horizontal spacings between two adjacent points are determined by $h_x = L_x / N_x$ and $h_z = L_z / N_z$. For simplicity, we use the same symbols to denote variables in physical and frequency domains; for example, $v(m, n; y, t)$ denotes the frequency representation of $v(r, s; y, t) = v(x_r, y, z_s, t)$, where $m \in \mathbb{Z}_x = \{-N_x/2, -N_x/2 + 1, \dots, N_x/2 - 1\}$ and $n \in \mathbb{Z}_z = \{-N_z/2, -N_z/2 + 1, \dots, N_z/2 - 1\}$. The corresponding spatial wavenumbers are determined by $\kappa_m = m 2\pi / L_x$ and $\kappa_n = n 2\pi / L_z$.

We consider the design problem with wall-actuation taking place along the aforementioned two-dimensional lattice. Furthermore, we assume that the states are available

for measurement, implying that the control input at (x_r, z_s) is obtained from

$$\mathbf{u}(r, s; t) = - \sum_{\tilde{r} \in \mathbb{N}_x, \tilde{s} \in \mathbb{N}_z} \left(\int_{-1}^1 \mathcal{K}_1(r - \tilde{r}, s - \tilde{s}; y) \phi_1(\tilde{r}, \tilde{s}; y, t) dy + \mathcal{K}_2(r - \tilde{r}, s - \tilde{s}) \phi_2(\tilde{r}, \tilde{s}; t) \right), \quad (3.5)$$

where \mathcal{K}_1 and \mathcal{K}_2 are the corresponding state-feedback gains. The frequency representation of Eq. (3.5), for each $m \in \mathbb{Z}_x$ and $n \in \mathbb{Z}_z$, is given by

$$\mathbf{u}(m, n; t) = - \int_{-1}^1 \mathcal{K}_1(m, n; y) \phi_1(m, n; y, t) dy - \mathcal{K}_2(m, n) \phi_2(m, n; t). \quad (3.6)$$

For computational purposes, the wall-normal operators in Eqs. (3.4) and (3.6) are approximated using pseudospectral method with N_y Chebyshev collocation points [118]. This yields the discretized evolution model

$$\begin{aligned} \dot{\phi}_{m,n}(t) &= A_{m,n} \phi_{m,n}(t) + B_{1m,n} \mathbf{d}_{m,n}(t) + B_{2m,n} \mathbf{u}_{m,n}(t), \\ \mathbf{v}_{m,n}(t) &= C_{1m,n} \phi_{m,n}(t), \end{aligned} \quad (3.7)$$

parameterized by $m \in \mathbb{Z}_x$ and $n \in \mathbb{Z}_z$. Here, $\phi_{m,n}(t)$ and $\mathbf{u}_{m,n}(t)$ are column-vectors with $(2N_y + 2)$ and 2 components, respectively, and the dot is the derivative with respect to time. Furthermore, the control action is determined by

$$\mathbf{u}_{m,n}(t) = -K_{m,n} \phi_{m,n}(t) = - \begin{bmatrix} K_{1m,n} & K_{2m,n} \end{bmatrix} \begin{bmatrix} \phi_{1m,n}(t) \\ \phi_{2m,n}(t) \end{bmatrix} \quad (3.8)$$

where the $2 \times (2N_y + 2)$ matrix $K_{m,n}$ denotes the discretized form of the state-feedback gain in the frequency domain.

3.2 Design of localized optimal feedback gains

We consider the problem of designing structured optimal feedback gains for controlling the onset of turbulence. To this end, we determine the stabilizing gains that minimize a performance index J obtained by penalizing flow receptivity and control effort. These are, respectively, quantified by the variance amplification of velocity fluctuations \mathbf{v} in the presence of zero-mean white stochastic disturbance \mathbf{d} , and by the kinetic energy of the blowing and suction along the walls. In addition, to obtain the well-posed optimal control formulation, the penalty on \mathbf{u} is introduced in the performance index as well.

The above described optimal control problem amounts to finding the stabilizing

gains that minimize the variance amplification of the performance output

$$\zeta_{m,n}(t) = \begin{bmatrix} W^{1/2} C_{1m,n} \\ 0 \end{bmatrix} \phi_{m,n}(t) + \begin{bmatrix} 0 \\ R^{1/2} \end{bmatrix} \mathbf{u}_{m,n}(t). \quad (3.9)$$

Here, R is the positive definite matrix, and W denotes a $3N_y \times 3N_y$ diagonal matrix with $\{\mathbf{w}, \mathbf{w}, \mathbf{w}\}$ on its main diagonal where the vector \mathbf{w} contains the integration weights at the Chebyshev collocation points [119]. Substitution of Eq. (3.8) into Eqs. (3.7) and (3.9) yields the following evolution model of the closed-loop system

$$\begin{aligned} \dot{\phi}_{m,n}(t) &= (A_{m,n} - B_{2m,n} K_{m,n}) \phi_{m,n}(t) + B_{1m,n} \mathbf{d}_{m,n}(t), \\ \zeta_{m,n}(t) &= \begin{bmatrix} W^{1/2} C_{1m,n} \\ -R^{1/2} K_{m,n} \end{bmatrix} \phi_{m,n}(t). \end{aligned} \quad (3.10)$$

Mathematically, the problem of steady-state variance (i.e., the \mathcal{H}_2 norm) minimization for system given by Eq. (3.10), can be formulated as [117]

$$\text{minimize : } J(K) = \sum_{m \in \mathbb{Z}_x, n \in \mathbb{Z}_z} \text{trace} (X_{m,n} Q_{Bm,n}), \quad (3.11a)$$

$$\text{subject to : } A_{\text{clm},n}^* X_{m,n} + X_{m,n} A_{\text{clm},n} = -(Q_{Cm,n} + K_{m,n}^* R K_{m,n}), \quad (3.11b)$$

where $*$ denotes the complex conjugate transpose, $A_{\text{clm},n} = A_{m,n} - B_{2m,n} K_{m,n}$, $Q_{Bm,n} = B_{1m,n} W^{-1} B_{1m,n}^*$, and $Q_{Cm,n} = C_{1m,n}^* W C_{1m,n}$. The solution to Eq. (3.11) in the absence of structural constraints is given by

$$K_{m,n} = R^{-1} B_{2m,n}^* X_{m,n}, \quad (3.12)$$

where $X_{m,n}$ is determined from the algebraic Riccati equation

$$A_{m,n}^* X_{m,n} + X_{m,n} A_{m,n} - X_{m,n} B_{2m,n} R^{-1} B_{2m,n}^* X_{m,n} + Q_{Cm,n} = 0.$$

In general, actuation based on the optimal solution given by Eq. (3.12), necessitates centralized implementation that requires knowledge of the entire flow field. The problem of designing optimal centralized feedback gains for controlling transition is considered by [56]. As shown by [66], the magnitude of the centralized feedback gains decays exponentially in space, implying that they can be spatially truncated. Although this suggests a way for obtaining localized controllers, the problem of designing localized optimal feedback gains is more challenging. The main difference between the problem considered here and in [56] is that we ask the following question: Can actuation based on local flow information prevent transition to turbulence? To answer this, we a priori impose structural constraints on the feedback gains. It is assumed that each actuator uses information only from the points that are located within a small relative distance.

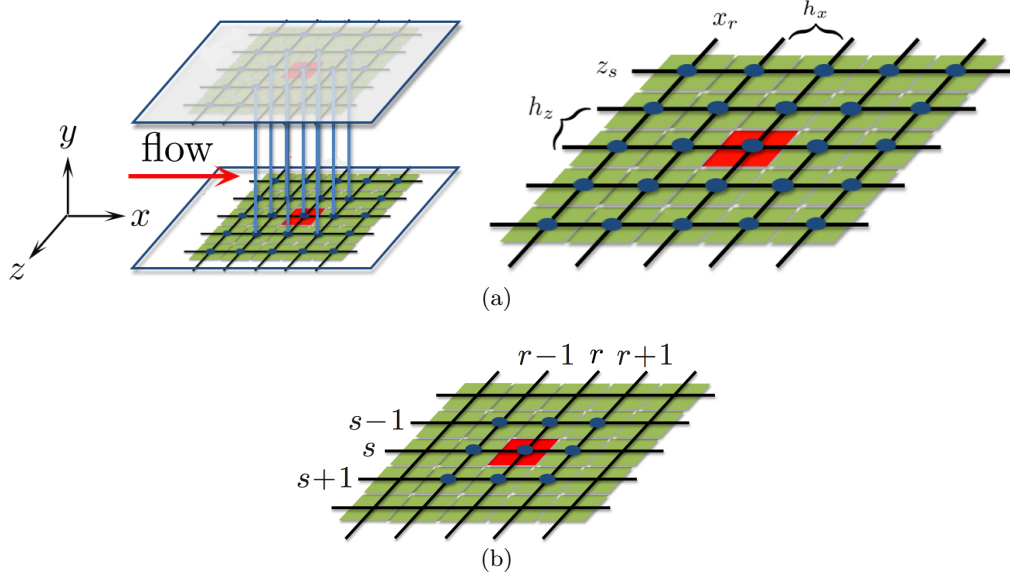


Figure 3.2: Sketch of a localized control strategy where the actuator placed at (r, s) uses information from only the nearest neighbors on the two-dimensional lattice.

The set of all such relative distances in units of h_x and h_z is denoted by S . In other words, only the feedback gains that correspond to the points in S are allowed to be nonzero. For example, when information from only the nearest neighbors is used, we have (see Figure 3.2 for an illustration)

$$S = \{(r, s) \mid r = \{-1, 0, 1\}, s = \{-1, 0, 1\}\}.$$

Furthermore, by $F(r, s)$ we denote the corresponding structured feedback gains.

For spatially invariant systems, the structured optimal state-feedback problem can be formulated as [68]

$$\text{minimize : } J(F) = \sum_{m \in \mathbb{Z}_x, n \in \mathbb{Z}_z} \text{trace} (X_{m,n} Q_{Bm,n}), \quad (\text{P1})$$

$$\text{subject to : } A_{clm,n}^* X_{m,n} + X_{m,n} A_{clm,n} = -(Q_{Cm,n} + C_{2m,n}^* F^* R F C_{2m,n}), \quad (\text{P2})$$

where F denotes the block-row matrix, which is independent of m and n , and contains the structured feedback gain $F(r, s)$,

$$F = \text{row} \{F(r, s)\}_{(r,s) \in S}, \quad (\text{P3})$$

and $C_{2m,n}$ is given by the block-column matrix

$$C_{2m,n} = \text{col} \left\{ e^{-i2\pi(rm/N_x + sn/N_z)} I \right\}_{(r,s) \in S}. \quad (\text{P4})$$

Here, I is the identity matrix of size $2N_y + 2$, and $A_{\text{clm},n} = A_{m,n} - B_{2m,n} F C_{2m,n}$ denotes the dynamical generator of the closed-loop system.

Note that in the absence of structural constraints (i.e., $S = \mathbb{N}_x \times \mathbb{N}_z = \{(r,s) \mid r \in \mathbb{N}_x, s \in \mathbb{N}_z\}$), the structured optimal control problem (P1)-(P4) reduces to the unstructured problem given by Eq. (3.11).

3.2.1 Computation of the structured optimal feedback gains

We briefly describe the method that is used to solve the optimal control problem (P1)-(P4) with specified S . This method is adopted from the developments of [69], where efficient descent methods for structured optimal design are introduced.

The necessary conditions for optimality of the stabilizing feedback gain F with $R = rI_{2 \times 2}$ in (P2), $r > 0$, are given by [69]

$$\begin{aligned} A_{\text{clm},n}^* X_{m,n} + X_{m,n} A_{\text{clm},n} &= -(Q_{C_{2m,n}} + r C_{2m,n}^* F^* F C_{2m,n}), \\ A_{\text{clm},n} Y_{m,n} + Y_{m,n} A_{\text{clm},n}^* &= -Q_{B_{2m,n}}, \\ F &= \frac{1}{r} \left(\sum_{m \in \mathbb{Z}_x, n \in \mathbb{Z}_z} B_{2m,n}^* X_{m,n} Y_{m,n} C_{2m,n}^* \right) \left(\sum_{m \in \mathbb{Z}_x, n \in \mathbb{Z}_z} C_{2m,n} Y_{m,n} C_{2m,n}^* \right)^{-1}. \end{aligned} \quad (\text{3.13})$$

This system of equations is nonlinear in the unknown matrices $X_{m,n}$, $Y_{m,n}$, and F . Moreover, as seen from the last condition in Eq. (3.13), the structural constraints on F introduce coupling between all wavenumbers; this is in contrast to the unstructured optimal control problem given by Eq. (3.11).

Next, we describe the algorithm that is employed for solving Eq. (3.13) [69]:

Descent method for solving Eq. (3.13):

given stabilizing F^0 that satisfies the structural constraints imposed by S ,

for $i = 0, 1, 2, \dots$, **do**:

- (1) compute descent direction \tilde{F}^i ;
- (2) determine step-size q^i ;
- (3) update $F^{i+1} = F^i + q^i \tilde{F}^i$;

until the stopping criterion $\|\nabla J(F^i)\|_F < \epsilon$ is achieved, where $\|\cdot\|_F$ denotes the Frobenius norm and ϵ is the convergence tolerance.

We consider the gradient descent direction that provides linear rate of convergence to the local minimum. More sophisticated descent directions, such as Newton or quasi-Newton directions, provide faster convergence at the expense of increased computational

cost; for example, see [69]. The gradient direction is given by $\tilde{F}^i = -\nabla J(F^i)$ where $\nabla J(F^i)$ is determined from [69]

$$\nabla J(F^i) = \frac{2}{N_x N_z} \sum_{m \in \mathbb{Z}_x, n \in \mathbb{Z}_z} (r F C_{2m,n} - B_{2m,n}^* X_{m,n}) Y_{m,n} C_{2m,n}^*.$$

For the step-size rule, the backtracking line search [120] is used where in addition to guaranteeing descent of the performance index, we also guarantee the stability of the updated closed-loop system. Namely, we repeat $q^i = \beta q^i$ ($0 < \beta < 1$) until both of the following conditions are satisfied:

- (a) descent: $J(F^i + q^i \tilde{F}^i) < J(F^i) + \alpha q^i \sum_{m,n} (\nabla J(F^i))^T \tilde{F}^i$ with $0 < \alpha < 0.5$;
- (b) closed-loop stability: $A_{m,n} - B_{2m,n} F C_{2m,n}$ is stable for all $m \in \mathbb{Z}_x$ and $n \in \mathbb{Z}_z$.

3.3 Localized control of transition

As discussed in § 3.1, the problem of controlling the onset of turbulence is formulated as the receptivity (i.e., the \mathcal{H}_2 norm) reduction problem. Therefore, to assess the effectiveness of feedback controllers, we compare the receptivity of controlled flows to the receptivity of flow with no control. We consider the stochastically forced linearized NS equations in the subcritical regime where the flow with no control is linearly stable. The energy density of fluctuations in the presence of stochastic forcing is used to quantify the flow receptivity. The zero-mean stochastic forcing which is white in time and y , and purely harmonic in horizontal directions, yields a nonzero steady-state variance of velocity fluctuations $E(\kappa_m, \kappa_n)$ [27]. For any $m \in \mathbb{Z}_x$ and $n \in \mathbb{Z}_z$, this quantity can be obtained from

$$\begin{aligned} E(\kappa_m, \kappa_n) &= \text{trace} (Z_{m,n} Q_{Bm,n}), \\ (A_{m,n} - B_{2m,n} F C_{2m,n})^* Z_{m,n} + Z_{m,n} (A_{m,n} - B_{2m,n} F C_{2m,n}) &= -Q_{Cm,n}. \end{aligned} \quad (3.14)$$

For the flow with no control (i.e., for $F = 0$), the streamwise-constant fluctuations are the most amplified by the linearized dynamics [7, 27, 28]. These fluctuations correspond to the streamwise streaks that are ubiquitous in wall-bounded shear flows. The large amplification of streaks is physically associated with the vortex-tilting (lift-up) mechanism that arises from the non-normal coupling between dynamics of the wall-normal velocity and vorticity fluctuations [24, 26]. This non-normal coupling is also responsible for the pseudo-resonance phenomenon [25, 64] where large amplification of harmonic disturbances, which are not associated with eigenvalues of the linearized model, is obtained. On the other hand, the least stable modes of the uncontrolled flow, i.e., the Tollmien-Schlichting (TS) waves, are much less amplified than the streamwise streaks. This highlights the importance of amplification of the streamwise constant fluctuations

in the early stages of transition. Therefore, a control strategy that is capable of reducing the receptivity of streamwise streaks to stochastic disturbances represents a viable approach for controlling the onset of turbulence.

3.3.1 Receptivity of the controlled flows

For the controlled flows, we consider three state-feedback gains: (a) the centralized gains determined by Eq. (3.12); (b) the truncated gains obtained by enforcing the structural constraints by spatial truncation of the centralized feedback gains; and (c) the localized optimal gain F that is designed using the method presented in § 3.2.1. For the truncated and localized controllers, we consider the case where each actuator uses information from only its nearest neighbors (for an illustration, see Figure 3.2).

Figure 3.3 compares the energy amplification of the controlled flows with $R_c = 2000$ and the flow with no control for different horizontal wavenumbers. The optimal centralized controller significantly reduces flow receptivity for all wavenumbers. Compared with the flow with no control, an 89% reduction in amplification of the most energetic structures (i.e., streaks) is achieved (cf. peak values in Figure 3.3(a)).

Next, we look at the flows that are controlled by the truncated centralized and localized optimal feedback gains. Figures 3.3(b) and 3.3(c) illustrate that truncated centralized gains introduce instability at small streamwise wavenumbers. The numerical simulations of § 3.3.2 confirm that the flow controlled with these gains diverges from the laminar profile and becomes turbulent. In addition, for the stable wavenumbers, Figure 3.3 shows that the variance amplification of the truncated centralized controller is much larger than that of the centralized controller. This justifies the need for designing localized optimal controllers that satisfy the structural constraints and exhibit similar performance to that of the centralized controller.

In order to obtain the localized optimal gains, we have used the truncated centralized gains to initialize the iterative scheme described in § 3.2.1. Although the truncated gains are not stabilizing, it turns out that the initial gradient direction can be used to obtain stabilizing structured gains. We are currently also developing algorithms based on the augmented Lagrangian method [69] that does not require stabilizing gains for the initial iteration.

Figure 3.3 shows that the localized optimal gains maintain stability for all wavenumbers. In addition, the variance amplification of the localized controller is similar to that of the centralized controller. In particular, Figure 3.3(a) shows that amplification of the most energetic modes is almost the same for localized optimal and centralized controllers. Therefore, the properly designed localized controller is a good candidate for controlling the onset of turbulence, as verified in direct numerical simulations of § 3.3.2.

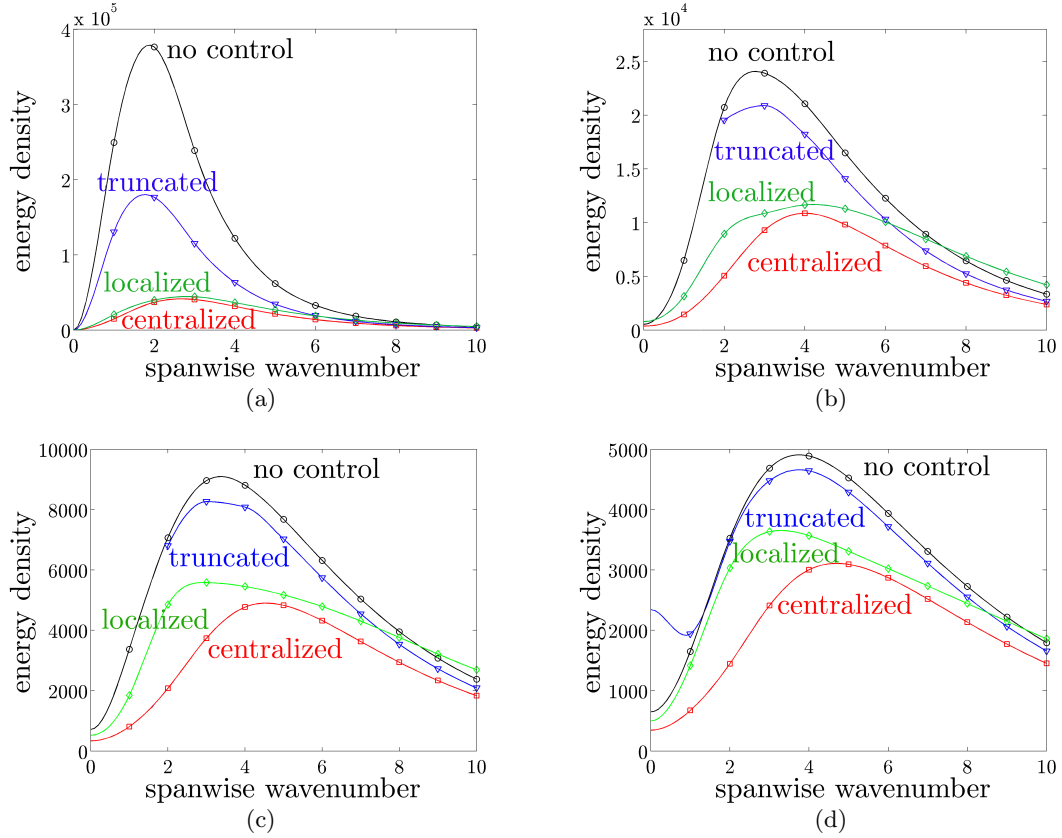


Figure 3.3: Energy density of the velocity fluctuations $E(\kappa_n)$ for the uncontrolled flow with $R_c = 2000$ (\circ), optimal centralized (\square), truncated centralized (∇), and localized optimal (\diamond) controllers for (a) $\kappa_m = 0$; (b) $\kappa_m = 0.5$; (c) $\kappa_m = 1$; and (d) $\kappa_m = 1.5$. The truncated controller is unstable for $\kappa_m = \{0.5, 1\}$ and $\kappa_n = \{0, 1\}$ and the energy density is not defined for any combination of these wavenumbers. Note: The energy density is computed at the discrete set of wavenumbers κ_n and κ_m (symbols) and the lines are plotted for visual aid.

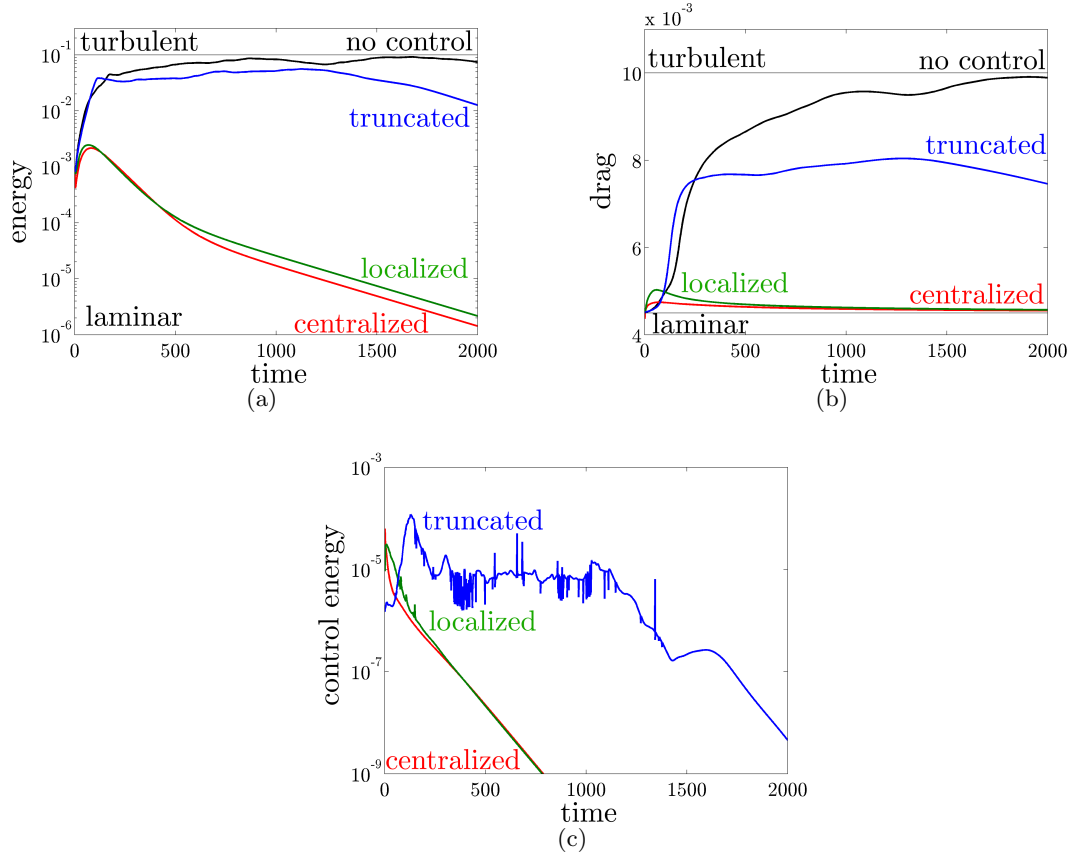


Figure 3.4: (a) Energy of the velocity fluctuations $E(t)$; (b) skin-friction drag coefficient $C_f(t)$; and (c) control energy $(v_u^2(t) + v_l^2(t))/2$ for the flow with no control, and optimal centralized, truncated centralized, and localized optimal controllers. The results are obtained using DNS with $R_c = 2000$.

3.3.2 Direct numerical simulations

We simulate a channel flow with $R_c = 2000$ that is driven by a constant pressure gradient and is subject to actuation in the form of blowing and suction at the walls. This value of R_c is smaller than the Reynolds number at which linear instability occurs ($R_c = 5772$) and larger than the value for which transition usually takes place in experiments and DNS ($R_c \approx 1000$). The fully nonlinear NS equations are discretized with spectral accuracy using Fourier modes in horizontal directions and Chebyshev polynomials in y , as described in § 3.1.2. The lengths of the computational box in units of the channel half-height δ are $L_x = 4\pi$ and $L_z = 2\pi$, with $N_x \times N_y \times N_z = 52 \times 97 \times 42$ points in x , y , and z directions (after dealiasing in x and z). In our study, 42 collocation points in y were enough for computing convergent feedback gains. These gains are then interpolated and scaled to determine the feedback gains for 97 Chebyshev collocation points.

The flow is initialized with a perturbation that is capable of driving the uncontrolled flow to turbulence. For the optimal centralized, truncated optimal centralized, and localized optimal feedback gains, we evaluate the energy of velocity fluctuations $E(t)$ around the laminar parabolic profile and the skin-friction drag coefficient $C_f(t)$.

Figure 3.4(a) shows $E(t)$ for the controlled flows and the flow with no control. Compared with its initial value, the energy of three-dimensional fluctuations in the uncontrolled flow is increased by approximately two orders of magnitude, resulting in divergence from the laminar parabolic profile. On the other hand, the optimal centralized controller provides decay of fluctuations' energy to zero after a small transient growth. Our results agree with the study of [56] where it was shown that the optimal centralized controller is capable of preventing transition. The truncated centralized controller introduces faster growth of $E(t)$ relative to the flow with no control, thereby promoting divergence from the laminar flow. On the other hand, Figure 3.4(a) shows that the localized optimal controller is capable of maintaining the laminar flow by providing performance comparable to that of the optimal centralized controller.

Figure 3.4(b) shows the skin-friction drag coefficient $C_f(t)$. We see that the drag coefficients of the optimal centralized and localized controllers are equal to 4.5×10^{-3} , which corresponds to the drag coefficient of the laminar flow. On the other hand, the drag coefficient of the uncontrolled flow is 10^{-2} , which is a clear indicator of a fully developed turbulent flow. The drag coefficient of the truncated centralized controller is approximately 7.5×10^{-3} . This suggests that although the truncated gains cannot maintain the laminar flow, they achieve 16% reduction in drag relative to the uncontrolled turbulent flow.

Figure 3.4(c) shows the control effort which is quantified by the kinetic energy of blowing and suction at the walls $(v_u^2(t) + v_l^2(t))/2$. We see that the control effort in the centralized and localized controllers decays to zero, implying that both controllers reject the initial disturbance and maintain the laminar flow. On the other hand, the control effort in the truncated centralized controller remains large and it only goes down after

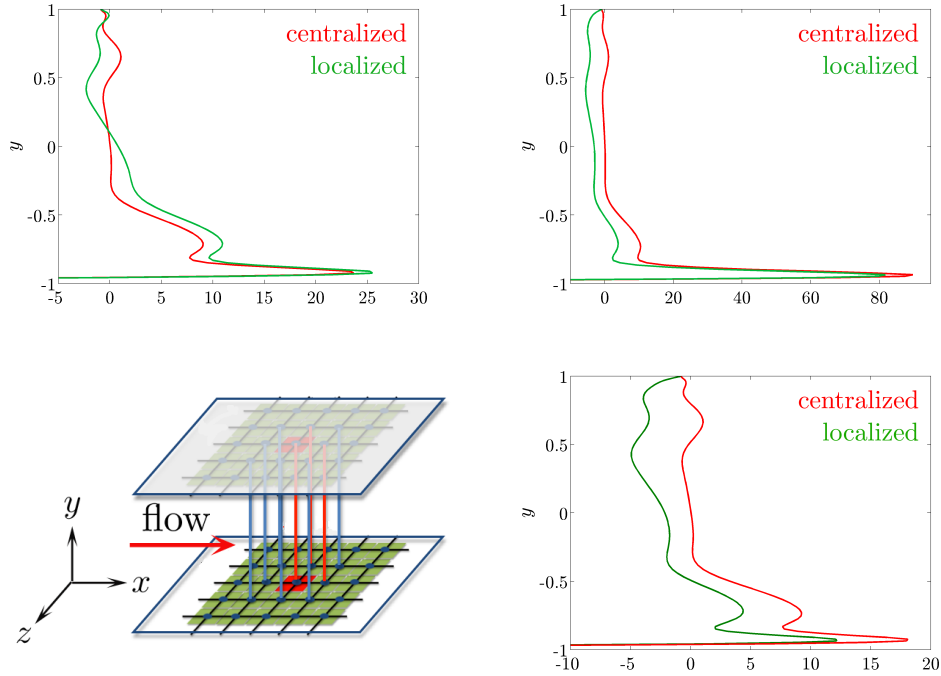


Figure 3.5: The optimal centralized and localized optimal feedback gains used by the actuator at the lower wall placed at $(r, s) = (0, 0)$, from the wall-normal velocity information at locations (a) $(r, s) = (0, -1)$; (b) $(r, s) = (0, 0)$; and (d) $(r, s) = (-1, 0)$. The results are obtained for the flow with $R_c = 2000$.

the lifetime of turbulence due to the initial disturbance ends. Note that the total control effort in the localized controller is larger than the centralized controller. This means that the actuators in the localized controller should work harder to compensate for the lack of flow information from far away sensors. The optimal centralized and localized optimal feedback gains used by the actuator at the lower wall, from its own wall-normal velocity information and the wall-normal velocity at its lateral neighbor and at its front neighbor are compared in Figure 3.5. We see that relative to the centralized controller, the localized controller pays less attention to its own flow information and that in its front, but it pays more attention to the flow information that is coming from its lateral neighbor.

3.4 Summary

We consider design of localized optimal flow controllers for preventing transition to turbulence. We formulate an optimal control problem for minimizing the flow receptivity and control effort. In addition, structural constraints are imposed on the feedback gains such that only the gains that are associated with the nearest neighbors are nonzero. This problem is solved using recently developed techniques for optimal design of state-feedback controllers with structural constraints. We show that spatial truncation of the optimal centralized gains can introduce flow instability. Therefore, the truncated feedback gains may not be suitable for controlling transition, and they may even promote turbulence in the situations where the uncontrolled flow stays laminar. On the other hand, we demonstrate that the localized optimal controller can exhibit receptivity reduction similar to that of the optimal centralized controller. Furthermore, our simulations of the nonlinear flow dynamics show that transition can be prevented using localized optimal gains.

Chapter 4

Model-based design of transverse wall oscillations for turbulent drag reduction

Turbulent flows are ubiquitous in nature and engineering. Dissipation of kinetic energy by turbulent flow around airplanes, ships, and submarines increases resistance to their motion. This motivates design of control strategies for enhancing performance of vehicles and other systems involving turbulent flows. Utility of different approaches for maintaining the laminar flow, reducing skin-friction drag, and preventing separation is surveyed in [11, 13]. While traditional flow control techniques combine physical intuition with costly numerical simulations and experiments, model-based techniques utilize developments from control theory to improve flow manipulation. Recent research suggests that traditional strategies can be significantly enhanced by flow control design based on analytical models and optimization tools [42].

The effectiveness of model-based feedback [56, 57] and sensor-less [115, 116] techniques for controlling the onset of turbulence at low Reynolds numbers stems from their ability to reduce receptivity and enhance robustness of the flow. Model-based approach to flow control design has been motivated by realization that a mechanism which initiates transition is governed by the degradation of robustness [25, 64] and the consequential noise amplification [7, 27, 28]. Consequently, the above mentioned techniques have utilized Navier-Stokes (NS) equations linearized around the laminar flow as a control-oriented model with the objective of reducing sensitivity to modeling imperfections.

While most model-based efforts to date have considered the problem of maintaining the laminar flow, in this chapter we show that turbulence modeling in conjunction with judiciously selected linearization can extend utility of these methods to control of turbulent flows. Control-oriented turbulence modeling is challenging because of complex flow physics that arises from intricate interactions between the turbulent fluctuations

and the mean velocity. We build on recent research that demonstrates considerable predictive power of linearized analysis even in turbulent flows [73–75]. These papers have shown that the equations linearized around turbulent mean velocity, with molecular viscosity augmented by turbulent viscosity, qualitatively capture features of turbulent flows with no control. For the flow with control, we examine the class of linearized models considered by [73–75] and use turbulent viscosity hypothesis to quantify the influence of turbulent fluctuations on the mean velocity.

The difficulty here arises from the fact that the turbulent viscosity of the flow with control has to be determined. Even though we use the k - ϵ model to capture the influence of control on turbulent viscosity, in contrast to current practice we do not rely on numerical simulations for finding kinetic energy k and its rate of dissipation ϵ . Instead, we introduce a simulation-free method based on stochastically-forced linearized model of controlled flow to obtain k and ϵ from the second-order statistics of velocity fluctuations. These statistics are used to determine the turbulent viscosity for the flow with control, and thereby to compute the effect of control on the turbulent mean velocity and on the skin-friction drag. We utilize linearized equations subject to white-in-time stochastic forcing with appropriately selected second-order spatial statistics. Using analogy with homogenous isotropic turbulence [121], we select these to be proportional to the two-dimensional energy spectrum of the flow with no control. Note that while our approach takes advantage of the turbulent viscosity and the energy spectrum resulting from direct numerical simulations (DNS) of the uncontrolled flow [1, 2, 122, 123], *we do not rely on numerical or experimental data for determining the effect of control on the turbulent flow.*

Several experimental and numerical studies have shown the effectiveness of sensorless strategies for turbulence suppression in wall-bounded shear flows. The experiments of [124] and DNS of [125] showed that imposing a constant transverse strain on a turbulent boundary-layer can *transiently* reduce the turbulent kinetic energy and the Reynolds stresses. Motivated by this observation, [126] used DNS to establish a *sustained* turbulence suppression in a channel flow subject to transverse wall oscillations. For the flow with friction Reynolds number $R_\tau = 200$, skin-friction drag reduction of up to 40% was reported with maximum drag reduction taking place for the period of oscillations $T^+ \approx 100$ (in viscous time units). The numerical results of [126] were experimentally verified by [127–130], where a drag reduction of up to 45% was reported. It was argued that wall oscillations induce negative spanwise vorticity, thereby suppressing turbulence by hampering the vortex stretching mechanism [129]. In addition, the experiments of [130] showed that the near-wall flow is dragged laterally by wall oscillations which reduces the length of the streaks and increases the spacing between them.

Several alternative mechanisms for inducing transverse oscillations have also been investigated. For example, [131] used DNS of conductive fluids in a channel flow with $R_\tau = 100$ to show that time-periodic spanwise Lorentz force can reduce skin-friction drag up to 40%. The amount of drag reduction was found to decrease for larger R_τ . In

addition, [132, 133] studied the effect of Lorentz force in the form of spanwise traveling waves confined to the viscous sub-layer. For $R_\tau = 150$, their DNS showed a drag reduction of up to 30%. The drag-reducing mechanisms of transverse motions induced by spanwise oscillations, spanwise traveling waves, and riblets have been surveyed by [49]. Recently, turbulent drag reduction by waves of spanwise velocity that travel in the streamwise direction has been examined using DNS [134], experiments [135], and generalized Stokes layer theory [136]. It was shown that upstream traveling waves reduce drag at any speed. On the other hand, downstream waves reduce drag only at speeds that are much larger or much smaller than the convecting speed of near-wall turbulent structures.

Using DNS, it was shown that up to 40% of drag reduction can be achieved by oscillating a cylindrical pipe along its longitudinal axis [137]. In a series of papers, [9, 138–140] further studied drag reduction by transverse wall oscillations in channel flows. In addition to quantifying the saved power associated with drag reduction, they accounted for the input power necessary for maintaining wall oscillations; for small oscillation amplitudes, it was established that a net power gain with drag reduction of up to 10% can be achieved.

In contrast to the aforementioned studies, we use a model-based approach to examine the effect of transverse wall oscillations on the dynamics of a turbulent channel flow. We first show that the power necessary for maintaining wall oscillations increases quadratically with their amplitude, which is in agreement with DNS of [9]. This suggests that large control amplitudes may yield poor net efficiency. We thus confine our study to small oscillation amplitudes and use perturbation analysis (in the amplitude of oscillations) to identify the period of oscillations that achieves largest drag reduction in a computationally efficient manner. In addition, we quantify the net efficiency, discuss the drag reduction mechanisms, and compare the dominant structures in flows with and without control. The close agreement between our results and the results obtained in experiments and DNS [9, 126, 129, 138] demonstrates the predictive power of our model-based approach to flow control design.

Our presentation is organized as follows: in § 4.1, we formulate the problem and provide a brief overview of the governing equations, turbulent mean velocity, skin-friction drag coefficient, net efficiency, and the k - ϵ model. In § 4.2, we use judiciously selected stochastically forced linearized model to study the dynamics of infinitesimal fluctuations around the turbulent base flow. We also describe an efficient method for computing the second-order statistics of fluctuations. These statistics are used to determine the influence of control on turbulent viscosity. In § 4.3, we apply our theoretical developments to the problem of turbulent drag reduction with transverse wall oscillations, and provide a thorough analysis of the effect of control on skin-friction drag and net efficiency. In § 4.4, we use characteristic eddy decomposition to visualize the effect of control on turbulent flow structures. We conclude with a brief summary of our contributions and outlook for future research in § 4.5.

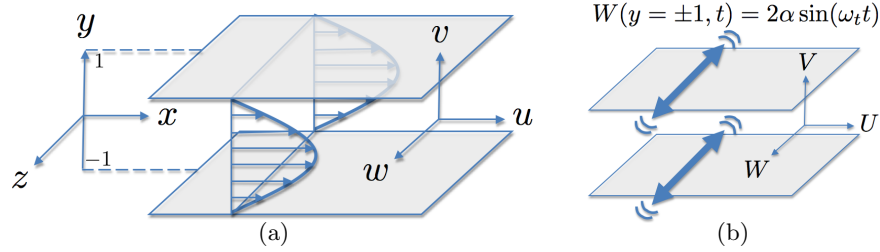


Figure 4.1: (a) Pressure driven channel flow; and (b) Channel flow subject to transverse wall oscillations.

4.1 Problem formulation

The pressure-driven channel flow of incompressible Newtonian fluids, with geometry shown in Figure 4.1(a), is governed by the non-dimensional NS and continuity equations

$$\begin{aligned} \mathbf{u}_t &= -(\mathbf{u} \cdot \nabla)\mathbf{u} - \nabla P + (1/R_\tau) \Delta \mathbf{u}, \\ 0 &= \nabla \cdot \mathbf{u}, \end{aligned} \quad (4.1)$$

where \mathbf{u} is the velocity, P is the pressure, ∇ is the gradient, and $\Delta = \nabla \cdot \nabla$ is the Laplacian. The Reynolds number $R_\tau = u_\tau h / \nu$ is defined in terms of the channel's half-height h and the friction velocity $u_\tau = \sqrt{\tau_w / \rho}$, (x, y, z) are the streamwise, wall-normal, and spanwise coordinates, and t is time. Here, τ_w is the wall-shear stress, ρ is fluid density, and ν is kinematic viscosity. In (4.1), spatial coordinates are non-dimensionalized by h , velocity by u_τ , time by h/u_τ , and pressure by ρu_τ^2 . When normalized by ν/u_τ , the wall-normal coordinate is denoted $y^+ = R_\tau(1 + y)$. The subscripts are used to denote the spatial and temporal derivatives, e.g., $\mathbf{u}_t = \partial \mathbf{u} / \partial t = \partial_t \mathbf{u}$.

Throughout this chapter we assume that the bulk flux, which is obtained by integrating the streamwise velocity over spatial coordinates, remains constant. This constraint is commonly imposed in experiments and DNS of turbulent flows and it can be satisfied by adjusting the uniform streamwise pressure gradient P_x . In addition to the driving pressure gradient, which balances the wall-shear stress $P_x = -\tau_w$ [70], the flow is also subject to zero-mean transverse wall oscillations of amplitude α and frequency ω_t ; see Figure 4.1(b). The period of oscillations normalized by h/u_τ (outer units) is given by $T = 2\pi/\omega_t$, which is equivalent to $T^+ = R_\tau T$ when normalized by ν/u_τ^2 (viscous units). The streamwise and wall-normal velocities satisfy no-slip and no-penetration boundary conditions at the walls.

The velocity in a turbulent flow can be decomposed into the sum of the turbulent mean velocity, $\mathbf{U} = [U \ V \ W]^T$, and the fluctuations around \mathbf{U} , $\mathbf{v} = [u \ v \ w]^T$, $\{\mathbf{u} = \mathbf{U} + \mathbf{v}, \mathbf{U} = \mathcal{E}(\mathbf{u}), \mathcal{E}(\mathbf{v}) = 0\}$, where $\mathcal{E}(\cdot)$ is the expectation operator. This

yields the Reynolds-averaged NS equations (RANS) for \mathbf{U} [70–72],

$$\begin{aligned}\mathbf{U}_t &= -(\mathbf{U} \cdot \nabla) \mathbf{U} - \nabla \mathcal{E}(P) + (1/R_\tau) \Delta \mathbf{U} - \nabla \cdot \mathcal{E}(\mathbf{v}\mathbf{v}^T), \\ 0 &= \nabla \cdot \mathbf{U}.\end{aligned}\tag{4.2}$$

Comparison of (4.2) and (4.1) shows that the second-order statistics of fluctuations $\mathcal{E}(\mathbf{v}\mathbf{v}^T)$, i.e., the Reynolds stresses, introduce additional flux in a turbulent flow. The Reynolds stress tensor quantifies the transport of momentum arising from turbulent fluctuations and it has profound influence on the mean velocity, and thereby on skin-friction drag [70]. The difficulty in determining statistics of fluctuations arises from the nonlinearity in the NS equations which makes the n th velocity moment depend on the $(n + 1)$ th moment [70].

4.1.1 Turbulent mean velocity

The steady-state solution of (4.2) subject to a uniform pressure gradient, $P_x = -\tau_w$, and the transverse wall oscillations,

$$W(y = \pm 1, t) = 2\alpha \sin(\omega_t t),$$

is determined by $[U(y) \ 0 \ W(y, t)]^T$. It can be shown that U arises from the uniform pressure gradient, while W is induced by the wall oscillations,

$$\begin{cases} 0 = (1/R_\tau) U'' - [\mathcal{E}(\overline{uv})]' + \tau_w, \\ U(y = \pm 1) = 0, \end{cases}\tag{4.3a}$$

$$\begin{cases} W_t = (1/R_\tau) W'' - [\mathcal{E}(\overline{vw})]', \\ W(y = \pm 1, t) = 2\alpha \sin(\omega_t t). \end{cases}\tag{4.3b}$$

Here, overline denotes averaging over x and z , and prime represents differentiation with respect to y . The closure problem can be overcome by expressing the higher order unknown moments in terms of the lower-order known moments. According to the turbulent viscosity hypothesis [70–72], the turbulent momentum is transported in the direction of the mean rate of strain,

$$\mathcal{E}(\overline{\mathbf{v}\mathbf{v}^T}) = (2/3) k I - (\nu_T/R_\tau) (\nabla \mathbf{U} + (\nabla \mathbf{U})^T),\tag{4.4}$$

where $k(y) = (1/2)\mathcal{E}(\overline{uu} + \overline{vv} + \overline{ww})$ is the turbulent kinetic energy, $\nu_T(y)$ is the turbulent viscosity normalized by ν , and I is the identity operator. From (4.4), we see that

$$\mathcal{E}(\overline{uv}) = -(\nu_T/R_\tau) U', \quad \mathcal{E}(\overline{vw}) = -(\nu_T/R_\tau) W',$$

which upon substitution to (4.3) yields

$$\begin{cases} 0 = (1 + \nu_T) U'' + \nu_T' U' + R_\tau \tau_w, \\ U(y = \pm 1) = 0, \end{cases} \quad (4.5a)$$

$$\begin{cases} R_\tau W_t = (1 + \nu_T) W'' + \nu_T' W', \\ W(y = \pm 1, t) = 2\alpha \sin(\omega_t t). \end{cases} \quad (4.5b)$$

where $(1 + \nu_T)$ represents an effective viscosity that accounts for both molecular and turbulent dissipation [72].

For given turbulent viscosity ν_T and driving pressure gradient $P_x = -\tau_w$, (4.5) is an uncoupled system of equations for U and W ; U can be obtained by solving (4.5a),

$$U(y) = -R_\tau \tau_w \int_{-1}^y \frac{\xi}{1 + \nu_T(\xi)} d\xi, \quad (4.6)$$

and W can be obtained by solving (4.5b). In particular, the spanwise velocity W is periodic in time

$$W(y, t) = \alpha (W_p(y) e^{i\omega_t t} + W_m(y) e^{-i\omega_t t}), \quad (4.7)$$

where $i = \sqrt{-1}$, and $W_m = W_p^*$, with $*$ denoting the complex conjugate. An equation for W_p is obtained by substituting (4.7) in (4.5b)

$$\begin{aligned} i R_\tau \omega_t W_p &= (1 + \nu_T) W_p'' + \nu_T' W_p', \\ W_p(\pm 1) &= -i. \end{aligned} \quad (4.8)$$

The difficulty in determining U and W from (4.5) arises from the fact that ν_T depends on the fluctuations around the turbulent mean velocity, and thus it is not known a priori. A significant body of work has been devoted to finding an expression for ν_T that yields the turbulent mean velocity in the uncontrolled flow [141–143]. [143] extended the turbulent viscosity model, originally introduced by [142], from the pipe flow to the channel flow,

$$\nu_{T0}(y) = \frac{1}{2} \left(\left(1 + \left(\frac{c_2}{3} R_\tau (1 - y^2) (1 + 2y^2) (1 - e^{-(1-|y|) R_\tau / c_1}) \right)^2 \right)^{1/2} - 1 \right). \quad (4.9)$$

This expression employs the law of the wall in conjunction with van Driest's damping function and Reichardt's middle law [143]. The parameters c_1 and c_2 appear in the van Driest's wall law and in the von Kármán's log law [72], respectively. These two parameters are selected to minimize least squares deviation between the mean streamwise velocity (4.6) obtained with $\tau_w = 1$ and turbulent viscosity (4.9), and the mean streamwise velocity obtained in experiments and simulations. Application of this procedure yields $\{R_\tau = 186, c_1 = 0.61, c_2 = 46.2; R_\tau = 547, c_1 = 0.455, c_2 = 29.4; R_\tau =$

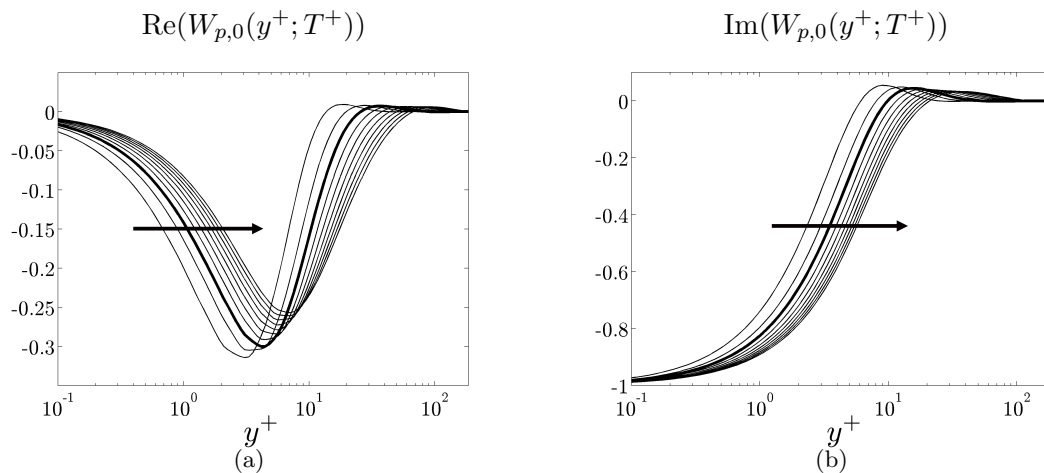


Figure 4.2: (a) The real part; and (b) the imaginary part of the solution $W_{p,0}(y^+; T^+)$ to system (4.8)-(4.9) with $R_\tau = 186$ and $30 \leq T^+ \leq 300$. T^+ increases in the direction of the arrows.

934, $c_1 = 0.43$, $c_2 = 27$] for the corresponding mean velocities in a turbulent channel flow obtained using DNS [1, 2].

Under the assumption that the turbulent viscosity (4.9) captures interactions of fluctuations with background turbulence, the system of equations (4.5)-(4.9) yields a solution $\mathbf{U}_0 = [U_0(y) \ 0 \ W_0(y, t)]^T$. By construction, U_0 approximates the mean streamwise velocity in the uncontrolled turbulent flow, and W_0 is the spanwise velocity induced by the wall oscillations obtained under the assumption that the turbulent viscosity is not modified by control. Figure 4.2 shows that the solution $W_{p,0}(y^+; T^+)$ of the system (4.8)-(4.9) with $R_\tau = 186$ and $30 \leq T^+ \leq 300$ is localized in the viscous wall region, $y^+ < 50$. In addition, as expected from the analogy to the solution of the Stokes second problem (for example, see [144]), $W_{p,0}$ shifts away from the wall as T^+ increases.

As shown above, if the turbulent viscosity of the flow with no control ν_{T0} is used to model ν_T , the oscillations induce W_0 but have no impact on U_0 (which, in this case, arises only from the uniform pressure gradient). The implications of this assumption for determining the skin-friction drag coefficient and the control net efficiency are discussed in § 4.1.2.

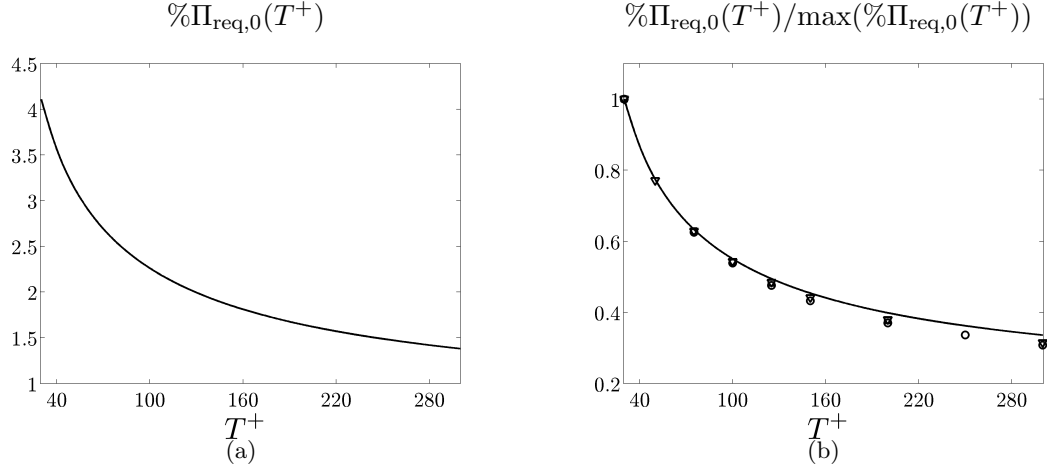


Figure 4.3: (a) The required power, $\% \Pi_{\text{req},0}(T^+)$, as a function of the period of oscillations T^+ for the flow with $R_\tau = 186$; (b) Comparison between $\% \Pi_{\text{req},0}(T^+)$ (solid curve) and $\% \Pi_{\text{req}}(T^+)$ (symbols). Symbols show DNS data at $R_\tau = 200$ [9] for control amplitudes $\alpha = 2.25$, \circ ; $\alpha = 6$, \square ; and $\alpha = 9$, ∇ . The results in (b) are normalized by their largest values.

4.1.2 Skin-friction drag coefficient and net efficiency

As mentioned in § 4.1, the pressure gradient $P_x = -\tau_w$ has to be adjusted in order to maintain the constant bulk flux,

$$U_B = \frac{1}{2} \int_{-1}^1 U(y) dy.$$

Since the skin-friction drag coefficient is proportional to τ_w and inversely proportional to U_B^2 [70, 144],

$$C_f = 2\tau_w/U_B^2,$$

for the flow with constant U_B , reduction (increase) in wall-shear stress τ_w induces drag reduction (increase). The change in the skin-friction coefficient relative to the flow with no control is given by

$$\%C_f = 100 \frac{C_{f,u} - C_{f,c}}{C_{f,u}} = 100(1 - \tau_{w,c}), \quad (4.10)$$

where the subscripts u and c denote the quantities in the uncontrolled and controlled flows, respectively. Thus, the control leads to drag reduction when $\tau_{w,c} < 1$.

The drag reduction induces saving in power (per unit area of the channel surface

and normalized by ρu_τ^2) [83]

$$\Pi_{\text{save}} = 2U_B(1 - \tau_{w,c}).$$

Compared to the power required to drive the flow with no control, $\Pi_u = 2U_B$, the saved power is determined by the relative change in the skin-friction coefficient,

$$\% \Pi_{\text{save}} = 100 \frac{\Pi_{\text{save}}}{2U_B} = 100(1 - \tau_{w,c}) = \% C_f.$$

On the other hand, the wall oscillations require an input power to balance the spanwise shear stresses at the walls. The required power over one period T per unit area of the channel walls is determined by [83]

$$\Pi_{\text{req}} = \frac{1}{T} \int_0^T (W(y,t) \tau_{23}(y,t)) dt \Big|_{y=1} - \frac{1}{T} \int_0^T (W(y,t) \tau_{23}(y,t)) dt \Big|_{y=-1},$$

where $\tau_{23}(y,t) = \rho\nu W'(y,t)$ denotes the spanwise shear stress. An equation for Π_{req} (normalized by ρu_τ^2) can be obtained by substituting for $W(y,t)$ from (4.7) and using $W_p(y = \pm 1) = -i$,

$$\Pi_{\text{req}} = \frac{2\alpha^2}{R_\tau} \text{Im} \left(W'_p \Big|_{y=-1} - W'_p \Big|_{y=1} \right).$$

The required power exerted by wall oscillations expressed in fraction of the power necessary to drive the uncontrolled flow is given by

$$\% \Pi_{\text{req}} = 100 \frac{\alpha^2}{R_\tau U_B} \text{Im} \left(W'_p \Big|_{y=-1} - W'_p \Big|_{y=1} \right), \quad (4.11)$$

where $\text{Im}(\cdot)$ denotes the imaginary part of a complex number. The net efficiency of control is quantified by the difference of the saved and required powers

$$\% \Pi_{\text{net}} = \% \Pi_{\text{save}} - \% \Pi_{\text{req}}.$$

Since the net efficiency is obtained from U and W , determining the turbulent mean velocities is essential for assessing the efficiency of wall oscillations. For the spanwise mean velocity W_0 determined in § 4.1.1, the required power grows quadratically with α , $\% \Pi_{\text{req}} = \alpha^2 \% \Pi_{\text{req},0}$,

$$\% \Pi_{\text{req},0} = 100 \frac{1}{R_\tau U_B} \text{Im} \left(W'_{p,0} \Big|_{y=-1} - W'_{p,0} \Big|_{y=1} \right). \quad (4.12)$$

Figure 4.3(a) shows that $\% \Pi_{\text{req},0}(T^+)$ decreases monotonically with T^+ , and Figure 4.3(b) demonstrates close correspondence between $\% \Pi_{\text{req},0}$ (solid curve) and the DNS results

of [9] (symbols).

The apparent lack of influence of the wall movements on U_0 , observed in § 4.1.1, is at odds with experiments and simulations that have shown that properly designed oscillations can reduce drag by as much as 40% [9, 126–129, 138, 139]. Thus, model-based control of turbulent flows requires thorough examination of the influence of control on ν_T . For spanwise wall oscillations we address this problem in § 4.2.2.

4.1.3 The k - ϵ model for ν_T

Direct numerical simulations can be used to study the effect of control on turbulent flows. However, resolving all scales of motion at large Reynolds numbers may be prohibitively expensive, which motivates use of the Reynolds-averaged equations in conjunction with turbulence modeling. The challenge here is to establish a relation between ν_T and the second-order statistics of velocity fluctuations. The most widely used method for computing ν_T in engineering flows is the k - ϵ model [145, 146],

$$\nu_T = c R_\tau^2 \frac{k^2}{\epsilon}, \quad (4.13)$$

where k is the turbulent kinetic energy, ϵ is its rate of dissipation, and $c = 0.09$ is a model constant. Both k and ϵ are determined by the second-order statistics of fluctuations,

$$\begin{aligned} k(y) &= (1/2) \mathcal{E} (\overline{u u} + \overline{v v} + \overline{w w}), \\ \epsilon(y) &= \mathcal{E} \left(2 (\overline{u_x u_x} + \overline{v_y v_y} + \overline{w_z w_z} + \overline{u_y v_x} + \overline{u_z w_x} + \overline{v_z w_y}) + \right. \\ &\quad \left. \overline{u_y u_y} + \overline{w_y w_y} + \overline{v_x v_x} + \overline{w_x w_x} + \overline{u_z u_z} + \overline{v_z v_z} \right). \end{aligned} \quad (4.14)$$

and they are updated by solving two transport equations [72]. Even though these are less complex than the NS equations, they are still computationally expensive, and *not convenient for control design and optimization*. In § 4.2, we instead develop a simulation-free method, which is computationally efficient and amenable to control design, for determining the effect of fluctuations on ν_T in the flow with control.

4.2 Stochastically forced flow with control

Since ν_T in the k - ϵ model (4.13) is determined by the second-order statistics of velocity fluctuations, we use *stochastically forced linearized NS equations* to compute k and ϵ in the flow with control. Here, we utilize the fact that the second-order statistics of linear time-periodic systems can be obtained from the solution of the corresponding Lyapunov equation [89]. It is well-known that the analysis of the steady-state variance of infinitesimal fluctuations around the laminar flow can be used to identify flow structures that initiate the onset of turbulence [7, 27, 28]. In this chapter, we show that judiciously selected linearization of the turbulent flow with control can be used to determine turbulent

viscosity in a computationally efficient way.

Next, we examine the effect of control on small-amplitude fluctuations around $\mathbf{U}_0 = [U_0(y) \ 0 \ W_0(y, t)]^T$. The turbulent mean velocity \mathbf{U}_0 is obtained by solving (4.5) under the assumption that the turbulent viscosity (4.9) captures interactions of fluctuations with background turbulence. An equivalent expression for \mathbf{U}_0 can be found from the steady-state solution of the modified NS equations subject to wall-oscillations,

$$\begin{aligned} \mathbf{u}_t &= -(\mathbf{u} \cdot \nabla) \mathbf{u} - \nabla P + (1/R_\tau) \nabla \cdot ((1 + \nu_{T0}) (\nabla \mathbf{u} + (\nabla \mathbf{u})^T)), \\ 0 &= \nabla \cdot \mathbf{u}. \end{aligned} \quad (4.15)$$

Model (4.15) is obtained by augmenting the molecular viscosity in the NS equations (4.1) with the turbulent viscosity ν_{T0} , and it facilitates analysis of the dynamics of turbulent flow fluctuations (up to first order),

$$\begin{aligned} \mathbf{v}_t &= -(\mathbf{U}_0 \cdot \nabla) \mathbf{v} - (\mathbf{v} \cdot \nabla) \mathbf{U}_0 - \nabla p + (1/R_\tau) \nabla \cdot ((1 + \nu_{T0}) (\nabla \mathbf{v} + (\nabla \mathbf{v})^T)), \\ 0 &= \nabla \cdot \mathbf{v}. \end{aligned} \quad (4.16)$$

Recent research has demonstrated capability of (4.16) to qualitatively predict experimental and numerical features of turbulent flows [73–75].

Our simulation-free design of drag-reducing transverse oscillations involves four steps:

- (i) *the turbulent mean velocity in the presence of control is obtained from the RANS equations (4.5) where closure is achieved using the turbulent viscosity of the uncontrolled flow (4.9);*
- (ii) *k and ϵ are determined from the second-order statistics of fluctuations that are obtained from the stochastically forced NS equations linearized around the turbulent mean velocity determined in (i);*
- (iii) *for the flow with control, the modifications to k and ϵ are used to determine the modification to the turbulent viscosity, ν_T ;*
- (iv) *the modified ν_T is used to determine the effect of fluctuations on the mean velocity, and thereby skin-friction drag and control net efficiency.*

Figure 4.4 represents these four steps using a block-diagram. We note that the slow time evolution of the mean flow (relative to the time evolution of fluctuations) is used to separate the update of the mean velocity (Steps (i) and (iv)) from the computation of the statistics (Step (ii)) and the update of ν_T (Step (iii)). Also note that Step (i) amounts to finding the steady-state solution of system (4.15) subject to wall oscillations, and that Step (ii) amounts to the analysis of the linearized model (4.16) in the presence of stochastic forcing.

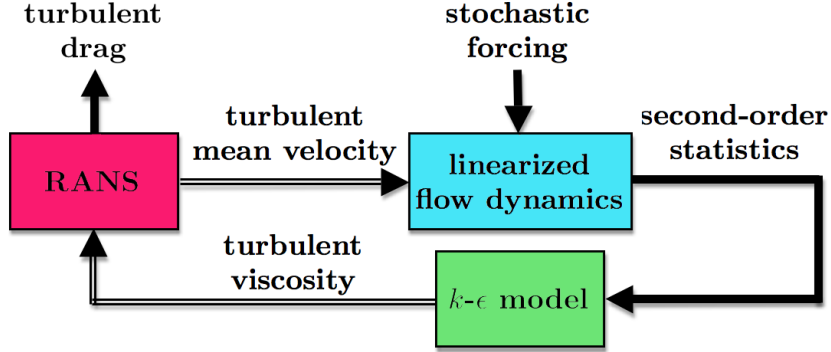


Figure 4.4: Block diagram representing Steps (i)-(iv) of our simulation-free approach for determining the effect of control on skin-friction drag in turbulent flows. The hollow arrows indicate that some of the coefficients in the model of the output subsystems are determined by the outputs of the corresponding input subsystems.

4.2.1 Computation of the velocity correlations

The evolution form of the linearized model (4.16) that governs the dynamics of fluctuations around $[U_0(y) \ 0 \ W_0(y, t)]^T$ is given by

$$\begin{aligned}\psi_t(y, \boldsymbol{\kappa}, t) &= A(\boldsymbol{\kappa}, t) \psi(y, \boldsymbol{\kappa}, t) + \mathbf{f}(y, \boldsymbol{\kappa}, t), \\ \mathbf{v}(y, \boldsymbol{\kappa}, t) &= C(\boldsymbol{\kappa}) \psi(y, \boldsymbol{\kappa}, t),\end{aligned}\quad (4.17)$$

where $\boldsymbol{\psi} = [v \ \eta]^T$ is the state, $\eta = i\kappa_z u - i\kappa_x w$ is the wall-normal vorticity, and \mathbf{f} is the stochastic forcing. System (4.17) represents a $\boldsymbol{\kappa}$ -parameterized family of PDEs in y and t with time-periodic coefficients. Here, $\boldsymbol{\kappa}$ denotes the streamwise and spanwise wavenumbers, $\boldsymbol{\kappa} = (\kappa_x, \kappa_z)$, and the same symbol is used to denote the variables in physical and wavenumber spaces (the distinction should be clear from the context). The operators A and C in (4.17) are given by

$$\begin{aligned}A &= \begin{bmatrix} A_{11} & 0 \\ A_{21} & A_{22} \end{bmatrix}, \quad C = \begin{bmatrix} C_u \\ C_v \\ C_w \end{bmatrix} = \frac{1}{\kappa^2} \begin{bmatrix} i\kappa_x \partial_y & -i\kappa_z \\ \kappa^2 & 0 \\ i\kappa_z \partial_y & i\kappa_x \end{bmatrix}, \\ A_{11} &= \Delta^{-1} \left((1/R_\tau) \left((1 + \nu_{T0}) \Delta^2 + 2\nu'_{T0} \Delta \partial_y + \nu''_{T0} (\partial_{yy} + \kappa^2) \right) + \right. \\ &\quad \left. i\kappa_x (U_0'' - U_0 \Delta) + i\kappa_z (W_0'' - W_0 \Delta) \right), \\ A_{21} &= -i\kappa_z U_0' + i\kappa_x W_0', \\ A_{22} &= (1/R_\tau) \left((1 + \nu_{T0}) \Delta + \nu'_{T0} \partial_y \right) - i\kappa_x U_0 - i\kappa_z W_0,\end{aligned}\quad (4.18)$$

where $\Delta = \partial_{yy} - \kappa^2$ is the Laplacian, $\Delta^2 = \partial_{yyyy} - 2\kappa^2 \partial_{yy} + \kappa^4$, $\kappa^2 = \kappa_x^2 + \kappa_z^2$, and $\{v(\pm 1, \boldsymbol{\kappa}, t) = v'(\pm 1, \boldsymbol{\kappa}, t) = \eta(\pm 1, \boldsymbol{\kappa}, t) = 0\}$.

We next briefly describe a method for determining the steady-state statistics of the linearized system (4.17) driven by a zero-mean white stochastic forcing, with second-order statistics,

$$\mathcal{E}(\mathbf{f}(\cdot, \boldsymbol{\kappa}, t_1) \otimes \mathbf{f}(\cdot, \boldsymbol{\kappa}, t_2)) = M(\boldsymbol{\kappa}) \delta(t_1 - t_2). \quad (4.19)$$

Here, δ is the Dirac delta function, $\mathbf{f} \otimes \mathbf{f}$ is the tensor product of \mathbf{f} with itself, and $M(\boldsymbol{\kappa})$ is spatial spectral-density of forcing. For homogeneous isotropic turbulence, the steady-state velocity correlation tensors can be reproduced by the linearized NS equations subject to white-in-time forcing with second-order statistics proportional to the turbulent energy spectrum [121]; see Appendix C. Using this analogy, we select $M(\boldsymbol{\kappa})$ to guarantee equivalence between the two-dimensional energy spectra of the uncontrolled turbulent flow and the flow governed by stochastically forced NS equations linearized around $\mathbf{U}_0 = [U_0(y) \ 0 \ 0]^T$. To this end, we use the DNS-based energy spectrum of the uncontrolled flow [1, 2], $E(y, \boldsymbol{\kappa})$, to define

$$M(\boldsymbol{\kappa}) = \frac{\bar{E}(\boldsymbol{\kappa})}{\bar{E}_0(\boldsymbol{\kappa})} M_0(\boldsymbol{\kappa}), \quad M_0(\boldsymbol{\kappa}) = \begin{bmatrix} E(y, \boldsymbol{\kappa}) I & 0 \\ 0 & E(y, \boldsymbol{\kappa}) I \end{bmatrix}.$$

Here, $\bar{E}(\boldsymbol{\kappa}) = \int_{-1}^1 E(y, \boldsymbol{\kappa}) dy$ is the two-dimensional energy spectrum of the uncontrolled flow, and $\bar{E}_0(\boldsymbol{\kappa})$ is the energy spectrum obtained from the linearized NS equations subject to a white-in-time forcing \mathbf{f} with spatial spectrum $M_0(\boldsymbol{\kappa})$.

For the time-periodic system (4.17), the operator A in (4.18) can be written as

$$A(\boldsymbol{\kappa}, t) = A_0(\boldsymbol{\kappa}) + \alpha (A_{-1}(\boldsymbol{\kappa}) e^{-i\omega_t t} + A_1(\boldsymbol{\kappa}) e^{i\omega_t t}), \quad (4.20)$$

where the expressions for A_0 , A_{-1} , and A_1 are obtained by substituting W from (4.7) into the expression for A given by (4.18), and comparing with (4.20)

$$\begin{aligned} A_0 &= \begin{bmatrix} A_{0,11} & 0 \\ -i\kappa_z U'_0 & A_{0,22} \end{bmatrix}, \\ A_{0,11} &= \Delta^{-1} \left((1/R_\tau) \left((1 + \nu_{T0}) \Delta^2 + 2\nu'_{T0} \Delta \partial_y + \nu''_{T0} (\partial_{yy} + \kappa^2) \right) + i\kappa_x (U''_0 - U_0 \Delta) \right), \\ A_{0,22} &= (1/R_\tau) \left((1 + \nu_{T0}) \Delta + \nu'_{T0} \partial_y \right) - i\kappa_x U_0, \\ A_1 &= \begin{bmatrix} i\kappa_z \Delta^{-1} (W''_{p,0} - W_{p,0} \Delta) & 0 \\ i\kappa_x W'_{p,0} & -i\kappa_z W_{p,0} \end{bmatrix}, \\ A_{-1} &= \begin{bmatrix} i\kappa_z \Delta^{-1} (W''_{m,0} - W_{m,0} \Delta) & 0 \\ i\kappa_x W'_{m,0} & -i\kappa_z W_{m,0} \end{bmatrix}. \end{aligned} \quad (4.21)$$

It is a standard fact that the response of the linear time-periodic system (4.17) subject

to a stationary input is a cyclo-stationary process [147], meaning that its statistical properties are periodic in time. For example, the auto-correlation operator of ψ is given by

$$\begin{aligned} X(\boldsymbol{\kappa}, t) &= \mathcal{E}(\psi(\cdot, \boldsymbol{\kappa}, t) \otimes \psi(\cdot, \boldsymbol{\kappa}, t)) = \\ &X_0(\boldsymbol{\kappa}) + X_1(\boldsymbol{\kappa}) e^{i\omega_t t} + X_1^+(\boldsymbol{\kappa}) e^{-i\omega_t t} + X_2(\boldsymbol{\kappa}) e^{i2\omega_t t} + X_2^+(\boldsymbol{\kappa}) e^{-i2\omega_t t} + \dots, \end{aligned} \quad (4.22)$$

where $+$ denotes the adjoint of an operator. The averaged effect of forcing (over one period T) is determined by X_0

$$\frac{1}{T} \int_0^T X(\boldsymbol{\kappa}, t) dt = X_0(\boldsymbol{\kappa}). \quad (4.23)$$

In the remainder of the chapter, we consider small amplitude of wall oscillations α . This choice is motivated by the observation that the power required to maintain the oscillations increases quadratically with α (cf. (4.11)). Hence, large amplitudes may be prohibitively expensive from control expenditure point of view. Furthermore, for sufficiently small value of α the velocity correlations can be computed efficiently using perturbation analysis in α [89]. We thus use perturbation analysis to identify frequency of wall oscillations that yields the largest drag reduction.

For the time-periodic system (4.17), the normal modes are determined by Bloch waves [85, 86]

$$\begin{aligned} \mathbf{f}(y, \boldsymbol{\kappa}, t) &= \sum_{n \in \mathbb{Z}} \mathbf{f}_n(y, \boldsymbol{\kappa}) e^{i(\theta + n\omega_t)t}, \\ \boldsymbol{\psi}(y, \boldsymbol{\kappa}, t) &= \sum_{n \in \mathbb{Z}} \boldsymbol{\psi}_n(y, \boldsymbol{\kappa}) e^{i(\theta + n\omega_t)t}, \\ \mathbf{v}(y, \boldsymbol{\kappa}, t) &= \sum_{n \in \mathbb{Z}} \mathbf{v}_n(y, \boldsymbol{\kappa}) e^{i(\theta + n\omega_t)t}, \end{aligned}$$

where $\theta \in [0, \omega_t)$ is the angular frequency. The frequency response of the time-periodic system (4.17) is an operator that maps the bi-infinite input column vector $\text{col} \{\mathbf{f}_n\}_{n \in \mathbb{Z}}$, into the bi-infinite output column vector $\text{col} \{\mathbf{v}_n\}_{n \in \mathbb{Z}}$ [88, 89]. The system states can also be defined as a bi-infinite column vector $\text{col} \{\boldsymbol{\psi}_n\}_{n \in \mathbb{Z}}$.

As discussed in § 4.2.1, $\psi(\cdot, \boldsymbol{\kappa}, t)$ is a cyclo-stationary process with second-order statistics given by (4.22). The kernel representation $\mathcal{K}_{X_r}(y, \xi, \boldsymbol{\kappa})$ of the auto-correlation operator X_r of $\psi(\cdot, \boldsymbol{\kappa}, t)$,

$$\mathcal{E}(\psi(y, \boldsymbol{\kappa}, t) \psi^*(\xi, \boldsymbol{\kappa}, t)) = \sum_{r \in \mathbb{Z}} \mathcal{K}_{X_r}(y, \xi, \boldsymbol{\kappa}) e^{ir\omega_t t},$$

can be expressed in terms of $\{\psi_n\}_{n \in \mathbb{Z}}$

$$\mathcal{K}_{X_r}(y, \xi, \boldsymbol{\kappa}) = \sum_{n \in \mathbb{Z}} \psi_n(y, \boldsymbol{\kappa}) \psi_{n-r}^*(\xi, \boldsymbol{\kappa}).$$

Furthermore, the frequency representation of the auto-correlation operator of $\psi(\cdot, \boldsymbol{\kappa}, t)$ is a self-adjoint bi-infinite block-Toeplitz operator that is parameterized by $\boldsymbol{\kappa}$

$$\mathcal{X}(\boldsymbol{\kappa}) = \text{Toep} \{ \dots, X_2^+, X_1^+, \boxed{X_0}, X_1, X_2, \dots \},$$

where the box denotes the element on the main block diagonal of \mathcal{X} .

For the case where \mathbf{f} is a zero-mean white process in y and t with second-order statistics given by (4.19), we have $\mathbf{f}_0 = \mathbf{f}$, and $\mathbf{f}_n = 0$ for $n \neq 0$. Thus, the frequency representation of the spectrum of \mathbf{f} is given by a bi-infinite block-diagonal operator $\mathcal{M}(\boldsymbol{\kappa})$ with block diagonals equal to $M(\boldsymbol{\kappa})$. The auto-correlation operator of the state, $\mathcal{X}(\boldsymbol{\kappa})$, can be obtained from the following Lyapunov equation [88, 89]

$$\begin{aligned} \mathcal{F}(\boldsymbol{\kappa}) \mathcal{X}(\boldsymbol{\kappa}) + \mathcal{X}(\boldsymbol{\kappa}) \mathcal{F}^+(\boldsymbol{\kappa}) &= -\mathcal{M}(\boldsymbol{\kappa}), \\ \mathcal{F}(\boldsymbol{\kappa}) &= \mathcal{A}(\boldsymbol{\kappa}) - \mathcal{G}(0). \end{aligned} \tag{4.24}$$

Here, \mathcal{G} is a bi-infinite block-diagonal operator

$$\mathcal{G}(\theta) = \text{diag} \{ i(\theta + n\omega_t) I \}_{n \in \mathbb{Z}},$$

and \mathcal{A} is a bi-infinite block-Toeplitz operator

$$\mathcal{A}(\boldsymbol{\kappa}) = \text{Toep} \{ \dots, 0, \alpha A_1, \boxed{A_0}, \alpha A_{-1}, 0, \dots \}.$$

The solution to (4.24) can be efficiently computed using perturbation analysis in α [88, 89]. The operator \mathcal{F} is decomposed into a block-diagonal operator \mathcal{F}_0 and an operator \mathcal{F}_1 that contains the first upper and lower block sub-diagonals

$$\begin{aligned} \mathcal{F} &= \mathcal{F}_0 + \alpha \mathcal{F}_1, \\ \mathcal{F}_0 &= \text{diag} \{ A_0 - i n \omega_t I \}_{n \in \mathbb{Z}}, \\ \mathcal{F}_1 &= \text{Toep} \{ \dots, 0, A_1, \boxed{0}, A_{-1}, 0, \dots \}. \end{aligned} \tag{4.25}$$

For sufficiently small α , the solution to (4.24) can be written as [89]

$$\mathcal{X} = \mathcal{X}_0 + \alpha \mathcal{X}_1 + \alpha^2 \mathcal{X}_2 + \alpha^3 \mathcal{X}_3 + \dots \tag{4.26}$$

Substituting (4.25) and (4.26) into (4.24) and collecting equal powers of α yields the

following set of Lyapunov equations

$$\begin{aligned}\alpha^0 : \mathcal{F}_0 \mathcal{X}_0 + \mathcal{X}_0 \mathcal{F}_0^+ &= -\mathcal{M}, \\ \alpha^n : \mathcal{F}_0 \mathcal{X}_n + \mathcal{X}_n \mathcal{F}_0^+ &= -(\mathcal{F}_1 \mathcal{X}_{n-1} + \mathcal{X}_{n-1} \mathcal{F}_1^+).\end{aligned}$$

Since \mathcal{F}_0 is block-diagonal, \mathcal{X}_n inherits the structure of the right-hand-side of the equation at $\mathcal{O}(\alpha^n)$. The structure of the above equations reveals that \mathcal{X}_0 is a self-adjoint block-diagonal operator, \mathcal{X}_1 is a self-adjoint block-Toeplitz operator where only the first upper and lower block sub-diagonals are non-zero, and \mathcal{X}_2 is a self-adjoint block-Toeplitz operator where only the main block diagonal and the second upper and lower block sub-diagonals are non-zero

$$\begin{aligned}\mathcal{X}_{\theta 0}(\boldsymbol{\kappa}) &= \text{Toep} \left\{ \dots, 0, \boxed{X_{0,0}}, 0, \dots \right\}, \\ \mathcal{X}_{\theta 1}(\boldsymbol{\kappa}) &= \text{Toep} \left\{ \dots, 0, X_{1,1}^+, \boxed{0}, X_{1,1}, 0, \dots \right\}, \\ \mathcal{X}_{\theta 2}(\boldsymbol{\kappa}) &= \text{Toep} \left\{ \dots, 0, X_{2,2}^+, 0, \boxed{X_{0,2}}, 0, X_{2,2}, 0, \dots \right\}.\end{aligned}$$

The above structure of the operator \mathcal{X} in conjunction with the fact that only the element on the main block diagonal of \mathcal{X} contributes to the averaged effect of forcing on the velocity correlations (cf. equation (4.23)) reveal that, up to second order in α , only $X_{0,0}$ and $X_{0,2}$ contribute to X_0

$$X_0(\boldsymbol{\kappa}) = X_{0,0}(\boldsymbol{\kappa}) + \alpha^2 X_{0,2}(\boldsymbol{\kappa}) + \mathcal{O}(\alpha^4). \quad (4.27)$$

The operators $X_{0,0}$ and $X_{0,2}$ are obtained from a set of decoupled Lyapunov equations whose size is equal to the size of each block in the bi-infinite Lyapunov equation (4.24) [89]

$$\begin{aligned}A_0 X_{0,0} + X_{0,0} A_0^+ &= -M, \\ (A_0 + i\omega_t I) X_{1,1} + X_{1,1} A_0^+ &= -(A_{-1} X_{0,0} + X_{0,0} A_1^+), \\ A_0 X_{0,2} + X_{0,2} A_0^+ &= -(A_{-1} X_{1,1}^+ + X_{1,1} A_{-1}^+ + A_1 X_{1,1} + X_{1,1}^+ A_1^+).\end{aligned}$$

The decoupling between different harmonics of $X(\boldsymbol{\kappa}, t)$ for small α is used for efficient computation of the second-order statistics of the time-periodic system (4.17).

The auto-correlation operator of the state $\boldsymbol{\psi}$ of stochastically forced flow with no control is determined by $X_{0,0}$. On the other hand, the operator $X_{0,2}$ represents the second-order correction to $X_{0,0}$ induced by wall oscillations. As shown in § 4.2.2 and § 4.2.3, $X_{0,2}$ determines the effect of fluctuations on k , ϵ , ν_T , and C_f in the flow with control.

4.2.2 Influence of fluctuations on turbulent viscosity

According to the k - ϵ model, ν_T is determined by the second-order statistics of velocity fluctuations. By considering dynamics of infinitesimal fluctuations, these statistics can be obtained from the auto-correlation operator X_0 . In the flow subject to small amplitude wall oscillations X_0 is given by (4.27), implying that $\mathcal{E}(\overline{\mathbf{v}\mathbf{v}^T})$, k , and ϵ can be expressed as

$$\begin{aligned}\mathcal{E}(\overline{\mathbf{v}\mathbf{v}^T}) &= \mathcal{E}(\overline{\mathbf{v}\mathbf{v}^T})_0 + \alpha^2 \mathcal{E}(\overline{\mathbf{v}\mathbf{v}^T})_2 + \mathcal{O}(\alpha^4), \\ k &= k_0 + \alpha^2 k_2 + \mathcal{O}(\alpha^4), \\ \epsilon &= \epsilon_0 + \alpha^2 \epsilon_2 + \mathcal{O}(\alpha^4).\end{aligned}\tag{4.28}$$

Here, the subscript 0 denotes the corresponding quantities in the uncontrolled turbulent flow, and the subscript 2 quantifies the influence of fluctuations in the controlled flow at the level of α^2 . A computationally efficient method for determining k_2 and ϵ_2 from $X_{0,2}$ is provided next.

We next show that the averaged effect (over one period T) of fluctuations around the mean velocity on k_2 and ϵ_2 can be obtained from $X_{0,2}(\boldsymbol{\kappa})$. Following (4.27), the second-order correction (in α) to the auto-correlation operator of velocity fluctuations \mathbf{v} averaged over one period T , $(1/T) \int_0^T \mathcal{E}(\mathbf{v}(\cdot, \boldsymbol{\kappa}, t) \otimes \mathbf{v}(\cdot, \boldsymbol{\kappa}, t)) dt$, is given by $C(\boldsymbol{\kappa})X_{0,2}(\boldsymbol{\kappa})C^+(\boldsymbol{\kappa})$. The Reynolds stress tensor $\mathcal{E}(\overline{\mathbf{v}\mathbf{v}^T})_2$ in (4.28) is then obtained from

$$\mathcal{E}(\overline{\mathbf{v}\mathbf{v}^T})_2(y) = \int_{\boldsymbol{\kappa}} \mathcal{K}_{\mathbf{v}\mathbf{v}}(y, y, \boldsymbol{\kappa}) d\boldsymbol{\kappa},$$

where $\mathcal{K}_{\mathbf{v}\mathbf{v}}(y, \xi, \boldsymbol{\kappa})$ denotes the kernel representation of the operator $C(\boldsymbol{\kappa})X_{0,2}(\boldsymbol{\kappa})C^+(\boldsymbol{\kappa})$. The kinetic energy of fluctuations around the base flow and its rate of dissipation is given by (cf. equation (4.14))

$$\begin{aligned}k_2(y) &= \int_{\boldsymbol{\kappa}} \mathcal{K}_k(y, y, \boldsymbol{\kappa}) d\boldsymbol{\kappa}, \\ \epsilon_2(y) &= \int_{\boldsymbol{\kappa}} \mathcal{K}_\epsilon(y, y, \boldsymbol{\kappa}) d\boldsymbol{\kappa},\end{aligned}\tag{4.29}$$

where $\mathcal{K}_k(y, \xi, \boldsymbol{\kappa})$ and $\mathcal{K}_\epsilon(y, \xi, \boldsymbol{\kappa})$ are the kernel representation of the operators \mathcal{N}_k and \mathcal{N}_ϵ , respectively

$$\begin{aligned}\mathcal{N}_k(\boldsymbol{\kappa}) &= (1/2) (C_u X_{0,2} C_u^+ + C_v X_{0,2} C_v^+ + C_w X_{0,2} C_w^+), \\ \mathcal{N}_\epsilon(\boldsymbol{\kappa}) &= 2 (\kappa_x^2 C_u X_{0,2} C_u^+ + D_v X_{0,2} D_v^+ + \kappa_z^2 C_w X_{0,2} C_w^+ - i\kappa_x D_u X_{0,2} C_v^+ + \\ &\quad \kappa_x \kappa_z C_u X_{0,2} C_w^+ + i\kappa_z C_v X_{0,2} D_w^+) + D_u X_{0,2} D_u^+ + D_w X_{0,2} D_w^+ + \\ &\quad \kappa^2 C_v X_{0,2} C_v^+ + \kappa_x^2 C_w X_{0,2} C_w^+ + \kappa_z^2 C_u X_{0,2} C_u^+.\end{aligned}$$

The operators D_u , D_v , and D_w are given by

$$\begin{bmatrix} D_u \\ D_v \\ D_w \end{bmatrix} = \partial_y C(\boldsymbol{\kappa}) = \frac{1}{\kappa^2} \begin{bmatrix} i\kappa_x \partial_{yy} & -i\kappa_z \partial_y \\ \kappa^2 \partial_y & 0 \\ i\kappa_z \partial_{yy} & i\kappa_x \partial_y \end{bmatrix}.$$

For small amplitude oscillations, substituting k and ϵ from (4.28) into (4.13) yields

$$\nu_T = c R_\tau^2 \frac{k^2}{\epsilon} = c R_\tau^2 \frac{(k_0 + \alpha^2 k_2 + \mathcal{O}(\alpha^4))^2}{\epsilon_0 + \alpha^2 \epsilon_2 + \mathcal{O}(\alpha^4)},$$

which in conjunction with Neumann series expansion leads to

$$\begin{aligned} \nu_T &= \nu_{T0} + \alpha^2 \nu_{T2} + \mathcal{O}(\alpha^4), \\ \nu_{T2} &= \nu_{T0} \left(\frac{2k_2}{k_0} - \frac{\epsilon_2}{\epsilon_0} \right). \end{aligned} \quad (4.30)$$

Therefore, up to second order in α , the influence of fluctuations on turbulent viscosity in the flow with control is determined by second-order corrections to the kinetic energy k_2 and its rate of dissipation ϵ_2 .

4.2.3 Skin-friction drag coefficient and net efficiency

We next show how velocity fluctuations in the flow with control modify the skin-friction drag coefficient and the net efficiency. As discussed in § 4.1.2, C_f is determined by U and $\% \Pi_{\text{net}}$ is determined by both U and W . The influence of fluctuations on U and W in the flow with control can be obtained by substituting ν_T from (4.30) into (4.5), and thereby expressing U , W , and τ_w as

$$\begin{aligned} U &= U_0 + \alpha^2 U_2 + \mathcal{O}(\alpha^4), \\ W_p &= W_{p,0} + \alpha^2 W_{p,2} + \mathcal{O}(\alpha^4), \\ \tau_w &= 1 + \alpha^2 \tau_{w,2} + \mathcal{O}(\alpha^4). \end{aligned} \quad (4.31)$$

The second-order correction to the mean streamwise velocity, U_2 , is obtained by substituting U and τ_w from (4.31) into (4.5), and collecting the terms quadratic in α

$$(1 + \nu_{T0}) U_2'' + \nu_{T0}' U_2' = -R_\tau \tau_{w,2} - (\nu_{T2} U_0'' + \nu_{T2}' U_0'),$$

which yields the following solution for U_2

$$U_2(y) = \tau_{w,2} U_0(y) - \int_{-1}^y \frac{\nu_{T2}(\xi) U_0'(\xi)}{1 + \nu_{T0}(\xi)} d\xi. \quad (4.32)$$

The second-order correction to the wall-shear stress, $\overline{\tau_{w,2}}$, is obtained from the requirement that the bulk flux of the flow with control remains constant, i.e.

$$\int_{-1}^1 U_2(y) dy = 0.$$

Integrating $U_2(y)$ in (4.32) from -1 to 1 , and enforcing the above requirement yields

$$\tau_{w,2} = \frac{1}{2U_B} \int_{-1}^1 \int_{-1}^y \frac{\nu_{T2}(\xi) U_0'(\xi)}{1 + \nu_{T0}(\xi)} d\xi dy.$$

An equation for $W_{p,2}$ is determined by substituting ν_T from (4.30) into (4.8)

$$(1 + \nu_{T0}) W_{p,2}'' + \nu_{T0}' W_{p,2}' - iR_\tau \omega_t W_{p,2} = -(\nu_{T2} W_{p,0}'' + \nu_{T2}' W_{p,0}').$$

An expression for the saved power is obtained by substituting τ_w from (4.31) into (4.10)

$$\%C_f = \% \Pi_{\text{save}} = \alpha^2 \% \Pi_{\text{save},2} + \mathcal{O}(\alpha^4), \quad \% \Pi_{\text{save},2} = -100 \tau_{w,2}.$$

In flows subject to small amplitude oscillations, the above equation shows that a positive (negative) value of $\% \Pi_{\text{save},2}$ signifies drag reduction (increase). On the other hand, the required power can be obtained by substituting W_p from (4.31) into (4.11)

$$\% \Pi_{\text{req}} = \alpha^2 (\% \Pi_{\text{req},0} + \alpha^2 \% \Pi_{\text{req},2}) + \mathcal{O}(\alpha^6), \quad (4.33)$$

where $\% \Pi_{\text{req},0}$ is given in (4.12), and $\% \Pi_{\text{req},2}$ is obtained by substituting W_p from (4.31) into (4.11)

$$\% \Pi_{\text{req},2} = 100 \frac{1}{R_\tau U_B} \text{Im} \left(W_{p,2}'|_{y=-1} - W_{p,2}'|_{y=1} \right).$$

We note the contrast in the way fluctuations influence saved and required powers; while fluctuations make $\mathcal{O}(\alpha^2)$ contribution to $\% \Pi_{\text{save}}$, they affect $\% \Pi_{\text{req}}$ only at the level of α^4 . This explains the close agreement, observed in § 4.1.2, between $\% \Pi_{\text{req},0}$ and the DNS results [9]. Finally, the net efficiency is given by

$$\% \Pi_{\text{net}} = \alpha^2 \% \Pi_{\text{net},2} + \mathcal{O}(\alpha^4), \quad \% \Pi_{\text{net},2} = \% \Pi_{\text{save},2} - \% \Pi_{\text{req},0}.$$

The developments of this section are used in § 4.3 to determine the skin-friction drag coefficient and the net efficiency in the flow subject to wall oscillations.

4.3 Turbulent drag reduction

In this section, we examine the effect of transverse wall oscillations on skin-friction drag and net efficiency in flows with $R_\tau = 186, 547, \text{ and } 934$. For these Reynolds numbers, the second-order statistics of the uncontrolled turbulent flow were obtained

R_τ	N_x	N_y	N_z	$\kappa_{x,\max}$	$\kappa_{z,\max}$	c_1	c_2	U_B
186	50	101	51	42.5	84.5	46.2	0.61	15.73
547	50	151	51	128	255.5	29.4	0.45	18.38
934	50	201	51	255	511.3	27.0	0.43	19.86

Table 4.1: The parameters used in our study. At each R_τ , c_1 and c_2 are selected to minimize the least squares deviation between the mean streamwise velocity obtained from (4.6)-(4.9) and the mean velocity obtained in DNS [1,2]. The bulk flux U_B is kept constant by adjusting the pressure gradient.

using DNS [1, 2]. As explained in § 4.2.1, we use this database to determine the spatial spectrum of the stochastic forcing (4.19) in the evolution model (4.17). This database also provides the turbulent kinetic energy in flow with no control, k_0 , and thereby its rate of dissipation,

$$\epsilon_0 = cR_\tau^2 \frac{k_0^2}{\nu_{T0}},$$

where ν_{T0} is defined by (4.9).

The differential operators in the wall-normal direction are discretized using N_y collocation points [118]. In horizontal directions, we use $N_x \times N_z$ wavenumbers with $0 < \kappa_x < \kappa_{x,\max}$ and $0 < \kappa_z < \kappa_{z,\max}$, where $\kappa_{x,\max}$ and $\kappa_{z,\max}$ are the largest wavenumbers used in the DNS of [1, 2]; table 4.1 provides summary of parameters used in our study. The DNS-based energy spectrum, taken from <http://torroja.dmt.upm.es/ftp/channels/data/>, is interpolated on the N_y collocation points in the wall-normal direction.

4.3.1 Saved power

We first examine the effect of period of oscillations T^+ on the turbulent drag reduction and the saved power. Figure 4.5(a) shows the second-order correction to the saved power, $\% \Pi_{\text{save},2}(T^+)$, for the controlled flow with $R_\tau = 186$. The positive value of $\% \Pi_{\text{save},2}$ indicates that drag is reduced for all values of T^+ that we considered, with the largest drag reduction taking place at $T^+ = 102.5$. Our theoretical predictions are in close agreement with DNS at $R_\tau = 200$ [126], where it was shown that $T^+ \approx 100$ yields the largest drag reduction for control amplitudes $\alpha = 3.1$ and 6.2 .

Figure 4.5(b) compares $\% \Pi_{\text{save},2}$ (solid curve) obtained using our analysis with $\% \Pi_{\text{save}}$ (symbols) obtained using DNS at $R_\tau = 200$ [9]. In DNS, the largest drag reduction takes place at $T^+ \approx 100$ for $\alpha = 2.25$ and 6 , and at $T^+ \approx 125$ for $\alpha = 9$. Thus, for small control amplitudes, perturbation analysis up to second order in α reliably predicts optimal period of drag reducing oscillations. For the optimal period of oscillations and $\alpha = 2.25$, our perturbation analysis predicts 13.6% drag reduction,

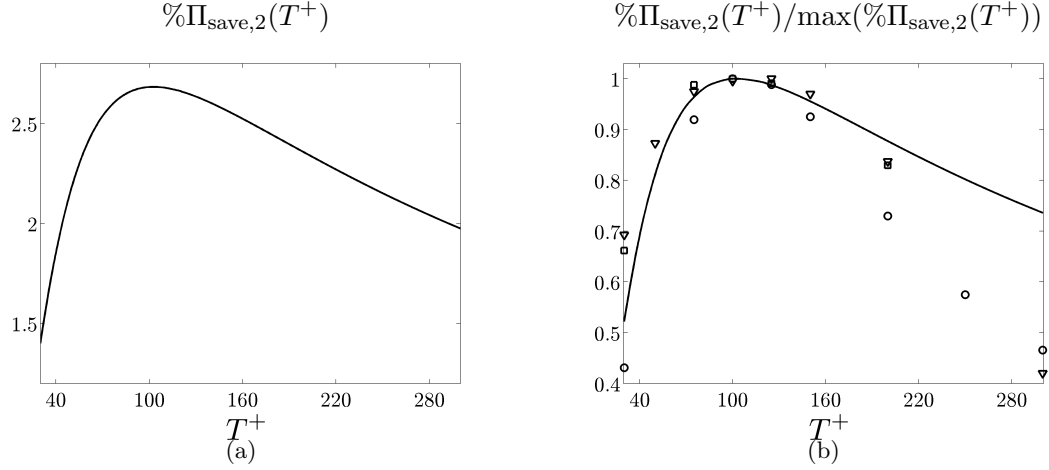


Figure 4.5: (a) Second-order correction to the saved power, $\% \Pi_{\text{save},2}(T^+)$, as a function of the period of oscillations T^+ for the flow with $R_\tau = 186$; (b) Comparison between $\% \Pi_{\text{save},2}(T^+)$ (solid curve) and $\% \Pi_{\text{save}}(T^+)$ (symbols). Symbols show DNS data at $R_\tau = 200$ [9] for control amplitudes $\alpha = 2.25$, \circ ; $\alpha = 6$, \square ; and $\alpha = 9$, ∇ . The results in (b) are normalized by their largest values.

whereas 17.4% drag reduction is obtained in DNS [9]. The quantitative differences between the DNS results and the results of perturbation analysis may be attributed to the effects of higher order corrections. Another factor that warrants further scrutiny is modeling of the spatial spectrum of stochastic forcing. Analysis of these effects is beyond the scope of the current study.

4.3.2 Required control power

We next study the power required to maintain wall oscillations. From (4.33) it follows that, up to second-order in α , $\% \Pi_{\text{req},0}$ defined by (4.12) determines the required power. From § 4.1.2, we recall that $\% \Pi_{\text{req},0}$ decreases monotonically with T^+ ; cf. Figure 4.3(a). Furthermore, Figure 4.3(b) shows that $\% \Pi_{\text{req},0}$ is larger than the required power obtained in DNS [9], and that the discrepancy increases with T^+ . Accounting for the effect of fluctuations in the flow with control reduces this discrepancy. From Figure 4.6(a), we see that the fourth-order correction to the required power, $\% \Pi_{\text{req},2}(T^+)$, is negative for $T^+ \gtrsim 45$ and that it decreases with T^+ . This is in agreement with our earlier observation that $\% \Pi_{\text{req},0}$ overestimates the required power obtained in DNS. The symbols in Figure 4.6(b) represent the difference between the required power obtained by [9] using DNS and the required power that we obtained using perturbation analysis up to second order in α , $\% \Pi_{\text{req}} - \alpha^2 \% \Pi_{\text{req},0}$, for $\alpha = 2.25, 6$, and 9 . This difference is in close agreement with the fourth-order correction to the required power, $\% \Pi_{\text{req},2}$ (solid curve).

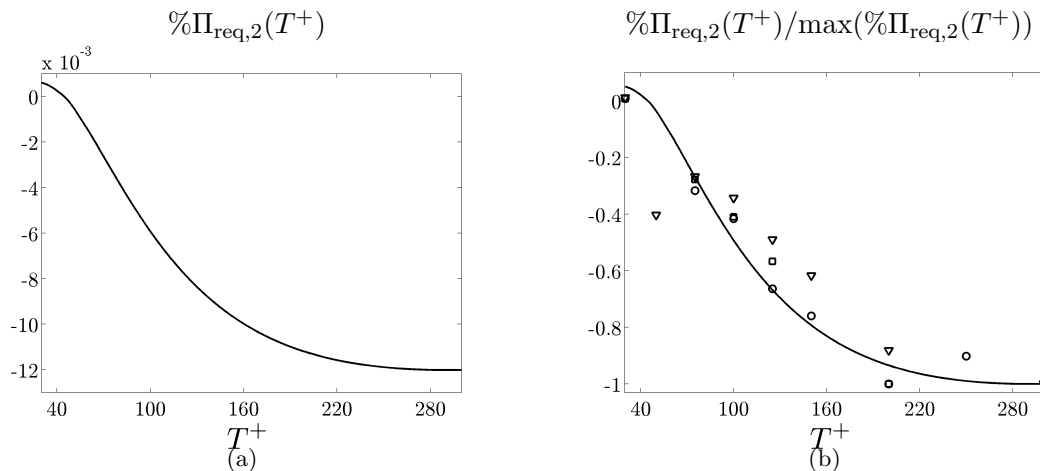


Figure 4.6: (a) Fourth-order correction to the required power, $\% \Pi_{\text{req},2}(T^+)$, as a function of the period of oscillations T^+ for the flow with $R_\tau = 186$; (b) Comparison between $\% \Pi_{\text{req},2}(T^+)$ (solid curve) and $\% \Pi_{\text{req}} - \alpha^2 \% \Pi_{\text{req},0}(T^+)$ (symbols). $\% \Pi_{\text{req}}$ is obtained using DNS at $R_\tau = 200$ [9] for $\alpha = 2.25$, \circ ; $\alpha = 6$, \square ; and $\alpha = 9$, ∇ . The results in (b) are normalized by largest values of $|\% \Pi_{\text{req},2}(T^+)|$ and $|\% \Pi_{\text{req}} - \alpha^2 \% \Pi_{\text{req},0}(T^+)|$.

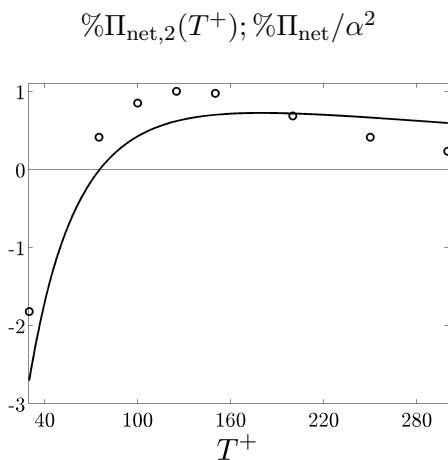


Figure 4.7: Comparison between second-order correction to the net efficiency $\% \Pi_{\text{net},2}(T^+)$ (solid curve) for the flow with $R_\tau = 186$ (solid curve), and $\% \Pi_{\text{net}}/\alpha^2$ (symbols). Symbols show DNS data at $R_\tau = 200$ [9] for $\alpha = 2.25$, \circ .

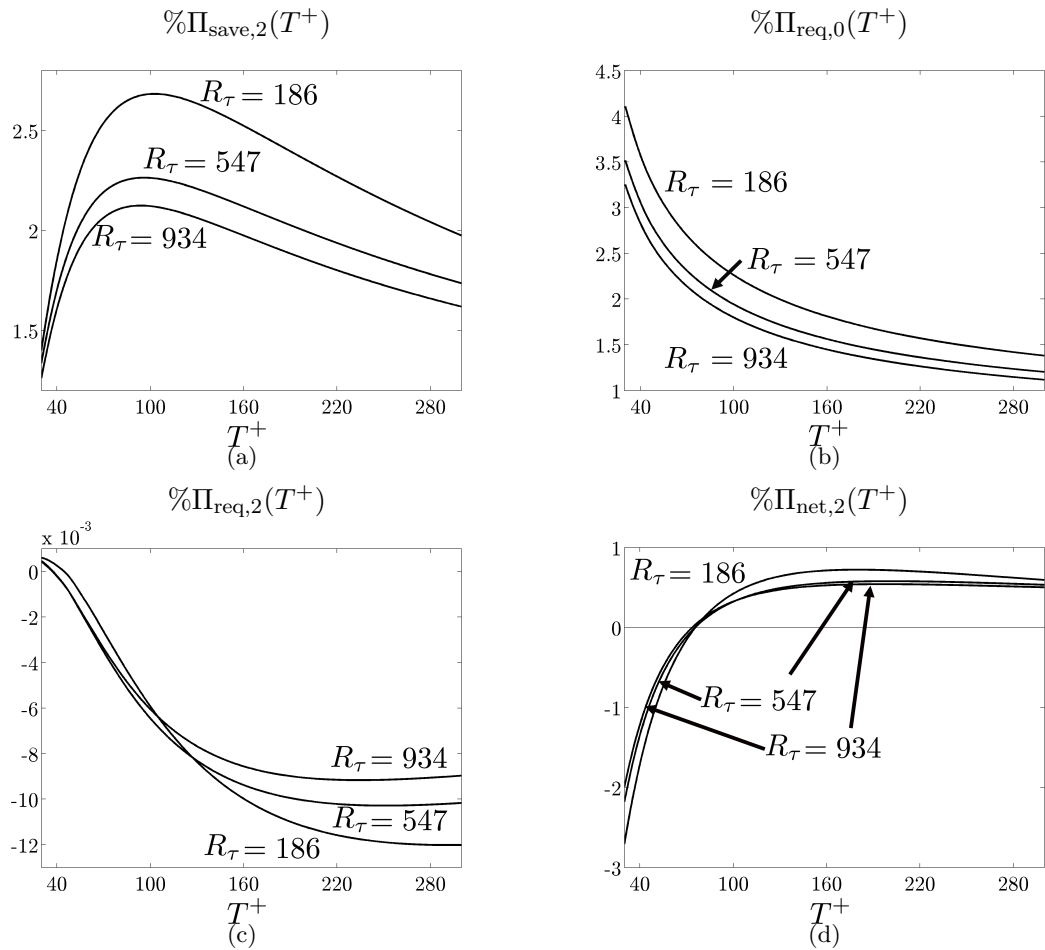


Figure 4.8: The second-order correction to (a) the saved power, $\% \Pi_{\text{save},2}(T^+)$; (b) the required power, $\% \Pi_{\text{req},0}(T^+)$; and (d) the net efficiency, $\% \Pi_{\text{net},2}(T^+)$; and (c) the fourth-order correction to the required power, $\% \Pi_{\text{req},2}(T^+)$, as a function of the period of oscillations T^+ for the flows with $R_\tau = 186$, 547, and 934.

4.3.3 Net efficiency

The net efficiency in the flow subject to wall oscillations is determined by the difference between the saved and required powers. The solid curve in Figure 4.7 shows the second-order correction to the net efficiency, $\% \Pi_{\text{net},2}(T^+)$, in the flow with $R_\tau = 186$. We see that $\% \Pi_{\text{net},2} > 0$ for $T^+ > 75$, indicating that, for small control amplitudes, a positive net efficiency can be achieved if the period of oscillations is large enough. Our prediction is in close agreement with DNS at $R_\tau = 200$ [9] where positive net efficiency of oscillations with $\alpha = 2.25$ is obtained for $T^+ > 70$. Furthermore, up to second order in α , the largest net efficiency takes place at $T^+ = 180$. This value differs from the value of T^+ that yields the largest saved power, $T^+ = 102.5$ (cf. § 4.3.1). This difference can be explained by the fact that the peak of $\% \Pi_{\text{net},2} = \% \Pi_{\text{save},2} - \% \Pi_{\text{req},0}$, takes place at a value of T^+ where the derivatives (with respect to T^+) of $\% \Pi_{\text{save},2}$ and $\% \Pi_{\text{req},0}(T^+)$ are equal to each other. Since $\% \Pi_{\text{req},0}(T^+)$ is a monotonically decreasing function, its derivative is negative for all T^+ . Therefore, the largest net efficiency takes place at some $T^+ > 102.5$ where the slope of the curve $\% \Pi_{\text{save},2}(T^+)$ is also negative. (Our analysis shows that this happens at $T^+ = 180$.) The symbols in Figure 4.7 show $\% \Pi_{\text{net}}/\alpha^2$ obtained from DNS at $R_\tau = 200$ [9] for $\alpha = 2.25$. Even though the essential trends are captured by $\% \Pi_{\text{net},2}$ (solid curve), the DNS net efficiency peaks at $T^+ = 125$, which is approximately 30% smaller than the value of T^+ predicted by perturbation analysis. This discrepancy may be attributed to a slower rate of decay of $\% \Pi_{\text{save},2}$ relative to $\% \Pi_{\text{save}}$ obtained in DNS for $T^+ > 100$; cf. Figure 4.5(b).

We note that in DNS the net efficiency becomes negative for large control amplitudes. At $R_\tau = 200$, [9] showed that $\% \Pi_{\text{net}}$ becomes negative for all T^+ if $\alpha \gtrsim 3.5$. Therefore, the positive net efficiency predicted by perturbation analysis is only valid for small control amplitudes. This can be explained by noting that perturbation analysis assumes quadratic increase of both saved and required powers with α . On the other hand, [9] showed that saved power exhibits slower than linear growth with α for large control amplitudes.

4.3.4 Drag reduction in flows with larger Reynolds numbers

After assessing utility of perturbation analysis for flows with $R_\tau = 186$, we turn our attention to the effect of control at $R_\tau = 547$ and 934. Figure 4.8(a) shows that the second-order correction to the saved power, $\% \Pi_{\text{save},2}$, is positive for all R_τ , and that the optimal T^+ slightly decreases with R_τ ($T^+ = 102.5, 96$, and 94 for $R_\tau = 186, 547$, and 934 , respectively). The corresponding periods of oscillations in outer units, $T = T^+/R_\tau$, are $T = 0.55, 0.18$, and 0.10 . Therefore, as R_τ increases, larger frequency of oscillations is required for the optimal drag reduction. In addition, since $\% \Pi_{\text{save},2}$ decreases with R_τ , the amount of drag reduction deteriorates at higher Reynolds numbers.

Figure 4.8(b) shows monotonic decrease of $\% \Pi_{\text{req},0}(T^+)$ with both T^+ and R_τ . We also note that a product between the bulk flux U_B and $\% \Pi_{\text{req},0}$ does not change with

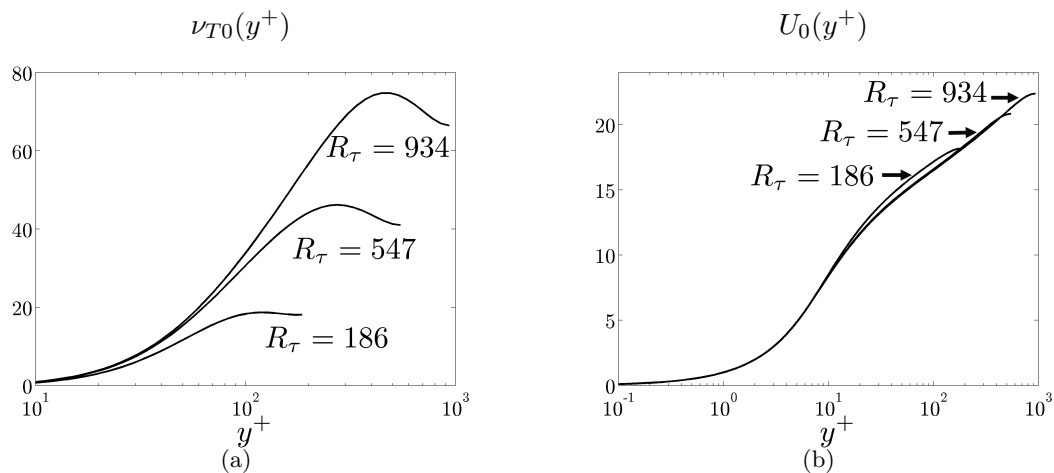


Figure 4.9: (a) The turbulent viscosity, $\nu_{T0}(y^+)$; and (b) the turbulent mean streamwise velocity, $U_0(y^+)$, in the uncontrolled flow with $R_\tau = 186, 547,$ and 934 .

R_τ . This demonstrates invariance under change in R_τ of the second-order correction to the required power (before normalization is done). The fourth-order correction to the required power, $\% \Pi_{\text{req},2}$, is also reduced as R_τ increases; see Figure 4.8(c). The difference between the quantities shown in Figures 4.8(a) and 4.8(b) determines the second-order correction to the net efficiency, $\% \Pi_{\text{net},2}$. From Figure 4.8(d) we see that the largest net efficiency reduces with R_τ , and that $\% \Pi_{\text{net},2}$ saturates for large Reynolds numbers.

4.3.5 Effect of control on turbulent viscosity and turbulent mean velocity

We next examine the effect of wall oscillations on the turbulent viscosity and the turbulent mean velocity. Figure 4.9 shows $\nu_{T0}(y^+)$ and $U_0(y^+)$ for $R_\tau = 186, 547,$ and 934 . We note that the profiles of U_0 for different R_τ lie on the top of each other, and that ν_{T0} does not scale in wall units. In particular, the peak of ν_{T0} takes place at $y^+ \approx R_\tau/2$, approximately half way between the walls and the channel centerline. On the other hand, the effect of control on ν_T is strongest in the viscous wall region, $y^+ < 50$; see Figure 4.10(a).

Figure 4.10 shows the second-order corrections to ν_{T2} and U_2 for $R_\tau = 186$ and $30 \leq T^+ \leq 300$. Since $\nu_{T2} < 0$ for all T^+ , perturbation analysis up to second order in α predicts turbulence suppression for all periods of oscillations; see Figure 4.10(a). Furthermore, turbulence suppression region shifts away from the walls with increase in T^+ . We note that suppression of the turbulent bursting process was observed in

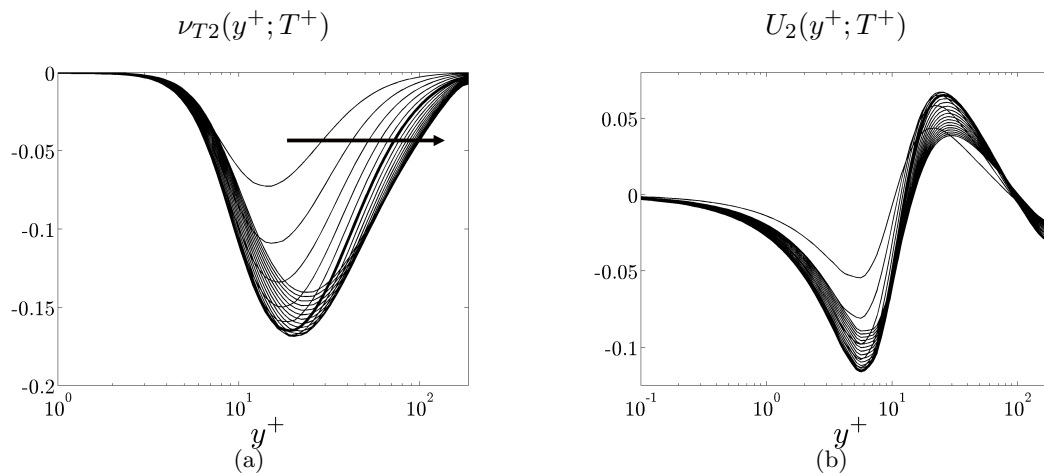


Figure 4.10: Second-order correction to (a) the turbulent viscosity, $\nu_{T2}(y^+; T^+)$; and (b) the mean streamwise velocity, $U_2(y^+; T^+)$, for $R_\tau = 186$ and different values of $30 \leq T^+ \leq 300$, where T^+ increases in the direction of the arrows. The thick curves correspond to the T^+ that yields the largest drag reduction (cf. Figure 4.11).

DNS for $25 \leq T^+ \leq 200$ [126]. Figure 4.10(b) shows that the oscillations reduce the mean velocity gradient in the immediate vicinity of the walls ($U_2 < 0$ for $y^+ \lesssim 13$). On the other hand, the mean velocity is shifted upward in the log-law region. Both these trends were previously observed in the experiments [129] and DNS [128, 138]. It was argued that the negative spanwise vorticity introduces near wall modifications to the mean streamwise velocity, and that it suppresses the production of turbulence by weakening the vortex stretching mechanism [129]. In spite of qualitative agreement, the value of y^+ above which the shift-up in U takes place differs in our study from the DNS results [138]; $y^+ > 13$ vs. $y^+ > 32$.

Figure 4.11 compares U_2 and ν_{T2} at three Reynolds numbers for the values of T^+ that induce the largest drag reduction. We see that ν_{T2} peaks at $y^+ \approx 20$ for all R_τ . This suggests that the optimal drag-reducing frequency minimizes the turbulent viscosity near the interface of the buffer layer and the log-law region. Even though the negative peak of ν_{T2} increases with R_τ (cf. Figure 4.11(a)), the ratio of ν_{T2} and ν_{T0} decreases with R_τ . Thus, wall oscillations are less effective in suppressing turbulence at larger Reynolds numbers. Finally, Figure 4.11(b) shows that the slope of U_2 decreases with R_τ ; this is in agreement with our earlier observation that smaller drag reduction is achieved at higher Reynolds numbers.

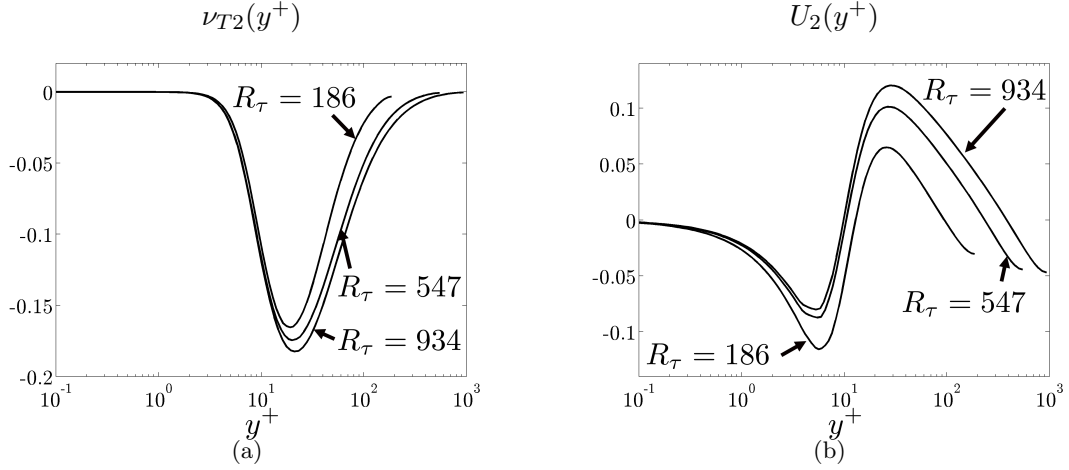


Figure 4.11: The second-order correction to (a) the turbulent viscosity, $\nu_{T2}(y^+)$; and (b) the mean streamwise velocity, $U_2(y^+)$, for the values of T^+ that yield the largest drag reduction for the flows with $R_\tau = 186$, $T^+ = 102.5$; $R_\tau = 547$, $T^+ = 96$; and $R_\tau = 934$, $T^+ = 94$.

4.3.6 Effect of control on turbulent kinetic energy

We examine the effect of control on the kinetic energy of fluctuations. Figure 4.12 compares the premultiplied two-dimensional energy spectrum of the uncontrolled flow, $\kappa_x \kappa_z \bar{E}(\boldsymbol{\kappa})$, with the premultiplied second-order correction to the energy spectrum, $\kappa_x \kappa_z \bar{E}_2(\boldsymbol{\kappa})$, in the flow subject to wall oscillations with the largest drag-reducing period $T^+ = 102.5$. The energy spectra are premultiplied by the spatial wavenumbers such that the area under the log-log plot is equal to the total energy of fluctuations. We see that the most energetic modes of the uncontrolled flow take place at $\kappa_x \approx 2.5$ and $\kappa_z \approx 6.5$; cf. Figure 4.12(a). In addition, wall oscillations further amplify the most energetic modes of the uncontrolled flow with small streamwise wavelengths (cf. red regions in Figure 4.12(b)), while they suppress the most energetic modes of the uncontrolled flow with large streamwise wavelengths (cf. blue regions in Figure 4.12(b)). The largest energy amplification takes place at $\kappa_x \approx 4.4$ and $\kappa_z \approx 10.2$, and the largest energy suppression occurs at $\kappa_x \approx 0.8$ and $\kappa_z \approx 8.8$. The total effect of control on the kinetic energy can be quantified by $\int_{\boldsymbol{\kappa}} E_2(\boldsymbol{\kappa}) d\boldsymbol{\kappa} / \int_{\boldsymbol{\kappa}} \bar{E}(\boldsymbol{\kappa}) d\boldsymbol{\kappa}$, which for wall oscillations with $T^+ = 102.5$ is approximately -1.5% . This yields 7.5% reduction in the total energy of fluctuations for $\alpha = 2.25$.

The effect of wall oscillations on the turbulent kinetic energy and its rate of dissipation is shown in Figure 4.13. We see that the second-order correction to the kinetic energy, k_2 , is negative for $T^+ = 102.5$, suggesting that the turbulent kinetic energy is

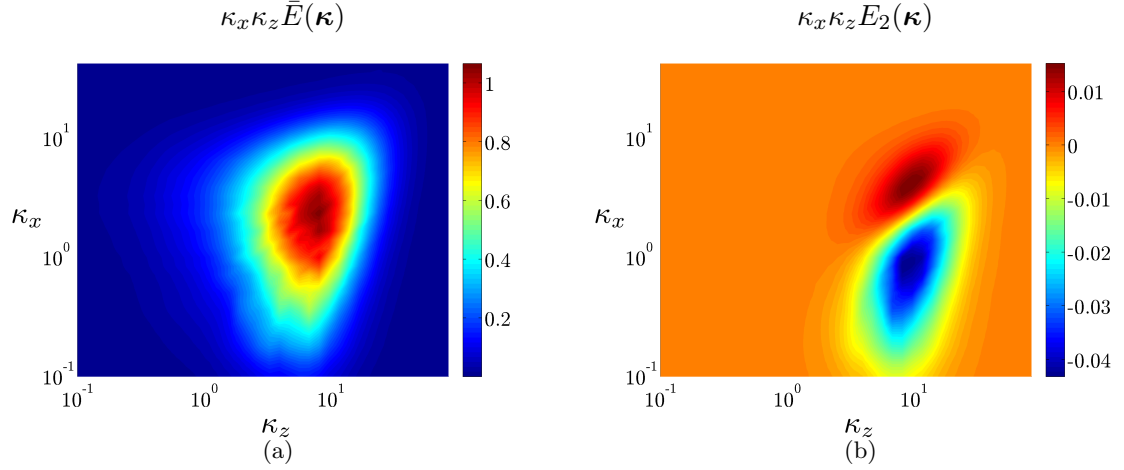


Figure 4.12: (a) Premultiplied DNS-based energy spectrum of the uncontrolled flow, $\kappa_x \kappa_z \bar{E}(\boldsymbol{\kappa})$, at $R_\tau = 186$ [1]; and (b) second-order correction to the energy spectrum, $\kappa_x \kappa_z E_2(\boldsymbol{\kappa})$, for the flow subject to wall oscillations with optimal drag-reducing period $T^+ = 102.5$.

reduced with the largest suppression taking place at $y^+ \approx 8.6$; cf. Figure 4.13(a). In addition, the second-order correction to the rate of dissipation of turbulent kinetic energy, ϵ_2 , is negative almost everywhere (except for a small region $5.4 \lesssim y^+ \lesssim 8.9$) and the largest reduction occurs in the viscous sublayer $y^+ < 5$; cf. Figure 4.13(c). Therefore, perturbation analysis up to second order in α captures the previously experimental and numerical observations that wall oscillations suppress both the production and dissipation of the turbulent kinetic energy [126, 128, 129, 138]. Figures 4.13(b) and 4.13(d) show that, relative to the flow with no control, the turbulent kinetic energy is reduced more than its rate of dissipation by wall oscillations with $T^+ = 102.5$ and $\alpha = 2.25$. This suggests that the turbulent production is suppressed more than the turbulent dissipation, which explains the reduced turbulent viscosity ν_T in the flow with control; cf. Figure 4.11(a).

4.4 Turbulent flow structures

In this section, we use stochastically forced linearized model (4.16) to examine the effect of wall oscillations on the turbulent flow structures. We only present results for $R_\tau = 186$ and note that similar flow structures are observed for all Reynolds numbers that we have considered.

In what follows, the velocity field is decomposed into *characteristic eddies* [148] by determining the spatial structure of the fluctuations that contribute most to the kinetic

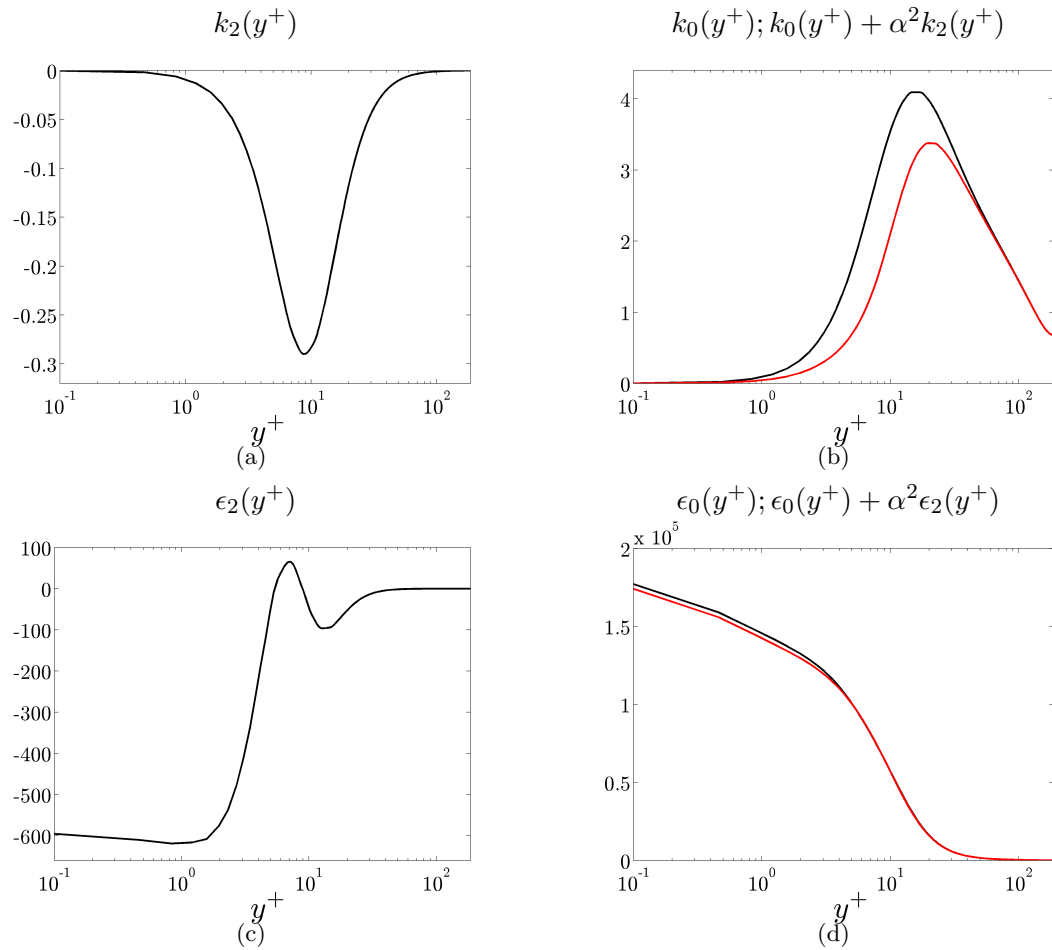


Figure 4.13: (Left column) Second-order correction to the turbulent kinetic energy $k_2(y^+)$ (a), and its rate of dissipation $\epsilon_2(y^+)$ (c), for the flow subject to wall oscillations with optimal drag-reducing period $T^+ = 102.5$ at $R_\tau = 186$. (Right column) Comparison between (b) the turbulent kinetic energy in the uncontrolled flow k_0 (black) and in the flow with control $k_0 + \alpha^2 k_2$ (red), and (d) its rate of dissipation in the uncontrolled flow ϵ_0 (black), and in the flow with control $\epsilon_0 + \alpha^2 \epsilon_2$ (red), for $\alpha = 2.25$.

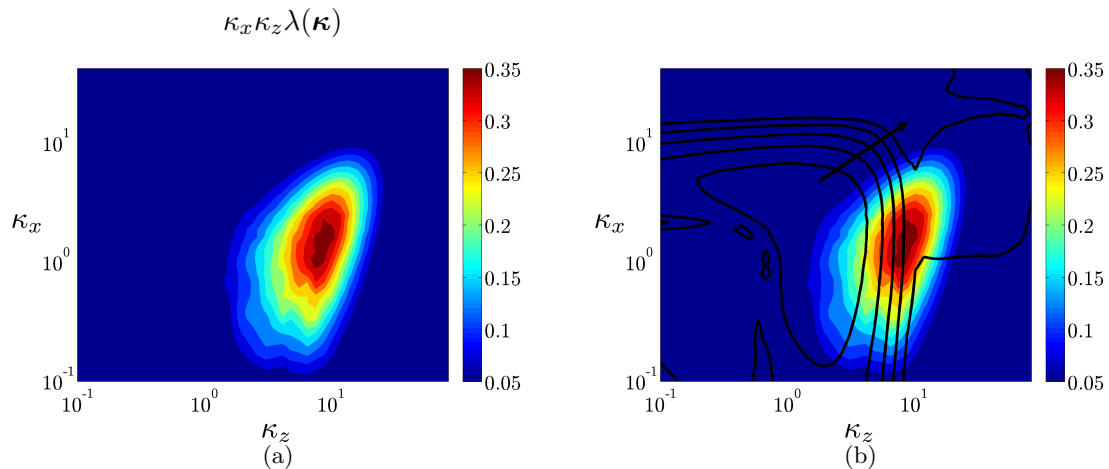


Figure 4.14: (a) Premultiplied largest eigenvalue, $\kappa_x \kappa_z \lambda(\boldsymbol{\kappa})$, of the auto-correlation operator $X_0(\boldsymbol{\kappa})$ in the uncontrolled flow with $R_\tau = 186$; (b) same as (a) with superimposed contours of the relative difference between the premultiplied two largest eigenvalues of $X_0(\boldsymbol{\kappa})$. The contour levels $\{10^{-1}, 10^{-2}, \dots, 10^{-5}\}$ decrease in the direction of the arrow.

energy at a given $\boldsymbol{\kappa} = (\kappa_x, \kappa_z)$. These most energetic structures are obtained from the principal eigenfunctions of the averaged (over one period T) auto-correlation operator, $X_0(\boldsymbol{\kappa})$, defined in § 4.2.1

$$[X_0(\boldsymbol{\kappa}) \phi(\cdot, \boldsymbol{\kappa})](y) = \lambda(\boldsymbol{\kappa}) \phi(y, \boldsymbol{\kappa}).$$

At each $\boldsymbol{\kappa}$, $\lambda(\boldsymbol{\kappa})$ is the largest eigenvalue of $X_0(\boldsymbol{\kappa})$, and $\phi(\cdot, \boldsymbol{\kappa}) = [v \ \eta]^T$ is the corresponding eigenfunction. The magnitude of ϕ is determined by the requirement that the kinetic energy of fluctuations associated with ϕ is equal to $\lambda(\boldsymbol{\kappa})$. On the other hand, the phase of ϕ is determined by requiring spatial compactness of $v(x, y, z)$ around $x = z = 0$ in the lower half of the channel [148]. This is achieved by making sure that $\int_{-1}^0 v(y, \boldsymbol{\kappa}) dy$ is a positive real number for all $\boldsymbol{\kappa}$. We note that enforcing compactness on $u(x, y, z)$ yields similar results.

In the flow with no control, the principal eigenfunctions $\phi(\cdot, \boldsymbol{\kappa})$ account for approximately 29% of the total kinetic energy; compare $\kappa_x \kappa_z \lambda(\boldsymbol{\kappa})$ shown in Figure 4.14(a) with $\kappa_x \kappa_z \bar{E}(\boldsymbol{\kappa})$ shown in Figure 4.12(a). Furthermore, the two largest eigenvalues of $X_0(\boldsymbol{\kappa})$ are almost equal to each other. As shown in Figure 4.14(b), the difference between them is negligible for the values of $\boldsymbol{\kappa}$ that correspond to the most energetic modes of the uncontrolled flow. In fact, the eigenfunctions corresponding to the second largest eigenvalue account for almost 28% of the total energy. This indicates that examining the effects of the eigenfunction corresponding to the second largest eigenvalue is equally important. Figure 4.15 illustrates that the eigenfunctions corresponding to the

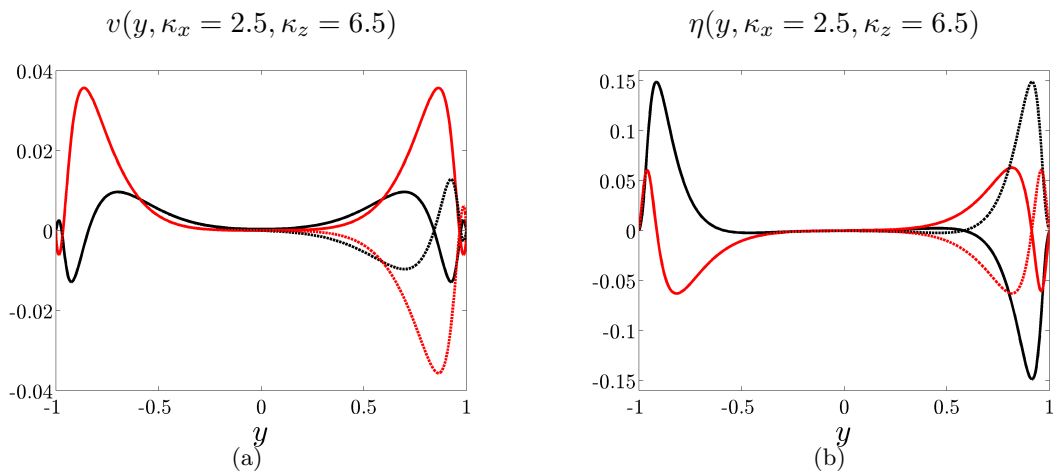


Figure 4.15: The real (black) and imaginary (red) parts of the principal eigenfunctions (v , (a); η , (b)) corresponding to the two largest equal eigenvalues of the auto-correlation operator $X_0(\boldsymbol{\kappa})$ for the most energetic mode $\kappa_x = 2.5$ and $\kappa_z = 6.5$ in the uncontrolled flow with $R_\tau = 186$. The two eigenfunctions are differentiated by solid and dotted curves.

two largest eigenvalues of X_0 at $\kappa_x = 2.5$ and $\kappa_z = 6.5$ are equal to each other in one half of the channel and are mirror image of each other in the other half. Imposing the v -compactness criterion on these two eigenfunctions aligns them in the lower half of the channel and it mirror-images them in the upper half. This implies that the flow structures that are obtained from the principal eigenfunction of $X_0(\boldsymbol{\kappa})$ in the lower half of the channel account for approximately 57% of the total kinetic energy of fluctuations.

The velocity components u , v , and w in the wavenumber space are obtained by acting with the operators C_u , C_v , and C_w on the principal eigenfunction of the operator $X_0(\boldsymbol{\kappa})$; see (4.18) for the definition of these operators. We use the flow symmetries in the spanwise direction [148] to determine the velocity profiles for the dominant characteristic eddy in the physical space

$$\begin{aligned}
 u(x, y, z) &= 4 \int_{\kappa_x, \kappa_z > 0} \operatorname{Re}(u(y, \boldsymbol{\kappa}) e^{i\kappa_x x}) \cos(\kappa_z z) d\boldsymbol{\kappa}, \\
 v(x, y, z) &= 4 \int_{\kappa_x, \kappa_z > 0} \operatorname{Re}(v(y, \boldsymbol{\kappa}) e^{i\kappa_x x}) \cos(\kappa_z z) d\boldsymbol{\kappa}, \\
 w(x, y, z) &= -4 \int_{\kappa_x, \kappa_z > 0} \operatorname{Im}(w(y, \boldsymbol{\kappa}) e^{i\kappa_x x}) \sin(\kappa_z z) d\boldsymbol{\kappa}.
 \end{aligned}$$

It is worth noting that the dominant characteristic eddy resulting from the analysis of the stochastically forced linearized model in the flow with no control qualitatively

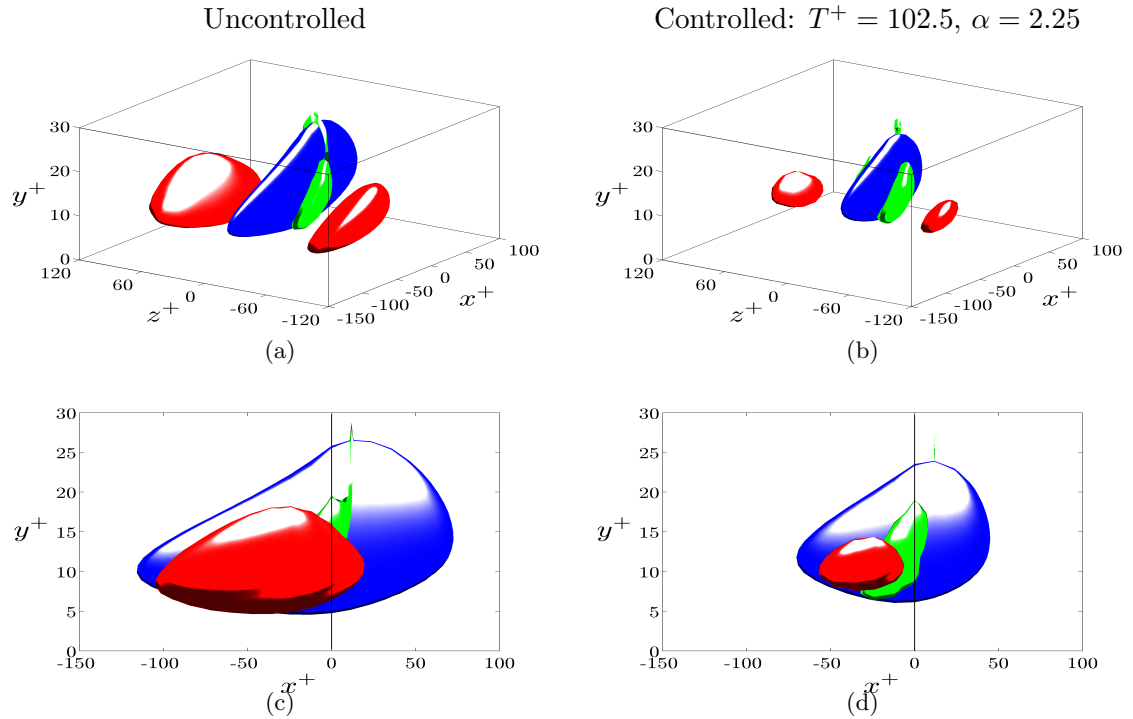


Figure 4.16: Three-dimensional iso-surfaces of the streamwise streaks (red and blue) and the vortex core (green) for the characteristic eddy in the flow with no control (left column) and the flow subject to wall oscillations (right column) with optimal drag-reducing period $T^+ = 102.5$ at $R_\tau = 186$. (a)-(b): bird's-eye view; (c)-(d): side view. The fast- (red) and slow- (blue) moving streaks are respectively shown at 70% and 60% of their largest values in the uncontrolled flow, and the vortex core is obtained based on the 'swirling strength' criterion [10] with $\lambda_{ci} > 12$, $|\lambda_{cr}/\lambda_{ci}| < 0.4$, and $\lambda_{ci}/12 - |\lambda_{cr}/\lambda_{ci}|/0.4 = 1.2$.

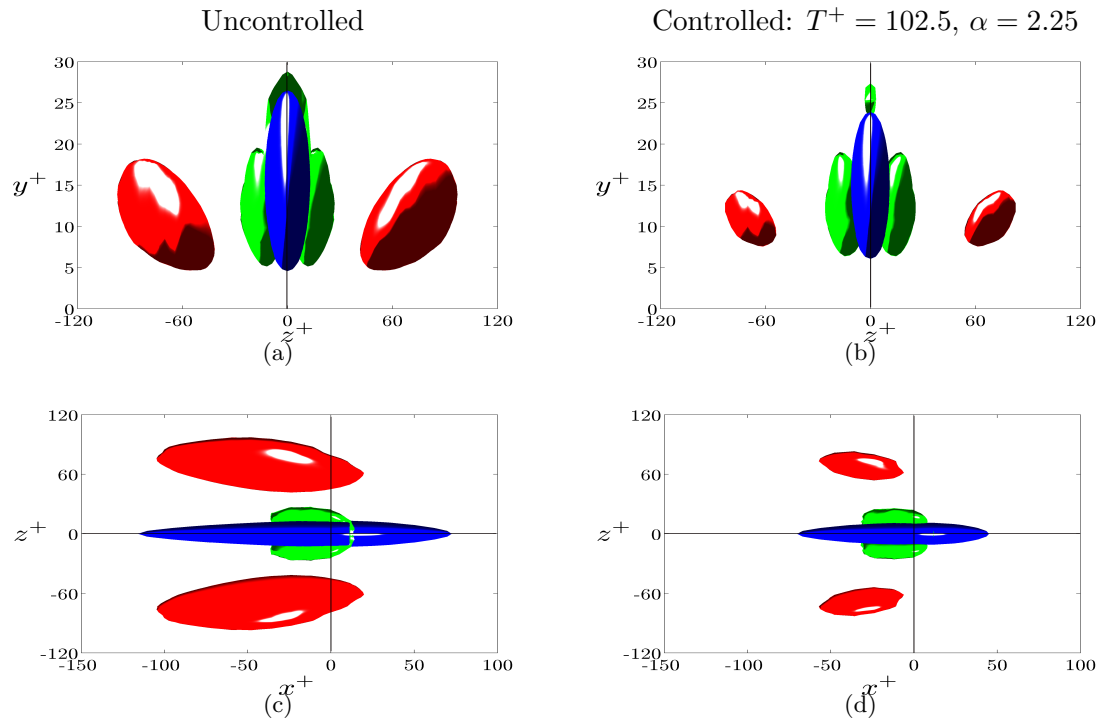


Figure 4.17: Three-dimensional iso-surfaces of the streamwise streaks (red and blue) and the vortex core (green) for the characteristic eddy in the flow with no control (left column) and the flow subject to wall oscillations (right column) with optimal drag-reducing period $T^+ = 102.5$ at $R_\tau = 186$. (a)-(b): front view; (c)-(d): top view. The fast- (red) and slow- (blue) moving streaks are respectively shown at 70% and 60% of their largest values in the uncontrolled flow, and the vortex core is obtained based on the ‘swirling strength’ criterion [10] with $\lambda_{ci} > 12$, $|\lambda_{cr}/\lambda_{ci}| < 0.4$, and $\lambda_{ci}/12 - |\lambda_{cr}/\lambda_{ci}|/0.4 = 1.2$.

agrees with the results obtained using eigenvalue decomposition of the DNS-based autocorrelation matrices; compare Figures 4.18 and 4.19 of this section with figure 15 in [148].

We next examine the effect of wall oscillations on the dominant characteristic eddy. Figures 4.16 and 4.17 compare the streamwise streaks and their surrounding vortex core for the dominant characteristic eddies in the uncontrolled flow (left column) and in the flow subject to wall oscillations with $T^+ = 102.5$ and $\alpha = 2.25$ (right column). In both cases, the iso-surfaces represent high- (red) and low- (blue) speed streaks at 70% and 60% of their largest absolute values in the uncontrolled flow, respectively. The vortex core (green surface) is obtained based on the ‘swirling strength’ criterion which identifies motions with large rate of rotation and large orbital compactness [10]. This criterion can be expressed in terms of the real and imaginary parts of the complex eigenvalues, $\lambda_{cr} \pm i\lambda_{ci}$, of the rate of strain tensor at each point inside the channel. The large rate of rotation requires $\lambda_{ci} > b_1$, where b_1 determines the strength of the swirling motion. In addition, orbital compactness is guaranteed if $|\lambda_{cr}/\lambda_{ci}| < b_2$, where b_2 determines the compactness of the swirling motion in the plane spanned by the real and imaginary parts of the eigenvector corresponding to $\lambda_{cr} \pm i\lambda_{ci}$. For example, $b_2 = 0$ identifies a pure circular motion, and larger values of b_2 allow for inclusion of the in-plane converging or diverging spiral motions to the vortex core. In Figures 4.16 and 4.17, we use $b_1 = 12$ and $b_2 = 0.4$ to identify the strong vortex core that surrounds the slow-moving streaks. We see that wall oscillations reduce intensity and spatial spread of both the streamwise streaks and the vortex core.

Figures 4.18 and 4.19 show the streamwise velocity, $u(x, y, z)$, and the spanwise vorticity, $\omega_z = v_x(x, y, z) - u_y(x, y, z)$, for the characteristic eddy in the uncontrolled flow (left column) and in the flow subject to wall oscillations with $T^+ = 102.5$ and $\alpha = 2.25$ (right column). The spanwise vortices are shown at 40%, 60%, and 80% of its largest value (black contours). The streamwise streaks (colored contours) are normalized by their largest absolute value. We see that wall oscillations suppress the largest spanwise vorticity by approximately 6.5% in the viscous sublayer $y^+ < 5$. In addition, the magnitude of streamwise streaks is reduced by approximately 12%. It was argued that transverse wall movements induce negative spanwise vorticity in the flow, thereby suppressing intensity of the streamwise streaks [129]. In addition, wall oscillations slightly move the center of the spanwise vortices away from the wall ($y^+ = 3.8$ vs. $y^+ = 4.3$), and they significantly reduce the upstream extent of the spanwise vortices.

4.5 Summary

This chapter has introduced a model-based approach to controlling turbulent flows. In contrast to standard practice that embeds turbulence models in numerical simulations, we have developed a simulation-free approach that enables computationally-efficient

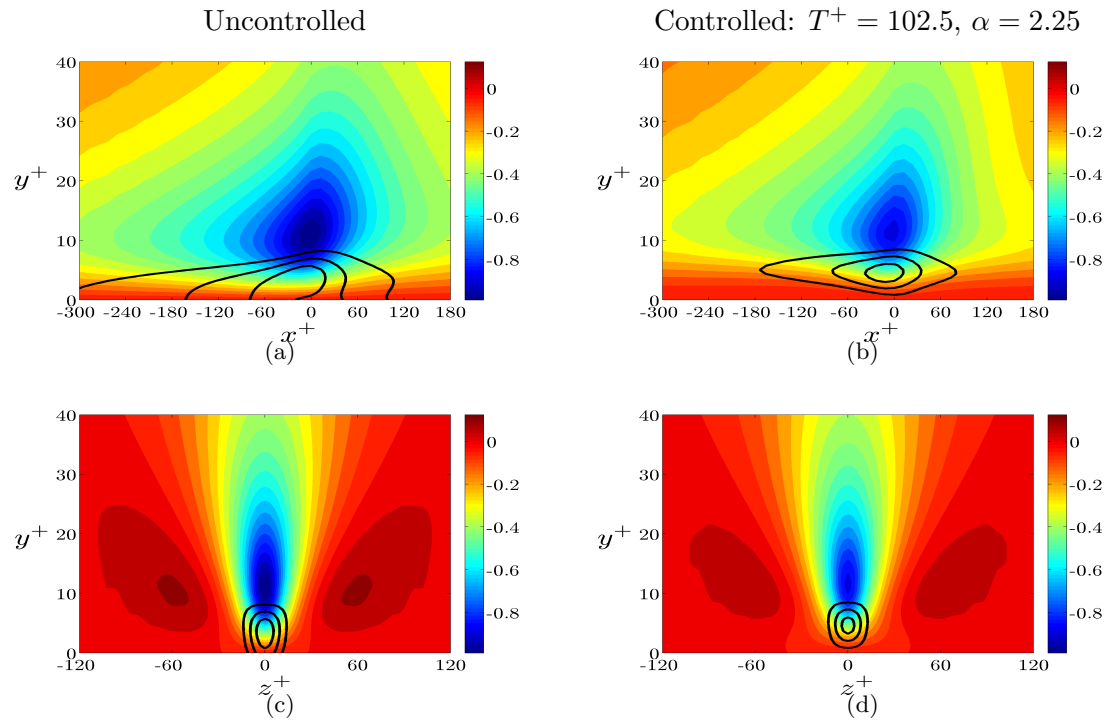


Figure 4.18: Cross sections of the streamwise velocity (colored contours) and the spanwise vorticity (black contours) for the characteristic eddy in the flow with no control (left column) and the flow subject to wall oscillations (right column) with optimal drag-reducing period $T^+ = 102.5$ at $R_\tau = 186$. (a)-(b): $z^+ = 0$; (c)-(d): $x^+ = 0$. The streamwise velocity is normalized by its largest absolute value in the uncontrolled flow, and the level sets for the spanwise vorticity correspond to 40%, 60%, and 80% of its largest value in the uncontrolled flow.

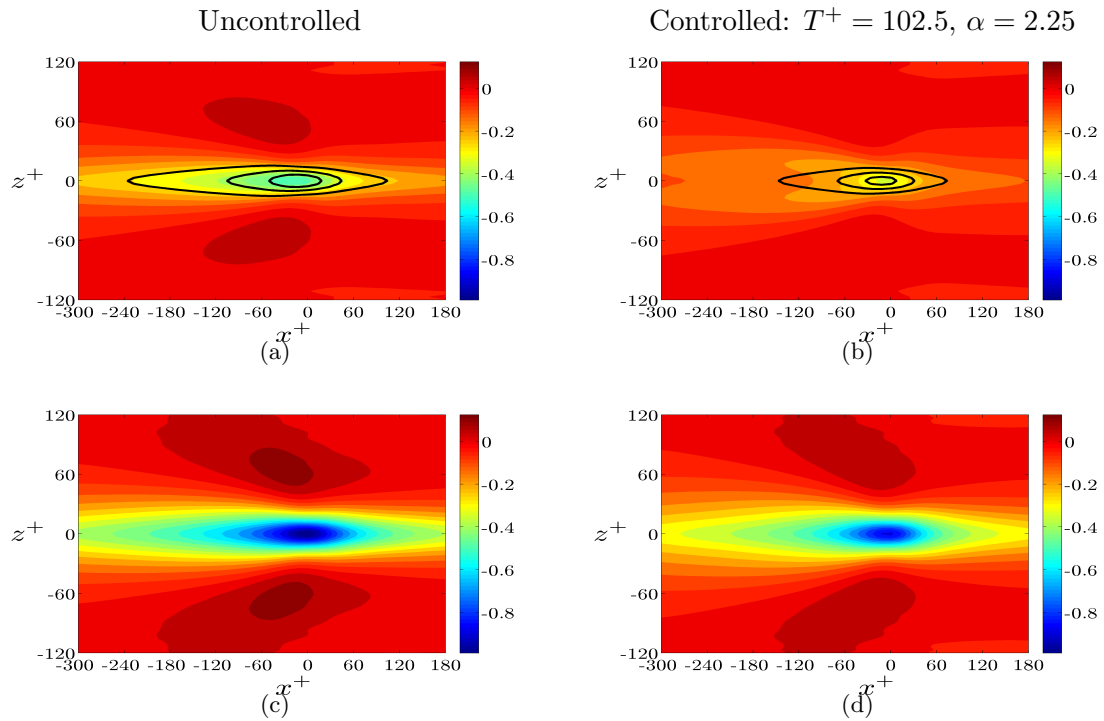


Figure 4.19: Cross sections of the streamwise velocity (colored contours) and the spanwise vorticity (black contours) for the characteristic eddy in the flow with no control (left column) and the flow subject to wall oscillations (right column) with optimal drag-reducing period $T^+ = 102.5$ at $R_\tau = 186$. (a)-(b): $y^+ = 3.8$; (c)-(d): $y^+ = 10.8$. The streamwise velocity is normalized by its largest absolute value in the uncontrolled flow, and the level sets for the spanwise vorticity correspond to 40%, 60%, and 80% of its largest value in the uncontrolled flow.

control design and optimization. This has been achieved by merging turbulence modeling with techniques from linear systems theory. In particular, we have used the turbulent viscosity hypothesis in conjunction with the k - ϵ model to determine the influence of turbulent fluctuations on the mean velocity in the flow with control.

We have shown that the study of dynamics is of prime importance in designing drag-reducing wall oscillations. This has allowed us to determine the influence of control on the turbulent viscosity in a simulation-free manner. This contribution goes well beyond the problem that was used to demonstrate the predictive power of our model-based control design – turbulent drag reduction by transverse wall oscillations. The computational complexity of determining the turbulent viscosity (in the flow with control) from the k - ϵ model has been significantly reduced by obtaining k and ϵ from the second-order statistics of judiciously selected, stochastically forced, linearized model.

The first step in our control-oriented modeling involves augmentation of the molecular viscosity with the turbulent viscosity of the flow with no control. The resulting model is then used to determine the turbulent mean velocity in the flow with control, and to study the dynamics of velocity fluctuations around it. By considering linearized equations in the presence of white-in-time stochastic forcing (whose spatial spectrum is selected to be proportional to the turbulent kinetic energy of the flow with no control), we have quantified the influence of control on the second-order statistics of velocity fluctuations and thereby on the turbulent viscosity. Finally, the modifications to the turbulent viscosity determine the turbulent mean velocity and skin-friction drag in the flow with control.

We have shown that perturbation analysis up to second order reliably predicts the optimal period of drag-reducing oscillations. Furthermore, even though the required power obtained using the turbulent viscosity of the uncontrolled flow agrees well with the values obtained in DNS, this agreement has been further improved by accounting for the effect of control on fluctuations (and, consequently, on turbulent viscosity). In addition, the predicted net efficiency resulting from perturbation analysis qualitatively agrees with the DNS results. Perturbation analysis has also captured suppression of the turbulent kinetic energy and its rate of dissipation by wall oscillations, as well as modifications to the streamwise component of the turbulent mean velocity (reduction in the viscous sublayer and buffer layer and increase in the log-law region). Finally, the spatial spectral density tensors of velocity fluctuations obtained from the solution of the corresponding Lyapunov equations determine the effect of control on the dominant flow structures. As previously observed in experiments, and confirmed by our analysis, wall oscillations reduce the spatial spread and magnitude of the dominant characteristic eddies and suppress the spanwise vorticity in the viscous sublayer.

Chapter 5

Conclusions and future directions

Conclusions

This dissertation develops a model-based paradigm for design of sensorless and feedback flow control strategies in wall-bounded shear flows. Direct numerical simulations are used to complement and verify the theoretical predictions of this dissertation.

We have shown that the stochastically forced linearized Navier-Stokes equations represent a powerful model for quantifying the influence of control on flow receptivity to disturbances. Our results have established that control strategies based on reducing the flow receptivity indeed prevent transition to turbulence at low Reynolds numbers. This was illustrated by designing a sensorless strategy based on traveling waves (Chapter 2) and an optimal state-feedback controller based on local flow information (Chapter 3) that maintain the laminar flow in the presence of perturbations that trigger turbulence in the flow with no control.

We have illustrated that turbulence modeling in conjunction with judicious linearization exhibits considerable predictive power for capturing the effect of control on turbulent flows. We have designed a sensorless strategy based on transverse wall oscillations for skin-friction drag reduction and showed that our simulation-free design is in close agreement with the design obtained from direct numerical simulations (Chapter 4).

We have shown that a large control amplitude requires large control expenditure and yields poor net efficiency. Our results have revealed that perturbation analysis (in the control amplitude) is well-suited for designing sensorless strategies based on small-amplitude periodic manipulation of the flow. This is because perturbation analysis significantly reduces the computational cost of analyzing temporally- and spatially-periodic systems by exploiting the structure of the operators that describe the flow dynamics. We conclude that perturbation analysis is a computationally-efficient tool for predicting the full-scale phenomena.

An outlook to future research directions is provided below.

Future research directions

The contribution of this dissertation goes beyond the concrete design problems that we have considered in Chapters 2, 3, and 4. The techniques presented here may be pursued in several directions that require further scrutiny and motivate future research:

Understanding the break-down of streamwise streaks and transition to turbulence. There is an abundance of experimental, numerical, and theoretical evidence that the streamwise streaks are the dominant flow structures that emerge in early stages of transition. In addition, experimental and numerical studies have shown that the streaks develop waviness and break down to turbulent spots. It has been shown that three-dimensional fluctuations around sufficiently strong streaks become unstable and trigger transition to turbulence [34,35]. However, it has also been suggested that break-down may occur in the absence of instabilities [22,36]. The computational tools that we have developed for analysis of systems with periodic coefficients may find use in better understanding of the streaks' break-down. This can be done by studying the receptivity of three-dimensional fluctuations around the two-dimensional spanwise-periodic streaks. Analysis of the nonlinear interaction of fluctuations with the original streaks and the interplay between them may provide more insight into the mechanisms for transition and provide guidelines for designing control strategies for preventing transition.

Developing superior control-oriented models of turbulent flows. We have illustrated that simple turbulence modeling (that relies on the turbulent viscosity hypothesis and the k - ϵ model) in conjunction with judicious linearization of the flow with control has significant predictive power for capturing full-scale phenomena. Even though it is well-known that the k - ϵ model does not reveal all aspects of turbulent flow physics, we have shown that it is well-suited for control design and optimization. Development of more sophisticated control-oriented turbulence models may further reduce the gap between theoretical predictions and experiments/simulations. In addition, the predictive power of the proposed approach can be enhanced by optimization of the power spectrum of the forcing. We expect that our model-based approach will find use in designing feedback-based and sensor-less turbulence suppression strategies in other geometries, including pipes and boundary layers.

Designing sensorless strategies based on wall-transpiration and periodic geometries. We have already developed computational tools for analysis of spatially-periodic systems. The inherent large scale of these systems poses significant challenges in their analysis. In Appendix D, we have overcome this obstacle by utilizing perturbation techniques that allows for efficient characterization of transient behavior of spatially-periodic systems. We have also shown how descriptor formulation can be used for computation of energy amplification in incompressible fluids in Appendix E. This approach avoids the need for finding the evolution model which is advantageous in many applications. The control-oriented models and analytical tools that we have developed may offer guidelines for simulation-free control design based on wall-transpiration using synthetic jets and more sophisticated periodic geometries, such as riblets, vortex

generators, and superhydrophobic surfaces.

Designing optimal localized feedback flow controllers. Research directions in the area of distributed control design include: (i) optimal sensor and actuator placement; (ii) understanding the effect of placing sensors and actuators on a discrete lattice; (iii) distributed measurement and estimation of relevant quantities for flow control; and (iv) developing computationally efficient tools for flow control optimization.

References

- [1] J. C. del Alamo and J. Jiménez. Spectra of the very large anisotropic scales in turbulent channels. *Physics of Fluids*, 15(6):41–44, 2003.
- [2] J. C. del Alamo, J. Jiménez, P. Zandonade, and R. D. Moser. Scaling of the energy spectra of turbulent channels. *J. Fluid Mech.*, 500(1):135–144, 2004.
- [3] W. S. Saric, H. L. Reed, and E. J. Kerschen. Boundary-layer receptivity to freestream disturbances. *Annu. Rev. Fluid Mech.*, 34:291–319, 2002.
- [4] M. Matsubara and P. H. Alfredsson. Disturbance growth in boundary layers subjected to free-stream turbulence. *J. Fluid Mech.*, 430:149–168, 2001.
- [5] P. Durbin and X. Wu. Transition beneath vortical disturbances. *Annu. Rev. Fluid Mech.*, 39:107–128, 2007.
- [6] T. Yoshino, Y. Suzuki, and N. Kasagi. Drag reduction of turbulence air channel flow with distributed micro sensors and actuators. *J. Fluid Sci. Tech.*, 3(1):137–148, 2008.
- [7] M. R. Jovanović and B. Bamieh. Componentwise energy amplification in channel flows. *J. Fluid Mech.*, 534:145–183, July 2005.
- [8] T. Min, S. M. Kang, J. L. Speyer, and J. Kim. Sustained sub-laminar drag in a fully developed channel flow. *J. Fluid Mech.*, 558:309–318, 2006.
- [9] M. Quadrio and P. Ricco. Critical assessment of turbulent drag reduction through spanwise wall oscillations. *J. Fluid Mech.*, 521:251–271, 2004.
- [10] P. Chakraborty, S. Balachandar, and R. J. Adrian. On the relationships between local vortex identification schemes. *J. Fluid Mech.*, 535:189–214, 2005.
- [11] M. Gad-el Hak. *Flow control: passive, active, and reactive flow management*. Cambridge University Press, 2000.
- [12] G. K. Batchelor. *An introduction to fluid dynamics*. Cambridge University Press, 2000.

- [13] R. D. Joslin. Aircraft laminar flow control. *Ann. Rev. Fluid Mech.*, 30:1–29, 1998.
- [14] B. Eckhardt, T. M. Schneider, B. Hof, and J. Westerweel. Turbulence transition in pipe flow. *Annu. Rev. Fluid Mech.*, 39:447–468, 2007.
- [15] T. Mullin. Experimental studies of transition to turbulence in a pipe. *Annu. Rev. Fluid Mech.*, 43:1–24, 2011.
- [16] B. J. Cantwell. Organized motion in turbulent flow. *Annu. Rev. Fluid Mech.*, 13:457–515, 1981.
- [17] S. K. Robinson. Coherent motions in the turbulent boundary layer. *Annu. Rev. Fluid Mech.*, 23:601–639, 1991.
- [18] J. Jiménez. Turbulent flows over rough walls. *Annu. Rev. Fluid Mech.*, 36:173–196, 2004.
- [19] A. J. Smits, B. J. McKeon, and I. Marusic. High-reynolds number wall turbulence. *Annu. Rev. Fluid Mech.*, 43:353–375, 2011.
- [20] M. V. Morkovin. On the many faces of transition. In C. S. Wells, editor, *Viscous Drag Reduction*, pages 1–31. Plenum Press, 1969.
- [21] P. Andersson, L. Brandt, A. Bottaro, and D. S. Henningson. On the breakdown of boundary layer streaks. *J. Fluid Mech.*, 428:29–60, 2001.
- [22] W. Schoppa and F. Hussain. Coherent structure generation in near-wall turbulence. *J. Fluid Mech.*, 453:57–108, 2002.
- [23] J. Hoepffner, L. Brandt, and D.S. Henningson. Transient growth on boundary layer streaks. *J. Fluid Mech.*, 537:91–100, 2005.
- [24] K. M. Butler and B. F. Farrell. Three-dimensional optimal perturbations in viscous shear flow. *Phys. Fluids A*, 4:1637, 1992.
- [25] L. N. Trefethen, A. E. Trefethen, S. C. Reddy, and T. A. Driscoll. Hydrodynamic stability without eigenvalues. *Science*, 261:578–584, 1993.
- [26] S. C. Reddy and D. S. Henningson. Energy growth in viscous channel flows. *J. Fluid Mech.*, 252:209–238, 1993.
- [27] B. F. Farrell and P. J. Ioannou. Stochastic forcing of the linearized Navier-Stokes equations. *Phys. Fluids A*, 5(11):2600–2609, 1993.
- [28] B. Bamieh and M. Dahleh. Energy amplification in channel flows with stochastic excitation. *Phys. Fluids*, 13(11):3258–3269, 2001.

- [29] N. Hoda, M. R. Jovanović, and S. Kumar. Energy amplification in channel flows of viscoelastic fluids. *J. Fluid Mech.*, 601:407–424, April 2008.
- [30] N. Hoda, M. R. Jovanović, and S. Kumar. Frequency responses of streamwise-constant perturbations in channel flows of oldroyd-b fluids. *J. Fluid Mech.*, 625:411–434, April 2009.
- [31] M. R. Jovanović and S. Kumar. Transient growth without inertia. *Phys. Fluids*, 22(2):023101 (19 pages), February 2010.
- [32] M. R. Jovanović and S. Kumar. Nonmodal amplification of stochastic disturbances in strongly elastic channel flows. *J. Non-Newtonian Fluid Mech.*, 166(14-15):755–778, August 2011.
- [33] X. Wu and P. Moin. Direct numerical simulation of turbulence in a nominally zero-pressure-gradient at-plate boundary layer. *J. Fluid Mech.*, 630:5–41, 2009.
- [34] F. Waleffe. On a self-sustaining process in shear flows. *Phys. Fluids*, 9(4):883–900, 1997.
- [35] F. Waleffe. Homotopy of exact coherent structures in plane shear flows. *Phys. Fluids*, 15:1517, 2003.
- [36] R. G. Jacobs and P. A. Durbin. Simulations of bypass transition. *J. Fluid Mech.*, 428:185–212, 2001.
- [37] L. Brandt, D. S. Henningson, and D. Ponziani. Weakly nonlinear analysis of boundary layer receptivity to free-stream disturbances. *Phys. Fluids*, 14(4):1424–1441, 2002.
- [38] J. Hoepffner and L. Brandt. Stochastic approach to the receptivity problem applied to bypass transition in boundary layers. *Phys. Fluids*, 20(2):024108, February 2008.
- [39] L. U. Schrader, L. Brandt, and D. S. Henningson. Receptivity mechanisms in three-dimensional boundary-layer flows. *J. Fluid Mech.*, 618(1):209–241, 2009.
- [40] A. Monokrousos, A. Bottaro, L. Brandt, A. Di Vita, and D. S. Henningson. Non-equilibrium thermodynamics and the optimal path to turbulence in shear flows. *Physical Review Letters*, 106(13):134502, 2011.
- [41] C. Cossu, L. Brandt, S. Bagheri, and D. S. Henningson. Secondary threshold amplitudes for sinuous streak breakdown. *Phys. Fluids*, 23:074103, 2011.
- [42] J. Kim and T. R. Bewley. A linear systems approach to flow control. *Annu. Rev. Fluid Mech.*, 39:383–417, 2007.

- [43] J. Lumley and P. Blossey. Control of turbulence. *Annu. Rev. Fluid Mech.*, 30:311–327, 1998.
- [44] T. R. Bewley. Flow control: new challenges for a new renaissance. *Prog. Aerosp. Sci.*, 37:21–58, 2001.
- [45] H. Choi, W. P. Jeon, and J. Kim. Control of flow over a bluff body. *Annu. Rev. Fluid Mech.*, 40:113–139, 2008.
- [46] C.-M. Ho and Y.-C. Tai. Review: MEMS and its applications for flow control. *J. Fluids Eng.*, 118:437447, 1996.
- [47] C.-M. Ho and Y.-C. Tai. Micro-electro-mechanical-systems (MEMS) and fluid flows. *Annu. Rev. Fluid Mech.*, 30:579–612, 1998.
- [48] N. Kasagi, Y. Suzuki, and K. Fukagata. Microelectromechanical systems-based feedback control of turbulence for skin friction reduction. *Annu. Rev. Fluid Mech.*, 41:231–251, 2009.
- [49] G. Karniadakis and K.-S. Choi. Mechanisms on transverse motions in turbulent wall flows. *Annu. Rev. Fluid Mech.*, 35:45–62, 2003.
- [50] D. M. Bushnell and K. J. Moore. Drag reduction in nature. *Annu. Rev. Fluid Mech.*, 23:65–79, 1991.
- [51] M. J. Walsh. Riblets as a viscous drag reduction technique. *AIAA J.*, 21(4):485–486, 1983.
- [52] S. S. Joshi, J. L. Speyer, and J. Kim. A systems theory approach to the feedback stabilization of infinitesimal and finite-amplitude disturbances in plane poiseuille flow. *J. Fluid Mech.*, 332(1):157–184, 1997.
- [53] T. R. Bewley and S. Liu. Optimal and robust control and estimation of linear paths to transition. *J. Fluid Mech.*, 365:305–349, 1998.
- [54] K. H. Lee, L. Cortelezzi, J. Kim, and J. Speyer. Application of reduced-order controller to turbulent flows for drag reduction. *Phys. Fluids*, 13(5):1321–1330, 2001.
- [55] J. Kim. Control of turbulent boundary layers. *Phys. Fluids*, 15(5):1093–1105, 2003.
- [56] M. Högberg, T. R. Bewley, and D. S. Henningson. Linear feedback control and estimation of transition in plane channel flow. *J. Fluid Mech.*, 481:149–175, 2003.

- [57] M. Högberg, T. R. Bewley, and D. S. Henningson. Relaminarization of $Re_\tau = 100$ turbulence using linear state-feedback control. *Phys. Fluids*, 15(11):3572–3575, 2003.
- [58] J. Hoepffner, M. Chevalier, T.R. Bewley, and D.S. Henningson. State estimation in wall-bounded flow systems. Part 1. Perturbed laminar flows. *J. Fluid Mech.*, 534:263–294, 2005.
- [59] M. Chevalier, J. Hoepffner, T.R. Bewley, and D.S. Henningson. State estimation in wall-bounded flow systems. Part 2. Turbulent flows. *J. Fluid Mech.*, 552:167–187, 2006.
- [60] R. Vazquez and M. Krstic. A closed-form feedback controller for stabilization of the linearized 2D Navier-Stokes Poiseuille flow. *IEEE Transactions on Automatic Control*, 52(12):2298–2312, 2007.
- [61] R. Vazquez and M. Krstic. *Control of Turbulent and Magnetohydrodynamic Channel Flows: Boundary Stabilization and State Estimation*. Birkhauser, 2007.
- [62] J. Cochran and M. Krstic. Motion planning and trajectory tracking for the 3-D Poiseuille flow. *J. Fluid Mech.*, 626:307–332, 2009.
- [63] A. S. Sharma, J.F. Morrison, B. J. McKeon, D. J. N. Limebeer, W. H. Koberg, and S. J. Sherwin. Relaminarisation of $Re_\tau = 100$ channel flow with globally stabilising linear feedback control. *Phys. Fluids*, 23:125105, 2011.
- [64] P. J. Schmid. Nonmodal stability theory. *Annu. Rev. Fluid Mech.*, 39:129–162, 2007.
- [65] J. Hoepffner and K. Fukagata. Pumping or drag reduction? *J. Fluid Mech.*, 635:171–187, 2009.
- [66] B. Bamieh, F. Paganini, and M. A. Dahleh. Distributed control of spatially invariant systems. *IEEE Trans. Automat. Control*, 47(7):1091–1107, 2002.
- [67] N. Motee and A. Jadbabaie. Optimal control of spatially distributed systems. *IEEE Trans. Automat. Control*, 53(7):1616–1629, 2008.
- [68] M. Fardad, F. Lin, and M. R. Jovanović. On the optimal design of structured feedback gains for interconnected systems. In *Proceedings of the 48th IEEE Conference on Decision and Control*, pages 978–983, Shanghai, China, 2009.
- [69] F. Lin, M. Fardad, and M. R. Jovanović. Augmented Lagrangian approach to design of structured optimal state feedback gains. *IEEE Trans. Automat. Control*, 56(12):2923–2929, December 2011.

- [70] W. D. McComb. *The Physics of Fluid Turbulence*. Oxford University Press Inc., 1991.
- [71] P. A. Durbin and B. A. Petterson Reif. *Theory and modeling of turbulent flows*. Wiley, 2000.
- [72] S. B. Pope. *Turbulent flows*. Cambridge University Press, 2000.
- [73] J. C. del Alamo and J. Jiménez. Linear energy amplification in turbulent channels. *J. Fluid Mech.*, 559:205213, 2006.
- [74] C. Cossu, G. Pujals, and S. Depardon. Optimal transient growth and very large-scale structures in turbulent boundary layers. *J. Fluid Mech.*, 619:79–94, 2009.
- [75] G. Pujals, M. García-Villalba, C. Cossu, and S. Depardon. A note on optimal transient growth in turbulent channel flows. *Phys. Fluids*, 21(1):015109, 2009.
- [76] K. Fukagata, K. Iwamoto, and N. Kasagi. Contribution of Reynolds stress distribution to the skin friction in wall-bounded flows. *Phys. Fluids*, 14:L73, 2002.
- [77] T.R. Bewley and O. M. Aamo. A "win-win" mechanism for low-drag transients in controlled two-dimensional channel flow and its implications for sustained drag reduction. *J. Fluid Mech.*, 499:183–196, 2004.
- [78] I. Marusic, D. D. Joseph, and K. Mahesh. Laminar and turbulent comparisons for channel flow and flow control. *J. Fluid Mech.*, 570:467–477, 2007.
- [79] T. R. Bewley. A fundamental limit on the balance of power in a transpiration-controlled channel flow. *J. Fluid Mech.*, 632:443–446, 2009.
- [80] K. Fukagata, K. Sugiyama, and N. Kasagi. On the lower bound of net driving power in controlled duct flows. *Physica D: Nonlinear Phenomena*, 238(13):1082–1086, 2009.
- [81] M. R. Jovanović, R. Moarref, and D. You. Turbulence suppression in channel flows by means of a streamwise traveling wave. In *Proceedings of the 2006 Summer Program*, pages 481–494, Center for Turbulence Research, Stanford University/NASA, 2006.
- [82] C. Lee, T. Min, and J. Kim. Stability of a channel flow subject to wall blowing and suction in the form of a traveling wave. *Phys. Fluids*, 20(10):101513, 2008.
- [83] I. G. Currie. *Fundamental Mechanics of Fluids*. CRC Press, 2003.
- [84] P. J. Schmid and D. S. Henningson. *Stability and Transition in Shear Flows*. Springer-Verlag, 2001.

- [85] F. Odeh and J. B. Keller. Partial differential equations with periodic coefficients and Bloch waves in crystals. *J. Math. Phys.*, 5:1499–1504, 1964.
- [86] A. Bensoussan, J. L. Lions, and G. Papanicolaou. *Asymptotic analysis for periodic structures*. North Holland, 1978.
- [87] M. Fardad, M. R. Jovanović, and B. Bamieh. Frequency analysis and norms of distributed spatially periodic systems. *IEEE Trans. Automat. Control*, 53(10):2266–2279, November 2008.
- [88] M. R. Jovanović. Turbulence suppression in channel flows by small amplitude transverse wall oscillations. *Phys. Fluids*, 20(1):014101 (11 pages), January 2008.
- [89] M. R. Jovanović and M. Fardad. H_2 norm of linear time-periodic systems: a perturbation analysis. *Automatica*, 44(8):2090–2098, August 2008.
- [90] M. Fardad and B. Bamieh. Perturbation methods in stability and norm analysis of spatially periodic systems. *SIAM J. Control Optim.*, 47(2):997–1021, 2008.
- [91] M. T. Landahl. Wave breakdown and turbulence. *SIAM J. Appl. Math.*, 28:735–756, 1975.
- [92] D. Shanks. Nonlinear transformations of divergent and slowly convergent sequences. *J. Math. and Phys.*, 34:1–42, 1955.
- [93] M. Van Dyke. *Perturbation Methods in Fluid Mechanics*. Applied Mathematics and Mechanics 8. Academic Press Inc., 1964.
- [94] A. Sidi. *Practical Extrapolation Methods: theory and applications*. Cambridge University Press, 2003.
- [95] J. F. Gibson. Channelflow: a spectral Navier-Stokes solver in C++. *Tech. Rep.*, 2007.
- [96] R. Peyret. *Spectral Methods for Incompressible Viscous Flow*. Springer, New York, NY, 2002.
- [97] C. Canuto, M. Y. Hussaini, A. Quarteroni, and T. A. Zang. *Spectral Methods in Fluid Dynamics*. Springer-Verlag, New York, NY, 1988.
- [98] M. S. Chong, A. E. Perry, and B. J. Cantwell. A general classification of three-dimensional flow fields. *Phys. Fluid A*, 2:765–777, 1990.
- [99] N. D. Sandham and L. Kleiser. The late stages of transition to turbulence in channel flow. *J. Fluid Mech.*, 245:319–348, 1992.

- [100] H. M. Blackburn, N. N. Mansour, and B. J. Cantwell. Topology of fine-scale motions in turbulent channel flow. *J. Fluid Mech.*, 310:269–292, 1996.
- [101] T. R. Bewley, P. Moin, and R. Temam. DNS-based predictive control of turbulence: an optimal benchmark for feedback algorithms. *J. Fluid Mech.*, 447:179–225, 2001.
- [102] A. E. Perry and M. S. Chong. A description of eddying motions and flow patterns using critical-point concepts. *Ann. Rev. Fluid Mech.*, 19:125–155, 1987.
- [103] M. S. Chong, J. Soria, A. E. Perry, J. Chacin, B. J. Cantwell, and Y. Na. Turbulence structures of wall-bounded shear flow found using DNS data. *J. Fluid Mech.*, 357:225–247, 1998.
- [104] U. Brosa. Turbulence without strange attractor. *J. Stat. Phys.*, 55(5):1303–1312, 1989.
- [105] S. Grossmann. The onset of shear flow turbulence. *Rev. Mod. Phys.*, 72:603–618, 2000.
- [106] B. Hof, J. Westerweel, T. M. Schneider, and B. Eckhardt. Finite lifetime of turbulence in shear flows. *Nature*, 443(7):59 – 62, 2006.
- [107] D. Borrero-Echeverry, M. F. Schatz, and R. Tagg. Transient turbulence in Taylor-Couette flow. *Phys. Rev. E*, 81(2):25301, 2010.
- [108] A. Scotti and U. Piomelli. Numerical simulation of pulsating turbulent channel flow. *Phys. Fluids*, 13(5):1367–1384, 2001.
- [109] F. Waleffe. Exact coherent structures in channel flow. *J. Fluid Mech.*, 435:93–102, 2001.
- [110] J. Jiménez, G. Kawahara, M. P. Simens, M. Nagata, and M. Shiba. Characterization of near-wall turbulence in terms of equilibrium and “bursting” solutions. *Phys. Fluids*, 17(1):015105, 2005.
- [111] R. R. Kerswell. Recent progress in understanding the transition to turbulence in a pipe. *Nonlinearity*, 18:R17–R44, 2005.
- [112] H. Choi, P. Moin, and J. Kim. Active turbulence control for drag reduction in wall-bounded flows. *J. Fluid Mech.*, 262:75–110, 1994.
- [113] H. Choi, R. Temam, P. Moin, and J. Kim. Feedback control for unsteady flow and its application to the stochastic Burgers equation. *J. Fluid Mech.*, 253:509–543, 1993.

- [114] T. Bewley and P. Moin. Optimal control of turbulent channel flows. *Active Control of Vibration and Noise, ASME-DE*, 75, 1994.
- [115] R. Moarref and M. R. Jovanović. Controlling the onset of turbulence by streamwise traveling waves. part 1: Receptivity analysis. *J. Fluid Mech.*, 663:70–99, November 2010.
- [116] B. K. Lieu, R. Moarref, and M. R. Jovanović. Controlling the onset of turbulence by streamwise traveling waves. part 2: Direct numerical simulations. *J. Fluid Mech.*, 663:100–119, November 2010.
- [117] K. Zhou, J. C. Doyle, and K. Glover. *Robust and Optimal Control*. Prentice Hall, 1996.
- [118] J. A. C. Weideman and S. C. Reddy. A MATLAB differentiation matrix suite. *ACM Transactions on Mathematical Software*, 26(4):465–519, December 2000.
- [119] A. Hanifi, P. J. Schmid, and D. S. Henningson. Transient growth in compressible boundary layer flow. *Physics of Fluids*, 8(3):826–837, 1996.
- [120] S. Boyd and L. Vandenberghe. *Convex optimization*. Cambridge University Press, New York, 2004.
- [121] M. R. Jovanović and T. T. Georgiou. Reproducing second order statistics of turbulent flows using linearized navier-stokes equations with forcing. *Bulletin of the American Physical Society*, 55, 2010.
- [122] J. Kim, P. Moin, and R. Moser. Turbulence statistics in fully developed channel flow at low Reynolds number. *J. Fluid Mech.*, 177:133–166, 1987.
- [123] R. D. Moser, J. Kim, and N. N. Mansour. DNS of turbulent channel flow up to $Re_\tau = 590$. *Phys. Fluids*, 11(4):943–945, 1999.
- [124] P. Bradshaw and N. S. Pontikos. Measurements in the turbulent boundary layer on an infinite swept wing. *J. Fluid Mech.*, 159(105):30, 1985.
- [125] P. Moin, T. H. Shih, D. Driver, and N. N. Mansour. Direct numerical simulation of a three-dimensional turbulent boundary layer. *Phys. Fluids A: Fluid Dynamics*, 2(10):1846, 1990.
- [126] W.J. Jung, N. Mangiavacchi, and R. Akhavan. Suppression of turbulence in wall-bounded flows by high-frequency spanwise oscillations. *Phys. Fluids A*, 4(8):1605–1607, 1992.
- [127] F. Laadhari, L. Skandaji, and R. Morel. Turbulence reduction in a boundary layer by a local spanwise oscillating surface. *Phys. Fluids*, 6(10):3218–3220, 1994.

- [128] Kwing-So Choi, J.-R. DeBisschop, and B. R. Clayton. Turbulent boundary-layer control by means of spanwise-wall oscillation. *AIAA J.*, 36(7):1157–1163, 1998.
- [129] K.-S. Choi. Near-wall structure of turbulent boundary layer with spanwise-wall oscillation. *Phys. Fluids*, 14(7):2530–2542, 2002.
- [130] P. Ricco. Modification of near-wall turbulence due to spanwise wall oscillations. *J. Turbul.*, (5), 2004.
- [131] T. W. Berger, J. Kim, C. Lee, and J. Lim. Turbulent boundary layer control utilizing the Lorentz force. *Phys. Fluids*, 12(3):631–649, 2000.
- [132] Y. Du and G. E. Karniadakis. Suppressing wall turbulence by means of a transverse traveling wave. *Science*, 288:1230–1234, 2000.
- [133] Y. Du, V. Symeonidis, and G. E. Karniadakis. Drag reduction in wall-bounded turbulence via a transverse travelling wave. *J. Fluid Mech.*, 457:1–34, 2002.
- [134] M. Quadrio, P. Ricco, and C. Viotti. Streamwise-travelling waves of spanwise wall velocity for turbulent drag reduction. *J. Fluid Mech.*, 627(1):161–178, 2009.
- [135] F. Auteri, A. Baron, M. Belan, G. Campanardi, and M. Quadrio. Experimental assessment of drag reduction by traveling waves in a turbulent pipe flow. *Phys. Fluids*, 22:115103, 2010.
- [136] M. Quadrio and P. Ricco. The laminar generalized stokes layer and turbulent drag reduction. *J. Fluid Mech.*, 667:135–157, 2011.
- [137] M. Quadrio and S. Sibilla. Numerical simulation of turbulent flow in a pipe oscillating around its axis. *J. Fluid Mech.*, 424:217–241, 2000.
- [138] A. Baron and M. Quadrio. Turbulent drag reduction by spanwise wall oscillations. *Appl. Sci. Res.*, 55(4):311–326, 1996.
- [139] M. Quadrio and P. Ricco. Initial response of a turbulent channel flow to spanwise oscillation of the walls. *J. Turbul.*, (4):007, 2003.
- [140] M. Quadrio. Drag reduction in turbulent boundary layers by in-plane wall motion. *Phil. Trans. R. Soc. A*, 369(1940):1428–1442, 2011.
- [141] W. V. R. Malkus. Outline of a theory of turbulent shear flow. *J. Fluid Mech.*, 1(5):521–539, 1956.
- [142] R. D. Cess. A survey of the literature on heat transfer in turbulent tube flow. *Westinghouse Research, Rep. 8-0529-R24*, 1958.

- [143] W. C. Reynolds and W. G. Tiederman. Stability of turbulent channel flow with application to Malkus's theory. *J. Fluid Mech.*, 27(2):253–272, 1967.
- [144] R. L. Panton. *Incompressible flows*. John Wiley & Sons, Inc., 1996.
- [145] W. P. Jones and B. E. Launder. The prediction of laminarization with a two-equation model of turbulence. *Int. J. Heat Mass Transf.*, 15(2):301–314, 1972.
- [146] B. E. Launder and B. I. Sharma. Application of the energy-dissipation model of turbulence to the calculation of flow near a spinning disc. *Lett. Heat Mass Transf.*, 1:131–137, 1974.
- [147] W. A. Gardner. *Introduction to Random Processes: with applications to signals and systems*. McGraw-Hill, 1990.
- [148] P. Moin and R. Moser. Characteristic-eddy decomposition of turbulence in a channel. *J. Fluid Mech.*, 200:471–509, 1989.
- [149] P. Wynn. Upon systems of recursions which obtain among the quotients of the Padé table. *Numerische Mathematik*, 8(3):264–269, 1966.
- [150] G. K. Batchelor. *The theory of homogeneous turbulence*. Athenaeum Press, 1953.
- [151] T. Kato. *Perturbation Theory for Linear Operators*. Springer-Verlag, 1995.
- [152] H. Baumgartel. *Analytic Perturbation Theory for Matrices and Operators*. Birkhauser, 1985.
- [153] B. Bamieh and J. B. Pearson. A general framework for linear periodic systems with applications to H^∞ sampled-data control. *IEEE Transactions on Automatic Control*, 37(4):418–435, April 1992.
- [154] M. Fardad. *The Analysis of Distributed Spatially Periodic Systems*. PhD thesis, University of California, Santa Barbara, 2006.
- [155] M. R. Jovanović. *Modeling, analysis, and control of spatially distributed systems*. PhD thesis, University of California, Santa Barbara, 2004.
- [156] R. F. Curtain and H. J. Zwart. *An Introduction to Infinite-Dimensional Linear Systems Theory*. Springer-Verlag, 1995.
- [157] R. Sincovec, A. Erisman, E. Yip, and M. Empton. Analysis of descriptor systems using numerical algorithms. *IEEE Transactions on Automatic Control*, 26(1):139–147, 1981.
- [158] T. Stykel. On some norms for descriptor systems. *IEEE Transactions on Automatic Control*, 51(5):842–847, May 2006.

- [159] D. J. Bender. Lyapunov-like equations and reachability/observability gramians for descriptor systems. *IEEE Transactions on Automatic Control*, 32(4):343–348, April 1987.
- [160] L. M. Manning, B. Bamieh, and J. M. Carlson. Eliminating spurious eigenvalues in the analysis of incompressible fluids and other systems of differential-algebraic equations. *J. Comp. Phys.*, 2007. submitted.
- [161] T. Stykel. *Analysis and numerical solution of Generalized Lyapunov Equations*. PhD thesis, Institut für Mathematik, Technische Universität Berlin, 2002.
- [162] F. L. Lewis. Fundamental, reachability, and observability matrices for discrete descriptor systems. *IEEE Transactions on Automatic Control*, 30(5):502–505, May 1985.
- [163] B. Kågström and L. Westin. Generalized schur methods with condition estimators for solving the generalized sylvester equation. *IEEE Transactions on Automatic Control*, 34(7):745–751, July 1989.
- [164] J. P. Boyd. *Chebyshev and Fourier Spectral Methods*. Dover, Mineola, NY., 2001.

Appendix A

Determining numerical adjoints

Consider the operator $A : \mathbb{H}_1 \mapsto \mathbb{H}_2$ that maps a function $h_1 \in \mathbb{H}_1[-1, 1]$ into a function $h_2 \in \mathbb{H}_2[-1, 1]$, where $\mathbb{H}_1[-1, 1]$ and $\mathbb{H}_2[-1, 1]$ are Hilbert spaces. The adjoint of this operator, denoted by $A^+ : \mathbb{H}_2 \mapsto \mathbb{H}_1$, is determined from

$$\langle h_2, A h_1 \rangle_{\mathbb{H}_2} = \langle A^+ h_2, h_1 \rangle_{\mathbb{H}_1},$$

where $\langle \cdot, \cdot \rangle_{\mathbb{H}_1}$ and $\langle \cdot, \cdot \rangle_{\mathbb{H}_2}$, respectively, represent the appropriate inner products in spaces \mathbb{H}_1 and \mathbb{H}_2 . We consider the case where each of these inner products can be expressed in terms of weighted inner products in $L_2[-1, 1]$, i.e.,

$$\langle h_2, Q_2 A h_1 \rangle = \langle A^+ h_2, Q_1 h_1 \rangle, \quad (\text{A.1})$$

where the operators Q_1 and Q_2 denote the weights in appropriate spaces, and $\langle \cdot, \cdot \rangle$ is the standard inner product in $L_2[-1, 1]$

$$\langle f, g \rangle = \int_{-1}^1 f(y)^* g(y) dy, \quad f, g \in L_2[-1, 1].$$

Here, $*$ denotes the complex conjugate transpose. By discretizing the above functions and operators in y , equation (A.1) can be rewritten as

$$\mathbf{h}_2^* \mathbf{Q}_2 \mathbf{A} \mathbf{h}_1 = \mathbf{h}_2^* (\mathbf{A}^+)^* \mathbf{Q}_1 \mathbf{h}_1,$$

where the vectors \mathbf{h}_1 and \mathbf{h}_2 are the discretized h_1 and h_2 , the matrices \mathbf{A} , \mathbf{A}^+ , \mathbf{Q}_1 , and \mathbf{Q}_2 denote the discretized versions of the corresponding operators, and the integration weights corresponding to the L_2 inner product in (A.1) are embedded in \mathbf{Q}_1 , and \mathbf{Q}_2 . Finally, the numerical approximation to the adjoint of operator A is obtained from

$$\mathbf{A}^+ = \mathbf{Q}_1^{-1} \mathbf{A}^* \mathbf{Q}_2.$$

Appendix B

Shanks transformation

The Shanks transformation [92, 94] is an extrapolation method. Extrapolation methods are used to overcome the problem of slow convergence or even divergence of sequences. Given a sequence $\{S_j\}$, the Shanks transformation generates a new sequence $\{\hat{S}_j\}$ that converges more quickly to the limit of $\{S_j\}$ when this limit exists. In the case where the limit of $\{S_j\}$ does not exist, the new sequence $\{\hat{S}_j\}$ either diverges more slowly than $\{S_j\}$ or converges to a value that $\{S_j\}$ is diverging from (called the anti-limit of $\{S_j\}$). The anti-limit has a useful meaning or interpretation in most applications. For example, consider a perturbation series

$$U = U_0 + \alpha U_1 + \alpha^2 U_2 + \alpha^3 U_3 + \alpha^4 U_4 + \alpha^5 U_5 + \dots,$$

that represents the solution of a nonlinear equation in U with a small parameter α

$$f(U; \alpha) = 0.$$

The Shanks transformation can be applied to the partial sums of the perturbation series

$$\begin{aligned} S_0 &= U_0, \\ S_1 &= U_0 + \alpha U_1, \\ S_2 &= U_0 + \alpha U_1 + \alpha^2 U_2, \\ S_3 &= U_0 + \alpha U_1 + \alpha^2 U_2 + \alpha^3 U_3, \\ &\vdots \end{aligned}$$

to obtain $U = \lim_{j \rightarrow \infty} \{S_j\}$ when the limit exists or to obtain its anti-limit if the limit does not exist. It turns out that in most applications, the limit or the anti-limit of the perturbation series is equal to the exact solution of the nonlinear equation that, for example, may be obtained from the Newton method.

The Shanks transformation of order n yields a sequence $\{\hat{S}_j = e_n(S_j)\}$ from $\{S_j\}$. An efficient recursive algorithm for computing this sequence is given by [149]

1. Set $\epsilon_1^j = \infty$ and $\epsilon_2^j = S_j$, $j = 0, 1, \dots$
2. Compute ϵ_{n+1}^{j-1} for $n > 2$ from the recursion

$$\frac{1}{\epsilon_{n+1}^{j-1} - \epsilon_n^j} + \frac{1}{\epsilon_{n-1}^{j+1} - \epsilon_n^j} = \frac{1}{\epsilon_n^{j-1} - \epsilon_n^j} + \frac{1}{\epsilon_n^{j+1} - \epsilon_n^j}.$$

3. Obtain $e_n(S_j) = \epsilon_{n+2}^j$.

Any sequence $\{e_n(S_j)\}_{n=0}^\infty$ with a fixed j , has the desired convergence properties of the Shanks transformation. For example,

$$U = \lim_{n \rightarrow \infty} \{e_n(S_j)\}, \quad j \text{ fixed.}$$

Appendix C

Matching the homogeneous isotropic turbulence spectrum by a stochastically-forced linearized model

We briefly overview the developments of [121] for matching the spectrum of homogeneous isotropic turbulence (HIT) using an appropriately selected stochastically-forced linearized model. Since HIT is invariant in all spatial directions, spatial Fourier transform can be employed in all directions. For incompressible flows subject to a solenoidal forcing $\bar{\mathbf{d}} = [d_1 \ d_2 \ d_3]^T$ ($\nabla \cdot \bar{\mathbf{d}} = 0$), the evolution of velocity fluctuations $\mathbf{v} = [u \ v \ w]^T$ around the uniform base flow ($U = 1$, after normalization) up to first order is governed by a linearized model that is obtained by neglecting the nonlinearities in the NS equations and eliminating pressure

$$\mathbf{v}_t(\bar{\boldsymbol{\kappa}}, t) = \bar{\mathbf{A}}(\bar{\boldsymbol{\kappa}}) \mathbf{v}(\bar{\boldsymbol{\kappa}}, t) + \bar{\mathbf{d}}(\bar{\boldsymbol{\kappa}}, t), \quad (\text{C.1})$$

where $\bar{\boldsymbol{\kappa}} = [\kappa_x \ \kappa_y \ \kappa_z]^T$ is the vector of spatial wavenumbers in x , y , and z , and

$$\bar{\mathbf{A}}(\bar{\boldsymbol{\kappa}}) = -(i\kappa_x + \bar{\kappa}^2/R_\lambda) \mathbf{I}.$$

Here, $\bar{\kappa}^2 = \kappa_x^2 + \kappa_y^2 + \kappa_z^2$, \mathbf{I} is an identity matrix in \mathbb{C}^3 , and $R_\lambda = U\lambda/\nu$ is the Reynolds number based on the Taylor microscale, λ [71, 72]. The spectrum of the velocity field at the steady-state $\Phi(\bar{\boldsymbol{\kappa}}) = \lim_{t \rightarrow \infty} \mathcal{E}(\mathbf{v}(\bar{\boldsymbol{\kappa}}, t) \mathbf{v}^*(\bar{\boldsymbol{\kappa}}, t))$ is obtained as a solution to the following Lyapunov equation

$$\bar{\mathbf{A}}(\bar{\boldsymbol{\kappa}}) \Phi(\bar{\boldsymbol{\kappa}}) + \Phi(\bar{\boldsymbol{\kappa}}) \bar{\mathbf{A}}^+(\bar{\boldsymbol{\kappa}}) = -\bar{\mathbf{M}}(\bar{\boldsymbol{\kappa}}), \quad (\text{C.2})$$

where $^+$ is the adjoint of an operator, and $\bar{\mathbf{M}}(\bar{\boldsymbol{\kappa}})$ is the power spectrum of a white-in-time forcing, i.e. $\mathcal{E}(\bar{\mathbf{d}}(\bar{\boldsymbol{\kappa}}, t_1) \bar{\mathbf{d}}^*(\bar{\boldsymbol{\kappa}}, t_2)) = \bar{\mathbf{M}}(\bar{\boldsymbol{\kappa}}) \delta(t_1 - t_2)$. For HIT, Φ is given by [150]

$$\Phi(\bar{\boldsymbol{\kappa}}) = \frac{E(\bar{\boldsymbol{\kappa}})}{4\pi\bar{\kappa}^2} \left(\mathbf{I} - \frac{\bar{\boldsymbol{\kappa}}\bar{\boldsymbol{\kappa}}^T}{\bar{\kappa}^2} \right), \quad (\text{C.3})$$

where

$$E(\bar{\boldsymbol{\kappa}}) = \lim_{t \rightarrow \infty} \mathcal{E}(\mathbf{v}^*(\bar{\boldsymbol{\kappa}}, t) \mathbf{v}(\bar{\boldsymbol{\kappa}}, t)) = \lim_{t \rightarrow \infty} \mathcal{E}(\langle \mathbf{v}(\bar{\boldsymbol{\kappa}}, t), \mathbf{v}(\bar{\boldsymbol{\kappa}}, t) \rangle_{\mathbb{C}^3})$$

denotes the energy spectrum of the velocity field \mathbf{v} , and $\langle \cdot, \cdot \rangle_{\mathbb{C}^3}$ is the standard inner product in \mathbb{C}^3 . Therefore, the adjoint of $\bar{\mathbf{A}}$ is $\bar{\mathbf{A}}^+ = \bar{\mathbf{A}}^*$. Substituting (C.3) in (C.2) yields the spectrum of the forcing $\bar{\mathbf{d}}$ that generates the second-order statistics of HIT

$$\bar{\mathbf{M}}(\bar{\boldsymbol{\kappa}}) = \frac{E(\bar{\boldsymbol{\kappa}})}{2\pi R_\lambda} \left(\mathbf{I} - \frac{\bar{\boldsymbol{\kappa}}\bar{\boldsymbol{\kappa}}^T}{\bar{\kappa}^2} \right). \quad (\text{C.4})$$

We next determine the spectrum of the forcing $\mathbf{d} = [d_2 \ d_\eta]^T$ that enters the model for evolution of the wall-normal velocity and vorticity, $\boldsymbol{\psi} = [v_2 \ \eta]^T$,

$$\boldsymbol{\psi}_t(\bar{\boldsymbol{\kappa}}, t) = \mathbf{A}(\bar{\boldsymbol{\kappa}}) \boldsymbol{\psi}(\bar{\boldsymbol{\kappa}}, t) + \mathbf{d}(\bar{\boldsymbol{\kappa}}, t). \quad (\text{C.5})$$

Using continuity, $\kappa_x u + \kappa_y v + \kappa_z w = 0$, one can show that the linear transformations

$$\mathbf{v} = \mathbf{W} \boldsymbol{\psi}, \quad \boldsymbol{\psi} = \mathbf{V} \mathbf{v}, \quad \mathbf{d} = \mathbf{V} \bar{\mathbf{d}}, \quad \mathbf{A} = \mathbf{V} \bar{\mathbf{A}} \mathbf{W}$$

with

$$\mathbf{W} = \frac{1}{\kappa^2} \begin{bmatrix} -\kappa_x \kappa_y & -i\kappa_z \\ 1 & 0 \\ -\kappa_y \kappa_z & i\kappa_x \end{bmatrix}, \quad \mathbf{V} = \begin{bmatrix} 0 & 1 & 0 \\ i\kappa_z & 0 & -i\kappa_x \end{bmatrix},$$

bring (C.1) into the evolution form given by (C.5). The spectrum of \mathbf{d}

$$\mathcal{E}(\mathbf{d}(\bar{\boldsymbol{\kappa}}, t_1) \otimes \mathbf{d}^*(\bar{\boldsymbol{\kappa}}, t_2)) = \mathbf{M}(\bar{\boldsymbol{\kappa}}) \delta(t_1 - t_2),$$

and the state auto-correlation matrix $\mathbf{X}(\bar{\boldsymbol{\kappa}}) = \lim_{t \rightarrow \infty} \mathcal{E}(\boldsymbol{\psi}(\bar{\boldsymbol{\kappa}}, t) \otimes \boldsymbol{\psi}^*(\bar{\boldsymbol{\kappa}}, t))$, are related by the following Lyapunov equation

$$\mathbf{A}(\bar{\boldsymbol{\kappa}}) \mathbf{X}(\bar{\boldsymbol{\kappa}}) + \mathbf{X}(\bar{\boldsymbol{\kappa}}) \mathbf{A}^+(\bar{\boldsymbol{\kappa}}) = -\mathbf{M}(\bar{\boldsymbol{\kappa}}). \quad (\text{C.6})$$

In order to determine \mathbf{A}^+ , we note that the energy spectrum $E(\bar{\boldsymbol{\kappa}})$ in terms of $\boldsymbol{\psi}$ is given by

$$E(\bar{\boldsymbol{\kappa}}) = \lim_{t \rightarrow \infty} \mathcal{E}(\boldsymbol{\psi}^*(\bar{\boldsymbol{\kappa}}, t) \mathbf{Q} \boldsymbol{\psi}(\bar{\boldsymbol{\kappa}}, t)) = \lim_{t \rightarrow \infty} \mathcal{E}(\langle \boldsymbol{\psi}(\bar{\boldsymbol{\kappa}}, t), \boldsymbol{\psi}(\bar{\boldsymbol{\kappa}}, t) \rangle_{\mathbf{Q}}),$$

where

$$\mathbf{Q} = \mathbf{W}^* \mathbf{W} = \begin{bmatrix} \bar{\kappa}^2/\kappa^2 & 0 \\ 0 & 1/\kappa^2 \end{bmatrix},$$

and $\langle \cdot, \cdot \rangle_{\mathbf{Q}}$ denotes the \mathbf{Q} -weighted inner product in \mathbb{C}^2 that preserves the kinetic energy, and $\kappa^2 = \kappa_x^2 + \kappa_z^2$. From the definition, the adjoint of \mathbf{A} is determined by

$$\langle \psi_1, \mathbf{A}\psi_2 \rangle_{\mathbf{Q}} = \langle \mathbf{A}^+ \psi_1, \psi_2 \rangle_{\mathbf{Q}} \Rightarrow \mathbf{A}^+ = \mathbf{Q}^{-1} \mathbf{A}^* \mathbf{Q}. \quad (\text{C.7})$$

Substituting \mathbf{A}^+ from (C.7) into (C.6) and multiplying both sides by \mathbf{Q}^{-1} yields

$$\mathbf{A}(\bar{\boldsymbol{\kappa}}) \mathbf{K}_{\mathbf{X}}(\bar{\boldsymbol{\kappa}}) + \mathbf{K}_{\mathbf{X}}(\bar{\boldsymbol{\kappa}}) \mathbf{A}^*(\bar{\boldsymbol{\kappa}}) = -\mathbf{K}_{\mathbf{M}}(\bar{\boldsymbol{\kappa}}),$$

where $\mathbf{K}_{\mathbf{X}} = \mathbf{X} \mathbf{Q}^{-1} = \langle \boldsymbol{\psi}(\bar{\boldsymbol{\kappa}}, t) \boldsymbol{\psi}^*(\bar{\boldsymbol{\kappa}}, t) \rangle$ and $\mathbf{K}_{\mathbf{M}} = \mathbf{M} \mathbf{Q}^{-1} = \langle \mathbf{d}(\bar{\boldsymbol{\kappa}}, t) \mathbf{d}^*(\bar{\boldsymbol{\kappa}}, t) \rangle$ denote kernel representations of the operators \mathbf{X} and \mathbf{M} . Therefore,

$$\mathbf{M} = \mathbf{K}_{\mathbf{M}} \mathbf{Q} = \langle \mathbf{d} \mathbf{d}^* \rangle \mathbf{Q} = \mathbf{V} \langle \bar{\mathbf{d}} \bar{\mathbf{d}}^* \rangle \mathbf{V}^* \mathbf{Q} = \mathbf{V} \bar{\mathbf{M}} \mathbf{V}^* \mathbf{Q}.$$

Substituting $\bar{\mathbf{M}}$ from (C.4) yields an expression for the forcing spectrum

$$\mathbf{M}(\bar{\boldsymbol{\kappa}}) = \frac{E(\bar{\boldsymbol{\kappa}})}{2\pi R_\lambda} \mathbf{I}.$$

Therefore, a white-in-time stochastic forcing with a spectrum proportional to the energy spectrum in HIT induces the second-order statistics of velocity fluctuations in HIT on the fluctuations that are obtained from the stochastically forced linearized equation (C.5).

Appendix D

Perturbation analysis of eigenvalues of a class of self-adjoint operators

We consider a class of spatially invariant systems whose coefficients are perturbed by spatially-periodic functions. We analyze changes in transient behavior under the effect of such perturbations. This is done by performing a spectral analysis of the state transition operator at every point in time. Computational complexity is significantly reduced by using a procedure that captures the influence of the perturbation on only the largest singular values of the state transition operator. Furthermore, we show that the problem of computing corrections of all orders to the maximum singular values collapses to that of finding the eigenvalues of a set of finite dimensional matrices. Finally, we demonstrate the predictive power of this method via an example.

D.1 Introduction

Perturbation theory of linear operators has been well studied over the last 50 years starting from the works of Rayleigh and Schrodinger [151]. It is a tool for efficiently approximating the influence of small perturbations on different properties of the unperturbed operator [151, 152]. In this chapter, we study the effect of a special class of perturbations on the eigenvalues of a set of self-adjoint operators. This class of operators are in close relation with systems with spatially-periodic coefficients.

Over the last decade, there has been a lot of excitement in analysis of periodic systems [153]. Systems with periodic coefficients in space arise in many important control problems. Fluid systems controlled by applying periodic body forcing or by imposing periodic boundary conditions in space are just an example of such systems [115]. A detailed analysis of such systems is given in [87, 154, 155].

It is shown in [87] that frequency response of systems with periodic coefficients in space takes a bi-infinite form. The simplest approach towards analysis of such systems is to approximate the bi-infinite operators using truncation. In the case where the system is defined in multiple spatial dimensions, numerical approximations would result in large matrices whose elements are themselves large matrices. Therefore the problem transforms into analysis of a large-scale system with at least several thousand states. From a computational point of view, the analysis of such systems is very expensive. Thus the mentioned approach is not efficient especially when one intends to perform a parametric study.

We utilize *reduction theory* [151, 152] to analyze the spectral behavior of the state transition operator of the spatially distributed system. This method allows us to focus on only the singular values of the state transition operator that are responsible for the largest transient growth. Thus, reduction theory effectively helps to collapse the original infinite dimensional problem to one of finite dimensional matrices. In [90] reduction theory was used to investigate the stability properties of marginally stable spatially invariant systems under spatially-periodic perturbations. Reference [90], differs from this work in that it investigated the effect of perturbation in the eigenvalues of the A -operator of the distributed system, as opposed to the singular values of the state transition operator.

Our presentation is organized as follows: We highlight the relevance of perturbation analysis of eigenvalues of certain self-adjoint operators in § D.2 and give a brief introduction to reduction theory in § D.2.1. Our main contribution is contained in § D.3 where we describe the class of spatially distributed systems under consideration, their perturbation, and their frequency domain representation. Reduction theory is then applied to singular value analysis of these systems. The theory is demonstrated using an illustrative example in § D.4 and we conclude with some remarks in § D.5.

D.2 Preliminaries

Consider the spatially distributed system

$$\frac{d}{dt}\psi = \mathcal{A}_0\psi + \mathcal{B}u, \quad \phi = \mathcal{C}\psi, \quad (\text{D.1})$$

where ψ , u , and ϕ denote the spatio-temporal system state, input, and output, respectively and $\mathcal{A}_0, \mathcal{B}, \mathcal{C}$ are partial differential operators. We assume that \mathcal{A}_0 generates a strongly continuous semigroup [156], and that the evolution operator is exponentially stable.

In the analysis of linear systems we are often interested in certain scalar quantities that capture the system response to initial conditions and deterministic or stochastic inputs. For example, a relevant quantity in transient response analysis is the worst-case amplification of all possible initial conditions as a function of time. Another quantity

of interest is the worst-case steady state gain of harmonic deterministic inputs. Both these quantities can be obtained by finding the largest eigenvalues of certain self-adjoint operators. Two such operators are

- $\mathcal{W}_0(t) = \mathcal{T}(t)\mathcal{T}(t)^*$, where $\mathcal{T}(t)$ is the state transition operator and $\mathcal{T}(t)^*$ is its transpose. In a finite dimensional setting we have $\mathcal{T}(t) = e^{\mathcal{A}_0 t}$. We will show later in § D.4 that the maximum eigenvalue of $\mathcal{W}_0(t)$ can be interpreted as the worst-case amplification of initial conditions at time t . Therefore, its application in transient response analysis of linear systems is imminent.
- $\mathcal{W}_0(\omega) = \mathcal{H}(\omega)\mathcal{H}(\omega)^*$, where $\mathcal{H}(\omega)$ is the frequency response of (D.1), i.e. $\mathcal{H}(\omega) = \mathcal{C}(i\omega\mathcal{I} - \mathcal{A}_0)^{-1}\mathcal{B}$. It is a standard fact that the maximum eigenvalue of $\mathcal{W}_0(\omega)$ determines the largest steady-state system gain of a deterministic input with frequency ω . In fact, the H_∞ norm of (D.1) can be obtained by taking "sup" over the maximum eigenvalue of $\mathcal{W}_0(\omega)$.

In both the above cases, we are interested in computing maximal eigenvalues of \mathcal{W}_0 . Our objective is to develop a method suitable for computing the effect of a particular class of perturbations on the eigenvalues of \mathcal{W}_0 . This class of perturbations is motivated by the structures that arise in systems with periodic coefficients in space. Following a brief review of perturbation theory in § D.2.1, we utilize these structures to develop more specific results for spatially-periodic systems in § D.3.

D.2.1 Perturbation theory

We consider a self-adjoint operator \mathcal{W}_0 with eigenvalue λ_0 of multiplicity m . Since \mathcal{W}_0 is self-adjoint, λ_0 is semi-simple meaning that it has a full set of corresponding independent eigenvectors g_0^i where $i = 1, 2, \dots, m$. Also consider the perturbed operator $\mathcal{W}(\alpha)$

$$\mathcal{W}(\alpha) = \mathcal{W}_0 + \sum_{r=1}^{\infty} \alpha^r \mathcal{W}_r, \quad 0 < \alpha < \alpha_0,$$

where each \mathcal{W}_r is a self-adjoint operator itself.

Theorem D.2.1 [151, 152] *For sufficiently small values of α_0 and in the case of the above self-adjoint perturbations, eigenvalues and eigenvectors of $\mathcal{W}(\alpha)$ can be written in the form of a perturbation series*

$$\begin{aligned} \mathcal{W}(\alpha) g^i(\alpha) &= \lambda^i(\alpha) g^i(\alpha), \quad i = 1, 2, \dots, m, \\ \lambda^i(\alpha) &= \lambda_0 + \sum_{r=1}^{\infty} \alpha^r \lambda_r^i, \quad g^i(\alpha) = g_0^i + \sum_{r=1}^{\infty} \alpha^r g_r^i. \end{aligned} \tag{D.2}$$

Note that we have accounted for the fact that λ_0 may split into m distinct eigenvalues λ^i as a result of the perturbation. By g_r^i and λ_r^i we denote the r th order correction to g^i and λ^i , respectively.

We follow the development of Kato [151] and Baumgartel [152] to solve for the unknown coefficients in problem (D.2). The reduction process gives an iterative procedure for computing higher order correction coefficients in the perturbation series (D.2) for λ^i .

Let e_1, e_2, \dots, e_m be the set of orthonormal eigenfunctions corresponding to λ_0 and let \mathcal{L}_0 be the space spanned by these eigenfunctions, i.e. $\mathcal{L}_0 = \text{span} \{e_1, e_2, \dots, e_m\}$. Also let \mathcal{P}_0 , called the eigenprojection of λ_0 , be the operator that projects the entire space onto the space \mathcal{L}_0 , i.e., $\mathcal{P}_0 = \sum_{i=1}^m e_i e_i^*$. Let \mathcal{S}_0 be the reduced resolvent operator determined from [152]

$$(\lambda \mathcal{I} - \mathcal{W}_0)^{-1} = \frac{\mathcal{P}_0}{\lambda - \lambda_0} + \sum_{i=0}^m \mathcal{S}_0^{i+1} (\lambda - \lambda_0)^i.$$

The step by step procedure is given below. Finding each correction term involves three steps [152].

Notation: By $\mathcal{M} \upharpoonright \mathcal{N}$ we denote restriction of \mathcal{M} to the space projected by \mathcal{N} . In other words, $\mathcal{M} \upharpoonright \mathcal{N}$ acts on an element from $\mathcal{N}X$ and maps the result back to $\mathcal{N}X$, where X is the appropriate Hilbert space.

- First order correction:
 1. Let \mathcal{P}_0 be eigenprojection of λ_0
 2. Define $\mathcal{B}_0 = \mathcal{P}_0 \mathcal{W}_1 \mathcal{P}_0$.
 3. λ_1^i 's are eigenvalues of $\mathcal{B}_0 \upharpoonright \mathcal{P}_0$.
- Second order correction: Repeat the steps from first order correction with the following modifications
 1. If $\lambda_1^i \neq 0$, let \mathcal{Q}_0^i be eigenprojection of λ_1^i .
If $\lambda_1^i = 0$, let $\mathcal{Q}_0^i = \mathcal{P}_0$ from Iteration 1.
 2. Define $\mathcal{C}_0^i = \mathcal{Q}_0^i (\mathcal{W}_2 + \mathcal{W}_1 \mathcal{S}_0 \mathcal{W}_1) \mathcal{Q}_0^i$.
 3. λ_2^i 's are eigenvalues of $\mathcal{C}_0^i \upharpoonright \mathcal{Q}_0^i$.

The n -th order correction can be obtained in a similar way [152]. The details of this procedure is explained in §§ D.2.2-D.2.4.

D.2.2 Elementary reduction

Following definition of g_0^i and λ_0 from § D.2.1, we have $g_0^i \in \mathcal{P}_0$ and we can write

$$g_0^i = \sum_{k=1}^m c_k^i e_k. \quad (\text{D.3})$$

We collect equal powers of α in (D.2). For instance

$$\begin{aligned} \alpha^0 : \quad & W_0 g_0^i = \lambda_0 g_0^i, \\ \alpha^1 : \quad & W_0 g_1^i + W_1 g_0^i = \lambda_0 g_1^i + \lambda_1^i g_0^i. \end{aligned} \quad (\text{D.4})$$

By substituting g_0^i from (D.3) into (D.4) and taking inner product of both sides of the equation for α^1 with an arbitrary eigenfunction e_q , one gets

$$\langle W_0 g_1^i, e_q \rangle + \left\langle W_1 \sum_{k=1}^m c_k^i e_k, e_q \right\rangle = \langle \lambda_0 g_1^i, e_q \rangle + \left\langle \lambda_1^i \sum_{k=1}^m c_k^i e_k, e_q \right\rangle.$$

The first terms on both sides of the above equation are equal considering the fact that W_0 is self-adjoint and the rest of the equation is simplified to

$$\sum_{k=1}^m c_k^i \langle W_1 e_k, e_q \rangle = c_q^i \lambda_1^i, \quad (\text{D.5})$$

knowing that e_1, \dots, e_m are orthonormal. For (D.5) to have nontrivial solutions for c_k^i , we require the following determinant condition

$$\det \{ \langle W_1 e_k, e_q \rangle - \lambda_1^i \delta_{k,q} \}_{k,q} = 0, \quad i = 1, 2, \dots, m, \quad (\text{D.6})$$

where $\{ \cdot \}_{k,q}$ denotes a matrix whose k, q -th element is given by the expression inside the brackets. Therefore, λ_1^i , the first order correction to λ_0 , is the i -th solution of (D.6).

D.2.3 Reduction process

Let P_0 be the operator that projects the entire space onto the space \mathcal{P}_0

$$P_0 = \sum_{i=1}^m \langle e_i, e_i \rangle, \quad P_0 W_0 = W_0 P_0 = \lambda_0 P_0, \quad P_0^2 = P_0,$$

where $\langle \cdot, \cdot \rangle$ denotes the appropriate inner product. P_0 defined by the above equations is called the eigenprojection of λ_0 . Similarly, define $P(\alpha)$ to be the eigenprojection

of $\lambda^i(\alpha)$, i.e.

$$P(\alpha)W(\alpha) = W(\alpha)P(\alpha) = \lambda^i(\alpha)P(\alpha), \quad P^2 = P.$$

We have $P(\alpha) = P_0 + \sum_{r=1}^{\infty} \alpha^r P_r$.

Now, define the auxiliary perturbation

$$B(\alpha) := \frac{1}{\alpha}(W(\alpha) - \lambda_0 I)P(\alpha) := B_0 + \sum_{r=1}^{\infty} \alpha^r B_r.$$

We note that $B(\alpha)$ is holomorphic everywhere and specially at $\alpha = 0$. It is easy to check that $B_0 = P_0 W_1 P_0$.

Define $B_0 \upharpoonright P_0$ to be restriction of operator B_0 to the space P_0 . Eigenvalues of $B_0 \upharpoonright P_0$, s^i are solutions of the following equation

$$\det(B_0 \upharpoonright P_0 - s^i I) = 0, \quad (\text{D.7})$$

which is the same equation as (D.6) with λ_1^i replaced by s^i . By comparison of (D.6) and (D.7), the first result of reduction process follows. The problem of finding first order correction to λ_0 is equivalent to finding nontrivial eigenvalues of $B_0 \upharpoonright P_0$.

Remark 1 *We note that since $B_0 \upharpoonright P_0$ is a restriction, it has many trivial zero eigenvalues. In fact, number of nontrivial eigenvalues of $B_0 \upharpoonright P_0$ is determined by rank of P_0 .*

Now define Q_0^i as the eigenprojection of eigenvalue λ_1^i of B_0

$$Q_0^i B_0 = B_0 Q_0^i = \lambda_1^i Q_0^i, \quad Q_0^{i^2} = Q_0^i,$$

and $Q^i(\alpha)$ as the eigenprojection of eigenvalue $\frac{\lambda^i(\alpha) - \lambda_0}{\alpha}$ of $B(\alpha)$. It can be shown that

$$Q^i(\alpha)P(\alpha) = P(\alpha)Q^i(\alpha) = Q^i(\alpha).$$

In other words, $Q^i(\alpha)$ reduces $P(\alpha)$. Up to the first order correction in $\lambda^i(\alpha)$, λ_0 with multiplicity m will split to m_1 distinct eigenvalues where m_1 is the difference between rank of P_0 and rank of Q_0^i .

Remark 2 *If $\lambda_1^i = 0$, no splitting of eigenvalues has occurred up to correction of first order. In this case $m_1 = 0$ and we have $Q_0^i = P_0$.*

D.2.4 Iterating the process

Since $B(\alpha)$ is a self-adjoint perturbation of B_0 , each of these m_1 perturbed eigenvalues λ_1^i are semi-simple themselves.

eigenvectors of λ_0 . Since $\mathcal{W}_{0\theta}$ is block-diagonal, $\mathcal{P}_{0\theta}$ is also block-diagonal

$$\mathcal{P}_{0\theta} = \begin{bmatrix} \ddots & & & & & \\ & P_0(n-1) & & & & \\ & & P_0(n) & & & \\ & & & P_0(n+1) & & \\ & & & & \ddots & \\ & & & & & \ddots \end{bmatrix}.$$

By looking at the structure of $\mathcal{P}_{0\theta}$ and $\mathcal{W}_{1\theta}$, it is easy to show the following lemma.

Lemma D.3.1 *A necessary condition for λ_1^i , the first order correction to eigenvalue λ_0 of $\mathcal{W}_{0\theta}$ after perturbation, to be nonzero is that λ_0 be an eigenvalue of at least two subsequent blocks in $\mathcal{W}_{0\theta}$.*

Proof. Recall from § D.2.1 that λ_1^i is given by eigenvalues of $\mathcal{B}_{0\theta} \upharpoonright \mathcal{P}_{0\theta}$, where $\mathcal{B}_{0\theta} = \mathcal{P}_{0\theta} \mathcal{W}_{1\theta} \mathcal{P}_{0\theta}$. But, $\mathcal{B}_{0\theta}$ is equal to zero unless $\mathcal{P}_{0\theta}$ has adjacent nonzero blocks.

Remark 3 *The above condition is not sufficient, because $\mathcal{B}_{0\theta}$ can be equal to zero even when $\mathcal{P}_{0\theta}$ satisfies the mentioned condition.*

Example 1 *Assume that λ_0 has multiplicity $m = 2$ and is an eigenvalue of the blocks $W_{0,0}(n-1)$ and $W_{0,0}(n)$ in $\mathcal{W}_{0\theta}$. Then only the adjacent blocks $P_0(n-1)$ and $P_0(n)$ in $\mathcal{P}_{0\theta}$ are nonzero and we have*

$$\begin{aligned} \mathcal{B}_{0\theta} \upharpoonright \mathcal{P}_{0\theta} &= \begin{bmatrix} 0 & B_{12} \\ B_{21} & 0 \end{bmatrix}, \\ B_{12} &= P_0(n-1) W_{1,-1}(n) P_0(n), \\ B_{21} &= P_0(n) W_{1,1}(n-1) P_0(n-1). \end{aligned}$$

Note that $\text{tr}(\mathcal{B}_{0\theta} \upharpoonright \mathcal{P}_{0\theta}) = 0$ and therefore, $\lambda_1^1 = -\lambda_1^2$. Thus, up to first order of correction, we have

- Case 1: $W_{1,1}(n-1) = (W_{1,-1}(n))^* = 0$;

$$\mathcal{B}_{0\theta} \upharpoonright \mathcal{P}_{0\theta} = 0 \quad \Rightarrow \quad \lambda_1^1 = \lambda_1^2 = 0.$$

In other words, λ_0 does not split.

- Case 2: $W_{1,1}(n-1) = (W_{1,-1}(n))^* \neq 0$;

$$\lambda_1^1 = -\lambda_1^2 \neq 0.$$

In other words, λ_0 splits into two eigenvalues that move in opposite directions along the real axis.

Similar results can be obtained for higher order corrections to the eigenvalues of \mathcal{W}_θ . Although the number of terms present in equations for higher order corrections increase, the structures remain simple.

Note that the size of $\mathcal{B}_{0\theta} \upharpoonright \mathcal{P}_{0\theta}$ is only m times (twice in the case of Example 1) the size of each of the blocks in the bi-infinite matrix \mathcal{W}_θ .

Remark 4 *In fact, at each iteration level $\{\alpha, \alpha^2, \dots\}$ of the reduction process, the maximum size of the problem is equal to the size of the constructive blocks of \mathcal{W}_θ times the multiplicity of $\{\lambda_0, \lambda_1^i, \dots\}$ in $\{\mathcal{W}_{0\theta}, \mathcal{B}_{0\theta} \upharpoonright \mathcal{P}_{0\theta}, \dots\}$, respectively. The problem size can be much smaller when $\{\mathcal{B}_{0\theta} \upharpoonright \mathcal{P}_{0\theta}, \mathcal{C}_{0\theta}^i \upharpoonright \mathcal{Q}_{0\theta}^i, \dots\}$ is block-diagonal.*

Therefore, by using perturbation analysis, the correction coefficients to the eigenvalues of \mathcal{W}_θ can be obtained by computing eigenvalues of a set of significantly smaller matrices compared to the the case where eigenvalues of \mathcal{W}_θ are computed after large-scale truncation of \mathcal{W}_θ .

D.4 Example: transient response analysis of a spatially-periodic system

We use the results of § D.3 in the transient response analysis of an exponentially stable spatially-periodic system. Systems that motivate transient response analysis are non-normal systems. These systems can have large transient growth before eventual decay. Consider the following non-normal system

$$\dot{\psi} = \mathcal{A}\psi, \quad \mathcal{A}\mathcal{A}^* \neq \mathcal{A}^*\mathcal{A}. \quad (\text{D.10})$$

The response of this system to initial condition ψ_0 is obtained by acting the C_0 -semigroup generated by \mathcal{A} on ψ_0

$$\psi(t) = \mathcal{T}(t)\psi_0.$$

A relevant quantity to consider in transient response analysis of (D.10) is the ratio between the norm of $\psi(t)$ and ψ_0 at a fixed time t

$$\begin{aligned} \frac{\|\psi(t)\|^2}{\|\psi_0\|^2} &= \frac{\langle \psi(t), \psi(t) \rangle}{\langle \psi_0, \psi_0 \rangle} = \frac{\langle \psi_0, \mathcal{T}^*(t) \mathcal{T}(t) \psi_0 \rangle}{\langle \psi_0, \psi_0 \rangle}, \\ \sup_{\psi_0} \frac{\|\psi(t)\|^2}{\|\psi_0\|^2} &= \lambda_1 \{ \mathcal{T}^*(t) \mathcal{T}(t) \} = \sigma_1^2 \{ \mathcal{T}(t) \}, \end{aligned}$$

where λ_1 and σ_1 denote the largest eigenvalues and singular values, respectively.

Therefore, the maximum eigenvalue of $\mathcal{W} = \mathcal{T}^*(t) \mathcal{T}(t)$ is equal to the supremum of the ratio between the norm of the solution at a fixed time t to that of the initial condition

over all initial conditions. In other words, the maximum eigenvalue of \mathcal{W} captures the worst-case amplification of initial conditions by the linear system at a fixed time t .

Now consider the following spatially-periodic system motivated by channel flow systems. The system has two distributed states with the following state equations

$$\partial_t \psi(x, t) = (A_0 + \alpha A_1) \psi(x, t), \quad A_1 = 2\mathcal{L} \cos(\Omega x),$$

where

$$A_0 = \begin{bmatrix} \frac{1}{R}(\partial_{xx} - c) & 0 \\ \partial_x & \frac{1}{R}(\partial_{xx} - c) \end{bmatrix}, \quad \mathcal{L} = \begin{bmatrix} 0 & -1 \\ 1 & 0 \end{bmatrix}.$$

One can think of $\alpha A_1 \psi$ as a state feedback control with a spatially-periodic gain. The frequency representation of this system is given in the beginning of § D.3 by

$$\begin{aligned} \partial_t \psi_\theta(t) &= \mathcal{A}_\theta(\alpha) \psi_\theta(t) = (\mathcal{A}_{0\theta} + \alpha \mathcal{A}_{1\theta}) \psi_\theta(t), \\ \mathcal{A}_0(n) &= \begin{bmatrix} -\frac{1}{R}((\theta + n\Omega)^2 + c) & 0 \\ i(\theta + n\Omega) & -\frac{1}{R}((\theta + n\Omega)^2 + c) \end{bmatrix}, \\ \mathcal{A}_1(n) &= \mathcal{A}_{-1}(n) = \begin{bmatrix} 0 & -1 \\ 1 & 0 \end{bmatrix}, \quad \forall n \end{aligned}$$

We use perturbation analysis of the maximum eigenvalue of \mathcal{W}_θ generated by $\mathcal{A}_{0\theta} + \alpha \mathcal{A}_{1\theta}$ in order to analyze the effect of the control parameter Ω on the transient response of the system. We verify the perturbation results by computing the maximum eigenvalues of the truncated \mathcal{W}_θ .

Figure D.1 shows the maximum eigenvalues of the unperturbed matrix $\mathcal{W}_0(\kappa_x)$ for $R = 15, c = 1$. The horizontal and vertical axes denote spatial frequency and time, respectively. We note that the solution, at a fixed frequency, shows transients as large as 8 times the norm of initial conditions before eventually decaying to zero. Also, at any given fixed time, the maximum eigenvalue has multiplicity $m = 2$.

By choosing Ω for the perturbed system, we sample the continuous spectrum in κ_x by samples separated by integer multiples of Ω (recall that $\kappa_x = \theta + n\Omega$). Thus, the smaller the frequency, the finer the sampling grid. In order for us to be able to analyze the effect of perturbation on the maximum eigenvalue of \mathcal{W}_0 , we need to make sure that we sample the frequencies at which these maximum eigenvalues occur when sampling over κ_x . This is done by choosing the appropriate value for θ for any choice of Ω .

We will compare the effect of two choices of Ω on transient response of the controlled system. Figures D.2(a) and D.2(b) show the maximum eigenvalues of the uncontrolled matrix given in Figure D.1 with the horizontal axis changed to n instead of κ_x to emphasize the sampling. We note that n and samples of κ_x (separated by integer multiples of Ω) are equivalent once the pair (Ω, θ) is specified.

Figure D.2(a) shows the spectrum for $(\Omega, \theta) = (2, 1)$. We note that in this case, the

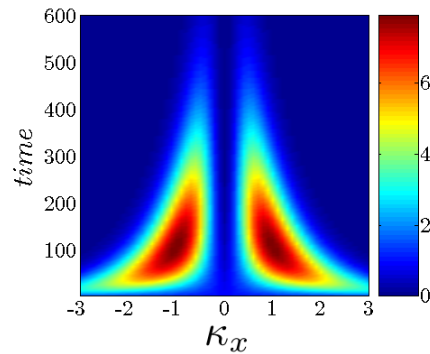


Figure D.1: The maximum eigenvalues of the unperturbed (uncontrolled) matrix $\mathcal{W}_0(\kappa_x)$ for $R = 15, c = 1$

maximum eigenvalues (corresponding to the red regions) occur at $n = -1, 0$. Therefore, the eigenprojection matrix of this eigenvalue with multiplicity 2, has two adjacent nonzero blocks on the main diagonal

$$\begin{matrix} \Omega = 2 \\ \theta = 1 \end{matrix} \quad \mathcal{P}_{0\theta} = \begin{bmatrix} \ddots & & & & & \\ & 0 & & & & \\ & & P_0(n-1) & & & \\ & & & P_0(n) & & \\ & & & & 0 & \\ & & & & & \ddots \end{bmatrix}.$$

Figure D.2(b) shows the spectrum for $(\Omega, \theta) = (2/3, 1/3)$. Note that with a smaller Ω , the maximum eigenvalues (corresponding to the red regions) occur at $n = -2, 1$. As a result, in this case, the eigenprojection matrix of this eigenvalue with multiplicity 2, has two nonzero blocks separated by two zero blocks on the main diagonal

$$\begin{matrix} \Omega = 2/3 \\ \theta = 1/3 \end{matrix} \quad \mathcal{P}_{0\theta} = \begin{bmatrix} \ddots & & & & & & \\ & 0 & & & & & \\ & & P_0(n-2) & & & & \\ & & & 0 & & & \\ & & & & 0 & & \\ & & & & & P_0(n+1) & \\ & & & & & & 0 \\ & & & & & & & \ddots \end{bmatrix}.$$

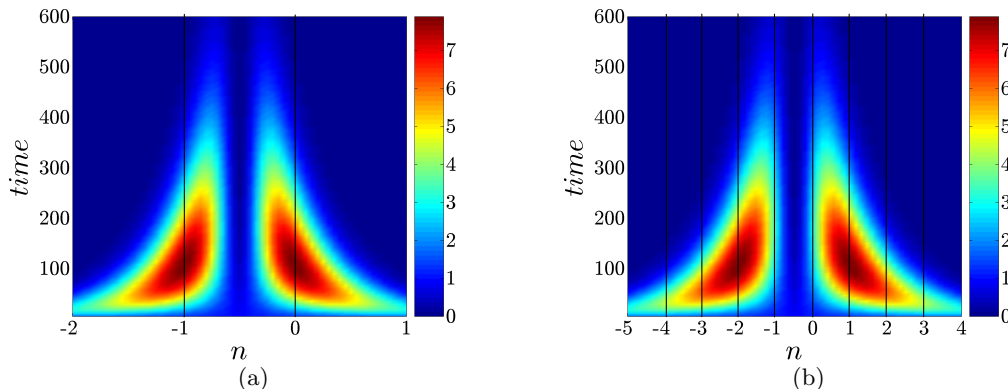


Figure D.2: The maximum eigenvalues of the unperturbed (uncontrolled) matrix $\mathcal{W}_{0\theta}$ for $R = 15, c = 1$. (a) $(\Omega, \theta) = (2, 1)$, (b) $(\Omega, \theta) = (2/3, 1/3)$.

Figures D.3(a) and D.3(b) show the results of perturbation analysis of the maximum eigenvalue for the choices of the pair (Ω, θ) discussed above. The cumulative sum of the perturbation series for the maximum eigenvalue up to first, second, and third order of correction are plotted versus time. The perturbation parameter, α , is 0.01. Eigenvalues of the unperturbed system (zeroth order correction) are also plotted to show the effect of control on transient response of the system. Finally, the maximum eigenvalues obtained from large scale truncation of \mathcal{W}_θ are given to compare with the results obtained by perturbation analysis.

Figure D.3(a) shows the transient response when $(\Omega, \theta) = (2, 1)$. We showed earlier that this choice of (Ω, θ) amounts to eigenprojection of the maximum eigenvalues of the unperturbed matrix that has adjacent nonzero blocks. Thus, from Lemma D.3.1, we expect that the control affects the maximum eigenvalues of the unperturbed operator at the order of α . The results shown in Figure D.3(a) agree with the expected response. First order correction is nonzero and higher order corrections converge to the results obtained by truncation. We note that the essential trends in this case are captured by the first order correction.

Figure D.3(b) shows the transient response for $(\Omega, \theta) = (2/3, 1/3)$. It can be seen from Figure D.2(b) that this choice of (Ω, θ) results in an eigenprojection matrix of the maximum eigenvalues of the unperturbed matrix that does not have adjacent nonzero blocks for $t < 270$. For this range of t , from Lemma D.3.1, we expect to see the effect of control on the maximum eigenvalues of the unperturbed operator only at the order of α^2 . The results shown in Figure D.3(b) agree with the expected response. It can be seen that for $t < 270$, the first order correction is zero. Higher order corrections are relatively small and converge to the results obtained by truncation. Thus, for the selected control amplitude ($\alpha = 0.01$), the control does not have significant effect on

the response of the uncontrolled system. This result is important since it reveals which perturbation frequencies influence the uncontrolled system the most.

However, in Figure D.3(b), the type of response seen for $t > 270$ is completely different from that of $t < 270$. This is due to the fact that for the former range of t , the maximum eigenvalue of the unperturbed operator has a different location and occurs at $n = -1, 0$, see Figure D.2(b). Therefore, the structure of the problem for this range of t is similar to that of the case where $(\Omega, \theta) = (2, 1)$. Thus, it is not surprising that the type of solution is generically different. We note that this result is totally non-intuitive and we were able to explain it due to the predictive power of perturbation theory even at the level of the first order correction.

The perturbation results are in perfect agreement with truncation results except for a small range $234 < t < 270$. This is simply the consequence of the fact that we have performed perturbation analysis only on the maximum eigenvalue of the unperturbed matrix. In other words, we are tracking the effect of perturbation only on the maximum eigenvalue of the unperturbed matrix. In general, there may exist eigenvalues close to the maximum eigenvalues of the unperturbed matrix that are influenced more by the perturbation than the larger (maximum) eigenvalues. This can be specially the case when the larger and smaller eigenvalues lead to different structures in the viewpoint of perturbation analysis. As can be seen in this example, the maximum eigenvalues of the unperturbed matrix for $234 < t < 270$ still occur at $n = -2, 1$ and therefore are not affected by the control at the order of α . However, for this time interval, the second largest eigenvalues occur at $n = -1, 0$ and are thus influenced by the control at the level of α . Since the effect of control is increasing these eigenvalues for the perturbed system they result in the largest eigenvalue, although the largest unperturbed eigenvalue remains almost unchanged. Therefore perturbation analysis of only the largest eigenvalues cannot capture transition trends between two sets of largest eigenvalues. Had we studied the effect of perturbation on the second largest eigenvalues as well as the maximum eigenvalues, we could have captured the truncation results by taking the maximum of the responses obtained by perturbation analysis of the two sets of largest eigenvalues. In other words, one should make sure that the non-maximum eigenvalues that are not tracked are not influenced by the perturbation in a way that become the maximum eigenvalues of the perturbed matrix.

D.5 Summary

We used perturbation theory to compute the correction coefficients for the eigenvalues of certain operators of interest in the transient response analysis of a class of spatially-periodic systems. We utilized the structure of the frequency representation of systems with periodic coefficients to develop specific results for the spectral perturbation of these systems. We showed that the frequency of the perturbation is of integral importance in the behavior of the perturbed system.

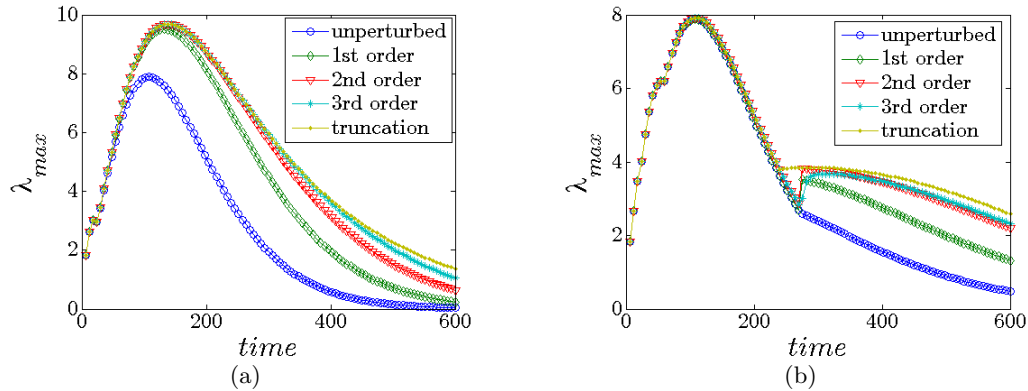


Figure D.3: Perturbation results for the maximum eigenvalues of the perturbed (controlled) matrix for $R = 15, c = 1, \alpha = 0.01$ (a) $(\Omega, \theta) = (2, 1)$, (b) $(\Omega, \theta) = (2/3, 1/3)$.

We showed that the maximum singular value of the state transition operator at a fixed time can be interpreted as the worst-case amplification of all possible initial conditions. In an example, we utilized perturbation theory in order to find the maximum singular values of the state transition operator in time. We were able to capture the effect of control frequency on the system's transient response.

We showed that this type of analysis significantly reduces the computational effort. More importantly, by exploiting structures of the matrices involved in this analysis, one can get general results and intuitions as to how to select control parameters (here Ω) that influence the uncontrolled system the most and predict their effect in a systematic way.

Appendix E

Remarks on computing the \mathcal{H}_2 norm of incompressible fluids using descriptor state-space formulation

We utilize descriptor state-space formulation for computation of energy amplification in incompressible channel flows. The dynamics of velocity and pressure fluctuations in these flows are described by a system of partial differential-algebraic equations. Typically, the evolution model is obtained by projecting the velocity fluctuations on a divergence-free subspace which eliminates pressure from the equations. This procedure results into a standard state-space representation and the problem of quantifying receptivity of velocity fluctuations to stochastic exogenous disturbances is solved using well-known \mathcal{H}_2 formalism. However, we show how energy amplification can be computed directly from the original system of the linearized Navier-Stokes and continuity equations. This approach avoids the need for finding the evolution model which is advantageous in many applications.

E.1 Introduction

Descriptor formulation of systems arise from formulating the system equations in terms of their natural physical variables [157]. A particular class of physical problems that can be written in descriptor formulation are those with algebraic constraints. For example, systems of incompressible fluids require the velocity fluctuations to lie on a divergence-free subspace, hence, resulting in a differential-algebraic equation.

It is a standard task in fluid mechanics to eliminate the algebraic constraint from the

equations and rewrite the equations in standard state-space formulation [84]. However, working with the original descriptor formulation is advantageous in many applications where obtaining the evolution formulation is a difficult task and often results in a more complicated representation comparing to that of the descriptor formulation in terms of the order of differential operators involved.

We consider channel flow of incompressible fluids and we show how the problem at hand can be approached, alternatively, using the available theory of computing the \mathcal{H}_2 norm of finite dimensional descriptor systems [158, 159].

Our presentation is organized as follows: An introduction to finite dimensional descriptor systems is provided in § E.2. We briefly review the theory of computing \mathcal{H}_2 norms of finite dimensional descriptor systems in § E.3. The system of incompressible channel flow is formulated in both descriptor and standard state-space formulations in § E.4. In § E.5, we show how the underlying operators are approximated using spectral schemes. Comparison between the obtained results from the standard and descriptor formulations is given in § E.6 and concluding remarks are provided based on the above comparison.

E.2 Preliminaries

Descriptor formulation is particularly suitable for defining systems of ordinary differential equations in time with algebraic constraints.

We consider the following linear time-invariant system

$$\begin{aligned} E \partial_t \psi(x, t) &= A \psi(x, t) + B u(x, t), \\ \phi(x, t) &= C \psi(x, t), \end{aligned} \tag{E.1}$$

where x and t denote spatial and temporal coordinates, ψ , u , and ϕ denote the spatio-temporal system state, input, and output, respectively, and E , A , B , and C are bounded operator valued matrices of appropriate dimensions. We denote by ∂_t the first derivative operator in time.

Remark 5 *We note that if E is nonsingular, system (E.1) can be transformed into standard state-space representation by pre-multiplying the first equation by E^{-1} from the left. However, if E contains differential operators in x , one should be careful about implementation of boundary conditions when inverting E . This can be very difficult especially for problems involving complicated geometry or boundary conditions. Therefore, even when E is nonsingular, definition and analysis of certain systems in descriptor form is preferred.*

The spatial differential operators involved in system (E.1) together with their boundary conditions can be approximated in descriptor form in a systematic way. However, this approximation is not always trivial if one decides to transform the system into a

standard state-space representation by eliminating the constraints from the equations. Moreover, approximating the boundary conditions numerically may result in overspecification of the boundary conditions [160].

For computational purposes, we numerically approximate the underlying differential operators in (E.1). Once we obtain finite dimensional approximation of the infinite dimensional descriptor system (E.1), we can use the theory developed for the finite dimensional descriptor systems.

E.2.1 Finite dimensional descriptor form

Consider the following linear time-invariant system

$$E \frac{d}{dt} \psi(t) = A \psi(t) + B u(t), \quad \phi(t) = C \psi(t), \quad (\text{E.2})$$

where ψ , u , and ϕ denote system state vector, input, and output, respectively, and E , A , B , and C are matrices of appropriate dimensions. We assume that the pencil $(sE - A)$ is regular, i.e., there is a $s \in \mathbb{C}$ for which the resolvent operator $(sE - A)^{-1}$ exists. Then, $(sE - A)^{-1}$ can be uniquely written in terms of its Laurent parameters around $s = \infty$ [159]

$$(sE - A)^{-1} = s^{-1} \sum_{k=-\nu}^{\infty} \zeta_k s^{-k}, \quad (\text{E.3})$$

where ζ_k denotes the Laurent parameters and ν is called the nilpotency index of the pencil $(sE - A)$. The Laurent parameters are very useful in analysis of descriptor systems because they separate the eigenspaces associated with finite (slow) and infinite (fast) generalized eigenvalues of the pencil $(sE - A)$ [158]. Another important property of the Laurent parameters is that $P_r = \zeta_0 E$ and $Q_r = -\zeta_{-1} A$ are projections on the space spanned by the eigenvectors ξ_i corresponding with the finite and infinite eigenvalues λ_i of the eigenvalue problem $\lambda_i E \xi_i = A \xi_i$, respectively. Also $P_l = E \zeta_0$ and $Q_l = -A \zeta_{-1}$ are projections on the space spanned by the eigenvectors ξ_i corresponding with the finite and infinite eigenvalues λ_i of the eigenvalue problem $\lambda_i \xi_i E = \xi_i A$, respectively [159].

The Laurent parameters are determined from the elements of the Weierstrass canonical form of the pair (A, E) . However, it is well-known that canonical forms involving Jordan structures are not numerically robust. Therefore, for computational purposes, it suffices to consider the *Weierstrass-like* canonical form of the pair (A, E) [161].

Weierstrass-like form: For a pair (A, E) , one can find invertible matrices U and V such that

$$E = V \begin{bmatrix} E_f & 0 \\ 0 & E_\infty \end{bmatrix} U, \quad A = V \begin{bmatrix} A_f & 0 \\ 0 & A_\infty \end{bmatrix} U, \quad (\text{E.4})$$

where E_f , A_f , and A_∞ are upper triangular invertible matrices and E_∞ is upper triangular and nilpotent. In the new coordinate system, we have

$$\psi = U^{-1} \begin{bmatrix} \psi_1 \\ \psi_2 \end{bmatrix}, \quad B = V \begin{bmatrix} B_1 \\ B_2 \end{bmatrix}, \quad C = [C_1 \quad C_2] U,$$

where ψ_1 and ψ_2 denote slow (causal) and fast (impulsive or noncausal) parts of the state vector, respectively. The projections on the fast and slow subspaces in Weierstrass-like form are determined from

$$P_l = V \begin{bmatrix} E_f & 0 \\ 0 & 0 \end{bmatrix} V^{-1}, \quad P_r = U^{-1} \begin{bmatrix} E_f & 0 \\ 0 & 0 \end{bmatrix} U,$$

$$Q_l = V \begin{bmatrix} 0 & 0 \\ 0 & -A_\infty \end{bmatrix} V^{-1}, \quad Q_r = U^{-1} \begin{bmatrix} 0 & 0 \\ 0 & -A_\infty \end{bmatrix} U.$$

Details regarding computation of the Weierstrass-like form is included in § E.3.1.

E.3 Computing the \mathcal{H}_2 norm

The \mathcal{H}_2 norm of (E.2) is determined by [159, 161, 162]

$$\|\mathcal{H}\|_2^2 = \text{trace}(C(G_c + G_{nc})C^*), \quad (\text{E.5})$$

where G_c and G_{nc} , the causal and non-causal reachability Gramians, satisfy the following generalized Lyapunov equations

$$E G_c A^* + A G_c E^* = -P_l B B^* P_l^*,$$

$$E G_{nc} E^* - A G_{nc} A^* = Q_l B B^* Q_l^*. \quad (\text{E.6})$$

Under certain reachability conditions for the pairs (A_f, B_1) and (E_∞, B_2) , unique projected solutions to (E.6) can be obtained by the following projections [159, 161]

$$G_c = P_r G_c P_r, \quad G_{nc} = Q_r G_{nc} Q_r. \quad (\text{E.7})$$

The approach towards solving the generalized Lyapunov equations relies heavily on the use of Weierstrass canonical form. Therefore, we first see how the Weierstrass transformation is obtained.

E.3.1 Obtaining the Weierstrass-like form

Use MATLAB[®]'s QZ algorithm to compute the generalized Schur form of (A, E) such that

$$E = W \begin{bmatrix} E_f & E_u \\ 0 & E_\infty \end{bmatrix} T, \quad A = W \begin{bmatrix} A_f & A_u \\ 0 & A_\infty \end{bmatrix} T, \quad (\text{E.8})$$

where E_f , A_f , and A_∞ are nonsingular upper-triangular matrices and E_∞ is nilpotent upper-triangular. To this end, one needs to use `ordqz.m` function in order to put all the finite generalized eigenvalues of (A, E) in E_f .

The invertible matrices U and V in the Weierstrass-like form (E.4) are determined by

$$V = W \begin{bmatrix} I & Z \\ 0 & I \end{bmatrix}, \quad U = \begin{bmatrix} I & -Y \\ 0 & I \end{bmatrix} T,$$

where Z and Y are obtained from the following system of generalized Sylvester equation [161]

$$\begin{aligned} E_f Y - Z E_\infty &= -E_u, \\ A_f Y - Z A_\infty &= -A_u. \end{aligned} \tag{E.9}$$

A fast algorithm for solving the system of Sylvester equations is given in [163].

E.3.2 Solving the generalized Lyapunov equation

We use the Weierstrass-like form discussed in § E.2.1 to reduce the generalized projected Lyapunov equations (E.6,E.7) to standard Lyapunov equations. This is not a trivial task, without using the Weierstrass transformation.

The causal reachability Gramian is determined by

$$E P_r G_c P_r^* A^* + A P_r G_c P_r^* E^* = -P_l B B^* P_l^*.$$

We substitute the underlying matrices with their Weierstrass-like form. After initial manipulation, we get

$$\begin{aligned} & \begin{bmatrix} E_f E_f & 0 \\ 0 & 0 \end{bmatrix} \tilde{G}_c \begin{bmatrix} E_f^* A_f^* & 0 \\ 0 & 0 \end{bmatrix} + \begin{bmatrix} A_f E_f & 0 \\ 0 & 0 \end{bmatrix} \tilde{G}_c \begin{bmatrix} E_f^* E_f^* & 0 \\ 0 & 0 \end{bmatrix} \\ &= - \begin{bmatrix} E_f & -E_f Z \\ 0 & 0 \end{bmatrix} \tilde{F} \begin{bmatrix} E_f^* & 0 \\ -Z^* E_f^* & 0 \end{bmatrix}, \end{aligned} \tag{E.10}$$

where

$$\begin{aligned} \tilde{G}_c &= \begin{bmatrix} \tilde{G}_{c1} & \tilde{G}_{c2} \\ \tilde{G}_{c3} & \tilde{G}_{c4} \end{bmatrix} = U G_c U^*, \\ \tilde{F} &= \begin{bmatrix} \tilde{F}_1 & \tilde{F}_2 \\ \tilde{F}_3 & \tilde{F}_4 \end{bmatrix} = W^* B B^* W. \end{aligned}$$

Note that because of the projections (E.7), only \tilde{G}_{c1} survives in (E.10) and we obtain the following standard Lyapunov equation

$$(E_f^{-1} A_f) \hat{G}_{c1} + \hat{G}_{c1} (E_f^{-1} A_f)^* = -(\tilde{F}_1 - \tilde{F}_2 Z^* - Z \tilde{F}_3 + Z \tilde{F}_4 Z^*), \tag{E.11}$$

where $\hat{G}_{c1} = E_f \tilde{G}_{c1} E_f^*$.

Therefore, $\tilde{G}_{c1} = E_f^{-1} \hat{G}_{c1} E_f^{-*}$. The projection defined in (E.7) requires all the other blocks of \tilde{G}_c to be zero. Finally,

$$G_c = U^{-1} \tilde{G}_c U^{-*} = T^* \begin{bmatrix} \tilde{G}_{c1} & 0 \\ 0 & 0 \end{bmatrix} T. \quad (\text{E.12})$$

Note that uniqueness of \tilde{G}_c is a direct consequence of the uniqueness of the solution of the standard Lyapunov equation (E.11).

Similar result is obtained for the noncausal reachability Gramian determined by

$$E Q_r G_{nc} Q_r^* E^* + A Q_r G_{nc} Q_r^* A^* = Q_l B B^* Q_l^*.$$

After similar manipulations to those carried to obtain G_c , we have

$$G_{nc} = U^{-1} \tilde{G}_{nc} U^{-*} = T^* \begin{bmatrix} Y \tilde{G}_{nc4} Y^* & Y \tilde{G}_{nc4} \\ \tilde{G}_{nc4} Y^* & \tilde{G}_{nc4} \end{bmatrix} T, \quad (\text{E.13})$$

where $\tilde{G}_{nc4} = A_\infty^{-1} \hat{G}_{nc4} A_\infty^{-*}$ and \tilde{G}_{nc4} is obtained by solving the following standard Lyapunov equation

$$(A_\infty^{-1} E_\infty) \hat{G}_{nc4} (A_\infty^{-1} E_\infty)^* - \hat{G}_{nc4} = \tilde{F}_4. \quad (\text{E.14})$$

Below, we summarize the procedure of computing the \mathcal{H}_2 norm for the descriptor system (E.2)

1. Compute the generalized Schur form of the pair (A, E) given in (E.8).
2. Solve the system of generalized Sylvester equation (E.9) for Y and Z .
3. Compute G_c and G_{nc} from (E.11)-(E.14).
4. Finally, the \mathcal{H}_2 norm is determined by (E.5).

E.4 Incompressible plane channel flow

We consider motion of incompressible Newtonian fluids between two infinite planes shown in Figure E.1.

The linearized Navier-Stokes equations govern evolution of velocity and pressure fluctuations (\mathbf{v}, p) around nominal velocity and pressure $(\bar{\mathbf{u}}, P)$ in the presence of forcing fluctuations \mathbf{d} , where $\mathbf{v} = [u \ v \ w]^T$ and $\mathbf{d} = [d_1 \ d_2 \ d_3]^T$. We assume the following nominal velocity profile

$$\bar{\mathbf{u}} = [U(y) \ 0 \ 0]^T, \quad U(y) = 1 - y^2.$$

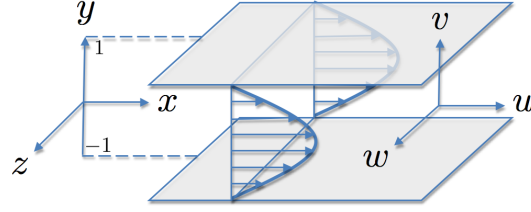


Figure E.1: Pressure driven channel flow.

Navier-Stokes equations for velocity fluctuations of incompressible fluids linearized around above profile are given by

$$\begin{aligned}\partial_t u &= \left(\frac{1}{R_c} \Delta - U \partial_x\right) u - U' v - \partial_x p + d_1, \\ \partial_t v &= \left(\frac{1}{R_c} \Delta - U \partial_x\right) v - \partial_y p + d_2, \\ \partial_t w &= \left(\frac{1}{R_c} \Delta - U \partial_x\right) w - \partial_z p + d_3,\end{aligned}\tag{E.15}$$

$$0 = \partial_x u + \partial_y v + \partial_z w,\tag{E.16}$$

where $\Delta = \partial_{xx} + \partial_{yy} + \partial_{zz}$ is the Laplacian operator with homogenous Dirichlet boundary conditions and R_c is the Reynolds number. Equation (E.16) is an algebraic constraint in time, i.e., it does not involve partial derivatives in time.

The set of equations (E.15) and (E.16) can be summarized in the following descriptor formulation

$$E \partial_t \psi = A \psi + B \mathbf{d}, \quad \mathbf{v} = C \psi,\tag{E.17}$$

where $\psi = [\mathbf{v} \ p]^T$ denotes vector of system states. Moreover,

$$E = \begin{bmatrix} I & 0 \\ 0 & 0 \end{bmatrix}, \quad A = \begin{bmatrix} \bar{A} & -D^T \\ D & 0 \end{bmatrix}, \quad B = C^T = \begin{bmatrix} I \\ 0 \end{bmatrix},$$

where

$$\bar{A} = \begin{bmatrix} \frac{1}{R_c} \Delta - U \partial_x & U' & 0 \\ 0 & \frac{1}{R_c} \Delta - U \partial_x & 0 \\ 0 & 0 & \frac{1}{R_c} \Delta - U \partial_x \end{bmatrix},$$

and $D = [\partial_x \ \partial_y \ \partial_z]$.

Since the underlying differential operators are spatially invariant in x and z directions, one can apply spatial Fourier transform in x and z and algebraize the differential operators in these directions. Differential operators in y direction will be approximated numerically. Details of the numerical issues are discussed in § E.5.

With a slight abuse of notation, we denote by (E.17) both physical and frequency

representations of our system. The choice of either is clear from the context. Therefore, the underlying operators in frequency domain are determined from

$$\bar{A} = \begin{bmatrix} \frac{1}{R_c} \Delta - i \kappa_x U & U' & 0 \\ 0 & \frac{1}{R_c} \Delta - i \kappa_x U & 0 \\ 0 & 0 & \frac{1}{R_c} \Delta - i \kappa_x U \end{bmatrix},$$

$$D = [i \kappa_x I \quad \partial_y \quad i \kappa_z I],$$

where $\Delta = -\kappa^2 + \partial_{yy}$ and κ_x and κ_z denote wave numbers in x and z directions, respectively, $\kappa^2 = \kappa_x^2 + \kappa_z^2$ and $i = \sqrt{-1}$.

The \mathcal{H}_2 norm of system (E.17) is interpreted as energy amplification of stochastic disturbances which are white zero-mean in y and t and are harmonic in x and z coordinates

$$E(\kappa_x, \kappa_z) = \text{trace} \left(\lim_{t \rightarrow \infty} \mathcal{E} \{ \mathbf{v}(\kappa_x, \cdot, \kappa_z, t) \otimes \mathbf{v}(\kappa_x, \cdot, \kappa_z, t) \} \right),$$

where \mathcal{E} is the expectation operator, and \otimes denotes the tensor product operator. Another interpretation of $E(\kappa_x, \kappa_z)$ is that it determines energy of the impulse response of (E.17)

$$E(\kappa_x, \kappa_z) = \int_0^\infty \text{trace} (\mathbf{v}(\kappa_x, \cdot, \kappa_z, t) \otimes \mathbf{v}(\kappa_x, \cdot, \kappa_z, t)) dt.$$

In § E.6, we utilize the method discussed in § E.3 to compute the \mathcal{H}_2 norm of linearized plane channel flow given in descriptor form (E.17). We will test our results by comparing the \mathcal{H}_2 norm obtained from the descriptor formulation of the system with the \mathcal{H}_2 norm obtained from the system formulated in standard state-space formulation.

It is a standard task in fluid mechanics to write (E.15) and (E.16) in standard state-space formulation [84]. This is done by eliminating pressure p from (E.15) by writing p in terms of velocity fluctuations and then using the algebraic constraint (E.16) to reduce the number of unknown fields to two. Therefore, only two state fields suffice to fully represent the system in standard formulation. A common choice of state variables is $\Psi = [v \quad \eta]^T$, where $\eta = u_z - w_x$ is the wall-normal vorticity. The standard state-space formulation of (E.17) is determined by

$$\partial_t \Psi = \mathcal{A} \Psi + \mathcal{B} \mathbf{d}, \quad \mathbf{v} = \mathcal{C} \Psi, \quad (\text{E.18})$$

where

$$\begin{aligned}\mathcal{A} &= \begin{bmatrix} -\Delta^{-1}(\mathrm{i}\kappa_x(U\Delta + U'') + \frac{1}{R_c}\Delta^2) & 0 \\ -\mathrm{i}\kappa_z U' & -\mathrm{i}\kappa_x U + \frac{1}{R_c}\Delta \end{bmatrix}, \\ \mathcal{B} &= \begin{bmatrix} -\mathrm{i}\kappa_x \Delta^{-1} \partial_y & -\kappa^2 \Delta^{-1} & -\mathrm{i}\kappa_z \Delta^{-1} \partial_y \\ \mathrm{i}\kappa_z & 0 & -\mathrm{i}\kappa_x \end{bmatrix}, \\ \mathcal{C} &= \frac{1}{\kappa^2} \begin{bmatrix} \mathrm{i}\kappa_x \partial_y & -\mathrm{i}\kappa_z \\ \kappa^2 & 0 \\ \mathrm{i}\kappa_z & \mathrm{i}\kappa_x \end{bmatrix},\end{aligned}$$

where $\Delta^2 = \partial_{yyyy} + 2\kappa^2 \partial_{yy} + (\kappa^2)^2$ with Dirichlet and Neumann boundary conditions.

Remark 6 *We note that while the number of elements of the state vector in standard formulation is two, the descriptor formulation requires four elements in its state vector. Therefore, assuming that each of these infinite dimensional elements are approximated with vectors of the same length, the problem size in descriptor formulation will have twice the size of the problem in standard formulation. In spite of the above mentioned advantage of the standard formulation, one sees that the entries in matrices \mathcal{A} , \mathcal{B} , and \mathcal{C} are substantially more complicated operators than those in E , A , B , or C . We note the following*

- *The operator-valued matrices in the standard formulation involve differential operators with two degrees higher than those in the descriptor formulation. Moreover, they contain integral operators like Δ^{-1} which add to complexity of the standard representation. We note that these issues are treated very well for problems with certain boundary conditions such as Dirichlet and Neumann boundary conditions.*
- *We also note that we have arrived at the standard formulation after certain analytical and algebraic manipulations on the descriptor formulation of the system [7]. For problems with more complicated nominal velocity profiles that involve components which also vary along other spatial coordinates such as x and z , this is an arduous undertaking [115].*

Therefore, simplicity of defining systems with algebraic constraints in the descriptor formulation together with reduction in the order of numerically approximated differential operators serve as important motivations for development of efficient analysis tools for these systems. In § E.6, we show that the \mathcal{H}_2 norm obtained from the descriptor formulation of plane channel flow compares very well to that obtained from the standard formulation.

E.5 Numerical approximation of spatial operators

Over the past decades, many different schemes are developed for numerical approximation of differential operators, in particular those with non-periodic boundary conditions [164]. These boundary conditions arise in applications with finite domains where

the differential operators lack invariance under spatial shifting transformations. Many fluid systems with bounded geometry like the channel flow system are of this kind.

We use the matrix differentiation suite developed by Weideman and Reddy [118] to numerically approximate differential equations in wall-normal direction, y . This tools is based on computation of differentiation matrices using *spectral collocation methods*. Chebyshev polynomials are selected as basis functions, since these polynomials are most appropriate for bounded non-periodic domains.

In spectral collocation methods, one-to-one mapping is established between the selected basis function and a non-uniform set of grid points chosen such that the approximation error decays exponentially as the number of grid points increases. Therefore, convergence rate of spectral methods ($\mathcal{O}(e^{-cN})$) are by far superior to that of finite difference methods ($\mathcal{O}(N^{-c})$), where N is the number of degrees of freedom in the expansion series for spectral methods or the number of grid points in the case of finite difference and spectral collocation methods.

Boundary conditions are implemented either with Galerkin schemes based on choice of Chebyshev polynomials or with boundary bordering method that eliminates first and last rows and columns of the differentiation matrix in the case that boundary points satisfy the boundary conditions.

E.5.1 Operators and their adjoints

We consider $(N + 2)$ grid points to approximate differential operators in wall-normal direction using the Galerkin spectral collocation scheme with Chebyshev polynomials. Effectively, functions and operators are approximated by finite vectors and matrices, respectively. We note the following

- Elements of the velocity and vorticity fields (u, v, w, η) satisfy Dirichlet boundary conditions and the first and last entries in their corresponding vector approximation are always zero and they can be removed. Therefore, the velocity and vorticity fields are approximated with N -dimensional vectors. On the other hand, there is no boundary condition on pressure p , nor there is one on input \mathbf{d} . So, the pressure and input fields are approximated with $(N + 2)$ -dimensional vectors.
- The first and last columns of the differentiation matrices acting on these functions can be removed due to the Dirichlet boundary conditions. Also the first and last rows of the operators resulting in velocity and vorticity fields can be removed.

Therefore, for example, E and A are $(4N+2) \times (4N+2)$, \bar{A} is $3N \times 3N$, D is $(N+2) \times 3N$, and B is $(4N+2) \times (3N)$, etc. Note that we have used the same notation for the functions and operators and their numerical approximations.

Operator adjoints are needed for the purpose of norm computations. To obtain the matrices approximating operator adjoints, one can analytically find the adjoint operators

and then approximate them numerically. An alternative way is computing the adjoint operators directly from approximated operators.

Adjoints of A and E are determined from

$$\langle \psi_1, A \psi_2 \rangle = \langle A^+ \psi_1, \psi_2 \rangle, \quad \langle \psi_1, E \psi_1 \rangle = \langle E^+ \psi_1, \psi_2 \rangle, \quad (\text{E.19})$$

where $^+$ denotes the adjoint operator and $\langle \cdot, \cdot \rangle$ denotes the $L^2[-1, 1]$ inner product

$$\langle f, g \rangle = \int_{-1}^1 f^* g \, dy. \quad (\text{E.20})$$

To numerically approximate the integral in (E.20), we use the integration matrix that contains appropriate integrating weights to account for the non-uniform distribution of the grid points in y [119]. Therefore, numerically

$$\langle f, g \rangle \approx f^* S g = \sum_{i=1}^N f(y_i) s_i g(y_i), \quad (\text{E.21})$$

where y_i 's denote selected grid points, s_i 's denote the appropriate integrating weights, and S is the positive definite diagonal matrix containing the integrating weights, s_i . We note that size of the integration weights are determined by size of the corresponding numerically approximated functions, i.e., N for (u, v, w) and $(N + 2)$ for p . Let $S(N)$ be the appropriate integrating weights for functions approximated by N grid points. To compute the necessary integrals needed for computing the adjoints numerically, we need the following integrating weight matrices

$$S_1 = \begin{bmatrix} S(N) & 0 & 0 \\ 0 & S(N) & 0 \\ 0 & 0 & S(N) \end{bmatrix},$$

$$S_2 = \begin{bmatrix} S(N) & 0 & 0 & 0 \\ 0 & S(N) & 0 & 0 \\ 0 & 0 & S(N) & 0 \\ 0 & 0 & 0 & S(N + 2) \end{bmatrix}.$$

From (E.19) and (E.21), we have

$$\psi_1^* S_2 A \psi_2 = (A^+ \psi_1)^* S_2 \psi_2.$$

Finally, adjoints of A and E are determined by

$$A^+ = S_2^{-1} A^* S_2, \quad E^+ = S_2^{-1} E^* S_2.$$

Adjoint of ζ_k can be obtained from A^+ and E^+ from (E.3). Adjoint of the projection operators onto subspaces associated with the finite and infinite eigenvalues of (A, E) are obtained similarly. For example, ζ_k^+ and P_r^+ are numerically approximated by

$$\begin{aligned} \zeta_k^+ &= S_2^{-1} \zeta_k^* S_2, \\ P_r^+ &= (\zeta_0 E)^+ = E^+ \zeta_0^+ = S_2^{-1} P_r^* S_2. \end{aligned}$$

Adjoint of B and C are determined form

$$\langle \psi, B \mathbf{d} \rangle = \langle B^+ \psi, \mathbf{d} \rangle, \quad \langle \mathbf{v}, C \psi \rangle = \langle C^+ \mathbf{v}, \psi \rangle.$$

and are numerically approximated by

$$B^+ = S_1^{-1} B^* S_2, \quad C^+ = S_2^{-1} C^* S_1.$$

Remark 7 *Note that the appropriate inner products for definition of \mathcal{A}^+ , \mathcal{B}^+ , and \mathcal{C}^+ in the standard state-space formulation (E.18) are different from that in (E.20). This is because the state vector, Ψ , is not in $L^2[-1, 1]$. Therefore, one should use a weighted inner product that yields the definition of energy of velocity fluctuations. See [7] for more details.*

E.5.2 Change of variables

The method of computing the \mathcal{H}_2 norm discussed in § E.3 is based on finite dimensional descriptor formulation in § E.2.1. Therefore, in § E.5.1, we showed how the differentiation operators and their adjoints are approximated numerically. In order to compute the \mathcal{H}_2 norm of the infinite dimensional system (E.17), we need to compute solutions of generalized projected Lyapunov equations that involve numerical approximation of operator adjoints. However, we saw that numerical approximation of the adjoint operators are not equal to complex conjugate transpose of numerically approximated operators. Rather, to obtain the adjoint operators, one should pre and post multiply the operators by symmetric positive definite matrices S_i^{-1} and S_i of appropriate size, $i = 1, 2$.

In order to be able to utilize the tools developed for solving the finite dimensional generalized Lyapunov equations in (E.6), we introduce the following change of variables

$$\begin{aligned} E_s &= S_2^{\frac{1}{2}} E S_2^{-\frac{1}{2}}, & A_s &= S_2^{\frac{1}{2}} A S_2^{-\frac{1}{2}}, \\ B_s &= S_2^{\frac{1}{2}} B S_1^{-\frac{1}{2}}, & C_s &= S_1^{\frac{1}{2}} C S_2^{-\frac{1}{2}}, \end{aligned} \tag{E.22}$$

where $S_i^{\frac{1}{2}}$ denotes matrix square root for a positive definite matrix S_i , i.e., $(S_i^{\frac{1}{2}})^2 = S_i$.

The same type of change of variable as that for A_s and E_s is done on projection operators like P_r .

The change of variables in (E.22), effectively connects the solution of the following generalized Lyapunov equations

$$\begin{cases} E G_c A^+ + A G_c E^+ = -P_l B B^+ P_l^+, \\ E G_{nc} E^+ - A G_{nc} A^+ = Q_l B B^+ Q_l^+, \end{cases} \quad (\text{E.23})$$

$$\begin{cases} E_s G_{cs} A_s^* + A_s G_{cs} E_s^* = -P_{ls} B_s B_s^* P_{ls}^*, \\ E_s G_{ncs} E_s^* - A_s G_{ncs} A_s^* = Q_{ls} B_s B_s^* Q_{ls}^*, \end{cases} \quad (\text{E.24})$$

via the following formulae

$$G_c = S_2^{-\frac{1}{2}} G_{cs} S_2^{\frac{1}{2}}, \quad G_{nc} = S_2^{-\frac{1}{2}} G_{ncs} S_2^{\frac{1}{2}}. \quad (\text{E.25})$$

Therefore, to solve the generalized Lyapunov equations involving adjoint matrices (E.23), we first solve the generalized Lyapunov equations (E.24) involving complex conjugate transpose of operators using the method discussed in § E.3.2, and then we obtain the desired solutions using (E.25).

E.6 Summary

We compute the \mathcal{H}_2 norm of plane channel flow both from descriptor and standard state-space formulations, equations (E.17) and (E.18), respectively. We have set $R_c = 2000$ and $N = 30$ in all computations.

Figure E.2 shows the \mathcal{H}_2 norm computed from both formulations as a function of κ_z for $\kappa_x = 0$. We see the the results match with less than 10^{-3} relative error.

Remark 8 *It turns out that the \mathcal{H}_2 norm associated with the non-causal or impulsive response of system (E.17) is very small ($\mathcal{O}(10^{-4})$) and is negligible in comparison with the \mathcal{H}_2 norm associated with the causal part. Therefore, only the summation of the two is shown and we have not shown separate plots for the causal and noncausal parts.*

Figure E.3 shows the \mathcal{H}_2 norm computed from both formulations as a function of κ_x for $\kappa_z = 0$. The results are very close with less than 10^{-2} relative error.

From the above results, we see that the \mathcal{H}_2 norm computed from the descriptor formulation compares very well with the \mathcal{H}_2 norm computed from the standard state-space formulation.

We note that size of the two standard Lyapunov equations (E.11) and (E.14) are determined by the number of finite and infinite generalized eigenvalues of (A, E) , respectively. In our problem with $N = 30$, these numbers turn out to be 58 and 64. Size of the Lyapunov equation that needs to be solved in standard formulation is equal to 60.

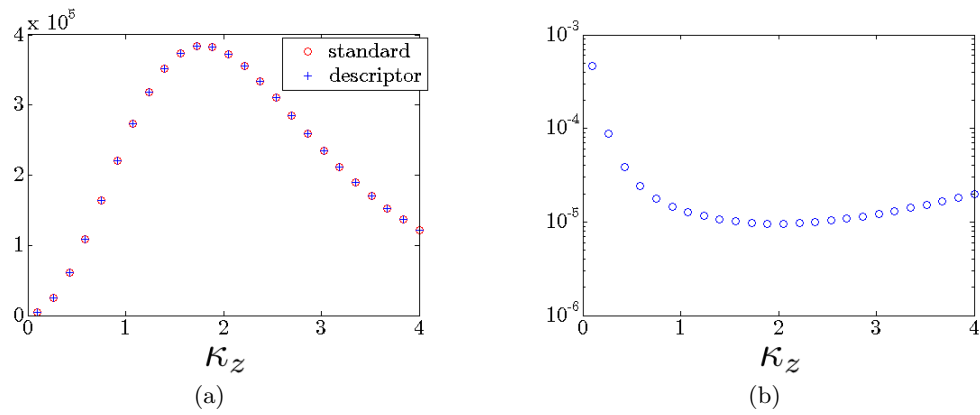


Figure E.2: (a) \mathcal{H}_2 norm computed from descriptor and standard state-space formulations for $R_c = 2000$ and $\kappa_x = 0$, (b) relative error.

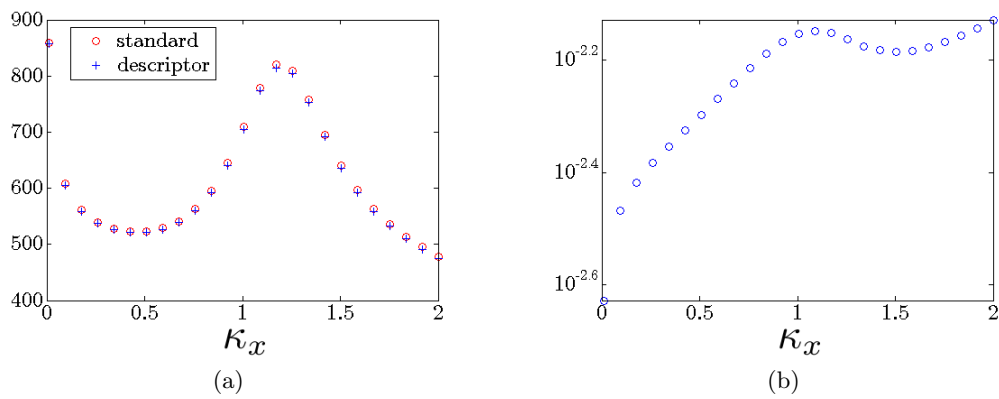


Figure E.3: (a) \mathcal{H}_2 norm computed from descriptor and standard state-space formulations for $R_c = 2000$ and $\kappa_z = 0$, (b) relative error.

Thus, cost of solving the required Lyapunov equations in both formulations is almost the same. Therefore, the difference in computational cost of obtaining the \mathcal{H}_2 norm from the two formulations is mainly determined by the cost of solving the additional Lyapunov equation plus cost of the QZ algorithms required for obtaining the Weierstrass transformation and solving the system of generalized Sylvester equations (E.9).